Reflectarray Antennas :

Operating Mechanisms, and Remedies for Problem Aspects

E'qab Rateb Fayeq Almajali

A thesis submitted to the
Faculty of Graduate and Postdoctoral Studies
In partial fulfillment of the requirements
For the PhD degree in Electrical Engineering

Ottawa-Carleton Institute for Electrical and Computing Engineering
School of Electrical Engineering and Computer Science
Faculty of Engineering
University of Ottawa

Abstract

Reflectarrays that emulate paraboloidal main-reflectors, and hyperboloidal or ellipsoidal sub-reflectors, have undergone a great deal of development over the past two decades. More recently, research on the topic has concentrated on overcoming some remaining disadvantages, re-examining certain design issues, and extending reflectarray functionality. This thesis concerns itself with fixed-beam offset-fed single-layer main-reflectarrays and sub-reflectarrays comprised of square or rectangular variable size conducting elements. Both full-wave analyses and experiment are used in all the deliberations. In order to examine reflectarray operating mechanisms the thesis first describes a component-by-component technique whereby the role of the various reflectarray parts can be assessed by determining their individual and aggregate contributions to the reflectarray near- and far-fields. This technique is used to diagnose the fact that feed-image-lobes that appear at off-centre frequencies are caused not only by the groundplane as first thought, but by an imbalance in the complex currents on the patches and groundplane at such frequencies. The use of sub-wavelength elements is shown to suppress such unwanted lobes. The thesis then uses receive- and transmit-modes analysis to show that beam squint at off-centre frequencies, often not accounted for when stating the gain bandwidth of a reflectarray, is due to the shifting of the true focal points away from the geometrical one at these frequencies. It is demonstrated that a two-feed reflectarray arrangement is capable of eliminating beam squint, and that the use of smaller focal length to aperture size (F/D) ratios removes the grating lobes that can appear in such two-feed reflectarrays due to clustering of the aperture amplitude distribution. Finally, the thesis studies the effect of the reality that the angle of incidence of the feed fields on the various reflectarray elements is not the same for all elements, even though this is most often assumed when using element reflection phase versus element size databases in performing reflectarray designs. Careful full-wave analysis reveals that it is not only the dependence of element reflection phase on incidence angle that is important, but that the individual element pattern beamwidths change and distort as this angle increases. This is important not only from the point of view of the coupling of the feed fields to the elements, but also as far as the angular sector within which the reradiated fields are important. Thus sub-reflectarrays, whose radiation patterns are considerably wider than main-reflectors, are more susceptable to incidence angle effects. It is shown that the use of sub-wavelength elements in a reflectarray largely ensures its immunity to such effects.

Acknowledgements

It would not have been possible to write this doctoral thesis without the help and support of the kind people around me, to only some of whom it is possible to give particular mention here.

Above all, I would like to thank my thesis supervisor, Dr. Derek McNamara, for his contributions, support and patience throughout the developments of this thesis. This thesis would not have been possible without his help and guidance over the past few years.

I would also like to acknowledge:

- Research collaborators Dr. Jafar Shaker and Dr. Reza Chaharmir at the Communication Research Centre Canada (CRC) for the fruitful discussions we had and the use of CRC's fabrication and measurement facilities.

- Mr. David Lee of CRC for his continuous technical assistance during measurements.

- Dr. Jonathan Ethier of CRC for his constructive suggestions that helped in diagnosing the source of grating lobes in two-feed reflectarray radiation pattern.

- Mr. Michel Cuhaci, the former manager of the Advanced Antenna Technology (RAAT) group at CRC, who gave me the opportunity to work on some projects at CRC.

- NSERC and the University of Ottawa for the financial support over the years.

Finally, I would like to thank my parents Rateb and Menwah Almajali for their care and guidance that began long before graduate studies. My wife Rania and my sister Ansam have given me their unequivocal support throughout, as always, for which my mere expression of thanks does not suffice.

List of Symbols

a_{nx}	hertzian dipole complex amplitude along the x-axis
a_{ny}	hertzian dipole complex amplitude along the y-axis
d	relectarray inter-element spacing
d_n	distance from the virtual focal point to the sub-reflectarray surface
D	diameter (generally of a reflectarray or a reflector)
d_x	unit cell size or inter-element spacing along the x-axis
d_y	unit cell size or inter-element spacing along the x-axis
e	eccentricity of a sub-reflector
$\vec{E}$	electric field (vector)
E_x	electric field component along the x-axis
E_y	electric field component along the y-axis
E_z	electric field component along the z-axis
E_{inc}	incident electric field
E_t	total electric field
f	frequency
f_0	centre frequency
F	focal length (generally of a reflectarray)
F_R	real focal length (generally of a sub-reflectarray)
F_V	virtual focal length (generally of a sub-reflectarray)
h	height or thickness of a dielectric substrate
$\bar{\mathrm{H}}$	magnetic field (vector)
H_x	magnetic field component along the x-axis
H_y	magnetic field component along the y-axis
H_z	magnetic field component along the z-axis
J_x	surface current density along the x-axis

J_y surface current density along the y-axis

k_0 free-space wave number

k wave number

$\hat{k}_{inc}$ propagation direction unit vector

L length of a conducting element (like a patch)

m integer number

w width of a conducting element (like a patch)

n integer number

$\hat{n}$ Normal unit vector

P geometrical focal point location

R_n distance from the focal point to the reflectarray surface

x rectangular coordinate

y rectangular coordinate

z rectangular coordinate

ε_r relative permittivity (dielectric constant)

θ_{inc} Incidence angle

λ wavelength

λ_0 free-space wavelength

μ permeability

μ_0 free-space permeability

μ_r relative permeability

ϕ_{inc} Incidence angle

ψ_n the required scattered field phase generated by a conducting element

ΔF change in focal length

δf change in frequency

Table of Contents

CHAPTER 1: Introduction **1**

1.1 Introductory Remarks on Reflectarrays **1**
1.2 Overview of Thesis **2**
Chapter 1 References **6**

CHAPTER 2: Literature Review and Theoretical Background **7**

2.1 Introduction **7**
2.2 Review of Half-Wavelength Reflectarray Antennas **8**
2.2.1 The Reflectarray Antenna 8
2.2.2 Reflectarray Foundational Works and General Design Guidelines 10
2.2.3 Recent Developments and Applications 15
2.3 Sub-Wavelength Reflectarrays **27**
2.3.1 Review of Sub-Wavelength Reflectarrays 27
2.3.2 Phasing Characteristics of Sub-Wavelength Elements 28
2.4 Reflectarray Problems Aspects **30**
2.4.1 Introductory Remarks 30
2.4.2 Feed-Image Lobe 31
2.4.3 Beam Squint in Offset-Fed Reflectarrays 35
2.4.4 Angle of Incidence Effects on Reflectarray Operation 37
2.5 Reflectarray Operating Mechanisms **41**
2.5.1 The Importance of Investigating Reflectarray Operating Mechanisms 41
2.5.2 Review of the Existing Work on Reflectarray Operating Mechanism 42
2.6 Conclusion **44**
Chapter 2 References **45**

CHAPTER 3: An Investigation of Reflectarray Operation Using Its Component Current Contributions **51**

3.1 Introduction **51**
3.2 Using 2D Method of Moments Analysis in Elucidating Reflectarray Operation **52**
3.2.1 Preliminary Remarks 52
3.2.2 Reflectarray Configuration and Computational Model 52
3.2.3 2D Reflectarray Design Considerations 53
3.2.4 Examination of the Contributions of the Constituent Currents 54
3.3 Investigating Reflectarray Operation Using 3D Analysis Technique **59**
3.3.1 Introduction 59
3.3.2 Extraction of the Conduction Currents on Reflectarray Components From the HFSS Model 59

3.3.3 Reflectarray Far-Field Radiation in Terms of Its Component Current Contribution 65
3.3.4 Reflectarray Near-Field in Terms of Its Component Current Contribution 69
3.4 Concluding Remarks 72
Chapter 3 References 73

CHAPTER 4: Feed Image Lobes in Offset-Fed Reflectarrays: Diagnosis and Solution 74

4.1 Introduction 74
4.2 Diagnosis of the Source of Feed-Image Lobes in the Radiation Patterns of Offset-fed Reflectarrays 75
4.2.1 Preliminary Remarks and Design Considerations 75
4.2.2 Feed-Image Lobe Behavior at Centre- and Off-Centre Frequencies 77
4.3 Feed-Image Lobe Reduction Using Sub-wavelength Reflectarray 98
4.3.1 Introduction 98
4.3.2 Feed-Image Lobe Suppression at Off-Centre Frequencies 98
4.4 Far-Field Measurement Results 103
4.5 Concluding Remarks 111
Chapter 4 References 112

CHAPTER 5: Beam Squint in Offset-Fed Reflectarrays: Diagnosis and Solution 114

5.1 Introduction 114
5.2 Invistigation into the Focal Region Shift in Reflectarrays 115
5.2.1 Preliminary Remarks 115
5.2.2 Full Wave Recive-Mode Analysis 116
5.2.3 Focal Point Behavior with Frequency 118
5.2.4 Impact of Geometrical and Non-Geometrical Factors on the Amount of Focal Point Shift in Reflectarrays 121
5.2.5 Fresnel Zone Boundary Considerations 126
5.3 Diagnosis of the Source of Beam Squint in the Radiation Patterns of Offset Fed-Reflectarrays 131
5.3.1 Introduction 131
5.3.2 Receive-Mode &Transmit-mode Analyses Reconciliation 131
5.3.3 Theoretical and Experimental Confirmation 135
5.4 Two-Feed Single-Beam Reflectarray 139
5.4.1 Introduction 139
5.4.2 Two-feed Single-Beam Reflectarray Elements Phase Realization 139
5.4.3 Improving Two-feed Reflectarray Gain and Bandwidth Using Sub-Wavelength Configuration 140
5.5 Beam Squint Suppression in Offset-Fed Reflectarrays 147
5.5.1 The Use of Two-feed Reflectarray to Suppress Beam Squint 147

5.5.2 Full Wave Analysis of the Two-Feed Reflectarray 149
5.5.3 Experimental Ratification 154

5.6 Identification & Mitigation of High Sidelobes in Two-feed Reflectarrays 157
5.6.1 Introduction 157
5.6.2 Identification of the Grating Lobe Source Using Feed Field, and Scattered Field, Distributions over the Reflectarray Aperture 157
5.6.3 Two-Feed Reflectarrays with Reduced Sidelobes 162
5.6.4 Experimental Ratification 165
5.7 Concluding Remarks 167
Chapter 5 References 168

CHAPTER 6: Angle of Incidence Effects on Reflectarray and Sub-Reflectarray Operation 170

6.1 Introduction 170
6.2 Some Background - Oblique Incidence Options 172
6.3 Reflection Phase versus Incidence Angle: Observations and Impact On Reflectarray Gain 173
6.4 Sub-Wavelength Sub-Reflectarrays 184
6.5 Concluding Remarks 195
Chapter 6 References 196

CHAPTER 7: Conclusions and Future Work 197

7.1 The Contributions of the Thesis 197
7.2 Future Work 199
Chapter 7 References 200

CHAPTER 1
Introduction

1.1 Introductory Remarks on Reflectarrays

High-directivity antennas are needed in many wireless communications, radar and remote sensing applications. Paraboloidal reflector antennas and constrained-fed planar array antennas were for a long time the only options available to the designer to achieve such performance. However, over the past two decades the reflectarray antenna [1,2] has emerged as an alternative. Like paraboloidal reflectors, it is fed by a low-directivity feed radiator located at a focal point. Unlike the conventional paraboloidal reflector it is a flat structure, and can consist of a structure as relatively simple as a single-layer grounded dielectric substrate on which is printed an array of properly dimensioned conducting shapes. Unlike a printed planar array it does not have a complicated constrained beamforming network. It is in essence a space-fed printed planar array. In this thesis we are interested solely in single-layer reflectarrays.

An ordered account of the great deal of development that has taken place on reflectarrays that emulate paraboloidal reflector antennas can be found in [1]. More recently, research on the topic has concentrated on overcoming some remaining disadvantages, examining certain design issues, and extending reflectarray functionality.

The disadvantages have been bandwidth limitations, lower than expected aperture efficiencies, the presence of feed-image-lobes, and beam-squinting. Bandwidth limitations have been much alleviated through the use of sub-wavelength elements [3,4,5]; by the term sub-

wavelength is meant elements whose inter-element spacing is less than the conventional half-wavelength value used earlier). The use of single-layer fragmented elements [6] has been shown to recover some of the "lost" aperture efficiency.

Design issues include questions as to whether, from a practical standpoint, the actual incidence angle of the feed fields on each reflectarray element needs to be accounted for in the design database.

Extensions have included the design of sub-reflectarrays to emulate ellipsoidal or hyperboloidal sub-reflectors of dual systems [7], and reconfigurable main-reflectarrays [8].

In this thesis we diagnose the causes of, and provide solutions to, the feed-image-lobe and beam-squinting problems in fixed-beam offset-fed single-layer reflectarrays of square and rectangular conducting patches. We also examine the implications of angle-of-incidence issues for both main- and sub-reflectarrays, show that this effects more than just the values of the reflection phases of the various elements, and demonstrate how the lower sensitivity of sub-wavelength elements to such effects permits the design of improved sub-reflectarrays. The above is made possible by an ability that has been developed to perform a detailed examination of the individual contributions of the various reflectarray components to its performance, and investigate the operating mechanism of reflectarrays, using full-wave analysis.

1.2 Overview of the Thesis

In Chapter 2, we will review the literature and the theoretical background necessary for the developments that form the subject of this thesis. We will begin by outlining the concept, design guidelines and some important developments of reflectarray antennas. Multi-feed reflectarrays, as well as sub-reflectarrays, are given some emphasis as they are used in the developments of this thesis. We will also review progress in sub-wavelength reflectarrays, considering most of their important aspects. This is done because the sub-wavelength concept is used in this thesis to propose solutions for some problem issues, like the feed-image lobe in Chapter 4 and the angle of incidence effects in Chapter 6. We next discuss the problem aspects we aim to diagnose and

mitigate in this thesis. Feed-image lobe, beam squint and angle of incidence problem concepts are explained, and their effects elaborated on, using results obtained by the author from fully simulated reflectarray models. The literature pertaining to the above problems will also be summarized, with some emphasis on the reported diagnostics and solutions.

In Chapter 3 we will discuss a component-by-component technique we use to assess the role of the various reflectarray parts, namely the elements[1], the groundplane and the dielectric substrate in reflectarray antenna operation. This is achieved by determining these parts' individual and aggregate contributions to the reflectarray near- and far-fields using the conduction currents on the elements and the ground plane as well as the polarization current within the dielectric substrate. The technique will be applied to 2D- and 3D-reflectarray models. We include a 2D model despite having a 3D one in order to elucidate the technique; it will be shown that we cannot directly output all that is needed from the available 3D-reflectarray model. Furthermore, our experience with the 2D modelling provides the confidence needed to be sure that we are correctly interpreting the physical quantities we indirectly extract from the output of the 3D-reflectarray models. As a consequence of applying the above mentioned technique, we will show for the first time in the literature that the radiating elements and the groundplane contribute almost equally to the reflectarray near- and far-fields. This is confirmed from the current amplitude distributions which look identical on these parts. The polarization current contribution is shown to be somewhat minor, although the substrate role cannot be reduced to this contribution as its existence affects the conduction currents distribution on the conduction parts of the reflectarray. The significance of this technique stems from the fact that it forms the corner stone in diagnosing the source of the feed-image lobe problem issue we will discuss in Chapter 4, and the cause of reflectarray and sub-reflectarray performance degradation due to the angle of incidence effects which will be explained in Chapter 6.

In Chapter 4, we will begin by thorough utilization of the technique devised in Chapter 3 to establish the source of the unwanted feed-image lobe problem aspect in offset-fed reflectarrays. We will show, as a consequence of this analysis, that both the groundplane and the conducting elements contribute to the feed image lobe, with little contribution to it created by the

[1] The conducting shapes on the reflectarray substrate (like a patch element).

polarization current. The individual and combined current density contributions will be generated and studied at the centre frequency and at some off-centre frequencies to confirm that in a properly designed reflectarray the feed image lobe does not appear at the centre frequency because the contributions of the element and groundplane currents interfere destructively around the specular direction. At off-centre frequencies we show that there is an imbalance between the element and groundplane currents, and hence their individual contributions to the far-fields, caused by the changes in the element reflection phases with frequency (phase error). This leads to the creation of the feed image lobe in the resultant reflectarray pattern. Accordingly, we next demonstrate theoretically and experimentally, the use of sub-wavelength reflectarrays to eliminate feed image lobes in reflectarrays of patch or dipole elements, hence improving reflectarray performance.

In Chapter 5 we diagnose the cause of, and provide a solution to, the beam-squinting problem in fixed-beam offset-fed single-layer reflectarrays. We start by thoroughly investigating the focal point shift[2] with frequency in offset fed-reflectarrays, an important reflectarray operating aspect that has not been given enough consideration in the literature. The impact of important factors such as reflectarray size, focal length, element type and lattice size on the amount of focal shift versus frequency is established using a full-wave receive-mode[3] analysis. This, and the reconciliation of the receive-mode analysis results with corresponding transmit-mode results are used to show that beam squint is mainly caused by such focal shift due to the creation of a phase tilt on the reflectarray surface at off-centre frequencies. A solution to beam squint is next found and validated. This solution is based on having two focal points and hence two feeds, instead of one, placed at each of the symmetrically located focal points. These focal points are found to migrate in unison as the frequency changes, resulting in an aperture phase distribution that does not have a net tilt at any frequency, which eliminates any chance of beam squint creation. Prior to showing the use of the two-feed reflectarray as a means to suppress beam squint, the gain and bandwidth of this configuration are shown to be substantially improved by using a sub-wavelength element spacing instead of the half-wavelength one. The cause of another problem

[2] The focal point shift concept will be discussed in Chapter 2.
[3] Receive- and transmit-modes of operation will be explained in Chapter 5.

aspect of the two-feed reflectarray, namely the appearance of grating lobes[4], is identified and accordingly solved at the end of this chapter.

In Chapter 6, the angle of incidence effect on reflectarray and sub-reflectarray operation will be investigated. We show that not only does incidence angle alter the element reflection phase, but that for oblique incidence the element beamwidth narrows and the element pattern deforms. We examine the impact of including incidence angle effects in the design database of half-wavelength reflectarrays, and compared to that for sub-wavelength reflectarrays, for designs with F/D = 1.0 and F/D = 0.5. Although it is shown that the inclusion of the angle of incidence effect in the half-wavelength reflectarray design improves its performance, the sub-wavelength reflectarray performance is shown to decently outperform its corresponding half-wavelength one even when the angle of incidence changes are included in the latter design. This sub-wavelength superiority is shown to be caused by its very much smaller element pattern deformation with angle of incidence, in addition to its lower reflection phase change with incidence angle compared to half-wavelength lattices. We next utilize the lower sensitivity of sub-wavelength elements to the angle of incidence effects to design improved sub-reflectarrays. The sub-wavelength sub-reflectarrays are shown to outperform their corresponding half-wavelength ones, particularly when the design demands a pattern with a wide angular coverage. This is illustrated by first studying the scattered field of these sub-reflectarrays on their own, after which these scattered patterns are used to illuminate a solid main reflector, as is the case in practice.

Lastly, in Chapter 7, we conclude with a list of the major contributions of the thesis. We will also suggest some future work that would further improve the fixed-beam single-layer main-and sub-reflectarray performance.

[4] These grating lobes do not result from too large an element spacing, as will be illustrated in Chapter 5.

Chapter 1 References

[1] J.Huang and J.A.Encinar, Reflectarray Antennas (Wiley, 2008).

[2] J.Shaker, M.R.Chaharmir and J.Ethier, Reflectarray Antennas: Analysis, Design, Fabrication, and Measurement (Artech House, 2013).

[3] D.M.Pozar, "Wideband reflectarray using artificial impedance surface", Electronic Letters, Vol.43, No.3, pp.148-149, February 2007.

[4] M.Mussetta, P.Pirinoli, R.E.Zich and M.Orefice,"Design of printed microstrip reflectarrays reducing the groundplane reflection", Proceedings URSI General Assembly, New Delhi, India, 2005.

[5] P.Nayeri, F.Yang and A.Elsherbeni, "Broadband reflectarray antennas using double-layer subwavelength patch elements", IEEE Antennas Wireless Propagation Letters, Vol.9, pp. 1139-1142, July 2010.

[6] J.Ethier, D.A.McNamara, J.Shaker and M.R.Chaharmir, "Reflectarray design using similarity-shaped fragmented sub-wavelength elements", Electronics Letters, Vol.48, No.15, pp.900-902, July 2012.

[7] E.Almajali, D.A.McNamara, J.Shaker and M.R.Chaharmir, " Derivation and validation of the basic design equations for symmetric sub-reflectarrays", IEEE Transactions on Antenna and Propagation, Vol.60, No.2, pp. 2336-2346, February 2012.

[8] S.V.Hum and J.Perruisseau-Carrier, "Reconfigurable reflectarrays and array lenses for dynamic antenna beam control: a review", IEEE Transactions on Antenna and Propagation, Vol.62, No.1, pp.287-295, January 2014.

CHAPTER 2
Literature Review and Theoretical Background

2.1 Introduction

The main objective of this thesis is to improve reflectarray antenna performance. Thus we lay the foundation of reflectarray antennas in Section 2.2 by defining its concept and functionality, and describing the foundational papers as well as the practical reflectarray design guidelines which we use to design all reflectarrays in this dissertation. In Section 2.2 we also include a literature review of developments in reflectarrays, with an emphasis on multi-feed reflectarrays and sub-reflectarray antennas, since these works are used in the developments of this thesis. Section 2.3 is dedicated to a review of the features and developments of reflectarrays that use reduced inter-element spacing, so-called "sub-wavelength reflectarrays". Sub-wavelength reflectarrays are used to reduce the effects of some reflectarray problem issues in Chapters 4 and 6.

The improvement of reflectarray and sub-reflectarray performance in this thesis relies upon the diagnosing and troubleshooting of certain reflectarray problem aspects, which are shown to degrade reflectarray performance considerably, namely feed-image lobes, beam squint and the angle of incidence effects. Therefore in Section 2.4 these problem issues and their unwanted effects on reflectarray antenna performance are introduced. Included is a literature review of all papers discussed these problems as well as a description of all trials to mitigate them. This will enable the reader to recognise that despite the fact that these problems are deleterious, they have not been given enough consideration in the literature.

Lastly, in Section 2.5 the importance of investigating some reflectarray operating mechanisms based upon the determination of the reflectarray component current contributions to the far-field

and the behavior of the reflectarray focal point with frequency is highlighted, with related works in the literature reviewed. These mechanisms are used in Chapter 4 and Chapter 5 to diagnose and mitigate feed-image lobe and beam squint problems in offset-fed reflectarrays.

2.2 Review of Half-Wavelength Reflectarray Antennas

2.2.1 The Reflectarray Antenna

Prior to 2007 almost all reflectarrays reported in the literature used an inter-element spacing of a half-wavelength at the design frequency. In this thesis we will refer to theses as half-wavelength reflectarrays in counterpart to sub-wavelength reflectarrays reviewed in Section 2.3.

In many antenna applications it is desired to achieve a directive antenna pattern such that the energy radiated by the antenna is concentrated in a specified angular region. Two of the most common techniques that have been employed to achieve this are reflectors and arrays. The reflector utilizes a primary feed to illuminate a reflecting surface. The energy from the primary feed is collimated by the reflector surface to form an antenna pattern with the desired side lobe level. In contrast, the array utilizes discrete elements to form the desired antenna pattern. A feed network distributes the energy to each of the discrete elements of the array.

A reflectarray represents a combination of a reflector antenna and a planar array antenna that uses a suitable phasing scheme of its elements to convert the incident wavefrontfrom the feed to another wavefront with a prescribed phase [1, pp.1-2]. A reflectarray is basically either a flat or conformed reflecting surface that consists of an array of reflecting elements which are printed on grounded dielectric substrate(s) with a feed(s) antenna that spatially illuminates these elements. The elements are designed in such a way as to correctly transform the phase of the incident wave, as is done in the traditional curved reflectors or sub-reflectors [2, 3]. Note that by "elements" we will in this thesis mean just the conducting shapes on the reflectarray substrate, even though it is understood that these shapes plus the groundplane constitute the complete elements of the reflectarray. The most common feed type used to illuminate reflectarray

antennas is the feed-horn, either pyramidal or conical (e.g. corrugated) horns, although other less conventional feed types have been reported [4]. As with conventional curved reflector antennas, it is possible with offset feeds to eliminate the blockage effects in reflectarrays [5, 6]. Reference [7] shows that the aperture efficiency can be improved using the offset feed configuration. An example of a reflectarray comprised of printed elements spatially fed by a feed-horn is shown in Figure 2.1.

Although reflectarary antennas suffer from several problems, like limited bandwidth, feed-image lobes, beam squint and the performance degradation due to the angle of incidence effects, which are discussed with great detail in this thesis, they have several advantages over an array or a conventional reflector. Unlike the array, there is no complex feeding network which introduces a high loss, unwanted phase shifts of the transmitted or received signal as frequency changes, and spurious radiation. A reflectarray consequently can exhibit higher efficiency compared to phased arrays. In addition to the fact that beam scanning and beam shaping are easier and more efficient when performed using reflectarrays than conventional phased arrays, the use of lithographic technology as the method of fabrication paves the way for integration of active elements into the reflectarray elements which brings many possibilities of designing reconfigurable reflectarrays for beam scanning, adaptive beam shaping, and power amplification [8-10]. Reflectarrays from the other side are easier to manufacture than the classical curved reflectors. Offset reflectors are difficult to manufacture in many cases due to the particular surface shape, especially at higher microwave frequencies. For the most part, the reflectarray can be conformed to a given surface shape, reducing the bulk and mechanical complexity of the traditional reflector antennas; this advantage is of importance for new space applications because the large surface of the reflectarray can be folded or rolled as part of the spacecraft payload before being deployed [1, pp.137-140].

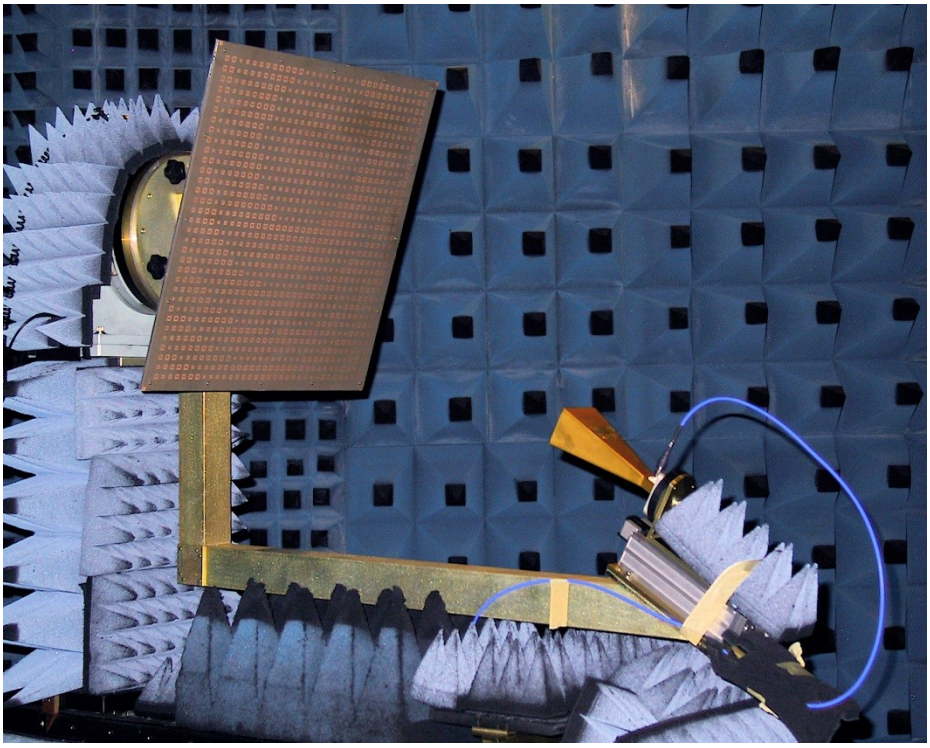

Figure 2.1: A reflectarray composed of printed elements spatially fed by feed-horn in an-echoic far-field chamber. (Courtesy of the RF Technologies group, Communication Research Centre Canada)

2.2.2 Reflectarray Foundational Works and General Design Guidlines

The first implementation of a reflectarray was done early 1960's [11]; the elements of that reflectarray were terminated waveguides of different lengths. By changing these lengths the correct phase transformation could be achieved to emulate the operation of a traditional parabolic reflector. This type of reflectarray was very cumbersome and the technology was apparently not pursued. However, with the rapid development of microstrip technology in the early 80's, and the need for high gain, low cost antennas, the microstrip reflectarray was conceived [12]. The reflectarray in [12] was designed using microstrip patches of an identical size and a plurality of individual phase-controlling passive transmission lines, each being coupled to a respective mictrostrip patch, were used to yield the required phasing scheme. Around the mid-1990s, a simple reflectarray design method to realize mictrostrip reflectarrays was first described by Pozar in [13]; instead of using phase controlling stubs or transmission lines attached to the patches [12], the patches sizes themselves are changed to obtrude the desired phase conversion. This

design technique, which we use in this thesis, is considered the reflectarray practical design approach [1, pp.79-81]. Its design guidelines are outlined as follows:

A- Reflectarray Design Parameter Selection

There are several design parameters that must be selected to design a reflectarray, and the values selected depend on the frequency, bandwidth, polarization, loss and cost. The first of these parameters is the aperture shape and size. The reflectarray aperture shape could be rectangular, circular, elliptical or any shape that suits the given application. In this thesis the shape of the prototype is always square with dimension D as shown in Figure 2.2. The use of such a square reflectarray shape rather than a circular one does not lead to any noticeable degradation of the reflectarray performance. The main factors that govern the size are the desired gain and the type of the classical curved reflector that we want to emulate using a reflectarray. The second parameter to be selected is the size of the unit cell *dx* and *dy* shown in Figure 2.2. The size of the unit cell determines the inter-element spacing and this spacing must be small enough to avoid grating lobes.

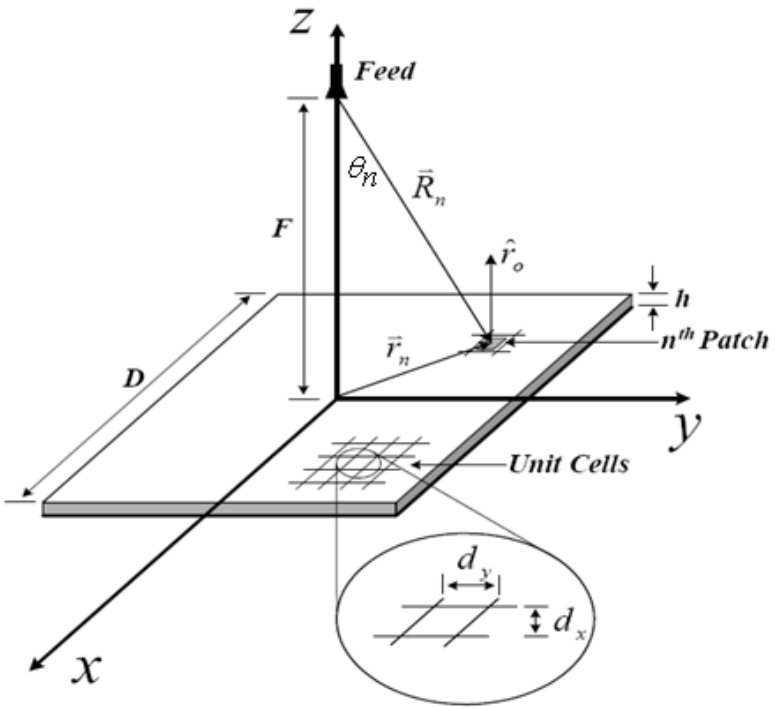

Figure 2.2: Reflectarray Design Parameters. (After [14])

The third design parameter to consider is the feed height from the reflectaray or what usually so called “the focal length” which is always denoted as *F* in this thesis. The spillover and taper efficiencies are greatly governed by this parameter and a proper feed-horn needs to be selected according to the *F/D* value of the reflectarray. Typically *F* is selected to have an edge taper of -10dB illumination, due to the feed pattern, at the edges of the reflectarray [1, 14].

The fourth point in the selection process is to choose the shape of the radiating elements that form the reflectarray. This depends mainly on the required bandwidth and polarization, as well as the ease of fabrication and analysis. As shown in Figure 2.3, there are several element shapes one can choose to achieve the required electrical phase conversion. One can use variable-size patches, dipoles, or rings [15-17] so that the elements can have different scattering impedances and thus different phases to compensate for the different feed-path delay.

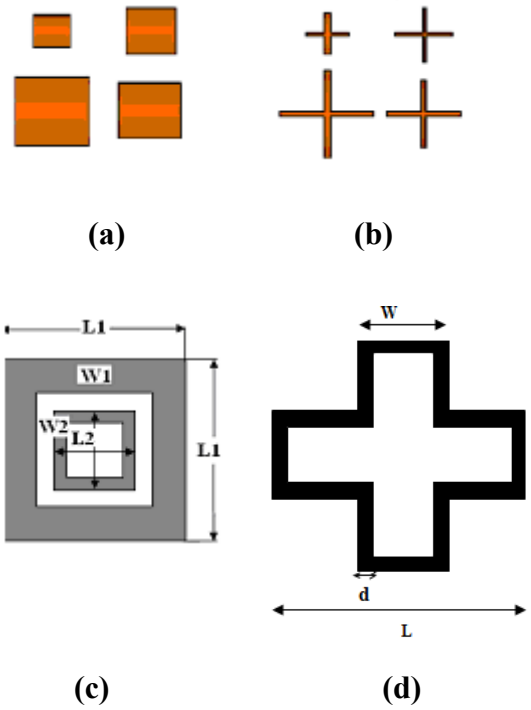

Figure 2.3: Various reflectarray elements, (a) variable-size patches, (b) variable-size cross dipoles, (c) variable-size double square rings and double circular rings ((c) Adapted from [17]), (d) variable-size single cross ring.

The types of radiating element we selected in this thesis are the variable-size rectangular and square patches for linear polarization. Using elements of variable size allows more freedom (than

fixed size elements with stubs for example) in laying out an array with reasonable bandwidth and simpler analysis, as well as having the capability to use dual or circular polarizations. It is worth mentioning that the design procedure for reflectarrays with any other variable-size element shape matches that for variable size patch except as far as the radiation pattern calculation is concerned since each element shape has its own radiating characteristics and hence its own pattern.

Finally one must select a substrate and its thickness. The selection of the substrate has an impact upon the bandwidth of the reflectarray and the manufacturing etching tolerance of the radiating elements, since it affects the slope of the reflected phase versus element size design curves, which will be discussed next, and affects the range of the reflected phase change [17].

B- The Database Generation and the Required Phase Realization

In reflectarrays of variable element sizes, which we use in this thesis, the element (patch) dimensions are adjusted to realize the required phase conversion. For example if the reflectarray is designed to emulate a parabolic reflector, an equi-phase aperture field distribution is needed to transform the incident spherical wavefront into a scattered planar wavefront. To achieve this objective, with reference to Figure 2.2, the phase (ψ_n) generated by each patch element on the reflectarray surface should satisfy equation (2.1) shown below [2]

$$k_0(R_n) - \psi_n = \pm 2n\pi \qquad (2.1)$$

where n is an integer, k_0 is the free space wavenumber, and ψ_n is the scattered phase generated by the *nth* patch located on the reflectarray surface at a distance R_n from the reflectarray focal point. Quantity $\pm 2n\pi$ is a constant added to fix the phase delay contour to a realizable value. To realize the desired phase values that are calculated using equation (2.1), one should start by generating a set of data for the phase of the reflected field of a uniform infinite array of identical patches versus patch size. This infinite array approach [1 pp.79-80, 2], which assumes all surrounding elements are identical, only approximates the final situation where the elements are not all identical, but has been shown to be a very good approximation; the desired phase that is to be imparted by the patch changes gradually on the surface of the reflectarray. Therefore, each

locality of the reflectarray can be assumed to be an infinite periodic structure that is illuminated by a plane wave whose angle of incidence is dictated by the relative location of the feed at the given locality. The infinite periodic structure approximation accounts approximately for the mutual coupling effects due to surrounding elements which gives an additional merit to this approach.

In this thesis the full-wave analysis to obtain the reflection phase data has been done using the commercial code HFSS [18]. HFSS is based on the finite element technique, and simulates the infinite array approach by using appropriate periodic boundary conditions (theoretical waveguide simulator). Its reliability has been proved practically in [19] through comparing theoretical waveguide simulator results with the results of an equivalent real waveguide simulator using the same patch dimensions. Figure 2.4(a) shows an example of a patch element unit cell (theoretical waveguide simulator), with the phase of the reflected field versus patch size obtained using HFSS at different frequencies shown in Figure 2.4(b). Once the desired reflection phases are obtained, the patch dimensions can be selected to satisfy any phase correction ψ_n required. In other words after all ψ_n values are calculated using equation (2.1), the corresponding required sizes, which satisfy these phase values, can be looked up from the generated reflection phase data. It should be noted, with reference to Figure 2.4, that if the E-field is x-directed then the dimension of the patch along the y-axis (width) is selected and remains fixed when the rectangular patch is used and the dimension of the patch along the x-axis (length) is varied, and vice versa depending upon the feed polarization. However, if a square patch is used, the E-field polarization can be either x- or y-directed with no fixed dimension.

In Figure 2.4(b), two phase related quantities are important. The first is the range of phase values actually achievable; ideally 360°. The second is the slope of the phase versus length curve. Regarding the attainable phase range, a 330° phase range is possible for patch elements if a thin substrate is selected. This phase range is enough for carrying out practical designs [1, pp.49]. If the thickness of the dielectric substrate is increased, the total phase range is reduced to

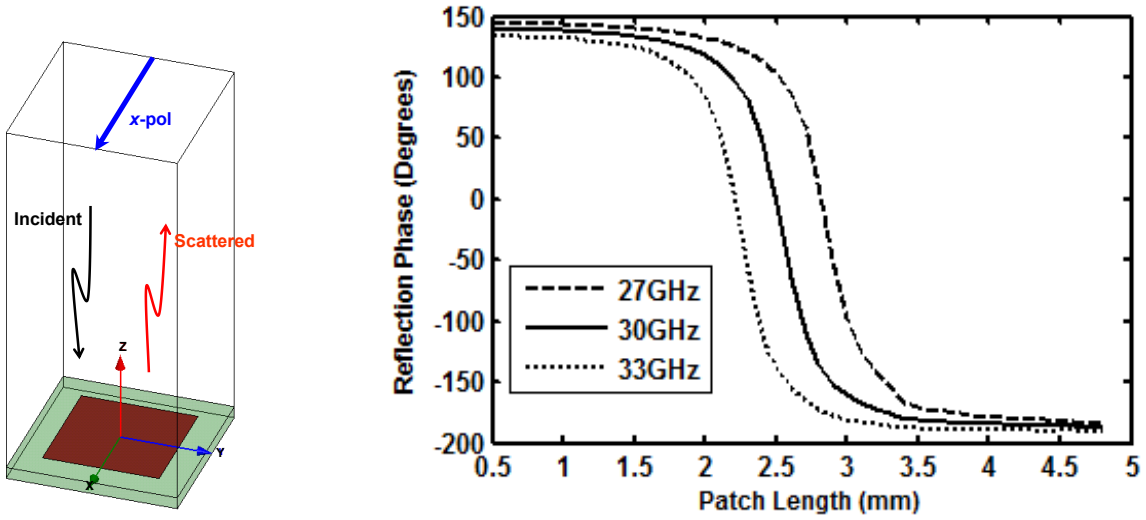

(a) **(b)**

Figure 2.4: (a) Patch element unit cell as part of an infinitely periodic structure, (b) reflected phase versus element length from an infinite array of identical square patches using HFSS, centre frequency=30GHz, E-plane=H-plane spacing=5mm, substrate is Rogers 3003 with thickness=0.508mm, incidence angle is 0^{o}.

less than 300^{o}, and then more phase errors will lead to bandwidth degradation of reflectarrays. The phase curve slope also affects the bandwidth of the reflectarray, as the curve with smaller slope leads to less phase error when the electrical size of the elements changes with frequency. Figure 2.4(b) also reveals that the reflection phase is most sensitive to frequency variations near resonance and less so near the edges of the S-shaped curve.

2.2.3 Recent Developments and Applications

Starting from early 2000s, much has been done to improve reflectarray antenna bandwidth performance and adding important functional features to reflectarrays such as beam shaping, enhancing the pattern scanning capability, using reflectarrays for dual-band operation, using multi-feed reflectarrays for spatial power combining and emulating sub-reflectors in dual-reflector systems by sub-reflectarrays. In what follows of this section a description of each of the aforementioned advances is given. More details about some of these developments and other reflectarray applications are elucidated in textbooks [1,20] and in [21] that are dedicated to communicate reflectarray theory and aspects in a pedagogic manner.

A. Improving Reflectarray Bandwidth

Improving the bandwidth characteristics of reflectarray antennas has been a main subject in reflectarray research and development since early 1990's. Many articles have been published suggesting solutions to the reflectaray bandwidth restricting factors. The bandwidth performance of reflectarrays is limited mainly by two factors: One is the relatively narrow bandwidth of the radiating element (patch) and the other is the differential spatial path delay [22, 23]. Once the elements sizes have been chosen to realize the desired phase at some central frequency, as elaborated in Section 2.2.2, these sizes might not achieve the required phase value for a different frequency. This leads to loss of gain of the reflectarray antenna for frequencies other than its design frequency as a result of growing phase error on the radiating aperture of the antenna. To improve the element bandwidth, techniques such as using a wide patch [14], thick substrate [24], stacking of multiple patches [25] and using more elaborate broadband radiating elements [26] have been employed. To the best of the author's knowledge, the highest 1dB gain bandwidth achieved using the aforementioned element bandwidth improvement techniques was 30% in [26] for a reflectarray of $D=16\lambda_o$. Multi cross loop elements were used in the design and the performance of the reflectarray was optimized at off-centre frequencies. For a relatively large reflectarray designed by the same authors in [27] using a similar element type and the same design technique, the bandwidth dropped to 12% since the size of the reflectarray tripled $(D=48\lambda_o)$. This reveals that the spatial phase delay dominates in reflectarrays of electrically large aperture size.

The second reflectarray bandwidth limiting factor is the spatial path/phase delay [22, 23]. Figure 2.5 demonstrates the special path delay concept. ΔS is the difference between the electrical paths S1 and S2. This difference may be several wavelengths at the centre frequency for a large aperture reflectarray. Since the phase shift in reflectarray elements is limited to the 360^o range, and phase delay is only compensated at the central frequency, the phase error at different frequencies increases for large values of phase delay which produces frequency excursion error in the radiated phase front [1, pp.4-5].

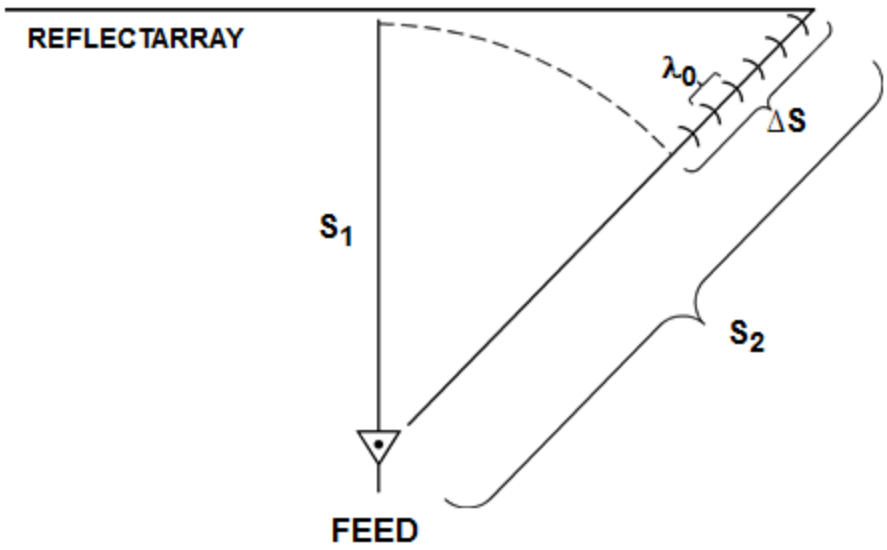

Figure 2.5: Differential spatial phase delay of reflectarray. (Adapted from [1])

Some sophisticated solutions have been presented in [1, pp.106-113] to overcome the spatial patch delay problem in large reflectarrays. One method uses time delay lines or partial time delay lines instead of the phase delays. This method introduces an additional insertion loss and needs real estate for the lines, which makes it more complex and pricy. Another method is to use, instead of a complete flat reflectarray surface, a concavely curved reflectarray with piecewise flat surfaces [28]. A reflectarray with piecewise flat surfaces is called the multifacet reflectarray, and is shown in Figure 2.6.

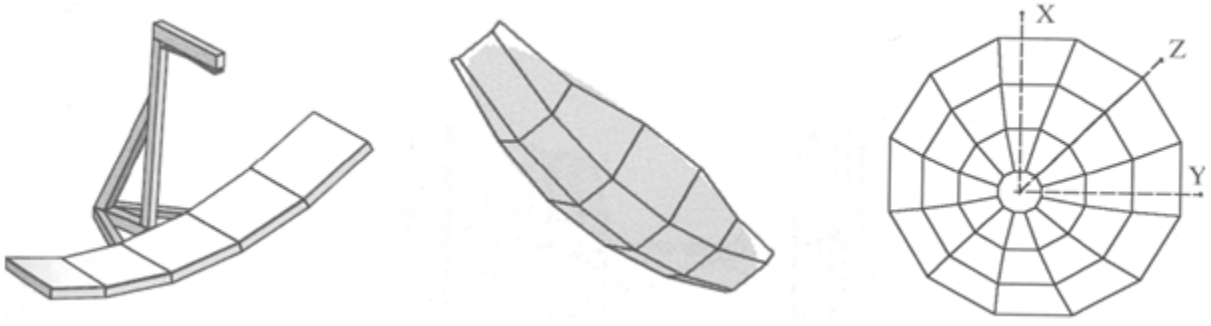

Figure 2.6: Multi-facet Configurations approximating parabolic surfaces. (After [1])

B. Reflectarray Beam Shaping

Another achievement which is important for spacecraft applications was the ability to shape the radiation pattern of the reflectarray into a contoured beam [29, 30]. Shaped countered beams are used in satellite applications to provide a specified coverage area on the surface of the earth. This shaping of the beam was accomplished in some cases by using a numerical phase-only synthesis technique where a very large number of elements is used to get the desired countered shaped beams. Basically with this technique the required phase is obtained by changing the dimensions of the array patches, and then optimization is used as a second step to improve the design performance. Figure 2.7 shows an example of the photo etching mask of a reflectarray design that gives shaped contour beams [30]. Another useful recent development for spacecraft applications is the inflatable reflectarray [31]. All reflectarray elements are printed on a thin membrane substrate that is mechanically supported and tensioned at its perimeter by inflatable tubes that decrease the surface rms error. When deflated, this antenna can be rolled up to form a light cylinder that reduces the mass and volume contribution of the antenna in the lunch vehicle. Figure 2.8 shows an example of inflatable reflectarray.

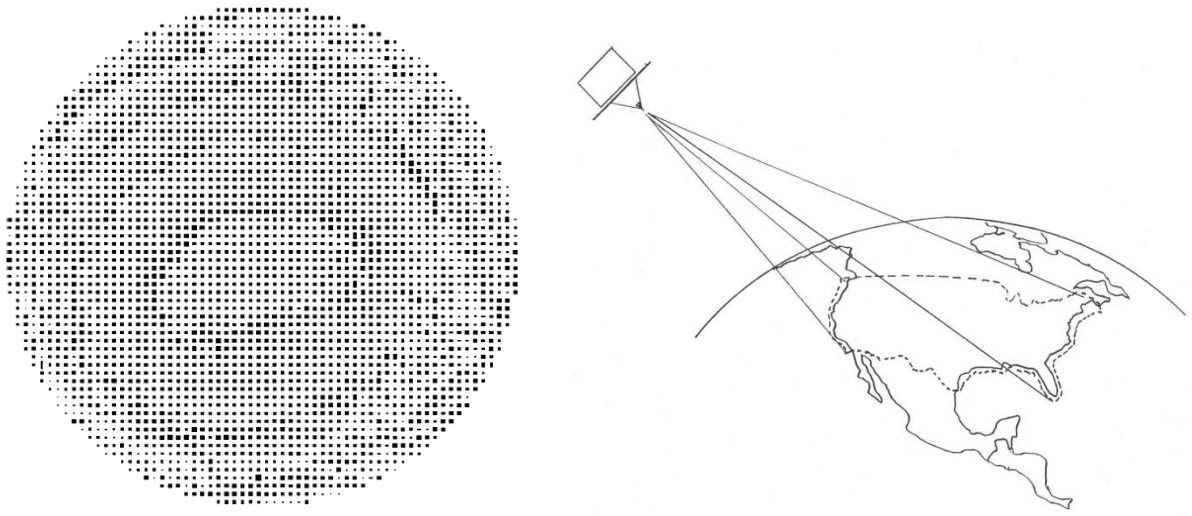

(a) **(b)**

Figure 2.7: a) Photo-etching mask of the first layer of the shaped beam reflectarray. (After [30]), b) Specified coverage area on the surface of the earth.

Figure 2.8: 1-m X-band inflatable microstrip reflectarray with circular polarization. (After [31].

C. Reconfigurable Reflectarrays & Beam Scanning

Reconfigurability is generally used to change the antenna radiation pattern. Many ways have been used to embed the re-configurability into the reflectarray antenna structure. One way is to use solid state tuning devices (diodes, transistors) integrated within the radiating element of the reflectarray to modify the phase or/and the amplitude of the signal transmitted or received by the radiating element. Recently much has been done to benefit from reflectarray reconfigurability to achieve beam scanning [32, 33, 34]. In [32] voltage-controlled varactor diodes were used to control the phase of equal size reflectarray patches as shown in Figure 2.9. Basically each rectangular element is split at the middle and connected at the edges by two varactor diodes. By varying the applied voltage across the diode terminals, their capacitances are changed and thus the patch electrical phases are changed. A beam scanning of $\pm 70^{o}$ has been achieved with a 70 element C-band reflectarray. To allow continuous tuning of the reflected signal phase over a 360^{o} range, a special reflectarray element has been presented in [33]. It consists of a patch printed on a flexible membrane substrate, aperture-coupled to a transmission line loaded with two varactor diodes. At C-band the loss in the varactor diodes was low. It would be higher at

millimeter wave frequencies. In order to overcome this Hum and Okoniewski [34] presented a new low-loss technique that uses low loss micro-electro mechanical devices (MEMS).

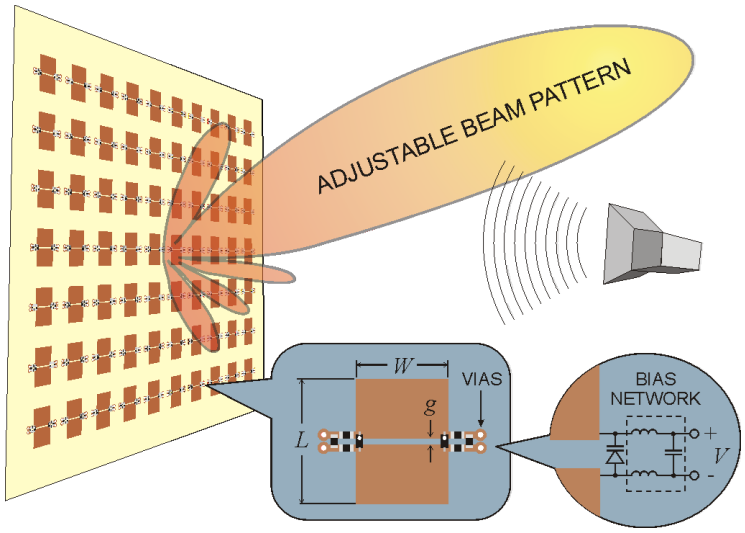

Figure 2.9: Geometry of the beam scanning reflectarray with tunable varactor diodes. (After [32]).

D. Multi-Band Reflectarrays

Reflectarrays can be designed to operate in different frequency bands simultaneously. One way to achieve this is to have the elements etched on different substrate layers as shown in Figure 2.10. Huang [35] introduced circular loops with gaps used as the cell element for two frequency bands. The lower band (X-band) elements were placed on the top layer of the substrate and upper band (Ka-band) smaller loops were placed on the lower substrate. Another possibility is to etch the different band elements in one layer. An example is the work done in [36] where a reflectarray composed of three sub-arrays etched on a single substrate was used to achieve a tri-band coverage. The sub-arrays were designed to generate pencil beam patterns at 32 GHz (Ka-band), 8.4 GHz (X-band), and 7.1 GHz (C-band), respectively.

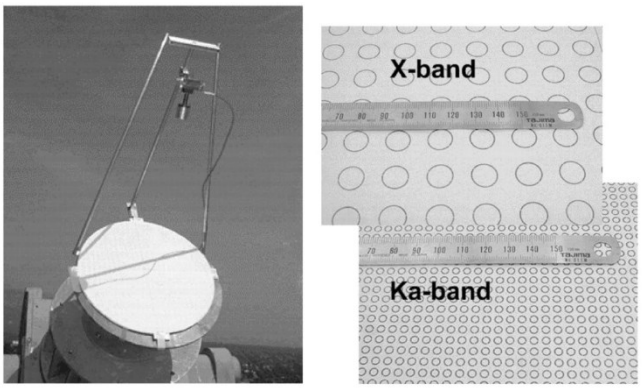

(a)

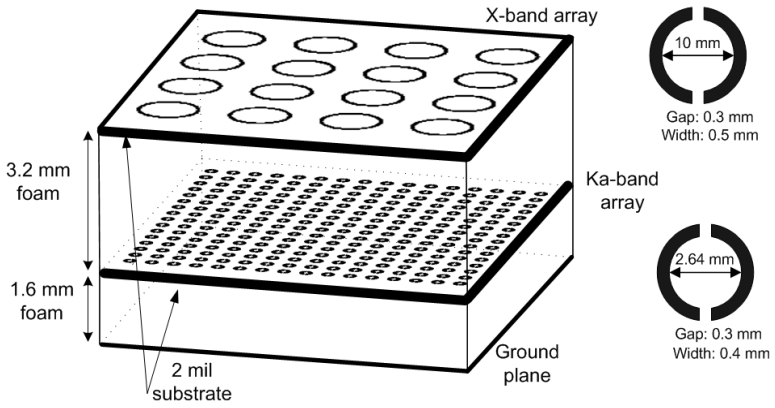

(b)

Figure 2.10: Dual band Reflectarray with stacked ring elements for X/Ka-band [35]. a) General view of the reflectarray, b) Configuration of the cell elements and their lattice structure.

E. Multi-Feed Reflectarray & Spatial Power Combining

A reflectarray that works as an antenna and spatial power combiner concurrently was described in [14, 37]. Unlike previous work on power combining using reflectarrays, this work did not include any active devices in its integration. The idea can be understood from Figure 2.11. Multiple feeds were used to illuminate the reflectarray to get a high gain single beam in the broadside direction. To achieve that, the phase correction factor given in equation (2.1) must be selected in such a way as to correctly make the total phase from all feeds constant for all patches

to end up with a planar phase front. For instance, if the fields incident from feeds #1 and #2 are considered such that at the *nth* patch their expressions are

$$E_1\left(\underline{r}_n^{(1)}\right) = \left|E_1\left(\underline{r}_n^{(1)}\right)\right| e^{-j(k_o r_n^{(1)} - \psi_n)} \tag{2.2}$$

and

$$E_2\left(\underline{r}_n^{(2)}\right) = \left|E_2\left(\underline{r}_n^{(2)}\right)\right| e^{-j(k_o r_n^{(2)} - \psi_n)} \tag{2.3}$$

then the total field at the *nth* patch is the sum of the fields from each of the feeds, or

$$E_T = \left|E_1\left(\underline{r}_n^{(1)}\right)\right| e^{-j(k_o r_n^{(1)} - \psi_n)} + \left|E_2\left(\underline{r}_n^{(2)}\right)\right| e^{-j(k_o r_n^{(2)} - \psi_n)} \tag{2.4}$$

The phase of this total field, which is aimed to be equal on the reflectarray surface, is therefore given by

$$\angle E_T = \tan^{-1}\left\{\frac{-\left|E_1\left(\underline{r}_n^{(1)}\right)\right|\sin(k_o r_n^{(1)} - \psi_n) - \left|E_2\left(\underline{r}_n^{(2)}\right)\right|\sin(k_o r_n^{(2)} - \psi_n)}{\left|E_1\left(\underline{r}_n^{(1)}\right)\right|\cos(k_o r_n^{(1)} - \psi_n) + \left|E_2\left(\underline{r}_n^{(2)}\right)\right|\cos(k_o r_n^{(2)} - \psi_n)}\right\} \tag{2.5}$$

Next ψ_n for each patch are selected to make the phase of the total field constant for all patches.

The importance of the spatial power combining using reflectarrays stems from the fact that it can be used at frequencies around 60GHz and higher, which are just starting to be used in wireless communications. Reflectarrays offer a way to achieve high gain from a printed antenna in spite of the high frequency because, as pointed out in Section 2.2.1, no transmission line feed networks (which have high losses at 60GHz and higher) are needed in a space-fed array such as a reflectarray. Also, at 60GHz and higher, it is very difficult to design efficient solid state sources; hence some sort of power combining is needed.

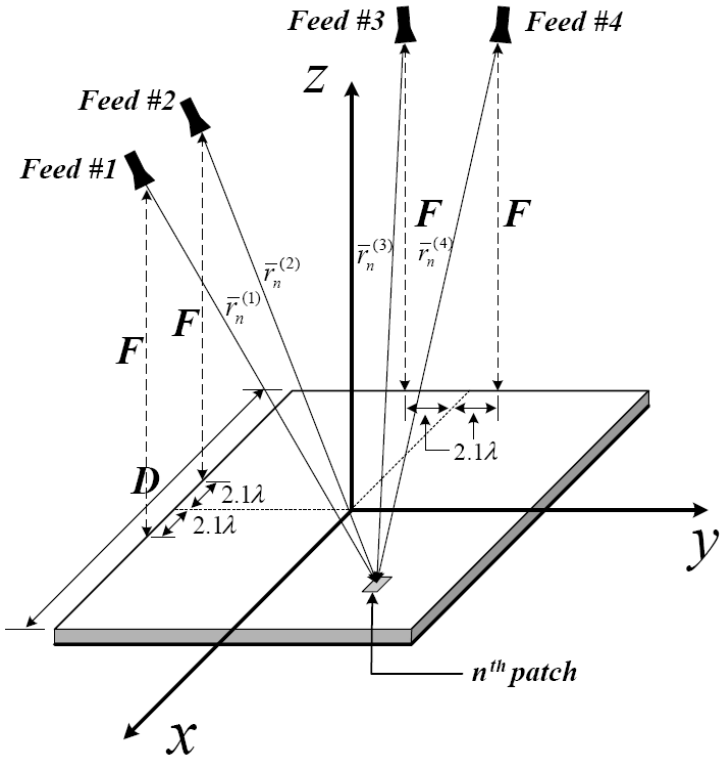

Figure 2.11: Geometry of Four feeds spatial power combining Reflectarray. (After [14]].

Power combining in the manner described in Figure 2.11 is possible at 60GHz and higher frequencies because no feed lines are needed for the very large number of elements. One gets an antenna and power-combiner in one.

Despite its potential advantages, the use of many feeds to illuminate the power combining reflectarray leads to more complexity and power loss due to the use of multi-feeds and consequently several feed lines, thus one may consider only two feeds to reduce the impact of these factors. In Chapter 5, we consider a two-feed reflectarray, which generates a single beam in the broadside direction, as a solution to eliminate beam squint in offset-fed reflectarrays. This two-feed reflectarray performance is substantially improved in the same chapter.

F. Sub-Reflectarray Antennas

In recent years the use of reflectarrays has been extended to emulate the ellipsoidal and hyperbolical subreflectors of a dual reflector antenna system [3, 38-45]. Such reflectarrays are called sub-reflectarrays in order to distinguish them from "main-reflectarrays" that emulate parabolic reflectors. Unlike main-reflectarrays, in sub-reflectarrays the goal is not to get a pencil beam of power directed in a specific direction in space, but to illuminate the parent parabolic reflector or its equivalent reflectarray with a power pattern that is just wide enough to illuminate the whole surface of the main reflector efficiently as illustrated in Figure 2.12.

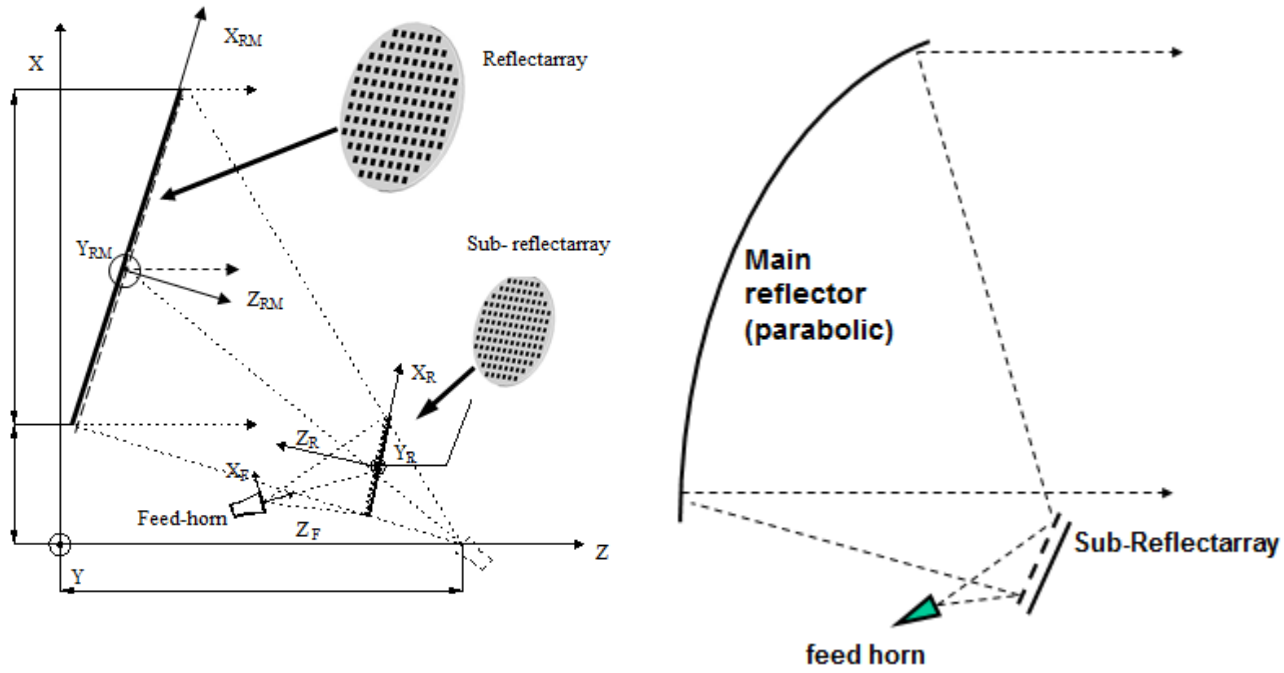

(a) **(b)**

Figure 2.12: Sub-reflectarray as part of dual reflector systems illuminating a) Parabolic Reflectarray , b) Parabolic Solid Reflector.

Sub-reflectarrays attracted researchers' attention due to the potential advantages expected to be drawn from them, not the least of which the development of beam shaping and beam scanning capabilities. For instance it has been reported in [44] that by introducing a phase progression on the surface of the sub-reflectarray in a dual reflector system, the main beam of the parent reflectarray (or reflector) can be scanned by an angle proportional to the phase progression

defined. This method would help in achieving beam scanning with lower loss, and is simpler to implement because sub-reflectarray are much smaller than main-reflectarrays. The Encinar group [40, 42] used sub-reflectarrays to replace the sub-reflectors in dual reflector antenna both for conventional Cassegrain and Gregorian systems. The Rahmat-Samii group [41] has shown that a sub-reflectarray can compensate for the surface distortion of the main reflector, and then showed in [43] that the sub-reflectarray can be used to compensate for the spherical aberration of a spherical main reflector. It is noticeable that in all the mentioned references no simple phase equation, similar to equation (2.6), is given, using which the required patch sizes for sub-reflectarays, can be set. Instead direct optimization is used to adjust the patch dimensions in such a way that the sub-reflectarray achieves the desired phase conversion. Such design equations were subsequently introduced in [39] for the first time, with a complete derivation and validation of these design equations given in [3]. These design equations have been used recently by Rahmat-Samii et al. [45] to implement a sub-reflectarray that illuminates a large parabolic reflector in a compact dual-refecor antenna system. In [38] a detailed investigation of the sub-reflectarray scattered field (both the amplitude and phase patterns) was done, with a parametric study of all associated features like focal point locations, edge taper effects, eccentricity change, and so on.

Unlike a main parabolic reflector that always has an eccentricity (e) of one, a subreflector can have $1 < e < \infty$ [38]. Therefore, the size of the sub-reflectarray depends on the eccentricity value of the subreflector it replaces and the focal length to size ratio (*F/D)* of the parabolic main reflector [38]. The eccentricity and *F/D* control the angular range of interest over which the main parabolic reflector is illuminated. This tells us that there are more degrees of freedom when the size of the sub-reflectarray is selected compared to that of a main-reflectarray (parabolic-type). Figure 2.13 shows a replacement of a solid hyperboloid by an equivalent sub-reflectarray. The feed-horn is always located at the real focal point, a distance F_R from the sub-reflectarray, whereas the virtual focal point is always located in the other side at a distance F_V from the sub-reflectarray. The required phase equation derived in [3] to design the hyperboloidal sub-reflectarray is

$$k_o(R_n - d_n) - \psi_n = \pm 2\pi n \tag{2.6}$$

where R_n is the distance between the feed phase center and point $\bar{P}$, which is the center coordinate of the *n-th* patch, d_n is the distance between the virtual focal point and point $\bar{P}$. From equation (2.6) it is evident that there is actually no need to refer to the solid sub-reflector each time we want to design a sub-reflectarray. The terms in the two design equations have meaning without having to be solid sub-reflector parameters. All features of solid sub-reflectors like changing the eccentricity to control the radiation patterns, can be simply accomplished by changing the virtual foci locations F_R and F_V, which leads to the change of R_n and d_n, hence a change in the element phasing requirements.

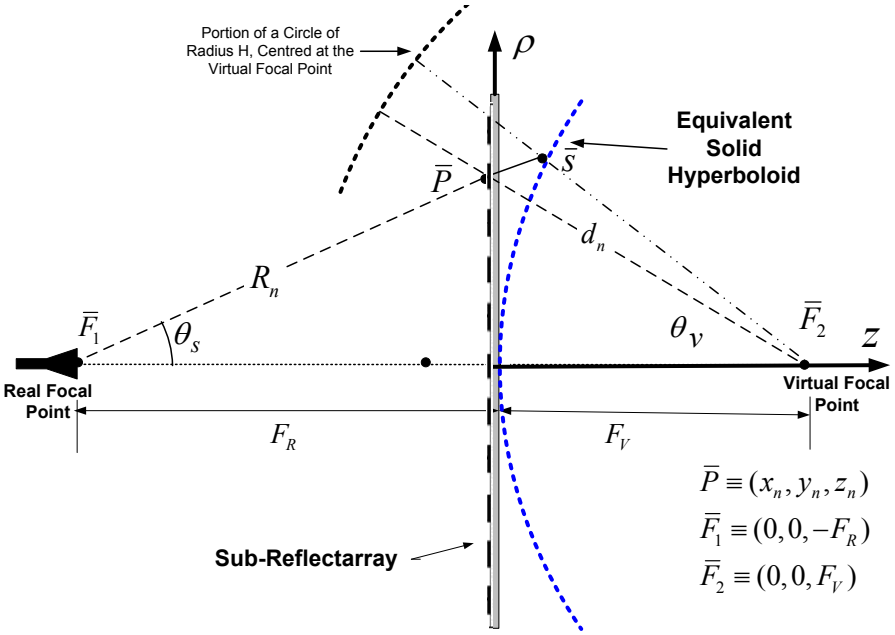

Figure 2.13: Replacement of a hyperboloidal subreflector by an equivalent sub-reflectarray. (Adapted from [38]).

We consider the performance improvement of sub-reflectarrays in Chapter 6 of this thesis.

2.3 Sub-Wavelength Reflectarrays

2.3.1 Review of Sub-Wavelength Reflectarrays

Reflectarray inter-element spacing represents an important factor in reflectarrays design, which is determined by the size of the reflectarray unit cell. This spacing is generally governed by the conventional array equation

$$\frac{d}{\lambda} \leq \frac{1}{1+\sin\theta} \tag{2.7}$$

where d is element spacing (the distance between the centers of adjacent unit cells), and θ is the main beam angle relative to the broadside direction or the incident angle from the feed at the outer most element. Based on (2.7), near reflectarray centre the element spacing could be relatively large (e.g. >0.9 λ) whereas for elements located toward the edge, the element spacing needs to be smaller since the wave's incident angles from the feed horn become large. Since it is practically difficult to design multi-spacing schemes, most designers have usually, since the first emergence of reflectarrays, used $\lambda/2$ as an inter-element spacing since it represents the threshold to prevent grating lobes [1, pp.82-85].

Recently several authors have described the use of reduced inter-element spacing as a means of improving the performance of reflectarray antennas. Reduced spacing was first used in [46] to improve a reflectarray scanning capability. The authors in [46] justified the reflectarary scanning improvement by the low quantization error caused by reduced spacing lattice; the smaller the cell size (that is, the smaller the spacing between reflectarray elements) the finer the sampling and hence the smaller the phase quantization. Reduced spacing was later shown in [47] to provide wider gain bandwidths as well, as confirmed in [48, 49]. A numerical investigation in [50] has used both reduced spacing and double-layer patch elements to further increase the 1-dB gain bandwidth. This was explained in terms of an increased reflection phase range available using the double-layer element, and decreased phase quantization over frequency. Recently, loop

elements of reduced inter-element spacing have been suggested to reduce the loss of a reflectarray that is etched on a lossy substrate [51]. In [52] the authors attributed the reduced inter-element spacing advantages to the strong coupling between elements that imposes a new paradigm that is based on coupled-resonance of the elements rather than the self-resonance that prevails in the conventional half-wavelength spaced reflectarrays. In this thesis, for the sake of brevity, the reflectarray of inter-element spacing less that $\lambda/2$ will be labeled the "sub-wavelength reflectarray" whereas that with the $\lambda/2$ lattice size will be referred to as the "half-wavelength reflectarray".

2.3.2 Phasing Characteristics of Sub-Wavelength Elements

A comparison between the reflection phase characteristics of sub-wavelength and half-wavelength patch elements is given in Figure 2.14. The phase curves in Figure 2.14(a) are generated using the method described in Section 2.2.2. Also, gain-bandwidth performances of two different reflectarrays that use sub-wavelength and half-wavelength patches as their elements are given in the same figure. The realized phase range for the case of sub-wavelength patches is reduced compared to the half-wavelength case. This imposes a limit on how far one could go in reducing the element spacing. Figure 2.14(a) reveals that using sub-wavelength patch elements of $\lambda/3$ spacing, one attains a slightly smaller phase range compared to the phase range of the half-wavelength patch elements. The slightly reduced phase range does not severely degrade the gain at the centre frequency; however the reduced spacing between elements boosts the overall gain-bandwidth performance as shown in Figure 2.14(b). The sensitivity of the reflection phase curves to frequency change decreases as the element spacing gets smaller. This reveals that the sub-wavelength element has a low dispersive nature [51], which further explains the larger gain bandwidth achieved using this type of element. This feature, as well as the low sensitivity of sub-wavelength elements to the angle of incidence, are elucidated and exploited in Chapter 5 and Chapter 6. In this thesis, we will use a sub-wavelength patch element that has the desired phase range (with $\lambda/3$ spacing) while still being restricted to a single layer design. We do this in order to mitigate some of the reflectarray problem aspects (discussed next in Section 2.4) with the least complicated reflectarray designs possible.

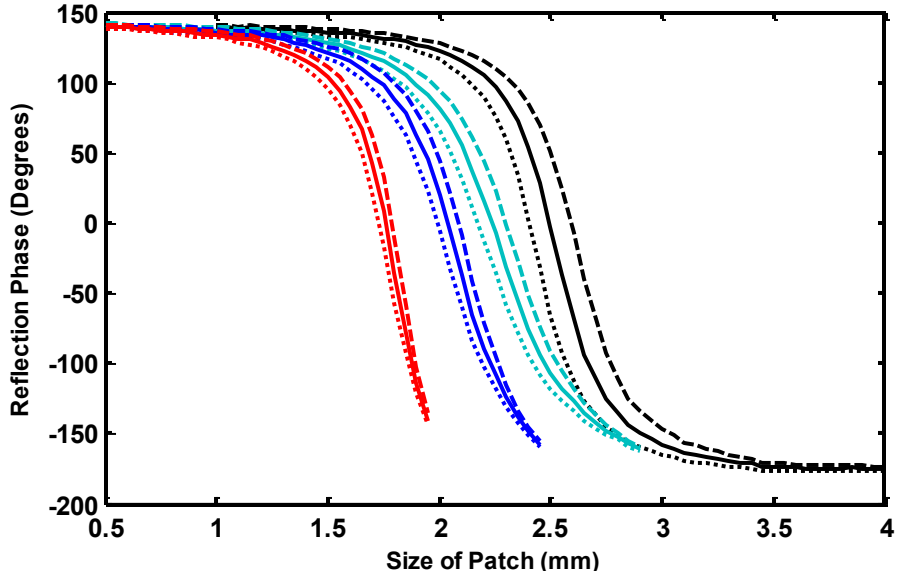

(a)

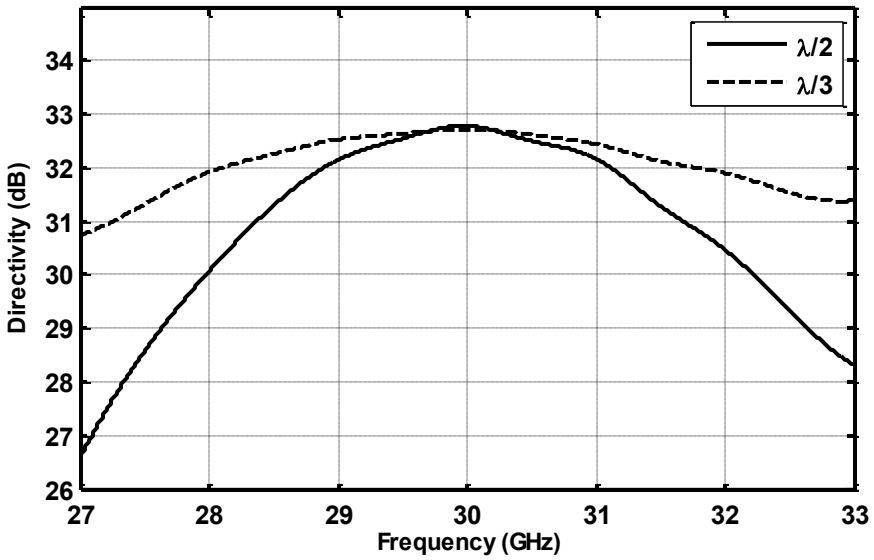

(b)

Fig. 2.14: a) Reflection coefficient phase versus patch size at 29 GHz (dotted line), 30 GHz (solid line) and 31 GHz (dashed line) for inter-element spacings λ / 2 (black), λ / 3 (light blue), λ / 4 (dark blue) and λ / 5 (red) at 30 GHz. b) Computed gain (in dBi) at 30 GHz, in the direction of maximum radiation, for a square reflectarray of 961 elements (cell size λ/2) and 2704 elements (cell size λ/3). The aperture size is 15.5λ×15.5λ for both reflectarrays at 30 GHz. (These results were computed by the author for the purpose of this illustration, how this is done is described in Section 6.3).

2.4 Reflectarray Problem Aspects

2.4.1 Introductory Remarks

Despite the tremendous efforts exerted to overcome reflectarray bandwidth limitations, of which a glimpse was given in Section 2.2.3, other problems like feed-image lobes, beam squint and the angle of incidence effect on reflectarray operation, which degrade reflectarray performance and do contribute partly to the reflectarray bandwidth problem, were not given enough consideration in the literature. The valid reasons behind the use of reflectarrays - particularly those of variable element sizes - to replace the conventional reflectors like the low cost, light weight and ease of manufacturing become questionable, as far as the bandwidth improvement is concerned, when complicated and pricy reflectarrays are used for this purpose. The aforementioned reasons, in addition to the fact that the vast majority of proposed solutions for the reflectarray bandwidth issue in the literature are applicable only for small to medium sized reflectarrays, as pointed out in Section 2.2.3, motivated the author of this dissertation to study the less considered reflectarray problem aspects namely, feed-image lobe, beam squint and the angle of incidence effect on reflectarray operation, which impose restrictions on the performance of both small and large reflectarrays.

Mitigating these unwanted problem aspects is shown in this thesis to improve reflectarray gain, side lobe level, and consequently the operational bandwidth. This improvement makes the use of a simple single-layer reflectarray, comprised of patches of variable size, a reasonable choice that fulfills the desired performance and satisfies the economic and mechanical advantages that made reflectarrays a viable alternative to conventional reflectors. It is worthwhile in this regard to point out that the bandwidth needed for a wide variety of potential applications is actually below the reflectarray bandwidth figures reported recently in the literature; for instance, Pozar in [30] stated that 5% bandwidth is enough for a significant number of satellite communications applications. This, in addition to the possibility of utilizing the frequency reuse in reflectarrays make the bandwidth problem less significant than what many researchers may claim; one never finds it stated in most publications what bandwidth is actually

needed. In what follows of this section the basic concepts of the problem issues listed in the previous paragraph are illustrated, and all their pertaining works in the literature are reviewed.

2.4.2 Feed-Image Lobe

The Feed-Image Lobe Concept – Explanation

The feed-Image lobe concept can be defined using a terminology that is borrowed from ray-optical models of scattering from smooth surfaces. The cross-section of the reflectarray geometry, which is shown schematically in Figure 2.15, draws attention to the so-called specular direction that has been indicated there. If the feed horn fields are pictured in terms of a bundle of rays, the specular direction is that in which the central ray from the feed (with incidence angle with respect to the normal denoted by θ_{inc} in Figure 2.15) would reflect if the reflectarray surface were replaced by a planar perfectly conducting (PEC) surface.

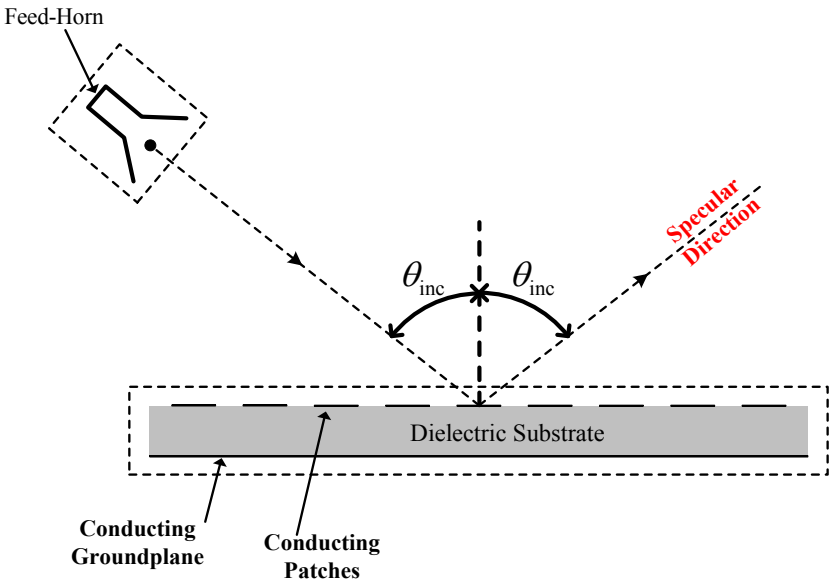

Figure 2.15: Cross-section of offset-fed reflectarray antenna geometry showing the incident angle and the "direction of specular reflection".

The measured and computed radiation pattern at 33GHz of an offset-fed reflectarray designed to have a main beam in the broadside direction at a centre frequency of 30 GHz, are shown as the black curve in Figure 2.16(a), and in Figure 2.16(b), respectively.

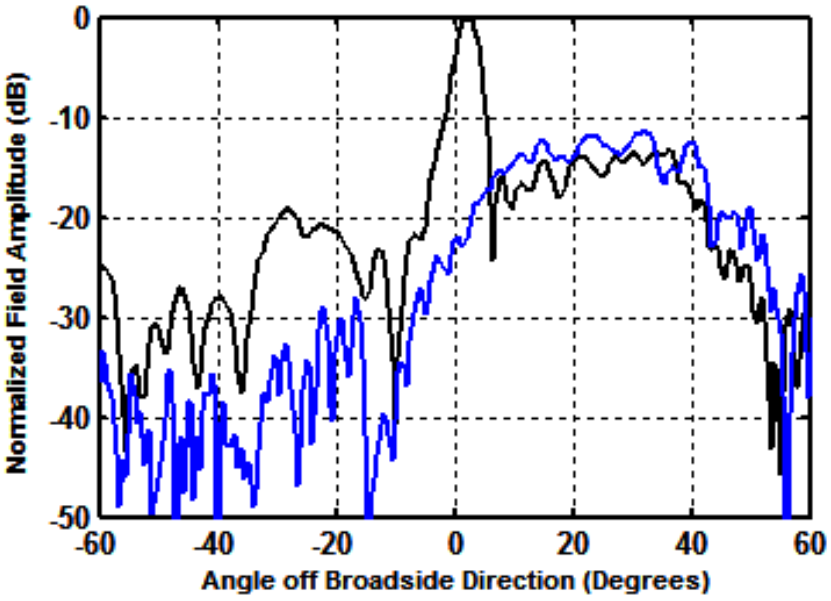

(a)

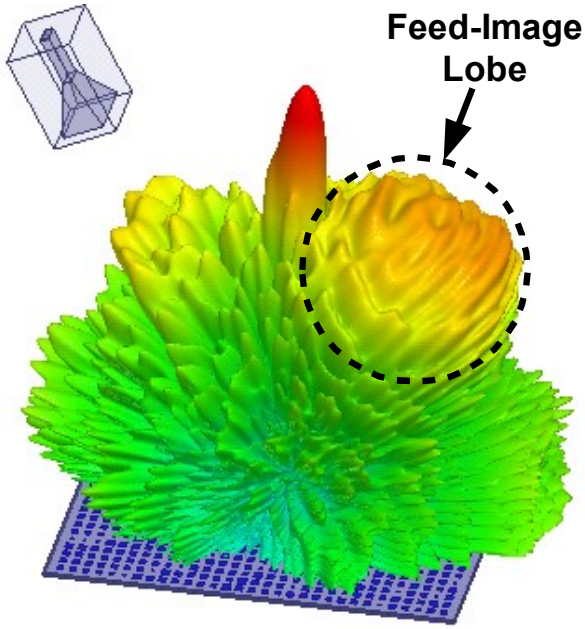

(b)

Figure 2.16: (a) Measured far-field E-plane patterns of a half-wavelength reflectarray, showing the feed image lobe centred about the specular direction of the reflectarray (——), plus the measured feed image pattern (——) obtained when the reflectarray is replaced by a solid conducting surface. (b) Plot of the far-field radiation pattern of the same reflectarray simulated using HFSS. All patterns shown are at 33GHz, whereas the design frequency is 30 GHz.

In practice, remembering that the complete ray picture of the feed is a collection of an infinite number of rays, with the latter PEC surface in place we obtain (at all frequencies) a scattered field distribution about the specular direction that is almost the same as the radiation pattern of the feed, as shown by the blue curve in Figure 2.16(a) at the off-centre frequency of 33 GHz. It is not identical to the feed pattern because the above-mentioned PEC surface is of finite extent. When we don't have the continuous PEC surface but the actual reflectarray present we obtain (at the off-centre frequency of 33 GHz) the scattered field represented by the black curve in Figure 2.16(a). It not only has a main lobe close to broadside as expected, but clearly also has what is usually referred to as a feed image lobe [53], about the specular direction. This is also depicted in the three-dimensional pattern plot in Figure 2.16(b). The feed image lobe represents energy that is wasted at the cost of the reflectarray gain and side lobe level, and so is undesirable. A properly designed reflectarray should not exhibit feed image lobes at its design frequency.

The Feed-Image Lobe Concept – Literature Review

The authors of [53] observed what is above (and elsewhere) now referred to as a feed image lobe, and attributed this to the scattering from the groundplane due to the fact that large portions of the reflectarray groundplane are not "shadowed" by the elements and hence are directly exposed to the incident feed fields. In order to reduce the amount of uncovered surface on the plane of the elements a triangular lattice was used [53] instead of the conventional square lattice. Although the results in [53] show a slight lowering of the measured feed image lobe, it still persists. The authors of [54] adopted a similar view, and found through full-wave simulation of reflectarrays consisting of fixed width and variable length dipoles that as the width of the dipoles increases the feed image lobe level decreases, and thus suggested that the feed image lobe level might indeed be proportional to the amount of groundplane directly exposed to the incident feed horn field. On the other hand, the authors of [55, 56] surmised that the appearance of a feed image lobe in reflectarrays might be due to the almost periodic error occurring in the actual reflection phase of the elements, especially those in the vicinity of Fresnel zone boundaries. At such boundaries, which occur almost periodically, an abrupt change in the element size occurs almost periodically, causing the environment of the elements there to depart significantly from that of the infinite periodic structure assumed in the calculation of the reflection phase versus

element size database, and hence leading to higher than desired scattered fields in certain directions. In Chapter 4 of this thesis, we show that the intuitive notions in [53-56] are partly true, but not entirely for the reasons given. We will show that in fact both the groundplane and the conducting elements contribute to the appearance of the feed image lobe in fixed-beam offset-fed single-layer reflectarrays of variable-size patch or dipole elements. Furthermore, a diagnosis of the source of the feed image lobe phenomenon is demonstrated by studying the individual and combined contributions of reflectarray conducting elements and the groundplane to the reflectarray far-fields. The source of the feed image lobe is examined and discussed and a successful means of suppressing the feed image lobe in offset-fed reflectarrays is demonstrated.

In [57] a description was given on how to "tune-out" the feed-image lobe in reflectarrays by increasing the thickness of the substrate in order to effect destructive interference between the scattered field from the elements on the front of the reflectarray and that from the ground plane. The use of this method is possible when all elements have fixed size, and element phases are controlled by delay lines. With the type of elements we are using in this thesis the range of achievable reflection phases versus patches size decreases substantially if the substrate thickness is increased. Thus the substrate thickness must be as small as possible (a very small fraction of a wavelength) to end up with a good reflectarray design, and so the technique proposed in [57] cannot be used here.

The authors of [58], also for fixed-size elements intended for realising a reconfigurable reflectarray, showed that the scattered field levels in the specular direction can be reduced by ensuring that the effective area of the elements is larger than the physical area of the lattice unit cell. According to the unit cell dimensions and frequency given in [58], the calculated specular reflection was very low for unit cells that are a half-wavelength per side, or smaller. We have used the approach in [58] to ascertain the role of the effective area on the feed image lobes under study in this dissertation. The effective area of an isolated microstrip patch was calculated from its directivity, the directivity being determined using expression (7-55) in [59]. Since our reflectarrays are comprised of patches of different sizes, we calculated the effective area for each of the patches on a half-wavelength reflectarray (that is, $\lambda / 2$ unit cell size) example, and found the average effective area well above the unit cell physical area. This confirms that the effective

area does not play role in the specular reflection appearance in reflectarrays with cell sizes $\leq \lambda / 2$. It is reported in [59] that the directivity (and hence the effective area) of patch antennas changes only gradually with patch dimensions if the substrate is thin. As such we found that in our reflectarray design even for those patches of small size the effective areas are close to the unit cell area.

2.4.3 Beam Squint in Offset-Fed Reflectarrays

The Beam Squint Concept-Explanation

The beam squint is an unwanted phenomenon observed in the radiation pattern performance of offset-fed reflectors and reflectarrays. When a single feed is used to illuminate an offset-fed reflectarray a frequency-dependent beam squint appears (in the plane of offset) as a deviation of the main beam from the desired direction. The computed radiation patterns at different frequencies of an offset-fed reflectarray designed to have a main beam in the broadside direction at a centre frequency of 30GHz, are shown in Figure 2.17. In Figures 2.17(a) the pattern generated at 30GHz does not exhibit any beam squint from the broadside direction as expected; however the patterns at 33GHz and 27GHz, which are shown in Figure 2.17(b) and (c), respectively, deviate decently from the design direction. The amount of beam squint becomes more pronounced the further one departs from the centre frequency. For a reflectarray mounted with its mechanical pointing angle fixed this represents a gain loss, and serves to seriously limit the effective gain-bandwidth of the antenna. It should be remembered that gain-bandwidths quoted in reflectarray publications often do not account for squint; the bandwidth is determined by simply observing the maximum gain value (irrespective of the fact that it may occur in a direction slightly different from that at the centre frequency). In offset-fed parabolic reflector antennas beam squint occurs when a circularly polarized feed is used, both at the design frequency and off-centre frequencies. It does not happen for linearly polarized feeds. The reasons are now well-understood [60]. Novel methods to compensate for such squint continue to be of interest [61]. In offset-fed reflectarrays beam-squint occurs even for linear polarization, but only at off-centre frequencies. The reasons are therefore clearly different from that of the solid reflector case mentioned above.

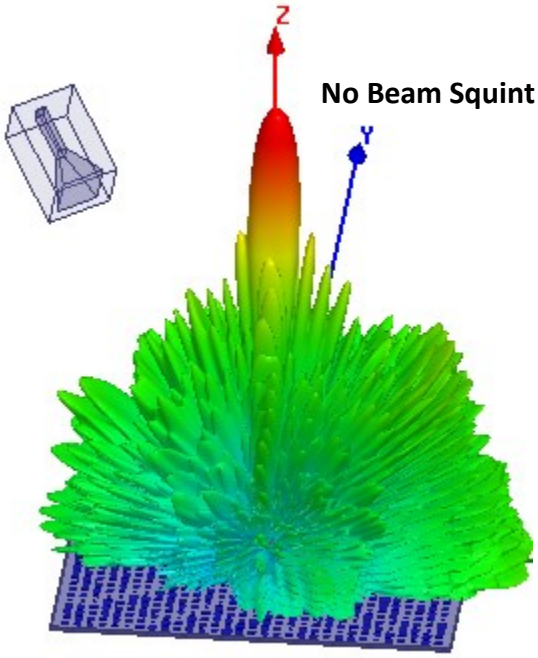

(a)

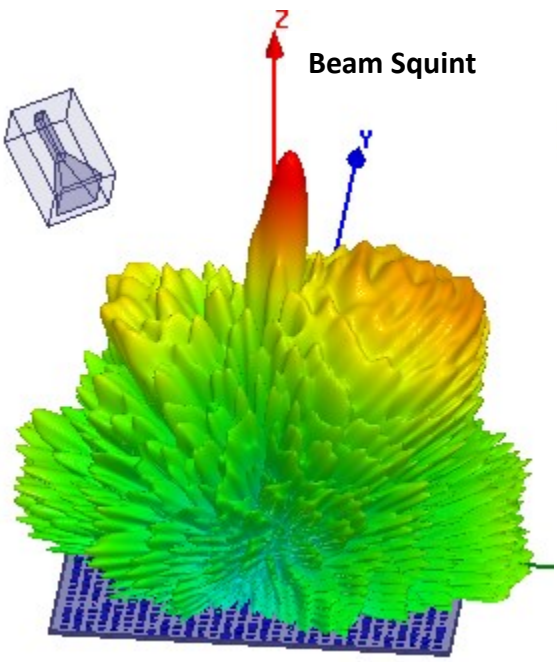

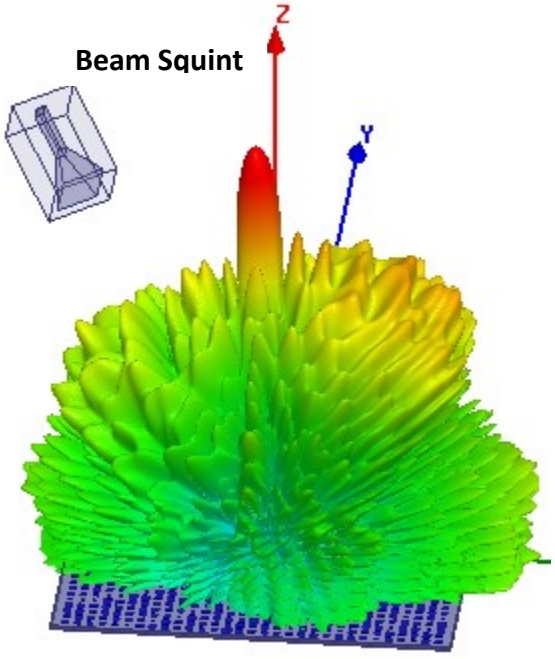

(b) (c)

2.17: Plot of far-field radiation patterns of a reflectarray designed at 30 GHz using square patches of variable sizes showing beam squint at off-centre frequencies. The reflectarray patterns are calculated using HFSS at a) 30GHz, b) 33GHz and c) 27GHz.

Although the beam squint in offset-fed solid parabolic reflector antennas has been the main subject of many papers, the only reference that directly addresses the beam squint issue in offset-fed reflectarrays appears to be [62]. Targonski and Pozar [62] used a scalar "geometrical" analysis of the type used to derive the widely-applied basic design equation (2.1) for reflectarrays, and showed that at all frequencies other than the centre frequency the reflectarray aperture phase distribution will have a slope other than that required to have a main lobe in the desired direction. The cause of this phase tilt, which results in beam squint, was not revealed in [62]. It was concluded though that the amount of squint with respect to frequency can be reduced if the reflectarray is so designed that the main beam is in the so-called specular direction; although a valid solution, designers do not always want the main beam in this direction as it is not always convenient to have it so. In this thesis the beam squint phenomenon will be examined from a different view point which establishes the source of the phase tilt; observation of the scattered near-fields allows us to show that the shift of location of the effective focal point with frequency is what leads to the phase tilt at off-centre frequencies and hence squinting of the main beam. We accordingly in Chapter 5 propose a new solution for beam squint that enables designers to direct the main beam towards the broadside direction. Furthermore, it is demonstrated in this thesis for the first time that beam squint is insensitive to some factors like the element type and the lattice size of the reflectarray.

2.4.4 Angle of Incidence Effects on Reflectarray Operation

The angle of incidence can be defined, with reference to Figure 2.15, as the angle that is formed between the incident wave from the feed and the orthogonal to the reflectarray surface. It becomes larger closer to the edges of the reflectaray and if the feed is placed close to the reflectarray surface as shown in Figure 2.18. As such compact reflectarrays, those of small F/D value similar to the reflectarray in Figure 2.18(b), are more prone to the angles of incidence effects. The reflection phases, which are generated by changing the patch size, are not dependent only on the patch size but also on the angle of incidence and the polarization, hence angle of incidence change need to be considered in designing reflectarrays.

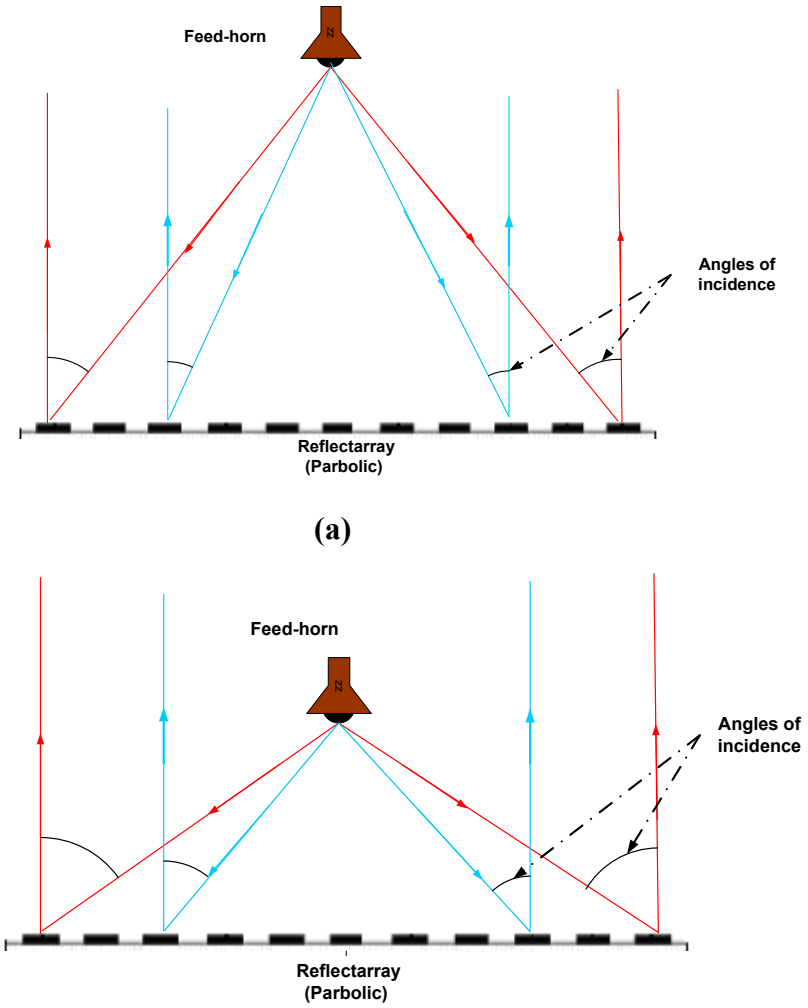

Figure 2.18: Cross-sections of a centre-fed reflectarray antenna showing the incident angle change based on the element location with respect to the feed and on the focal length (F) of the reflectarra, a) reflectarray of large focal length b) reflectarray of small focal length.

Most reflectarrays have been designed with large focal length ($F/D \geq 1$). Also, sub-reflecarray antennas have recently emerged as topics of interest. Thus the effect of angle of incidence on reflectarray and sub-reflectarray operation has received relatively sparse attention. Although much has been done to develop analysis methods to predict reflectarray far-field patterns, which accounts for the angles of incidence in an already-designed reflectarrays [63-65], to the best of the author's knowledge, there is no design technique, which is at least embedded in a commercial code, whereby the reflectarray elements sizes are selected during the design stage to satisfy all angles of incidence. In fact most reflectarrays of variable size elements are designed

using the approach outlined in Section 2.2.2, where the reflection phases are always generated using a reliable commercial code, in which the infinitely periodic approximation approach is embedded, like HFSS and CST [18, 66]. Using these codes, researchers usually use a reflection phase data that is generated only for a normally incident plane wave to carry out their designs. This may be considered acceptable for small angles of incidence since the effect upon reflectarray performance is minor. However when the angle of incidence becomes large (for small *F/D* values), a considerable degradation in the reflectarray performance is anticipated. This degradation is usually caused by the phase error generated by all elements that are located at large angles of incidence with respect to the feed position. Figure 2.19 shows the reflection phases generated using the infinite periodic structure approximation discussed in Section 2.2.2 for a square patch unit cell simulated at 30GHz with the TM polarization case at different angles of incidence. The reflection phase behavior reveals explicitly a high sensitivity to the angle of incidence beyond 30°. This partly justifies the tendency to design reflectarrays with relatively large F values. From the reflection phase curves shown in Figure 2.19, one may conclude that if a compact reflectarray with F/D=0.5 is designed using the normal incidence assumption, elements of sizes 2.2mm-4mm (which would be those located such that the incidence angle from the feed is larger than 30°) will generate a considerable phase error, particularly those elements

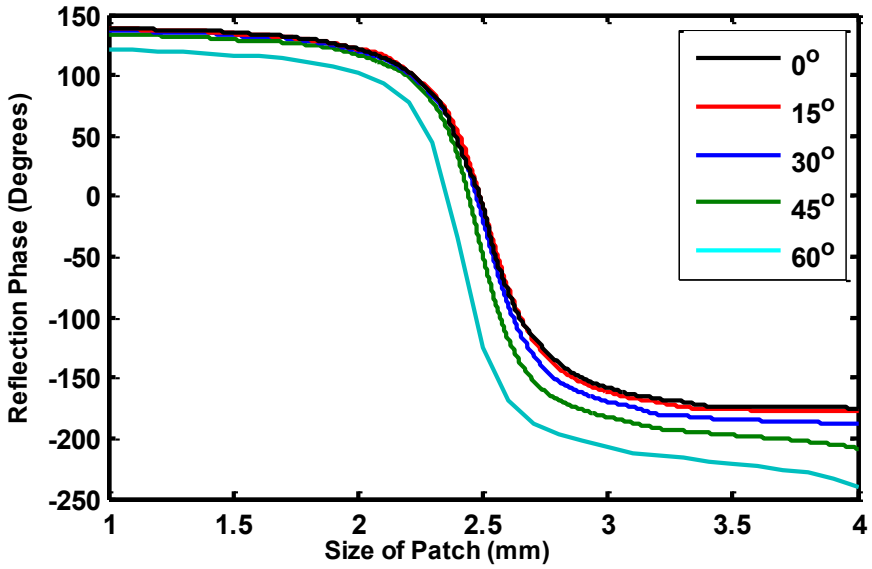

Figure 2.19: Reflection coefficient phase versus patch size at 30 GHz for different plane wave incidence angles on the infinite periodic structure for $\lambda/2$ spacing. HFSS [18] was used to generate the reflection phase curves in the figure.

that are near the reflectarray edges (incidence angle 45°). This happens simply because these elements phase values are different from the required ψ_n values which satisfy the required phasing condition.

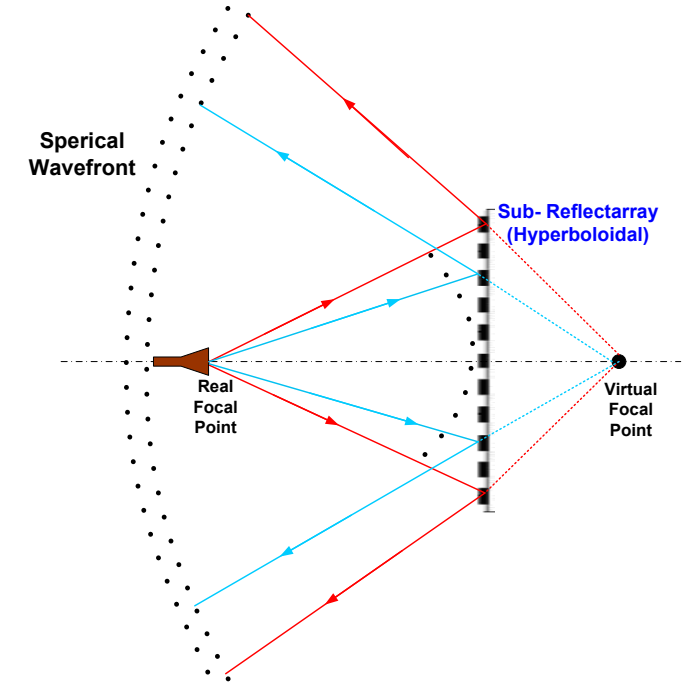

(a)

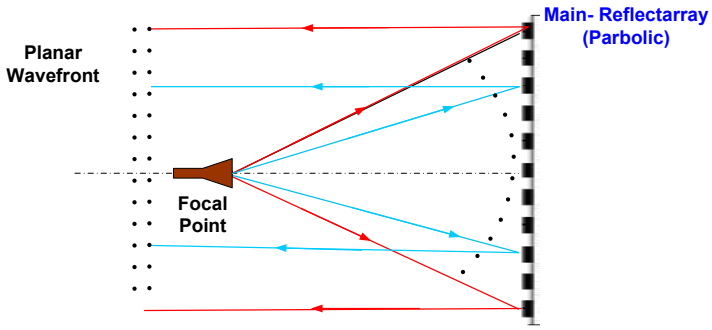

(b)

Figure 2.20: Cross sections showing the basic operation and the extent of radiation of a) a sub-reflectarray, b) an equivalent reflectarray.

In sub-reflectarrays, the angle of incidence effect is expected to be more significant than reflectarrays as a sub-reflectarray, as shown in Figure 2.20(a), is usually designed to radiate over a much wider angular region compared to a reflectarray of the same aperture size (as in Figure 2.20(b)). In fact, at least a double effect for the angle of incidence is expected in the sub-reflectarray case as sub-reflectarrays reflect the incoming wave with reflection angles that are usually larger than the incidence ones. Sub-reflectararys are used to illuminate large reflectors or main-reflectarrays, hence they convert the incident spherical wave from the feed to another spherical wavefront of wider angular extent that appears emanated from the sub-reflectaray virtual focal point (as in Figure 2.20(a)). The need for designing sub-reflectarrays and compact reflectarrays, using the aforementioned practical approach, motivated the author to study the angle of incidence effects on reflectarray performance, and to propose solutions that reduce these unwanted effects in Chapter 6.

2.5 Reflectarray Operating Mechanisms

2.5.1 The Importance of Investigating Reflectarray Operating Mechanisms

In order to diagnose the source of reflectarray problem aspects discussed in Section 2.4, one should first get physical insights into reflectarray operating mechanisms. For instance, the occurrence of feed image lobe on the reflectarray radiation pattern at off-centre frequencies points to some problem in the source of the far-field radiation, which is the conduction current on the conducting parts (patches and ground plane), and the polarization current within the dielectric substrate, of the reflectarray. The challenge then is to extract these currents' amplitude and phases in all reflectarray parts from a rigorously simulated reflectarray model and examining their separate and aggregate contributions to the reflectarray far-field, in order to determine what makes the currents create such an unwanted feed-image lobe in the far-field pattern. This dictates a component by component study of the current behavior at different frequencies which, in the author's opinion, reveals much about the reflectarray operation. For instance, the author never thought, before exploring the aforementioned mechanism, that the reflectarray groundplane contributes to the reflectarray far-field pattern in much the same way as the patches do; the

ground plane is always thought of as a PEC backing for the substrate that forces all the incoming energy to be reflected back into the upper half space. This is discussed in Sections 3.2 and 3.3.

Another reflectarray operating aspect, which is shown in this thesis to influence beam squint greatly, is the behavior of the reflectarray effective focal point with frequency. The progressive phase tilt on the reflectarray surface reported in [62], which occurs only at off-centre frequencies, brought to the author's attention the possibility that the reflectarray effective focal point shifts at off-centre frequencies might be the cause of such phase tilt. This stems from the fact that reflector/reflectarrays are always designed such that the phase centre of the feed-horn is coincident with the design focal point [14, 67], and so any misalignment between them is expected to break the phase synchronism on the reflectarray surface. This phase synchronism is what insures the right phase conversion and consequently the planar phase front of the scattered field from the reflectarray. This operating aspect, focal point shift with frequency, also gives some more physical insight into reflectarray operation as it also appears to impose some restrictions on the reflectarray bandwidth. This is discussed in Chapter 5.

2.5.2 Review of the Existing Work on Reflectarray Operating Mechanisms

Although reflectarray antennas have been widely studied, only a few of these studies have discussed the mechanisms of reflectarray operation in any detail. An itemization of the mechanisms of reflectarray operation is presented in [68]. In [69] it is shown that the field distribution on the radiating edges of the reflectarray elements (which are patches in [69], and in the present thesis) directly impacts the phase imparted by the element to the scattered field. It has been reported in [2] that when analyzing reflectarry elements using full-wave techniques it must be remembered that the radiated field is the sum of two components: the field radiated by the patches and the field reflected from the ground plane. Indeed, Pozar in [2] considered the two components, the one reflected field from the dielectric substrate and the ground plane (in the absence of the patches) and the scattered field from the patches. But these "component aspects" in [2] are in the context of integral equation formulations that use a modified Green's function. This separation of responses into two "components" is not the same as the separation of the responses into the contributions of the physical components making up the reflectarray. To the

best of the author's knowledge the separate contributions of the actual individual reflectarray components to the reflectarray radiation patterns, which we investigate in this thesis, have not elsewhere been explored in the literature.

As regards the focal point shift mechanism, the literature seems to be scarce as well. The authors of [14, 70] studied the focal shifts in reflectarray antennas for the first time. In [70] it was found, similar to solid parabolic reflectors [67], that when a reflectarray is illuminated by a plane wave impinging on the reflectarray surface from the main beam direction, a distinct focal field region is formed close to the nominal focal point. This focal point, which was found shifted a bit from the nominal focal point, was called in [70] the effective or the true focal point. In [14] the same authors reported that there are situations when the maximum gain of the reflectarray is achieved with the feed displaced from the nominal geometrical focal point, either slightly toward or away from the reflectarray. This shift apparently makes the feed coincident with the true focal point which is informatively revealed by considering the reflectarray in the receive-mode analysis. The impact of some reflectarray geometrical parameters, namely the reflectarray size D and focal length F was also studied in [14]. It is worthwhile to point out here that the focal shift in [14, 70] was obtained at the centre frequency and nothing was mentioned about the focal shift behavior at off-centre frequencies. We therefore, in this thesis, will refer to the focal shift reported in [70] as "the inherent focal shift" as it is caused by the finiteness of the reflectarray structure [70] and is of a different nature to the frequency dependent focal point shift we investigate in Chapter 5 of the present thesis.

2.6 Conclusion

We have reviewed the literature and the theoretical background necessary for the developments that form the subject of this thesis. In Section 2.2 we outlined the concept, design guidelines and some important developments of reflectarray antennas. Multi-feed reflectarrays as well as sub-reflectarrays were singled out as they are used in the developments of this thesis. In Section 2.3 we considered important aspects of sub-wavelength reflectarrays, which is used to develop solutions for some problem issues in this thesis, like the feed-image lobe in Chapter 4 and the degradation of reflectarray and sub-reflectarray performance due to angle of incidence effects in Chapter 6. In Section 2.4 we discussed the problem aspects we aim to diagnose and mitigate in this thesis. Feed-image lobe, beam squint and angle of incidence problem concepts were explained and their effects were elaborated on using results obtained by the author from fully simulated reflectarray models. We further in Section 2.4 summarized the literature pertaining to these problems, with some emphasis on their reported diagnostics and solutions. Lastly, in Section 2.5 we considered the operating mechanisms we will study in detail to diagnose feed-image lobe and beam squint problems. Investigating these operating aspects is integral to understanding many of the developments in Chapters 4 and 5 of this thesis.

Chapter 2 References

[1] J.Huang and J.A.Encinar, Reflectarray Antennas, IEEE Press. New York: John Wiley & Sons, pp.82-85, 2008.

[2] D.M.Pozar, S.D.Targonski and H.D.Syrigos, "Design of millimeter wave microstrip reflectarrays", IEEE Transactions on Antenna and Propagation, Vol.45, No.2, pp.287-295, February 1997.

[3] E.Almajali, D.A.McNamara, J.Shaker and M.R.Chaharmir, " Derivation and validation of the basic design equations for symmetric sub-reflectarrays", IEEE Transactions on Antenna and Propagation, Vol.60, No.2, pp.2336-2346, February 2012.

[4] B.Khayatian, Y.Rahmat-Samii and J.Huang, "Radiation characteristics of reflectarray antennas: Methodology and applications to dual configurations", Antennas and Propagation European Conference, EuCAP, pp.1-12, November 2006.

[5] D.C.Chang and M.C.Huang, "Microstrip reflectarray antenna with offset feed", Electronic Letters, Vol.28, No.16, pp.1498-1491, July 1992.

[6] R.D. Javor, X.D.Wu and K.Chang,"Offset feed microstrip reflectarray antenna", Electronic Letters, Vol.30, No.17, pp.1363-1365, August 1994.

[7] H.Deguchi, N.Takagi, M.Tsuji and H.Shigesawa, "Microstrip reflectarray with offset feed for improving effective aperture area", IEEE International Symposium on Antenna and Propagation, Vol.3, pp.290-293, June 2003.

[8] S.V.Hum and J.Perruisseau-Carrier, "Reconfigurable reflectarrays and array lenses for dynamic antenna beam control: a review", IEEE Transactions on Antenna and propagation, Vol.62, No.1, pp.287-295, January 2014.

[9] M.E.Bialkowski, A.W.Robinson and H.J.Song, "Design, development and testing of X-band amplifying reflectarrays", IEEE Transactions on Antenna and Propagation, Vol.50, No.8, pp.1065-1076, May 2002.

[10] H.Rajagopalan, Y.Rahmat-Samii and W.A.Imbriale, "RF MEMS actuated reconfigurable reflectarray patch-slot element", IEEE Transactions on Antenna and Propagation, Vol.56, No.12, December 2008.

[11] D.G.Berry, RG.Malech and W.A.Kennedy, "The reflectarray antenna", IEEE Transactions on Antennas and Propagation, Vol.11, No.6, pp.645-651, November 1963.

[12] R.E.Munson, H.Haddad and J.Hanlen, "Microstrip reflectarray antenna for satellite communication and RCS enhancement or reduction", U.S. Patent 4 684 952, August 1987.

[13] S.D.Targonski and D.M.Pozar, "Analysis and design of a reflectarray using patches of variable size", IEEE International Symposium on Antenna and Propagation, Vol.3, pp.1820-1823, June 1994.

[14] F.N.Arpin, "Multi-feed spatial power combining reflectarrays", Masters Thesis,University of Ottawa, Ontario, Canada, September 2004.

[15] D.M.Pozar and S.D.Targonski, "A microstrip reflectarray using cross dipoles", IEEE International Symposium on Antenna and Propagation, Atlanta, pp.1008-1011, July 1998.

[16] M.R.Chaharmir, J.Shaker, M.Cuhaci and A.Ittipiboon, "A broadband reflectarray antenna with double square rings", Microwave and Optical Technology Letters, Vol.48, No.7, pp. 1317-1320, July 2006.

[17] M.E.Bialkowski, A.M.Abbosh and K.H.Sayidmarie, "Investigations into phasing characteristics of printed single and double cross elements for use in a single layer microstrip reflectarray", IEEE Antennas and Propagation Society International Symposium, pp.1-4, July 2008.

[18] HFSS, Ansoft Product Suite, Ansys Inc., USA (www.ansoft.com).

[19] S.Xu, H.Rajagopalan, Y.Rahmat-Samii and W.A. Imbriale, "A novel reflector surface distortion compensating technique using a sub-reflectarray", IEEE International Symposium on Antenna and Propagation, pp.5315-5318, June 2007.

[20] J.Shaker, M.R.Chaharmir and J.Ethier, Reflectarray Antennas: Analysis, Design, Fabrication, and Measurement, Artech House, 2013

[21] J.Shaker and E.Almajali "Reflectarray Antennas". Chapter 8 of the Handbook of Reflector Antennas and Feed Systems, Vol.I. Artech House, 2013.

[22] J.Huang, "Bandwidth study of microstrip reflectarray and a novel phased reflectarray concept", IEEE Antennas and Propagation Society International Symposium, pp.582-585, June 1995.

[23] D.M.Pozar, "Bandwidth of reflectarrays", Electronic Letters, Vol.39, No.21, pp.1490–1491, October 2003.

[24] Q.Y.Li, Y.C.Jiao and G.Zhao, "A novel microstrip rectangular-patch/ring-combination reflectarray element", IEEE Antennas Wireless Propagation Letters, Vol. 8, pp. 1119-1122, 2009.

[25] J.A.Encinar and J.A.Zornoza, "Broadband design of three-layer printed reflectarrays", IEEE Transactions on Antenna and Propagation, Vol.57, No.10, pp.1662-1664, July 2003.

[26] M.R.Chaharmir, J.Shaker and H. Legay, "Broadband design of a single layer reflectarray using multi cross loop elements", IEEE Transactions on Antenna and Propagation, Vol. 57, No.10, pp.3363-3366, October 2009.

[27] M.R.Chaharmir, J.Shaker, G.Nicolas and D.Lee, "Design of broadband, single Layer dual-band large reflectarray using multi open loop elements", IEEE Transactions on Antenna and Propagation, Vol.58, No.9, pp.2875-2883, September 2010.

[28] R.Hodges and M.Zawadzki, "Design of large dual polarized Ku-band reflectarray for spaceborne radar altimeter", IEEE Antennas and Propagation Society Symposium, pp. 4356-4359, June 2005.

[29] D.M.Pozar, S.D.Targonski and R. Pokuls, "A shaped beam microstrip patch reflectarray", IEEE Transactions on Antenna and Propagation, Vol.47, No.7, pp.1167-1173, July 1999.

[30] J.A.Encinar and J.A.Zornoza, "Three- Layer printed reflectarrays for contoured beam space applications", IEEE Transactions on Antenna and Propagation, Vol.52, No.5, pp. 1138-1148, May 2004.

[31] J.Huang and A.Feria, "A one –meter X-band inflatable reflectarray antenna", Microwave and Optical Technology Letters, Vol.20, January 1999.

[32] S.V.Hum and M.Okoniewski, "An electronically tunable reflectarray using varactor-doid-tuned elements", IEEE Antennas and Propagation Society Symposium, Vol.2, pp.1827-1830, June 2004.

[33] M.Riel and J.J.Laurin, "Design of an electronically beam scanning reflectarray using aperture-coupled elements", IEEE Transactions on Antenna and propagation, Vol. 55, No. 5, pp. 1260-1266, May 2007.

[34] S.V.Hum, G.McFeetors and M.Okoniewski, "A reflectarray cell based on a tunable MEMES capacitor", IEEE Antennas and Propagation Society Symposium/URSI, Vol.2, pp.1827-1830, July 2006.

[35] J.Huang, C.Han and K.Chang, "A Cassegrain offset-fed dual-band reflectarray", IEEE Antennas and Propagation Symposium, Albuquerque, NM, pp.2439-2442, July 2006.

[36] A.Yu, F.Yang, A.Z.Elsherbeni and J. Huang, "Experimental demonstration of a single layer tri-band circularly polarized reflectarray", IEEE Antennas and Propagation Society Symposium, July 2010.

[37] F.Arpin, J.Shaker and D.A.McNamara, "Multi-feed single-beam power-combining reflectarray antenna", Electronics Letters, Vol.40, No.17, pp.1035-1037, August 2004.

[38] E.Almajali, "Contributions to the design of sub-reflectarrays", Masters Thesis, University of Ottawa, Ontario, Canada, January 2010.

[39] E.Almajali, D.A.McNamara, J.Shaker, and M.R.Chaharmir, "Experimental validation of design expressions for sub-reflectarrays," in Proceedings Asia-Pacific Microwave Conference (APMC 2009), Singapore, pp.1859–1862, December 2009.

[40] M.Arrebola, L.de Haro and J.A.Encinar, "Analysis of a cassegrain antenna with a reflectarray as subreflector", 29th ESA Antenna Workshop on Multiple Beams and Reconfigurable Antennas, ESA-ESTEC, Netherlands, April 2007.

[41] X.Shenheng, H.Rajagopalan, Y.Rahmat-Samii and W.A. Imbriale, "A novel reflector surface distortion compensating technique using a sub-reflectarray", IEEE Antennas and Propagation Symposium, pp.5315-5318, June 2007.

[42] M.Arrebola, L.de Haro, J.A.Encinar, and L.F. de la Fuente, "Contoured- beam gregorian antenna with a reflectarray as a sub-reflector", Antennas and Propagation European Conference, EuCAP, pp.1-6, November 2007.

[43] X.Shenheng and Y.Rahmat-Samii, "Sub-reflectarrays for spherical aberration compensation: concept and simulations", IEEE Antennas and Propagation Symposium, pp.1-4, July 2008.

[44] M.Arrebola, W.Hu, J.A.Encinar, R.Cahill, R.Dickie, V.Fusco, H.Gamble, Y.Álvarez and F.Las-Heras, "Experimental validation of a 94 GHz dual reflector antenna with a sub-reflectarray", ESA Antenna Workshop, Netherlands, May 2009

[45] H.Rajagopalan, X.Shenheng and Y.Rahmat-Samii "Experimental demonstration of reflectarrays acting as conic section subreflectors in a dual reflector system", IEEE Transactions on Antenna and propagation, Vol.61, No.11, pp.5475-5484, November 2013.

[46] J.Lanteri, J.Y.Dauvignac, Ch.Pichot and C.Migliaccio, "Beam-scanning improvement of reflectarrays by reducing the cell size at millimetre waves", Microwave Optical Technology Letters, Vol.48, No.5, pp.966-968, May 2006.

[47] D.M.Pozar,"Wideband reflectarray using artificial impedance surface", Electronic Letters, Vol.43, No.3, pp.148-149, February 2007.

[48] P.Nayeri, F.Yang and A.Elsherbeni, "A broadband microstrip reflectarray using sub-wavelength patch elements", IEEE International Antennas Propagation Symposium. Digest, Charleston, South Carolina, USA, June 2009.

[49] G.Zhao, Y.C.Jiao, F.Zhang and F.S.Zhang, "A subwavelength element for broadband circularly polarized reflectarrays", IEEE Antennas and Wireless Propagation Letters, Vol. 9, pp.330 – 333, July 2010.

[50] P.Nayeri, F.Yang and A.Elsherbeni, “Broadband reflectarray antennas using double-layer subwavelength patch elements”, IEEE Antennas Wireless Propagation Letters, Vol.9, pp. 1139-1142, July 2010.

[51] J.Ethier, M.R.Chaharmir, and J.Shaker, “Novel approach for low-loss reflectarray designs”, IEEE International Antennas Propagation Symposium Digest, USA, pp.373-376, July 2011.

[52] J.Ethier, M.R.Chaharmir, and J.Shaker, “Reflectarray design comprised of sub-wavelength coupled-resonant square loop elements”, Electronic Letters, Vol.47, No.22, pp.1215-1217, October 2011.

[53] M.Mussetta, P.Pirinoli, R.E.Zich and M.Orefice, “Design of printed microstrip reflectarrays reducing the groundplane reflection”, Proceedings URSI General Assembly, New Delhi, India, 2005.

[54] J.Budhu and Y.Rahmat-Samii,“Understanding the appearance of specular reflection in offset fed reflectarray antennas”, IEEE International Antenna and Propagation Symposium Digest, pp.97-100, USA, 2011.

[55] R.El-Hani and J.Laurin, “Phase analysis for off-specular reflectarray antennas”, IEEE International Antenna and Propagation Symposium Digest, pp.380-383, USA, 2011.

[56] R.El-Hani and J.Laurin, “Specular reflection analysis for off-specular reflectarray antennas”, IEEE Transactions on Antenna and propagation, Vol.61, No.7, pp.3582 – 3588, July 2013.

[57] R.Romanovsky, “Cellullar reflectarray antenna and method of making same”, US Patent 7,791,522, Sept 2010.

[58] S.V.Hum and M.Okoniewski, “A Technique for predicting specular reflections from reflectarrays”, IEEE International Antenna and Propagation Symposium Digest, pp.2116-21119, USA, July 2007.

[59] D.R.Jackson, “Microstrip Antennas”, Chap.7 in : J.L.Volakis (Edit.), Antenna Engineering Handbook (McGraw Hill, 2007) Fourth Edition, Sect.7.5

[60] N.A.Adatia and A.W.Rudge, “Beam squint in circularly polarized offset reflector antennas”, Electronic Letters, Vol.11, No.21, pp.513–515, October 1975.

[61] S.Xu and Y.Rahmat-Samii, “A novel beam squint compensation technique for circularly polarized conic-section reflector antennas” IEEE Transaction in Antennas and Propagation, Vol.58, No.2, pp.307–317, Feb 2010.

[62] S.D.Targonsk and D.M.Pozar, “Minimization of beam squint in microstrip reflectarrays using an offset feed”, IEEE International Symposium on Antenna and Propagation, Vol.2, pp.1326-1329, July 1996.

[63] Y.Zhuang, K.Wu, C.Wu and J.Lietva, “A combined full-wave CG-FFT method for rigorous analysis of large microstrip antenna arrays”, IEEE Transactions on Antennas and Propagation, Vol.44, No.1, pp.102-109, January 1996.

[64] B.Khayatian, Y.Rahmat-Samii and J.Huang, “Radiation characteristics of reflectarray antennas: Methodology and applications to dual configurations”, Antennas and Propagation European Conference, EuCAP, pp.1-12, November 2006.

[65] P.Nayeri, F.Yang and A.Elsherbeni, “Radiation analysis approaches for reflectarray antennas”, IEEE Antennas and Propagation Magazine, Vol.55, No.1, pp.127-134, February 2013.

[66] Code CST Microwave Studio, SONNET High Frequency Electromagnetic Software Company, USA (www.sonnetsoftware.com).

[67] H.Ling, S.W.Lee, P.T.C.Lam and W.V.T.Rusch, “Focal shifts in parabolic reflectors”, IEEE Transaction in Antennas and Propagation, Vol.33, No.7, pp.744-748, July 1985.

[68] A.G. Roederer, “Reflectarray antenna”, Antennas and Propagation European Conference, EuCAP, pp.18-22, April 2009.

[69] H.Rajagopalan, S.Xu and Y.Rahmat-Samii, “Reflectarray phase analysis: A simple and intuitive understanding”, IEEE International Symposium on Antenna and Propagation Digest, Canada, July 2010.

[70] F.Arpin, D.A.McNamara, J.Shaker and A.Ittipiboon, “A receive-mode analysis of reflectarray antennas”, 10th International Symposium of Antenna Technology & Applied Electromagnetics (ANTEM 2004), pp.569-572, Ottawa, Ontario, Canada, July 2004.

CHAPTER 3

An Investigation of Reflectarray Operation Using Its Component Current Contributions

3.1 Introduction

As part of efforts to improve reflectarray designs, there has been an interest in elucidating the physical mechanisms [1] responsible for reflectarray operation [2]. In this chapter we further investigate reflectarray operation by explicitly showing the contributions of the individual reflectarray components (namely the elements, groundplane and dielectric substrate) to the reflectarray far-field radiation pattern. As discussed in Chapter 2, a printed reflectarray is composed of radiating elements, a ground-plane, and a dielectric substrate. Thus the performance of the reflectarray in terms of field distributions in the near- and far-zones can be understood in terms of the sum of scattered fields from these constituent components. Electrical currents on the conducting parts (groundplane and cell elements), and polarization current that is attributed to the field within the dielectric substrate, can be used to estimate the scattered field from each respective component. In Section 3.2 a two-dimensional (2D) method of moments analysis is used to decompose the radiated field from a 2D reflectarray into its constituent components. In Section 3.3 it is shown how the fields, computed from a very complete full-wave 3D model using the high frequency structure simulator HFSS [3], can be separately post-processed to find the appropriate currents (not routinely available from HFSS) on the individual reflectarray components. The far- and near-field contributions of these currents are then used to assess the role played by these individual components in the overall reflectarray operation. This chapter is concluded in Section 3.4

3.2 Using 2D Method of Moments Analysis in Elucidating Reflectarray Operation

3.2.1 Preliminary Remarks

Although it is now computationally possible to analyse actual 3D reflectarray antennas using commercial electromagnetic simulation software (eg. [3]), it is not possible, at least at the time of writing, to directly output (from such software) the fields due to specific portions of the structure being modelled. This obstacle, which did not have a solution at the time we started this work, forced us to think about a viable alternative that supports the decomposition of reflectarray components' radiated fields. To achieve this goal, an existing two dimensional (2D) method of moments formulation [4] was implemented in a code [5] to rigorously simulate a full 2D reflectarray structure. Post processing in this code does include the field's computation due to currents on any part of the designed reflectarray. The experience with the 2D modelling provides the confidence needed to be sure that we are correctly interpreting the physical quantities we will indirectly extract from the output of the 3D models discussed in Section 3.3.

3.2.2 Reflectarray Configuration and Computational Model

Rigorous calculations should be carried out to find the current distribution on each constituent component of the reflectarray in order to calculate the contribution of that particular component to the reflectarray total radiated field. To achieve that, a 2D reflectarray was modelled using a 2D moment method formulation [4,5]. The computational model is shown in Figure 3.1. In this TEz case where the electric field lies entirely in the xy-plane, the magnetic line source generates an incident field which excites the horn walls to form the 2D feed horn for the reflectarray. It of course also excites the rest of the reflectarray structure consisting of the strip elements of different finite widths and infinite length, located on a substrate that is backed by a groundplane. This analysis is rigorous as far as the 2D reflectarray is concerned, and all interactions are accounted for. Although [5] uses sets of internal and external equivalent currents it is possible to use these to determine the physical conduction currents on the strips and groundplane (using the boundary condition on the tangential magnetic field) and polarisation currents in the substrate

(using the volume equivalence theorem). These are the current densities that generate the field scattered from the reflectarray structure.

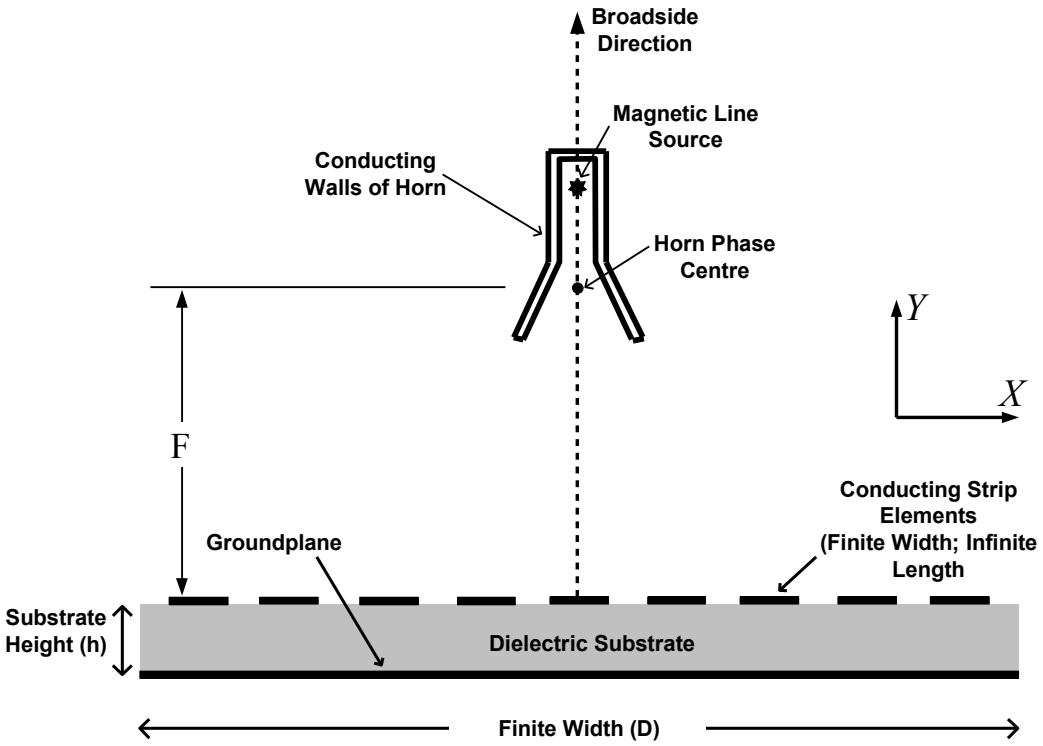

Figure 3.1: Two-dimensional on-axis reflectarray antenna model. D=16λ, F=15.5λ and the inter-element spacing is λ/2. The substrate h=0.508 mm (λ/20) and its ε_r =3, and the frequency is 30 GHz.

3.2.3 2D Reflectarray Design Considerations

The general reflectarray design procedure, which was illustrated in Section 2.2.2, is used here to design a 31-element 2D reflectarray. The individual strip widths are selected so that each element has the reflection phase required to generate a main beam in the broadside direction when illuminated by the feed from the desired focal point. The database of strip width versus reflection phase values shown in Figure 3.2 was generated via HFSS [3] using the appropriate infinite periodic structure models with normally incident x-polarised plane waves at 30 GHz. The feedhorn aperture width (1.75λ) and flare length (1.14λ) were chosen so that it illuminates the reflectarray with an edge taper of 10dB. It was first modelled on its own and its phase centre location determined; the phase centre has been calculated in advance using SABOR [6] to ensure

the coincidence between the real focal point and the calculated feed phase centre. By definition all radiation patterns of the 2D reflectarray are E-plane patterns.

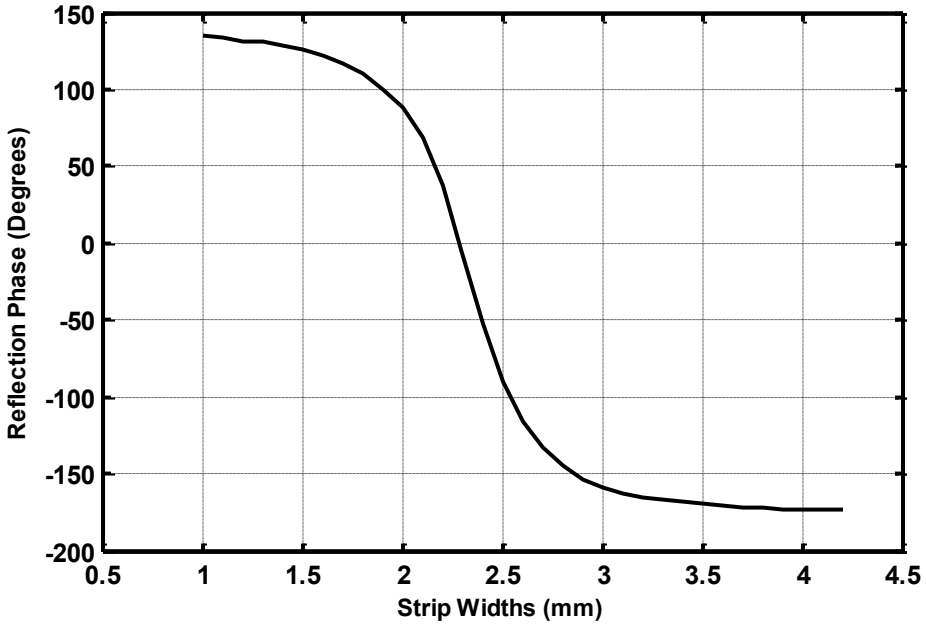

Figure 3.2: Phase response of the strip element with unit cell size of $\lambda/2$ generated for 30Ghz operating frequency. The substrate h=0.508 mm (λ/20) and its ε_r =3.

3.2.4 Examination of the Contributions of the Constituent Currents

In order to validate the code, the strips were first removed and the scattered field of the groundplane/substrate structure determined; as expected this was clearly the feed-horn image pattern reproduced about the broadside direction (the specular direction in this centre-fed case), except for additional ripples due to the finite width of the groundplane and presence of the substrate, as shown in Figure 3.3. Computations for the complete model (strips included) obtrude the magnitude of the conduction currents on the strips and groundplane shown in Figure 3.4. Note that these are directed across the strips and groundplane, in the x-direction. Observe that the spatial pattern of the current on the groundplane virtually replicates that on the strips; their peaks are coincident. The groundplane currents do not have peaks under the gaps between the strips as one might possibly expect; there is no "shadowing" by the strips.

Each strip-groundplane combination (the true elements of the reflectarray) indeed acts as an open cavity. Most of the strips have widths within 10% of the resonant width (that width for which the reflection phase at the reference plane of the element is 0° at 30 GHz). Those with significantly different (i.e. non-resonant) widths are the ones showing greatly reduced current magnitudes in Figure 3.4. The strip currents are discontinuous between adjacent strips where there is no conductor; in the plotted distribution these regions are simply bridged by straight lines. The computations also show that these strip and groundplane currents are 180° out of phase[5].

The radiation patterns due to the conduction currents on the strips and groundplane separately are shown in Figure 3.5. Their individual contributions are almost identical. It is noteworthy that the groundplane is as important as the elements themselves since it replicates their contribution to the entire reflectarray radiation pattern. Each appears to contain the feedhorn image pattern about the broadside direction. However, when we perform complex addition of these two individual patterns we obtain the result shown as the dashed curve in Figure 3.6, in which the feed image is not significant. The reason for the destructive interference of the two patterns beyond 5° is clear from the pattern phases shown in Figure 3.7. The phase of the pattern due to the groundplane currents has purposefully had 180° added to it, so where the two curves are almost coincident there will be destructive interference (viz. beyond 5°), and where they are not coincident constructive interference is possible, as in the main lobe region (out to 5°) of the reflectarray.

If we next add the contribution of substrate polarization current to the far-field radiation pattern we obtain the pattern shown as the solid line in Figure 3.6. This is the overall far-zone scattered field from the reflectarray structure. The polarization current contribution enhances the pattern somewhat by reducing the side lobe levels over some angular regions. Although the substrate's contribution may seem small, its presence of course impacts the conduction current distributions due to interactions between the parts of the reflectarray.

[5] We will discuss the currents' phase behaviour in Section 4.2.2.

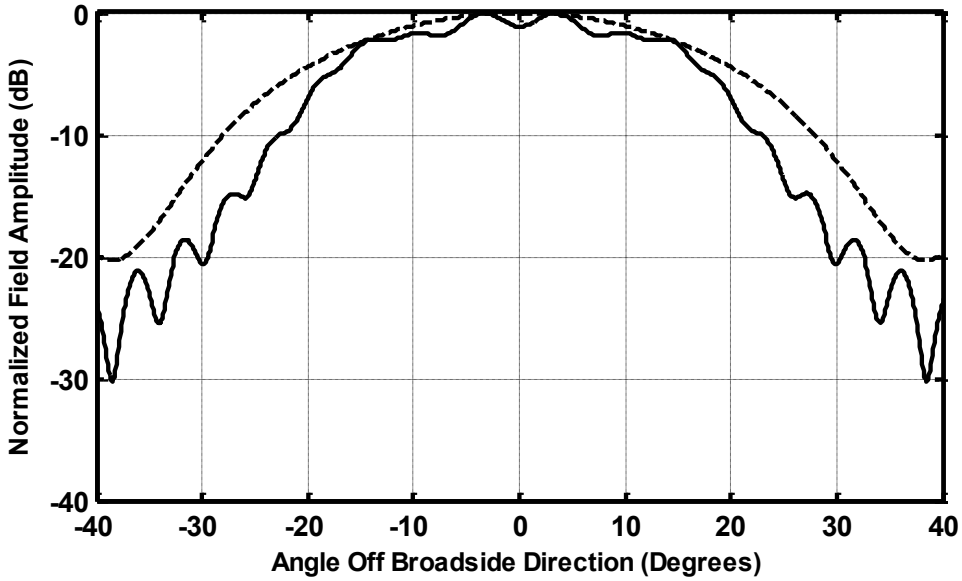

Figure 3.3: Scattered field (——) from the structure when the analysis is done with the strips absent. The pattern of the feed (rotated by 180°) on its own, with the entire reflectarray structure absent, is shown as the dashed line (— — —).

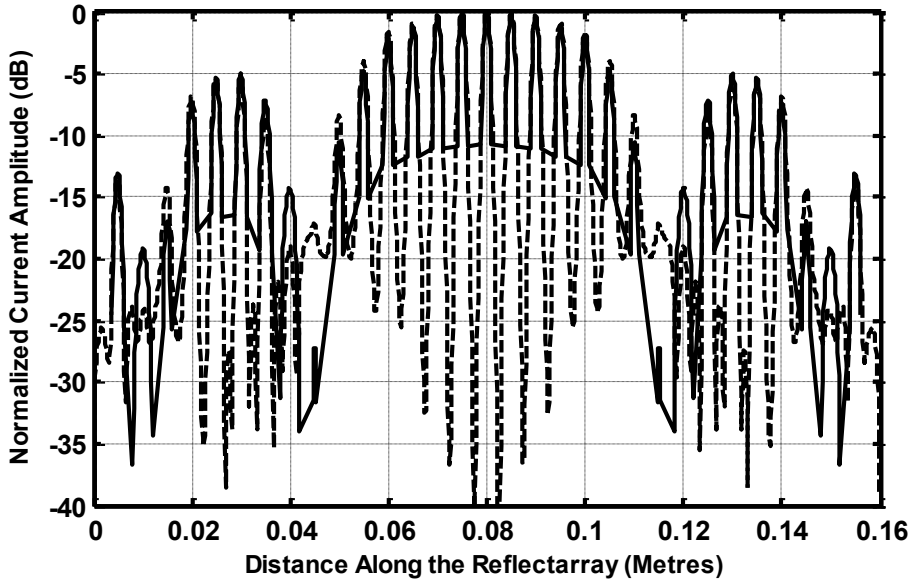

Figure 3.4: Normalized magnitude of the conduction current density on the radiating strips (——) and on the groundplane (— — —). The left hand edge of the groundplane is at x=0 and the right hand at x=0.16m.

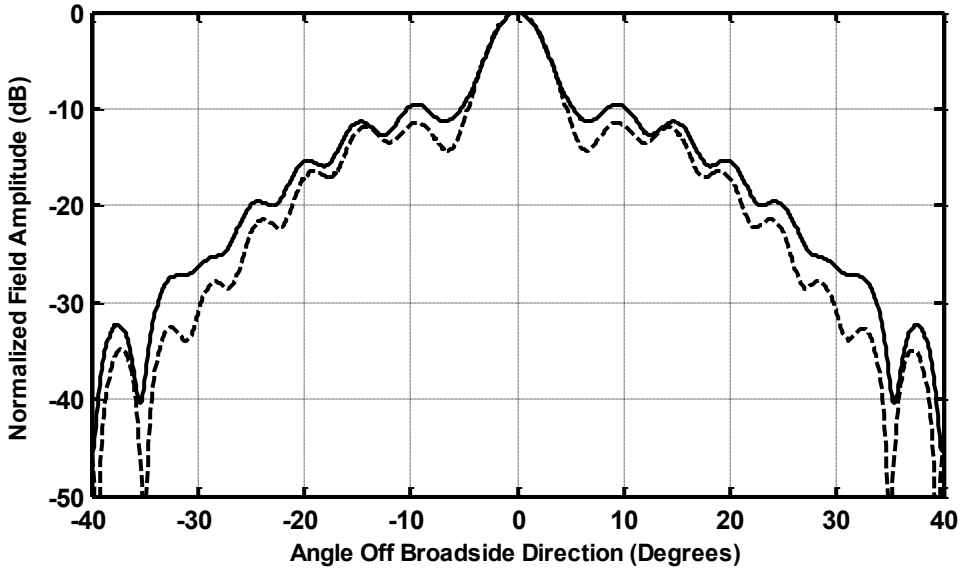

Figure 3.5: Radiation pattern contributions due to the conduction current density on the strips only (——), and on the groundplane only (— — —).

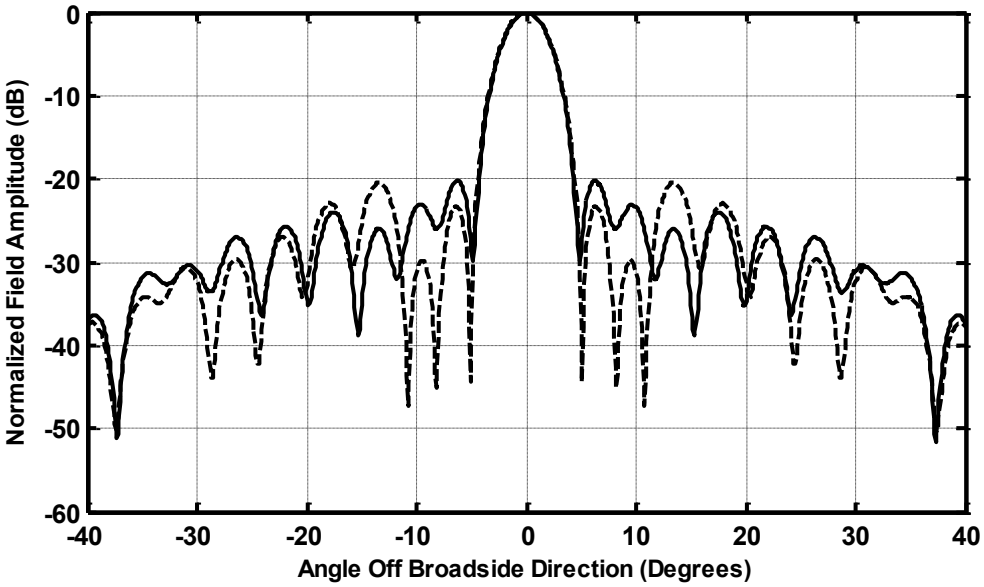

Figure 3.6: Radiation pattern due to the (complex) addition of the contributions of the conduction current densities on the strips and groundplane (— — —), and that (now the complete scattered pattern) when the contribution of the polarisation current density is added as well (——). This does not include the feedhorn contributions.

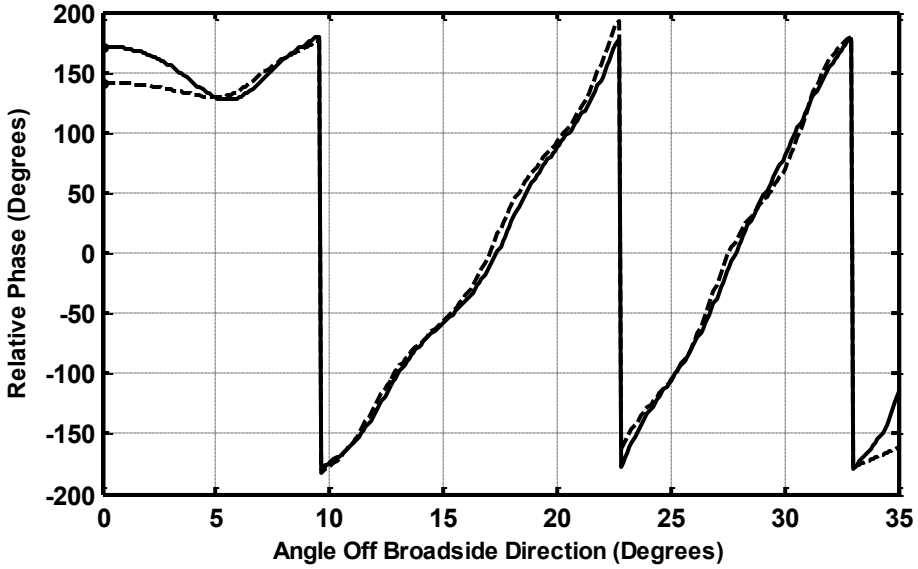

Figure 3.7: Phase of the radiation pattern contributions due to the conduction current density on the strips only (——), and on the groundplane only (– – –). The phase pattern due to the groundplane currents has purposefully had 180° added to it for this plot.

Although the determination of the contributions of reflectarray antenna's components to its far-field radiation pattern using the 2D analysis provides most of the traits of the actual three-dimensional (3D) one, we next proceed to develop a method of using a commercially available code HFSS to examine reflectarrays' operating mechanism, but of course for a true 3D reflectarray geometry. It is of note here that with the commercial codes, like HFSS we use in Section 3.3, not all the information that we had available from the in-house 2D code (over which we had complete control) is directly accessible. Furthermore, with HFSS, it is not possible to assess the role of the polarization currents to the far-fields without including the feed-horn interactions. The fact that our in-house 2D code is developed using the method of moment (MOM), which is different than the finite element frequency domain numerical technique (FEFD) used in analyzing the 3D HFSS reflectarray model in Section 3.3, reinforces the validity of our conclusions about the reflectarray operating mechanism.

3.3 Investigating Reflectarray Operation Using A 3D Analysis Technique

3.3.1 Introduction

Commercial codes for full-wave electromagnetic simulation are now widely available. The adage that no code is able to solve all problems is of course true, and so most engineers from time to time are in the situation where they are not able to get all they want from a given code. In such a situation one should think of ways to utilize these codes to the full. In this section it is shown how the fields, computed from a very complete full-wave HFSS model, can be separately post-processed to find the appropriate currents (not routinely available from HFSS) on the individual reflectarray components. The far- and near-field contributions of these currents are then used to assess the role played by these individual components in the overall reflectarray operation.

3.3.2 Extraction of the Conduction Currents on Reflectarray Components From the HFSS Model

Computational electromagnetics methods such as that embodied in HFSS provide superior tools for antenna analysis. The source currents and fields obtained from such modelling incorporate all the physical phenomena associated with a particular configuration. Commercial codes often do not allow one to completely extract all the physical quantities one might want, or to determine the contributions of individual pieces of the model. It is then necessary to establish how such “missing” quantities can be found from the rigorous numerical solutions, and hence use the models to the full. The modelling of a complete reflectarray is a case in point. As stated in Section 2.2.1, by "elements" we mean just the conducting shapes on the upper layer of the substrate, though it is understood that these shapes plus the groundplane constitute the elements of the reflectarray.

In a reflectarray model such as that depicted in Figure 3.8, HFSS calculates the fields over a highly dense mesh within the radiation box that encloses the entire reflectarray structure. It is worth mentioning here that all our simulations were done using the FEBI option in HFSS, where

both finite element and moment method (boundary integral) are used on the same structure. The finite element method is applied inside the radiation boxes (depicted in Figure 3.8), and the moment method is applied external to radiation box surfaces. The two formulations are connected via the tangential fields/equivalent currents on the surfaces of the radiation box, thereby rigorously accounting for all interactions between the feed and reflectarray in this case. HFSS-FEBI calculates the fields over a highly dense mesh within the radiation box that encloses the entire reflectarray structure. But it does not give direct access to both the amplitude and phase of current densities over a *user-specified* grid of points on selected parts of the reflectarray.

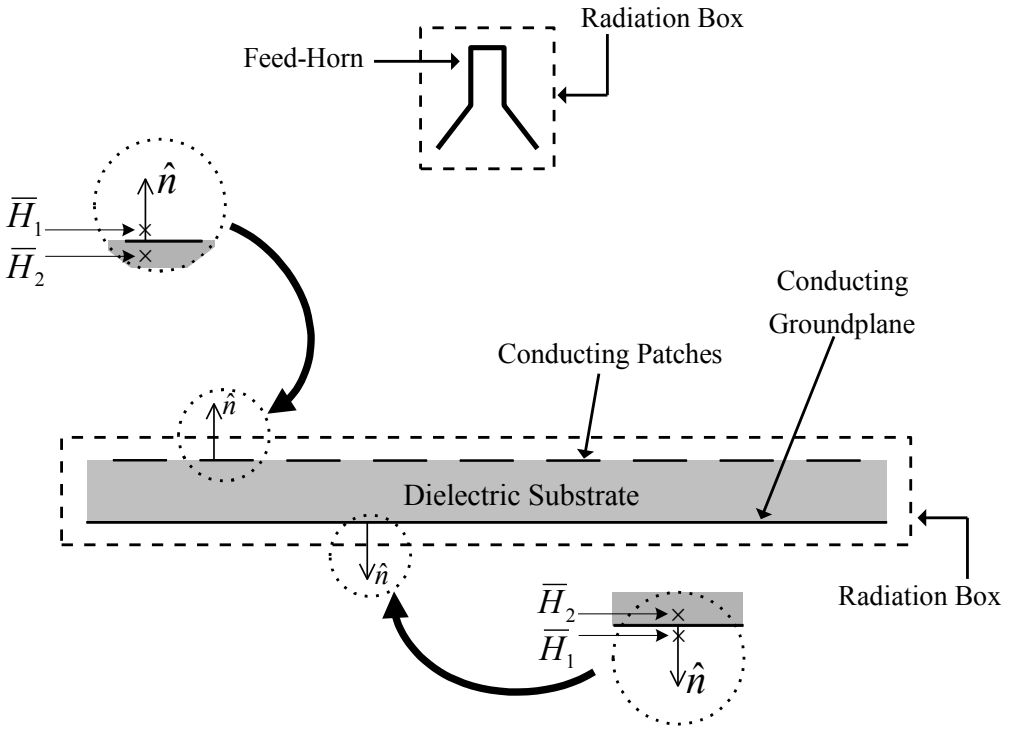

Figure 3.8: Cross section of reflectarray antenna geometry showing the radiation boxes and the quantities used in conduction current extraction.

We have therefore used separate post-processing of the field data (that can be exported in complex form over a user-defined grid of points) to extract such quantities. In particular we want to find the conduction current density on all conducting parts of the reflectarray (namely the elements and the groundplane). Hence, with reference to Figure 3.9, we define a grid of points $(x_n, y_n, 0)$ over the element plane, and a similar set $(x_n, y_n, -h)$ over the groundplane, each located

at the centre of a rectangular sampled subdivision of size Δx by Δy, which are selected to be much smaller than the reflectarray element lattice dimensions d_x and d_y.

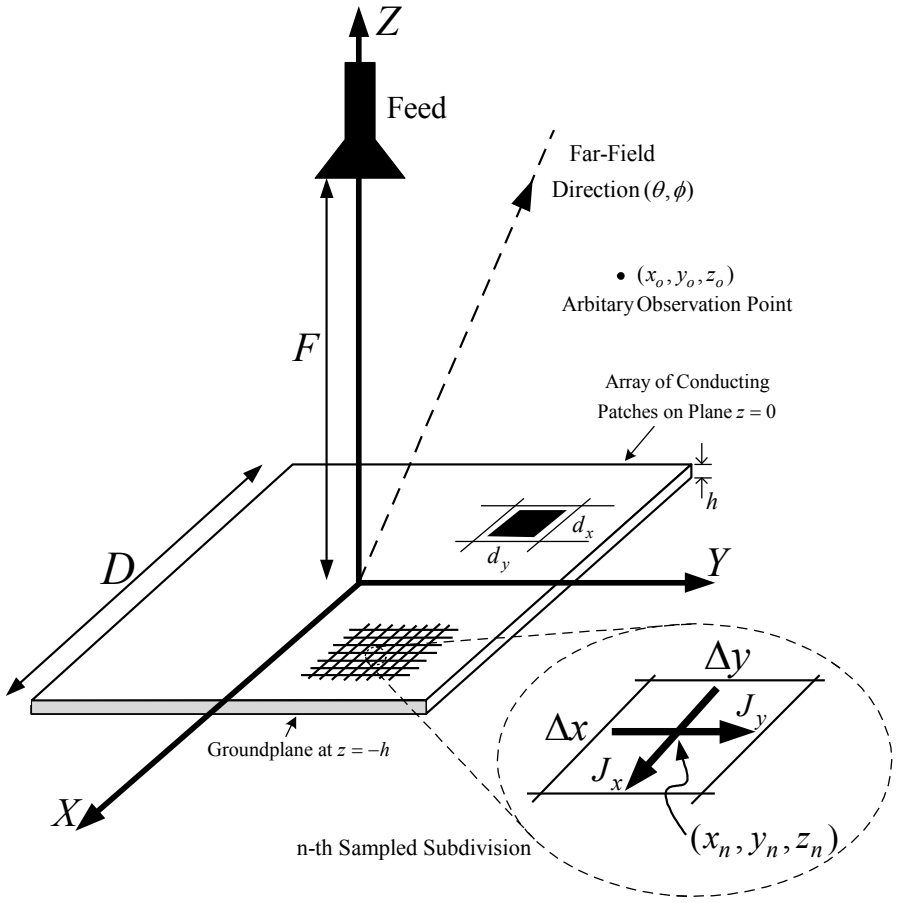

Figure 3.9: Reflectarray antenna of patch elements. The element and groundplane surfaces are divided into a grid of points, each at the centre of a subdivision.

The determination of the conduction current density at points on the element plane is described below in some detail. The procedure for that on the groundplane is similar. At points on the $z = 0$ element plane the current density is given by the boundary condition

$$\bar{\mathrm{J}}_s = \hat{\mathrm{n}} \times \bar{\mathrm{H}}_1 - \hat{\mathrm{n}} \times \bar{\mathrm{H}}_2 \tag{3.1}$$

that must apply at all air-conductor and conductor-substrate interfaces, where $\bar{\mathrm{J}}_s$ is the current density, $\hat{\mathrm{n}}$ is the unit normal vector, and $\bar{\mathrm{H}}_1$ and $\bar{\mathrm{H}}_2$ are the magnetic fields shown in Figure 3.8.

At points that lie on a conductor, expression (3.1) gives a conduction current density; we will see that at points that do not fall on a conductor (3.1) predicts values that are negligible, as expected. Since $\hat{n} = \hat{z}$ on the element plane, (3.1) becomes

$$\begin{aligned} \bar{\mathrm{J}}_s(x_n, y_n, 0) = &\left\{-\mathrm{H_y}(x_n, y_n, 0+\Delta z) + \mathrm{H_y}(x_n, y_n, 0-\Delta z)\right\}\hat{x} \\ &+ \left\{\mathrm{H_x}(x_n, y_n, 0+\Delta z) - \mathrm{H_x}(x_n, y_n, 0-\Delta z)\right\}\hat{y} \end{aligned} \tag{3.2}$$

The four terms in the curly brackets of (3.2), which are the fields just above or just below the grid point, are exported from HFSS for each of the grid points $(x_n, y_n, 0)$. The actual boundary condition (3.1) of course involves a limiting operation as $\Delta z \to 0$. Numerical experiments for decreasing values of Δz from 10^{-3}m through 10^{-7} m reveal that convergence is obtained at $\Delta z = 10^{-6}$m. Note that (3.2) in fact gives the vector sum of the current densities on the two sides of the zero thickness conducting surface to which it applies [7].

The field due to the complete surface current density distribution on the element plane can be obtained through evaluation of well-known superposition integrals [8,pp.282-284]. We have done this by approximating the field due to each subdivision as that of spatially orthogonal Hertzian dipoles of complex amplitudes

$$a_{nx} = \Delta x \Delta y \left\{-\mathrm{H_y}(x_n, y_n, 0+\Delta z) + \mathrm{H_y}(x_n, y_n, 0-\Delta z)\right\} \tag{3.3}$$

and

$$a_{ny} = \Delta x \Delta y \left\{\mathrm{H_x}(x_n, y_n, 0+\Delta z) - \mathrm{H_x}(x_n, y_n, 0-\Delta z)\right\} \tag{3.4}$$

The electric field components of the *n-th* subdivision at any observation point (x_o, y_o, z_o) at any distance from the subdivision are

$$E_x^n(x_o,y_o,z_o) = a_{nx}\left(\eta_o/jk\right)\left\{k^2\frac{e^{-jkR}}{4\pi R} - P(k,R) + (x_o-x_n)^2\frac{Q(k,R)}{R^2}\right\}$$

$$+a_{ny}\left(\eta_o/jk\right)(x_o-x_n)(y_o-y_n)\frac{Q(k,R)}{R^2} \tag{3.5}$$

$$E_y^n(x_o,y_o,z_o) = a_{nx}\left(\eta_o/jk\right)(x_o-x_n)(y_o-y_n)\frac{Q(k,R)}{R^2}$$
$$+a_{ny}\left(\eta_o/jk\right)\left\{k^2\frac{e^{-jkR}}{4\pi R} - P(k,R) + (y_o-y_n)^2\frac{Q(k,R)}{R^2}\right\} \tag{3.6}$$

and

$$E_z^n(x_o,y_o,z_o) = a_{nx}\left(\eta_o/jk\right)(x_o-x_n)(z_o-z_n)\frac{Q(k,R)}{R^2}$$
$$+a_{ny}\left(\eta_o/jk\right)(y_o-y_n)(z_o-z_n)\frac{Q(k,R)}{R^2} \tag{3.7}$$

where

$$R = \sqrt{(x_o-x_n)^2+(y_o-y_n)^2+(z_o-z_n)^2} \tag{3.8}$$

$$P(k,R) = (1+jkR)e^{-jkR}/4\pi R^3 \tag{3.9}$$

and

$$Q(k,R) = (3+j3kR-k^2R^2)e^{-jkR}/4\pi R^3 \tag{3.10}$$

The fields due to the current density over the entire element plane are then simply the sum of the above contributions for each subdivision. The above expressions could also be used to determine

the far-zone radiation patterns of the various current density distributions, but in such cases it is well-known that simpler expressions can be used. In the present instance the far-zone field components of the *n-th* subdivision (with the factor e^{-jkr}/r suppressed) are

$$E_\theta^n(\theta,\phi) = C_o \left\{ -a_{nx}\cos\theta\cos\phi - a_{ny}\cos\theta\sin\phi \right\} F_n(\theta,\phi) \tag{3.11}$$

and

$$E_\phi^n(\theta,\phi) = C_o \left\{ a_{nx}\sin\phi - a_{ny}\cos\phi \right\} F_n(\theta,\phi) \tag{3.12}$$

where

$$F_n(\theta,\phi) = e^{jk(x_n\sin\theta\cos\phi + y_n\sin\theta\sin\phi + z_n\cos\theta)} \tag{3.13}$$

with $C_o = j\omega\mu_o/4\pi$, and $z_n = 0$ ($z_n = -h$) for grid points on the element plane (groundplane). The field due to the current density over the entire element plane is the sum of the above contributions. Ludwig's third definition [9] is used to convert these to the co- and cross-polarisation components actually measured on an antenna test range.

The procedure for finding the fields due to the groundplane current distribution (where $\hat{n} = -\hat{z}$) is similar, except that instead of (3.2) we use

$$\begin{aligned} \bar{\mathrm{J}}_s(x_n, y_n, -h) = &\left\{ \mathrm{H_y}(x_n, y_n, -h-\Delta z) - \mathrm{H_y}(x_n, y_n, -h+\Delta z) \right\} \hat{x} \\ &+ \left\{ -\mathrm{H_x}(x_n, y_n, -h-\Delta z) + \mathrm{H_x}(x_n, y_n, -h+\Delta z) \right\} \hat{y} \end{aligned} \tag{3.14}$$

3.3.3 Reflectarray Far-Field Radiation in Terms of Its Component Current Contributions

To investigate the contributions of the reflectarray components to its far-field patterns a single layer centre-fed reflectarray of rectangular patches was designed and simulated at a centre frequency of 30GHz ($\lambda_0 = 10$mm) where the electric field is polarized along the x-axis in Figure 3.9. The substrate has $\varepsilon_r = 3$ and thickness $h = 0.508mm$. The reflectarray size is $15.5\lambda_0 \times 15.5\lambda_0$ and the feed phase centre located at $F = 15.5\lambda_0$ from its surface. We have used a subdivision size $\Delta x = \Delta y = \lambda_0 / 20,$ whereas we have $d_x = d_y = \lambda_0 / 2.$

Figure 3.10 shows the extracted conduction current densities on the patches and groundplane, obtained using equations (3.2) and (3.14). It is evident that the current density on the groundplane almost "images" that on the patches, with similar amplitudes. This tells us that the groundplane contributes to reflectarray operation in much the same way as do the patches. Those elements that are near resonance, in other words those that have resonant or near-resonant lengths (particularly those located near the centre of the reflectarray), have strong "images" on the groundplane, with which they form open resonators.

The individual and combined conduction current contributions of the patches and groundplane to the reflectarray fields in the far-zone are shown in Figure 3.11, using equations (3.11) through (3.13). These demonstrate that the groundplane and the patches separately contribute to the far-field almost equally[6], as might be expected from the current density distributions shown in Figure 3.10. The combined contributions of the patches and groundplane, which result from performing a complex addition of their patterns, give a pattern that is different from their separate contributions and more like that expected from a conventional reflectarray. The separate contribution of each exhibits high sidelobe levels over the 7°-17° angular region off the broadside direction. In the combined contribution this level is significantly suppressed.

[6] The relative power contribution of each reflectarray component will be illustrated in detail in Section 4.2.2.

The reason for the desirable destructive interference of the two patterns beyond 7° from broadside is clear from examination of the far-zone pattern phases in Figure 3.12. In this figure the phase of the pattern due to the groundplane currents has purposefully had 180° added to it, and thus where the two curves are almost coincident (namely beyond 7°) there will be destructive interference, and where they are not coincident (the main beam region) some constructive interference is possible. The effect of adding the substrate polarization current contribution to the far-field radiation pattern is shown in Figure 3.13 where the far-zone pattern due to conduction and polarization currents is compared to the far-zone pattern due to the conduction currents only. The addition of the polarization current contributions creates some changes on the overall far-zone scattered field pattern from the reflectarray structure by increasing or decreasing the side lobe levels over some angular regions. Similar to what was stated in Section 3.2.4, the substrate's presence impacts the conduction current distributions due to the interactions between the components of the reflectarray that are included in the HFSS model.

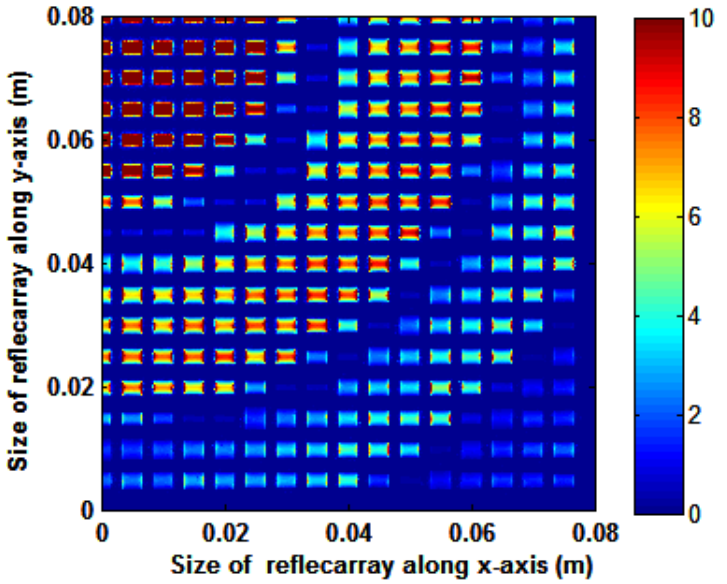

(a)

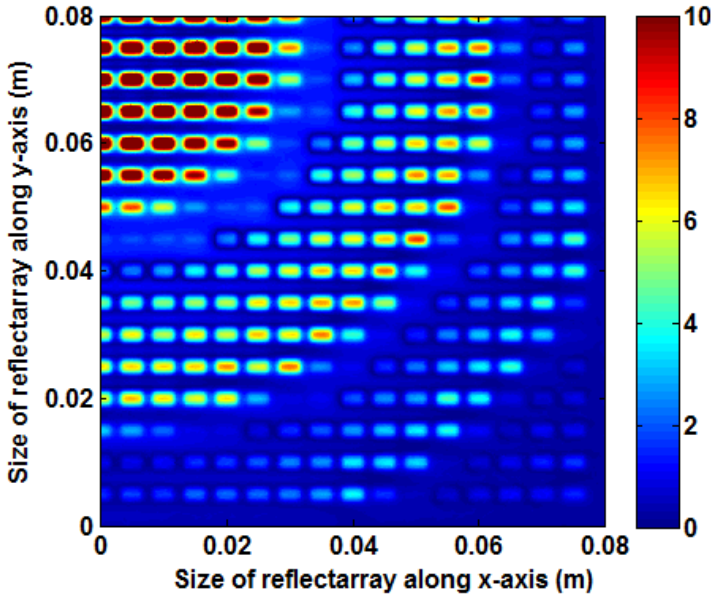

(b)

Figure 3.10: The extracted conduction surface current density on (a) the patch elements, and (b) the groundplane. One quadrant shown due to symmetry.

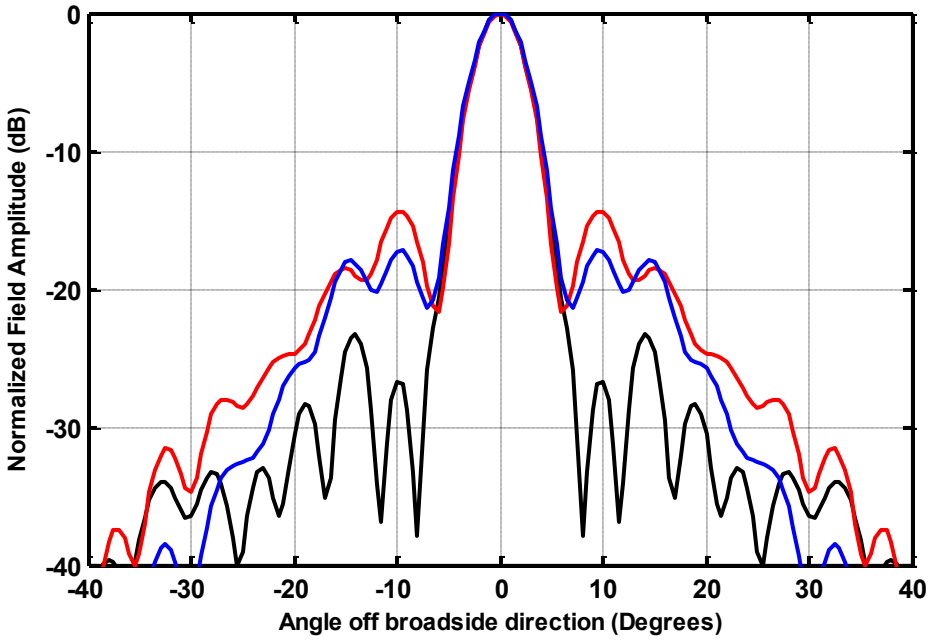

Figure 3.11: E-plane (scattered) far-field radiation patterns due to conduction currents on the patches (——), groundplane (——), and both the patches & groundplane (——), calculated using the extracted current densities at 30GHz.

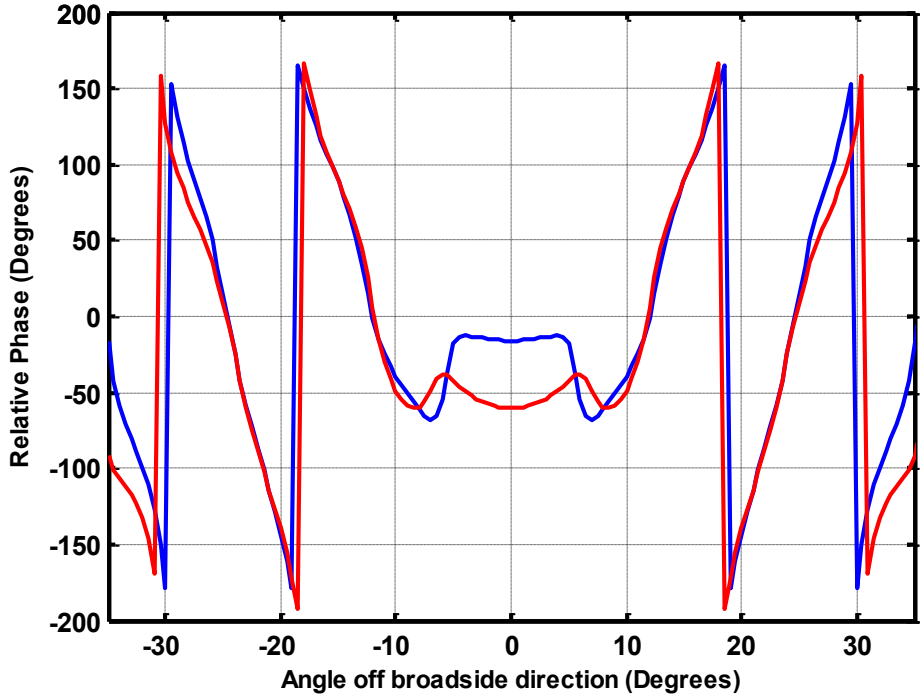

Figure 3.12: Phase of radiation patterns due to conduction current density on the patches only (——), and the groundplane only (——). The phase pattern due to groundplane currents has purposefully had 180° added for this plot.

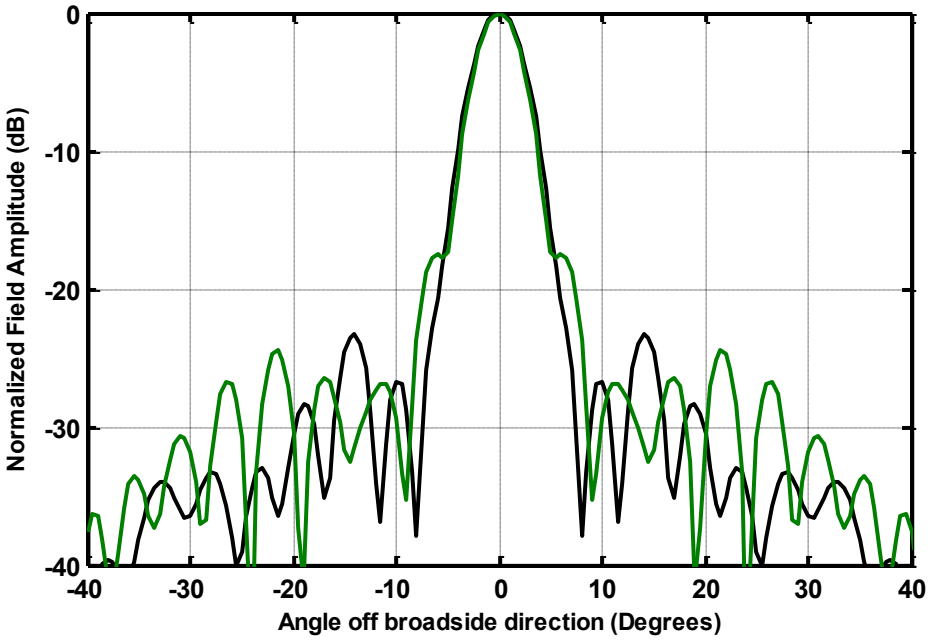

Figure 3.13: E-plane (scattered) far-field patterns computed from extracted conduction currents on both the patches & groundplane (——), and obtained directly from HFSS (——) and so due to conduction & polarization currents.

3.3.4 Reflectarray Near-Field in Terms of Its Component Current Contributions

In order to study the contributions of the reflectarray component currents in the reflectarray near-field region we perform a receive mode analysis by illuminating the reflectarray structure with an x-polarized plane wave as shown in Figure 3.14. We then extract the conduction currents on the patches and groundplane from the simulation model as before. These extracted currents are next used to calculate the reflectarray near-field along the reflectarray central axis (Line#1), and along the line transverse to it (Line#2). At the design frequency both these lines pass through the reflectarray focal point where the scattered field peaks [10]. Figures 3.15 and 3.16 show the separate and combined contributions of the conduction currents on the patches and groundplane. Once again we observe that the patches and groundplane function in much the same way; the scattered field due to their individual contributions peaks at the same point (the focal point), and hence each plays a role in the focusing properties of the reflectarray.

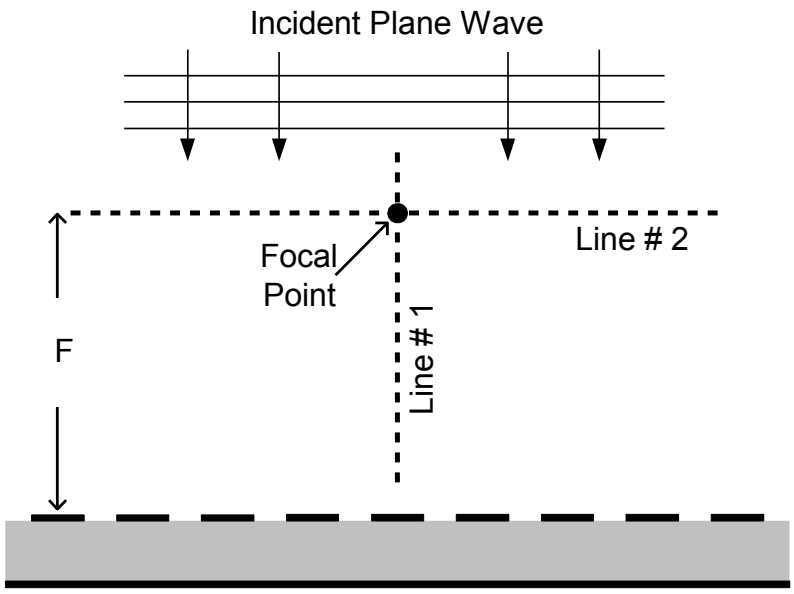

Figure 3.14: Sketch illustrating the configuration used for the receive-mode analysis of the reflectarray antenna.

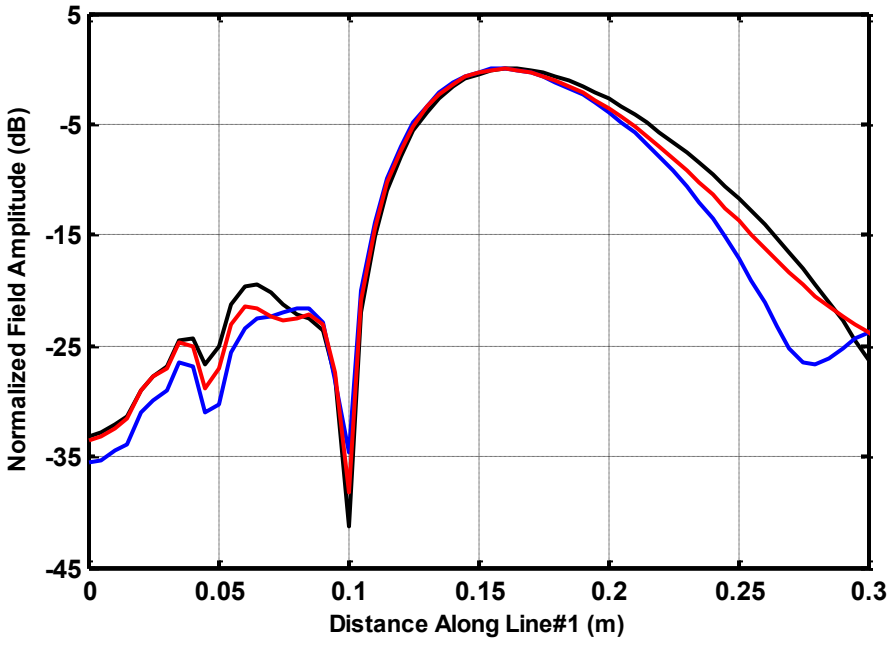

Figure 3.15: Scattered near-field along Line#1 due to the conduction currents on the patches (——), the groundplane (——), and both the patches & groundplane (——).

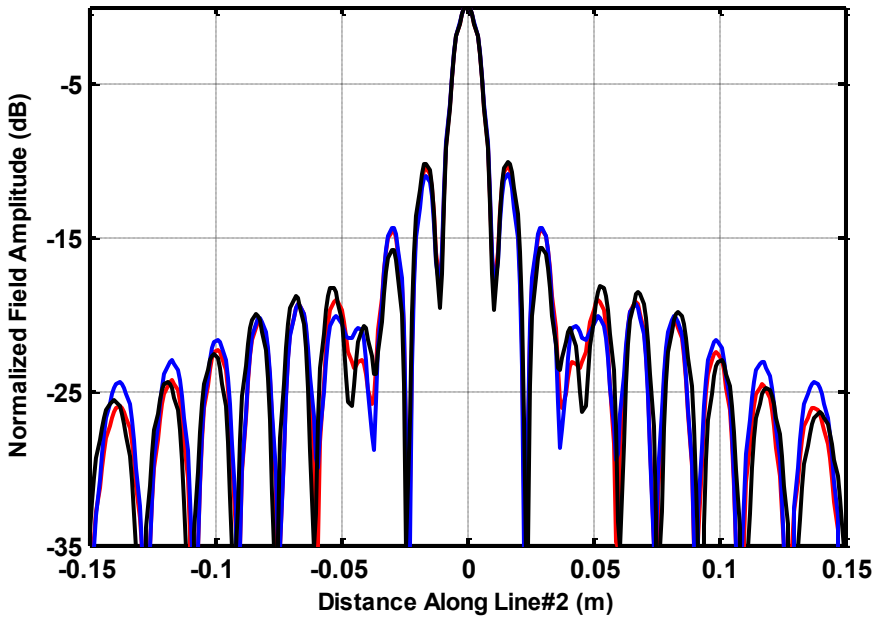

Figure 16: Scattered near-field along Line#2 due to the conduction currents on patches (——), the conduction currents on the groundplane (——), and the conduction currents on both the patches & groundplane (——).

3.4 Concluding Remarks

This chapter describes a component-by-component technique to elucidate reflectarray antenna operation whereby the role of the various reflectarray parts, namely the elements, the groundplane and the dielectric substrate, can be assessed by determining their individual and aggregate contributions to the reflectarray near- and far-fields. In Section 3.2, the above mentioned technique was applied to a 2D reflectarray model, which was simulated using a 2D in-house code that was developed based upon the method of moments numerical technique. This 2D code is developed such that one can calculate the contribution of the conduction and/or the polarization currents to the near- and far-fields directly and rigorously. In Section 3.3 a 3D reflectarray model was simulated using HFSS. The required conduction currents were extracted from the 3D reflectarray model prior to calculating their contribution to the reflectarray near- and far-fields. The results obtained in Sections 3.2 & 3.3 show that the radiating elements and the groundplane contribute almost equally to the reflectarray near- and far-fields. This is confirmed from the current amplitude distributions which look identical on these parts. The polarization current contribution was shown to be somewhat minor although the substrate role cannot be reduced to this contribution as its existence affects the conduction currents distribution on the conduction parts of the reflectarray. The significance of this component-by-component examination technique will be clear in Chapter 4, where it is used successfully to diagnose the source of the feed-image lobe problem in offset-feed reflectarrays. The fact that the 2D and 3D observations are so similar provides the confirmation needed to ensure that the technique for indirectly extracting the component current densities in the 3D model is indeed correct. Portions of the work described in this chapter have already been published in [11].

Chapter 3 References

[1] A.G.Roederer, "Reflectarray antenna", Antennas and Propagation European Conference, EuCAP, pp.18-22, April 2009.

[2] H.Rajagopalan, S.Xu and Y.Rahmat-Samii, "Reflectarray phase analysis: A simple and intuitive understanding", IEEE International Symposium on Antenna and Propagation Digest, Canada, July 2010.

[3] HFSS, Ansoft Product Suite, Ansys Inc., USA (www.ansoft.com).

[4] X.Yuan, R.F.Harrington and S.S.Lee, "Electromagnetic scattering by a dielectric cylinder partially covered by conductors", J. Electromagnetic Waves Applications, Vol.2 , pp.21-44, July 1987.

[5] E.Almajali and D.A.McNamara, "An accessible two-dimensional moment method analysis for composite antenna models", Proceeding of the 14th Symposium in Antenna Technology and Applied Electromagnetics, ANTEM, Ottawa, Canada, July 2010.

[6] Software for the Analysis of Horns and Reflectors (SABOR), SSR-UPM Spain (http://www.gr.ssr.upm.es/sabor.htm)

[7] E.H.Newman and M.R.Schrote, "On the current distribution for open surfaces", IEEE Transactions in Antennas and Propagation, Vol.31, pp.515-518, May 1983.

[8] C.A.Balanis, Advanced Engineering Electromagnetics (Wiley, 1989).

[9] A.C.Ludwig, "The definition of cross polarization," IEEE Transactions in Antennas and Propagation, Vol.21, pp.116–119, January 1973.

[10] F.Arpin, D.A.McNamara, J.Shaker and A.Ittipiboon, "A receive-mode analysis of reflectarray antennas", 10th International Symposium of Antenna Technology & Applied Electromagnetics, ANTEM, pp.569-572, Ottawa, Ontario, Canada, July 2004.

[11] **E.Almajali**, D.A.McNamara, J.Shaker and M.R.Chaharmir, "An investigation of reflectarray operation using its component current contributions", Proceedings of the 6th European Conference on Antennas and Propagation, EuCAP, Prague, Czech Republic, March 2012.

CHAPTER 4

Feed Image Lobes in Offset-Fed Reflectarrays: Diagnosis and Solution

4.1 Introduction

One problem of offset-fed reflectarray design that has not been studied in enough depth in the literature is the production of specular reflections or what is called the "feed-image lobe" [1], which reduces the gain of the reflectarray and increases the sidelobe level. In this chapter most aspects of this unwanted phenomenon are discussed in some detail. In Section 4.2 the source of specular reflection in offset fed reflectarrays is diagnosed using the technique demonstrated in Section 3.3, which is based on finding the individual and combined contribution of the conducting currents on the reflectarray elements (patches) and groundplane to their far-field radiation patterns. The behavior of the feed-image lobe is studied at the centre frequency and at off-centre frequencies; this establishes a clear understanding of the source of specular reflection as well as the impact of its frequency dependence on the reflectarray performance. A solution to eliminate the appearance of specular reflection in offset-fed reflectarrays is proposed and validated in Section 4.3. This feed-image lobe mitigation technique is based on the use of sub-wavelength reflectarrays of square patch elements using $\lambda/3$ inter-element spacing, instead of the conventional half-wavelength reflectarrays of the same element type. Measured far-field amplitude patterns are shown for all designs in Section 4.4, and compared to predictions. The chapter is concluded in Section 4.5.

4.2 Diagnosis of the Source of Feed-Image Lobes in the Radiation Patterns of Offset-fed Reflectarrays

4.2.1 Preliminary Remarks & Designs Consideration

In Chapter 3 it was shown that the physical sources of the scattered fields from a reflectarray are conduction currents on the elements and groundplane, as well as polarization currents within the substrate. As such if we determine these component current densities for an offset-fed reflectarray, their separate contributions to the far-zone radiation patterns could be used to establish the source of the feed image lobes. This is achieved by using a complete full-wave model of an offset-fed reflectarray with a pyramidal horn feed, implemented using the FEBI option of the High Frequency Structure Simulator HFSS [2]. As stated in Section 3.3, HFSS does not give direct access to both the amplitude and phase of current densities over a *user-specified* grid of points on selected parts of the reflectarray. A means of doing this, and subsequent computation of the fields due to such current densities, were described in Section 3.3; in essence, the conduction currents $\bar{J}_s$ are extracted from the simulated offset-fed reflectarray structure by applying the boundary condition $\bar{J}_s = \hat{n} \times \bar{H}_1 - \hat{n} \times \bar{H}_2$ at all air-conductor and conductor-substrate interfaces, using values for $\bar{H}_1$ and $\bar{H}_2$ extracted from HFSS (and indicated in Figure 4.1). This expression gives the vector sum of the current densities on the two sides of the zero thickness conducting surfaces to which the expression is applied.

In this chapter, in addition to resultant current densities, we will also examine the current densities on the two sides of the conducting surfaces. For the groundplane $\hat{n} \times \bar{H}_1$ gives the current density on its bottom surface, and $-\hat{n} \times \bar{H}_2$ gives that on its top surface. Similar remarks apply to the top and bottom surfaces of the elements. Note that the current density component J_x is much larger than J_y, and so only the former is shown in the figures.

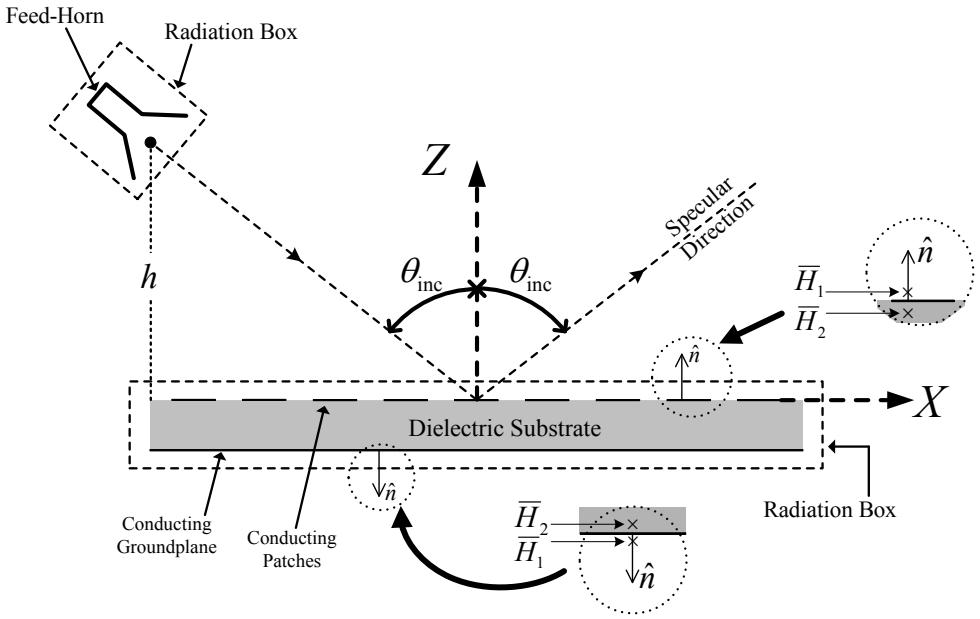

Figure 4.1 Cross-section of offset-fed reflectarray antenna geometry showing the radiation boxes, the incident angle and the "direction of specular reflection". The feed phase centre (at centre-frequency), which is also the nominal focal point of the reflectarray, is indicated by the dot (•).

To investigate the source of the feed image lobe we use a single-layer offset-fed reflectarray designed for a centre frequency of 30GHz. The substrate (Rogers 3003) has and thickness 0.508 mm. At 30GHz the reflectarray size is $15\lambda_0 \times 15\lambda_0$ and the feed is located a distance h = $15\lambda_0$ above its edge. The feed offset angle $\theta_{inc} = 26.5^\circ$. A pyramidal horn is used as a feed; it has aperture dimensions 17mm by 22 mm, a flare length of 11.4mm, and an average phase centre located 3.2mm inside the aperture. It is oriented with its beam peak pointed to the center of the reflectarray as depicted in Figure 4.1 and provides an illumination taper of between 9dB and 10dB at the four reflectarray edges. Both half-wavelength and sub-wavelength versions of the reflectarray are considered. The elements are square conducting patches of variable size, unless otherwise stated. An element is said to be resonant at some frequency if its reflection phase (in the infinite periodic environment used to set up the design database [3]) is 0° at that frequency.

4.2.2 Feed-Image Lobe Behavior at Centre- and Off-Centre Frequencies

A- Behavior At 30GHz (The Centre-Frequency)

Figure 4.2 shows the extracted conduction currents on the patches and groundplane at 30GHz. It is evident that the currents on the top of the groundplane peak whenever the currents on the bottom of the patches peak, with amplitudes being so similar that the groundplane current density distribution looks like a direct projection of that on the patches. The patches that have resonant or near-resonant lengths (those which have high current values) together with the groundplane form an open resonator [4]. Those patches whose dimensions deviate substantially from the resonant length, and are located in the vicinity of the Fresnel zone boundaries, carry low currents, with an accompanying low current on the groundplane at that location. It follows that since the groundplane currents are of the same order and distribution as that on the patches, as is clear from Figure 4.3, they should contribute to the reflectarray scattered field in much the same way as do the patch elements. This is confirmed from calculated far-field patterns of these currents that will be next discussed.

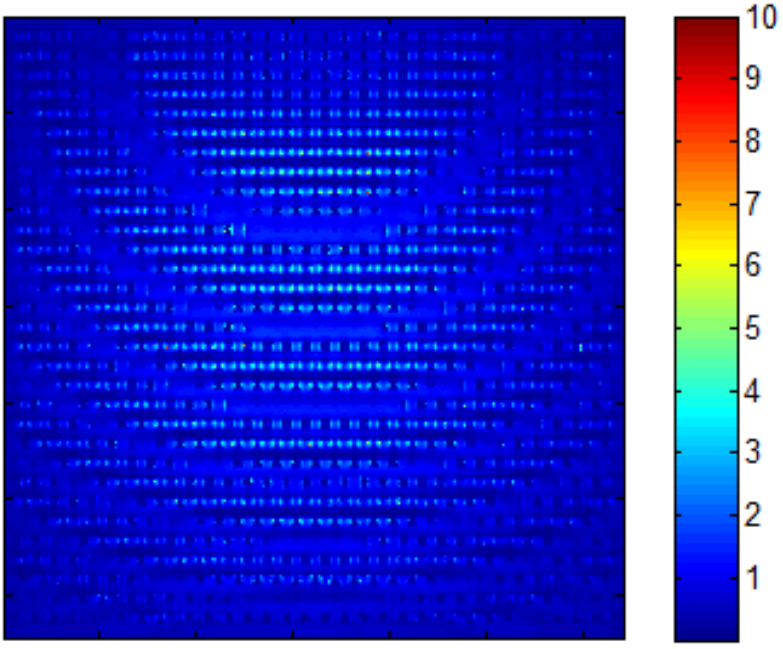

(a)

Figure 4.2: The extracted conduction surface current density at the 30GHz design frequency for half-wavelength reflectarray case (a) on the top of patch elements

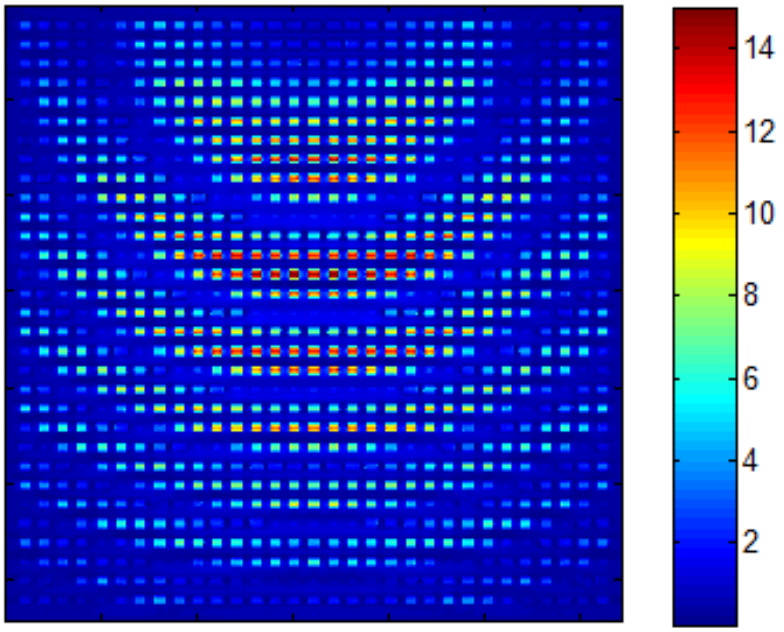

(b)

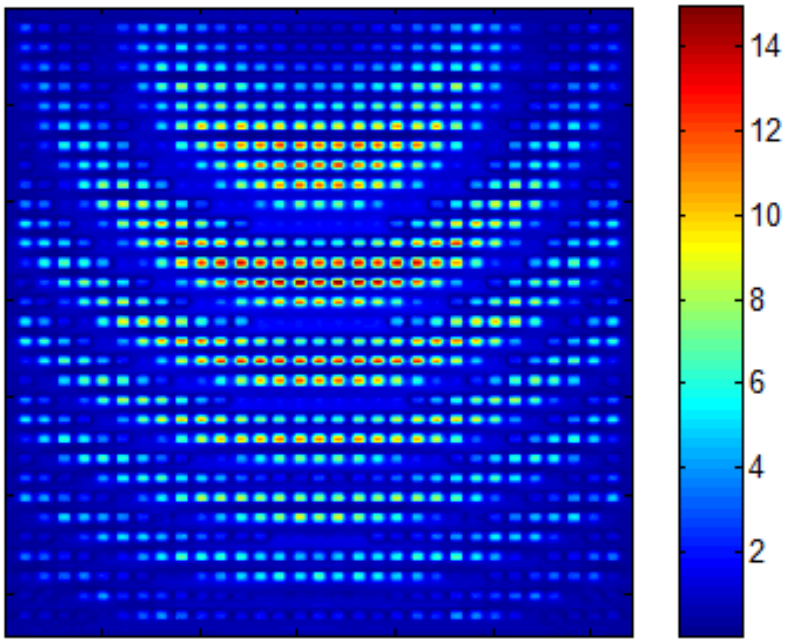

(c)

Figure 4.2 (continued): (b) on the bottom of patch elements, (c) on the top of groundplane

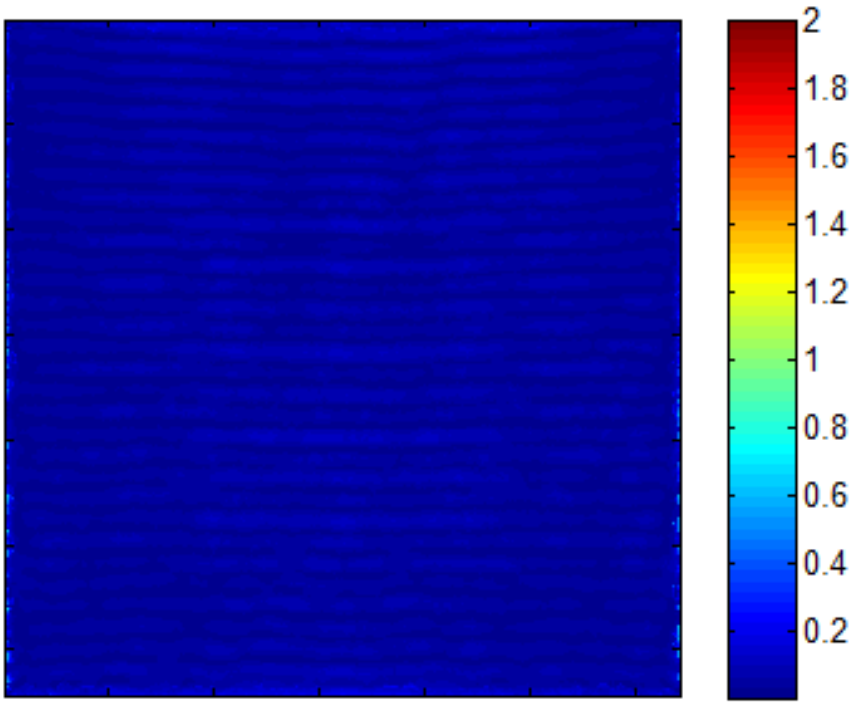

(d)

Figure 4.2 (continued): (d) on the bottom of groundplane.

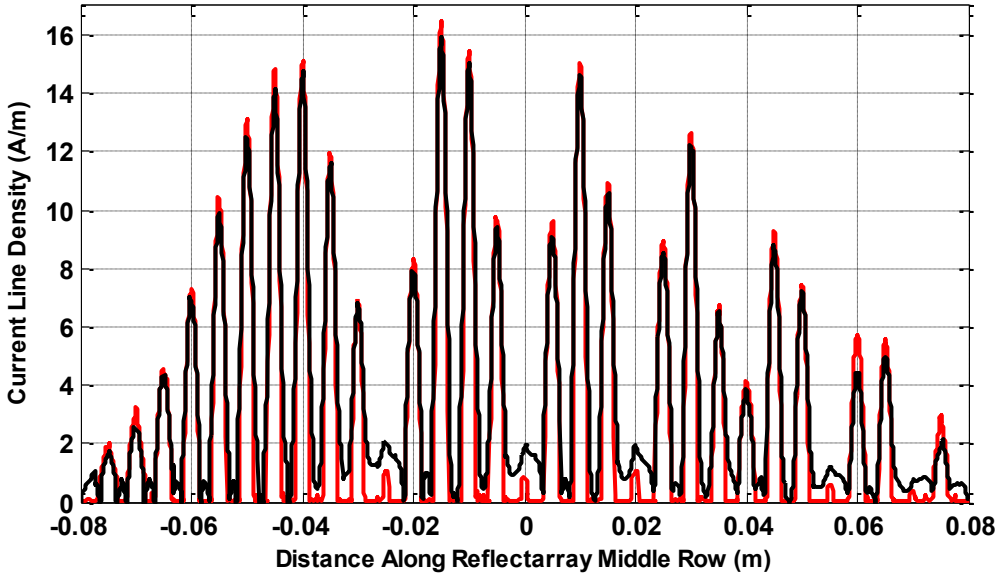

Figure 4.3: The extracted conduction surface current density on the patches (——) and groundplane (——) at points along reflectarray middle row (x-axis in Figure 4.1).

The calculated far-zone patterns due to the conduction currents on the patches and the groundplane, separately, are shown in Figure 4.4, where all computed fields were normalized to the maximum value of the computed field due to the patch currents only. The fields are shown in the plane in which the feed is offset (which happens to be the E-plane in the present example) since this is where any feed image lobe is prevalent. The individual contributions of these patch and groundplane currents are almost identical. Each appears to contain the feed-horn image pattern about the broadside direction. However, when we perform complex addition of these two individual patterns we obtain the result shown as the black curve in Figure 4.4, in which the feed image is not significant. In fact the combined field plot is lower than that of the individual contributions, and roughly 4.7 dB so at the pattern maximum. This appears counter-intuitive; when we perform a complex addition of the individual field contributions we obtain a lower field value. Exactly what is happening here is revealed in Figure 4.5. In spite of the above observation, the directivity of the combined radiation pattern, namely that of the actual reflectarray, is higher than the directivities of the two individual patterns. This must be so at the centre frequency as the patch sizes are selected in the design process to have a uniform scattered field phase distribution on the reflectarray aperture surface [3,5]; this is only so if there is a complete range of reflection phases possible using the particular type of element.

The field due to the complex addition of the contributions due to the conduction currents on the patches and groundplane, plus that due to the polarization currents in the substrate, is shown by the green curve (——) in Figure 4.4. It is clear that the polarization currents do not have a significant effect on the final pattern. As mentioned in Section 3.3, we should of course remember that, although the substrate's contribution looks minor, its presence impacts the conduction current distributions due to the interactions between the components of the reflectarray.

We next plot the phase of the individual far-zone fields (not the currents), namely those due to the patch currents and due to the groundplane currents. This is given in Figure 4.6. Only a portion of the angular range is shown in order to be able to enlarge the scale.

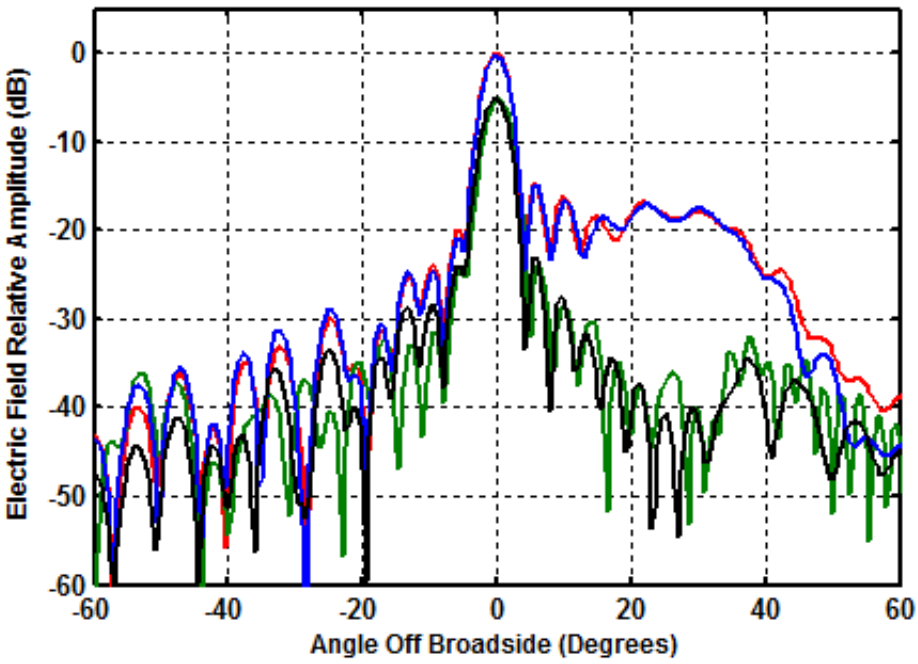

Figure 4.4: Calculated E-plane far-field radiation patterns (normalised to the maximum value of the field due to the patch currents) due to conduction currents on the patches (——), groundplane (——), both the patches & groundplane (——) and due to all conduction and polarization currents (——) calculated at centre frequency 30GHz. Half-wavelength reflectarray case.

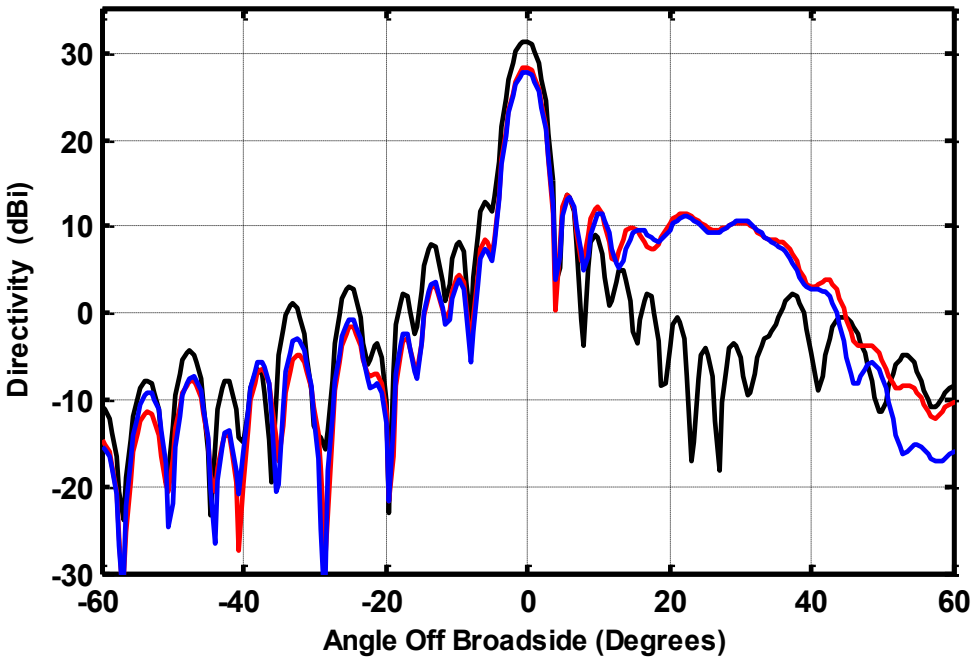

Figure 4.5: Calculated directivity due to conduction currents on the patches (——), groundplane (——), and both the patches & groundplane (——), at centre frequency 30GHz. Half-wavelength reflectarray case.

The phase of the pattern due to the groundplane currents has purposefully had 180° added to it similar to what was done in Section 3.2.3, so where the two curves are almost coincident there will be destructive interference (*viz*. beyond 5°), and where they are not coincident constructive interference is possible, as in the main lobe region (out to 5°) of the reflectarray. This therefore shows why they can add up on boresight while cancelling each other so well over the feed image lobe region.

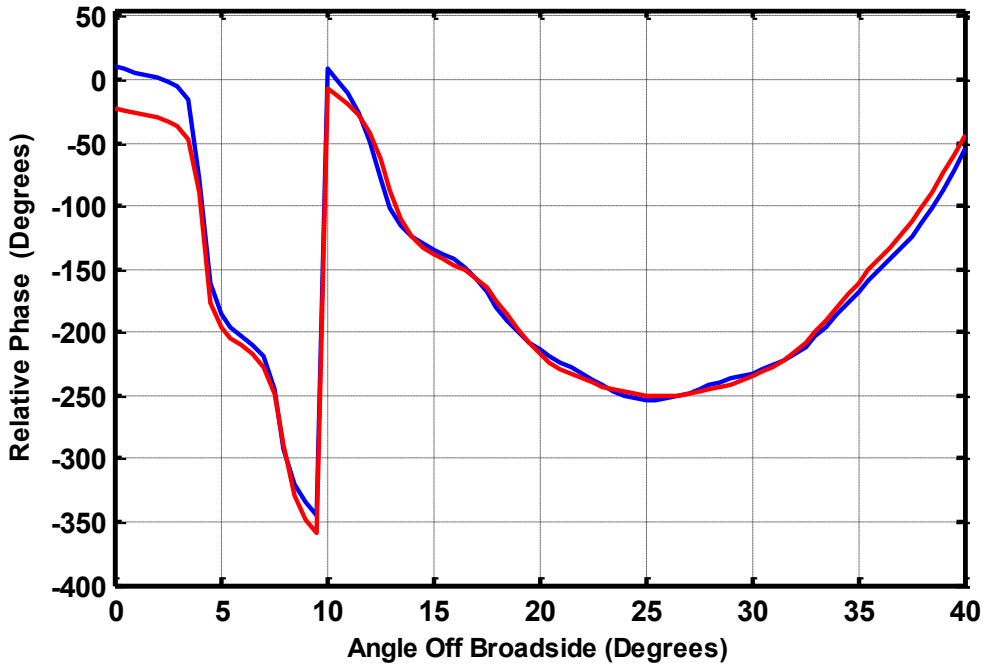

Figure 4.6: Calculated E-plane far-field phase due to conduction currents on the patches (——), groundplane (——), calculated at centre frequency 30GHz. Half-wavelength reflectarray case.

The phase distributions of the patch and groundplane currents were extracted as shown in Figure 4.7 and their difference found as shown in Figure 4.8. In unexposed regions of the groundplane, which are "shadowed" by the elements, this difference between the phases is almost 180°, except on tiny regions where the corresponding current amplitudes are very small anyway. One for a moment wonders how this situation can be of much use as far as radiation is concerned. However, it is immediately realised that the situation is similar to what one has for a microstrip patch radiator; the description of why the above phase difference is not prohibitively disadvantageous in the latter case is succinctly described in [6].

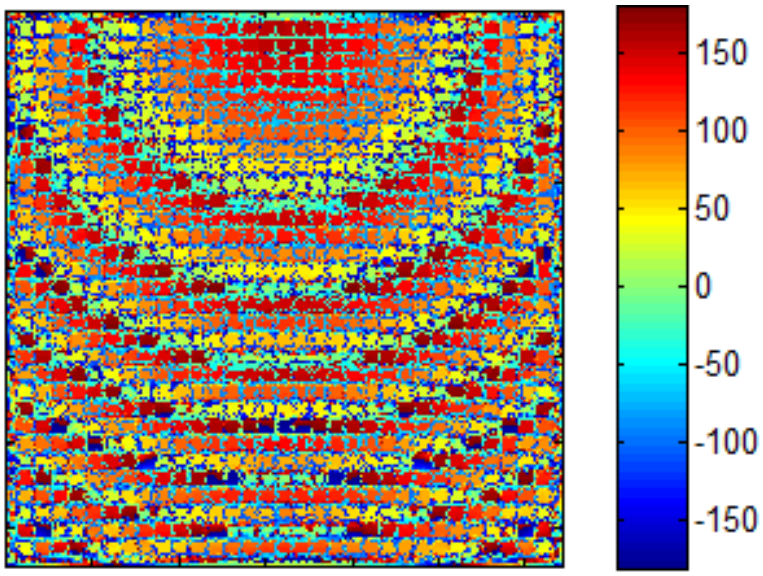

(a)

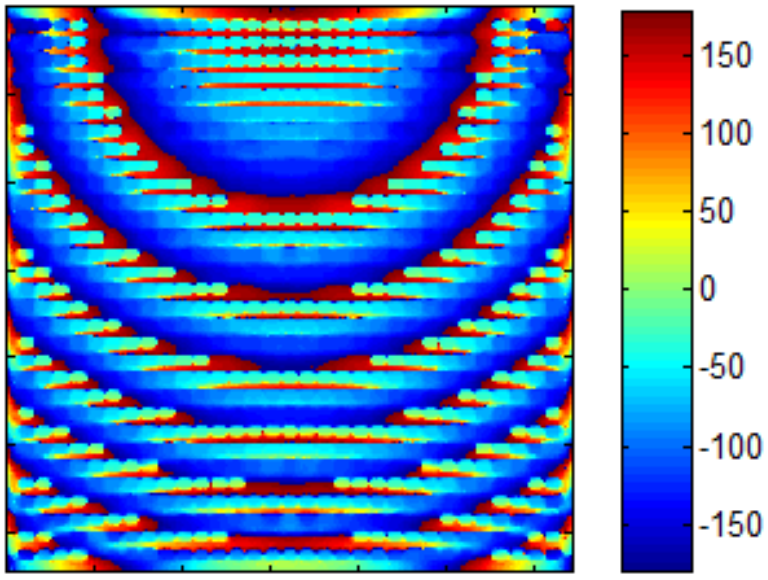

(b)

Figure 4.7: The extracted conduction surface current density phases at the 30GHz design frequency for half-wavelength reflectarray case (a) on the patches, (b) on the groundplane.

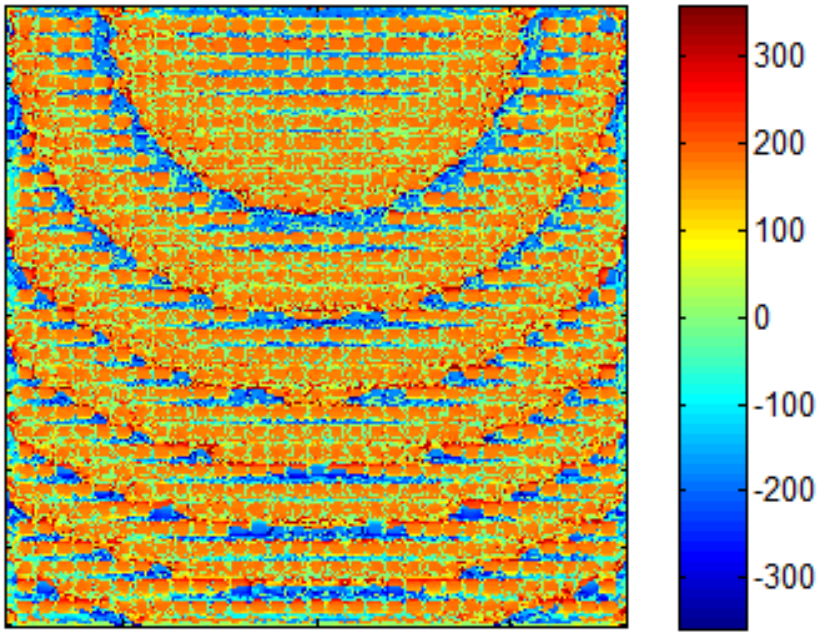

Figure 4.8: Difference between the phases of the conduction currents on the patches and the groundplane at 30GHz.

It is noteworthy that the predominant current density on the groundplane is on the unexposed regions directly underneath the patches rather than the exposed portions of the groundplane "visible" to the incident field wave through the space between the patches. Furthermore, we will in what follows show that at frequencies below and above the centre-frequency the feed image lobes will appear in the radiation patterns of the same reflectarray. Thus it does not appear possible to blame the exposure of portions of the groundplane (at least not in a simple geometrical sense) for the presence of feed image lobes that appear in reflectarray radiation patterns. To support this opinion, we designed a half-wavelength reflectarray of the same size but using variable length dipole elements (of width 0.5 mm), for which there is increased direct exposure of the groundplane. Figure 4.9 compares its pattern to that of the patch element reflectarray discussed above. The reflectarray with the dipole elements also has no feed image lobe at 30 GHz, in spite of the increased "exposure" of the groundplane offered by the dipole elements. We next examine the reflectarray at frequencies above and below the centre frequency.

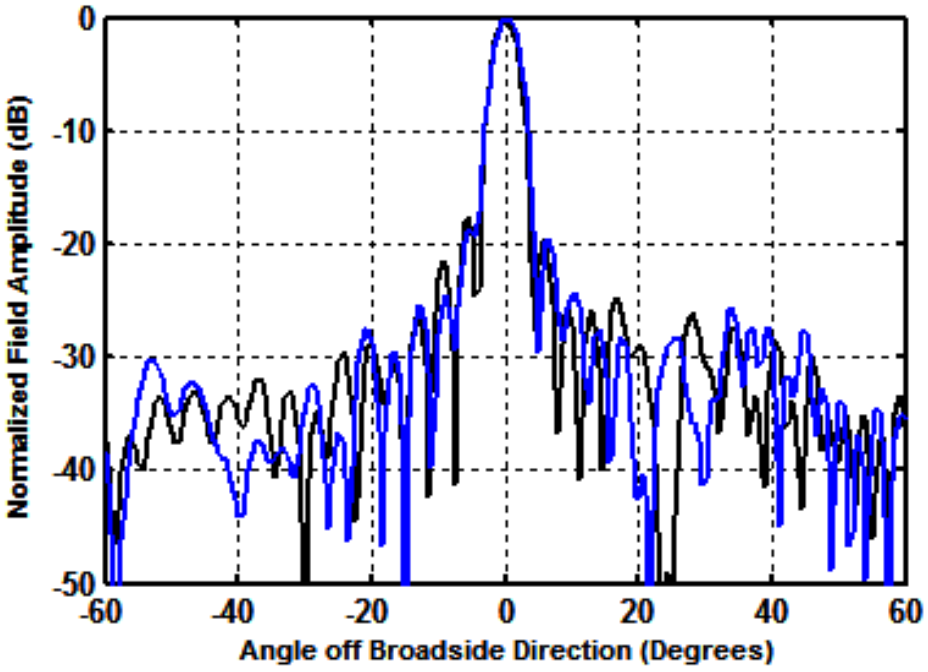

Figure 4.9: Normalized calculated E-plane far-field patterns, computed using the full-wave model at 30GHz, for the patch element (——) and dipole element (——) half-wavelength reflectarrays.

B- Behaviour at 33 GHz (Above Centre-Frequency)

The current densities on the elements and groundplane at 33 GHz are shown in Figure 4.10(a) and (b), respectively. A study of the actual numerical values from which these surface plots were generated makes it apparent that the current density over exposed portions of the groundplane is not insignificant (unlike the 30 GHz case). One should not be lulled by the appearance of the surface plots into thinking that the only exposed portions of the groundplane are those in the vicinity of the obvious Fresnel zone boundaries. It is clear from Figure 4.10(c), which is a plot of the numerical values of the respective current densities along the reflectarray's central row (x-axes in Figure 4.1) on the surfaces in Figures 4.10(a) and (b), that the amplitudes of the currents on the unexposed portions of the groundplane are now lower than that on the elements, also unlike the case at 30 GHz.

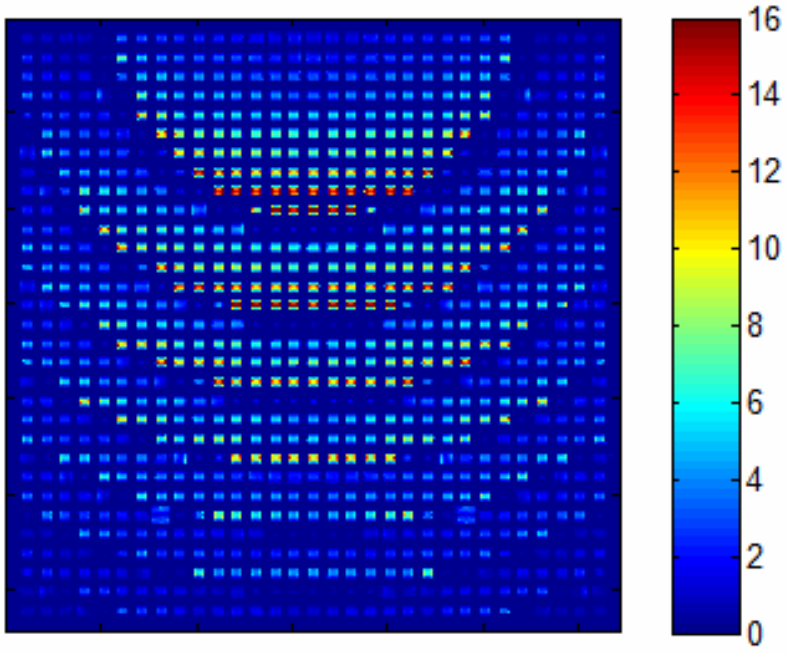

(a)

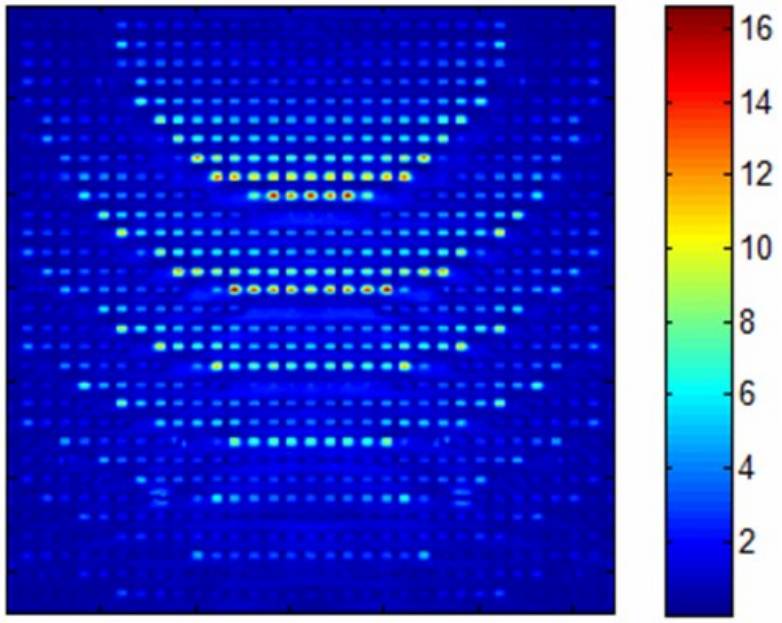

(b)

Figure 4.10: The extracted conduction surface current density at 33GHz on (a) the patch elements, and (b) the groundplane.

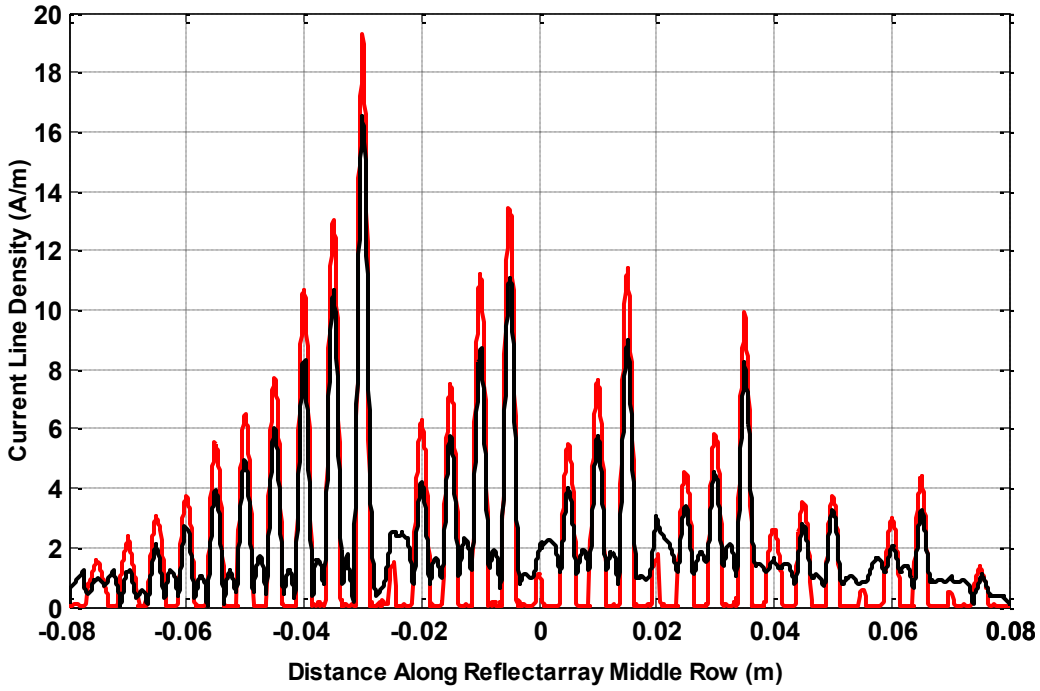

(c)

Figure 4.10 (continued): (c) currents from (a) and (b) shown at points along the reflectarray middle row on the patches (——) and groundplane (——).

In order to examine the effect of this amplitude imbalance we consider Figure 4.11(a), which shows the far-field patterns calculated from the extracted surface conduction currents at 33GHz, normalised to the maximum value of the field due to the patch currents only. Observe that, unlike the 30GHz calculated patterns in Figure 4.4, the groundplane and patches in this case separately do not contribute equally to the far-field, especially about the specular direction. The contribution due to the currents on the entire groundplane is smaller to that of the elements, and this imbalance gives a resultant combined far-field pattern with an undesirable feed image lobe at the -12dB level as shown in Figure 4.11(b) that is not present at 30GHz. As an aside we observe from Figure 4.11(a) that the polarization currents do not make a significant contribution to the feed image lobe since the combined patterns with or without them have much the same feed image lobe levels. This is observed at 30GHz too, and for this reason its contribution will not always be included in later pattern plots. In the radiation patterns presented in the remainder of this chapter we want to more immediately appreciate the heights of the sidelobes relative to their associated main lobe maxima.

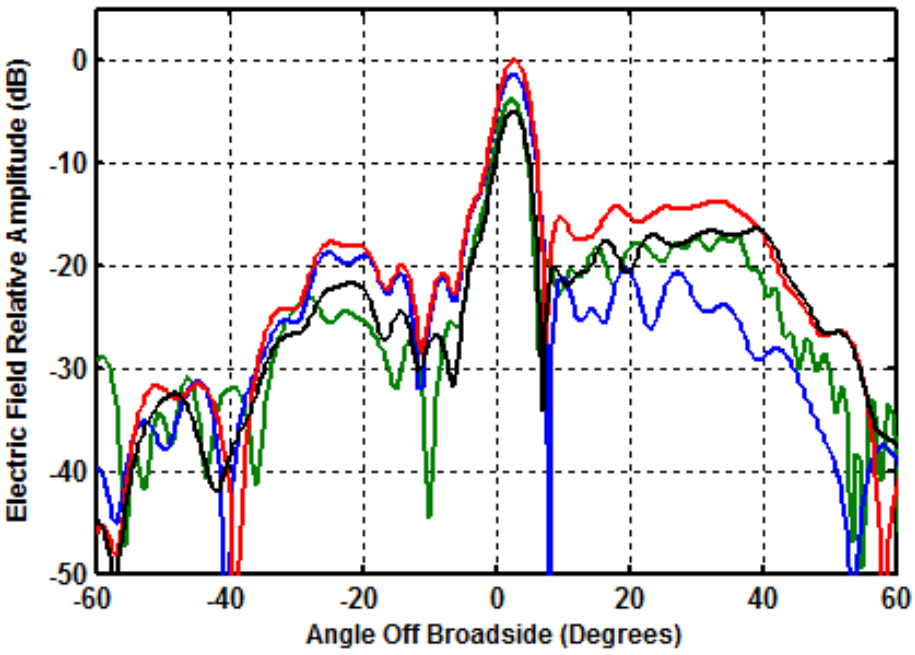

(a)

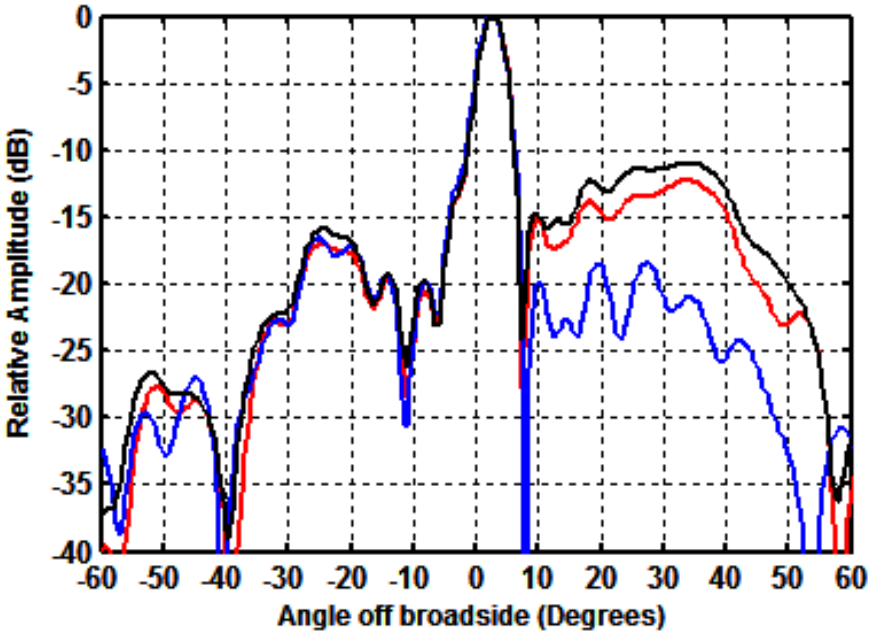

(b)

Figure 4.11: Calculated E-plane far-field radiation patterns due to conduction currents on the patches (——), groundplane (——), both the patches & groundplane (——), and due to all conduction and polarization currents (——), calculated at off-centre frequency 33GHz (a) normalised to the maximum value of the field due to the patch currents, using the full-wave model; (b) as in (a), except each is normalized to its own maximum value. Half-wavelength reflectarray case.

Henceforth we will therefore show patterns such as Figure 4.11(a) in the normalized form of Figure 4.11(b), where each pattern is normalized to its own maximum value. Obviously when we superpose any two patterns it is the complex un-normalized values that are added.

Figures 4.12(a) and (b) show the phases of the currents on the patches and groundplane at 33 GHz respectively. The phase difference of the phases of the currents on the patches and groundplane is shown in Figure 4.13. It is noteworthy that although the currents phases in Figure 4.12 look different from those observed in Figure 4.7, the phase difference is still roughly 180° as it was for the 30 GHz case in Figure 4.8, and yet Figure 4.11 reveals a feed image lobe at 33 GHz. Thus it is not a change in the phase difference between the patch and groundplane currents that can be blamed for the appearance of the feed image lobe; it is the imbalance in the amplitude of the two sets of currents. This amplitude imbalance is caused by the reflection phases of the elements having altered when the frequency moves away from 30GHz. Figure 4.14, which is similar to Figure 4.6, but at off-centre frequencies, reveals that the constituent fields due to the patch and groundplane currents do not interfere destructively (that is, their phases do not differ by 180°) over the feed image lobe region, and hence such a lobe appears.

If we artificially (by simply altering the numerical values) size-up the groundplane currents in the unexposed regions by making them equal in magnitude (without altering their computed phase) to that of the elements, these provide the far-field pattern contribution shown as the blue curve in Figure 4.15. The combined contributions of the actual element currents and sized-up groundplane currents are shown by the dashed curve in Figure 4.15. It shows a feed Image lobe that is lower than the true one (solid black curve). This confirms that not only the phases of the element and groundplane currents must be just right (which they are at 33GHz, as seen in Figure 4.13), but the magnitudes of the element and groundplane currents need to be roughly the same for feed image lobe elimination. This only happens at the centre frequency. Furthermore, if we remove the currents on the exposed regions of the groundplane at 33 GHz and recompute the radiation pattern, there is insignificant change to the feed image lobe. So groundplane exposure cannot in any sense be blamed for the feed image lobe at frequencies above the centre frequency.

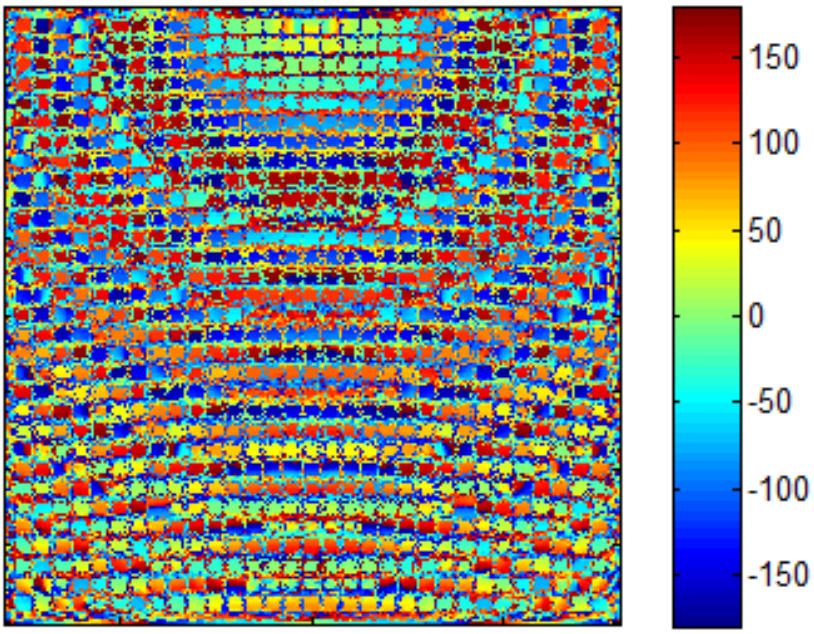

(a)

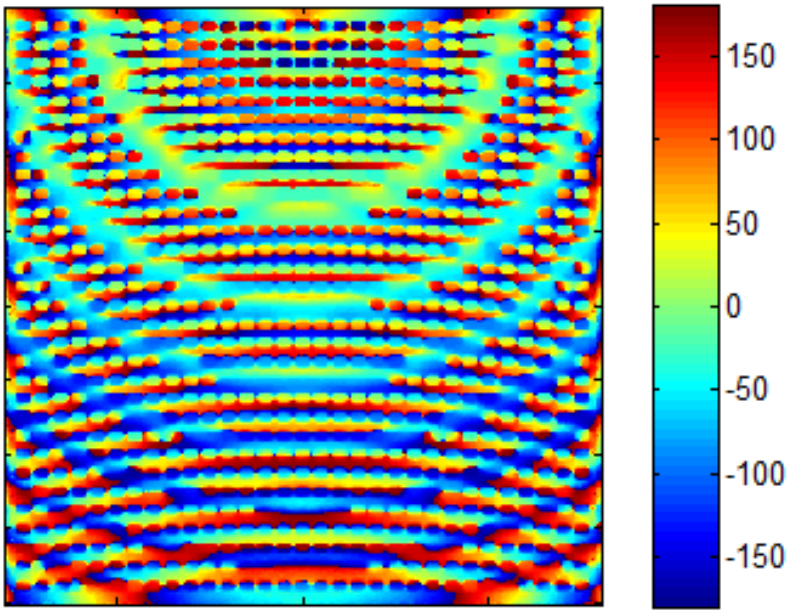

(b)

Figure 4.12: The extracted conduction surface current density phases at 33GHz for the half-wavelength reflectarray case (a) on the patches, (b) on the groundplane.

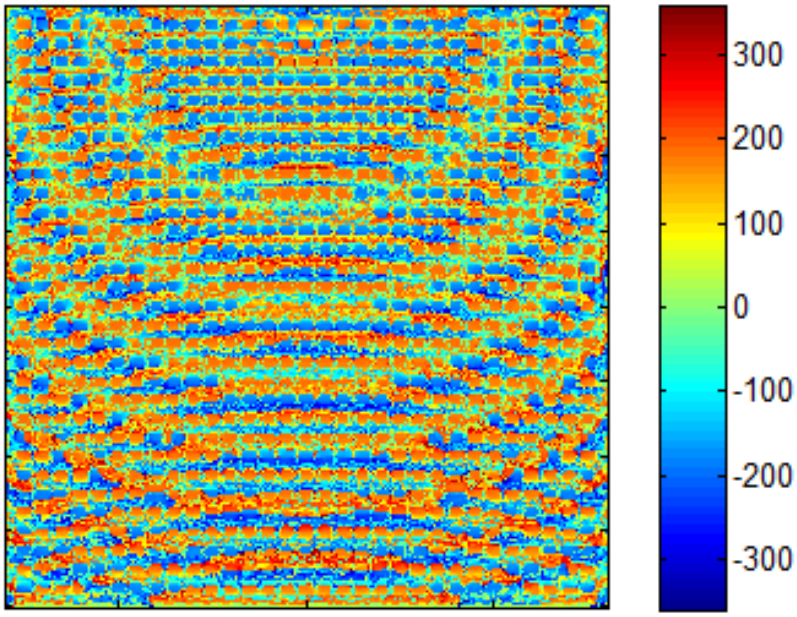

Figure 4.13: Difference between the phases of the conduction currents on the patches and the groundplane at 33GHz.

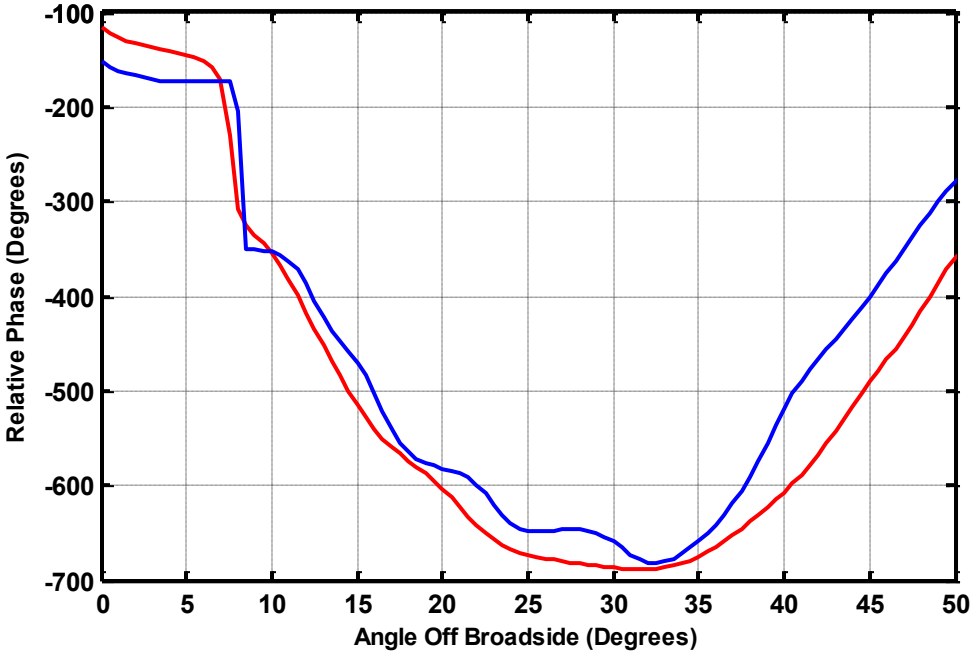

Figure 4.14: Calculated E-plane far-field phase due to conduction currents on the patches (——), groundplane (——), calculated at 33GHz. Half-wavelength reflectarray case.

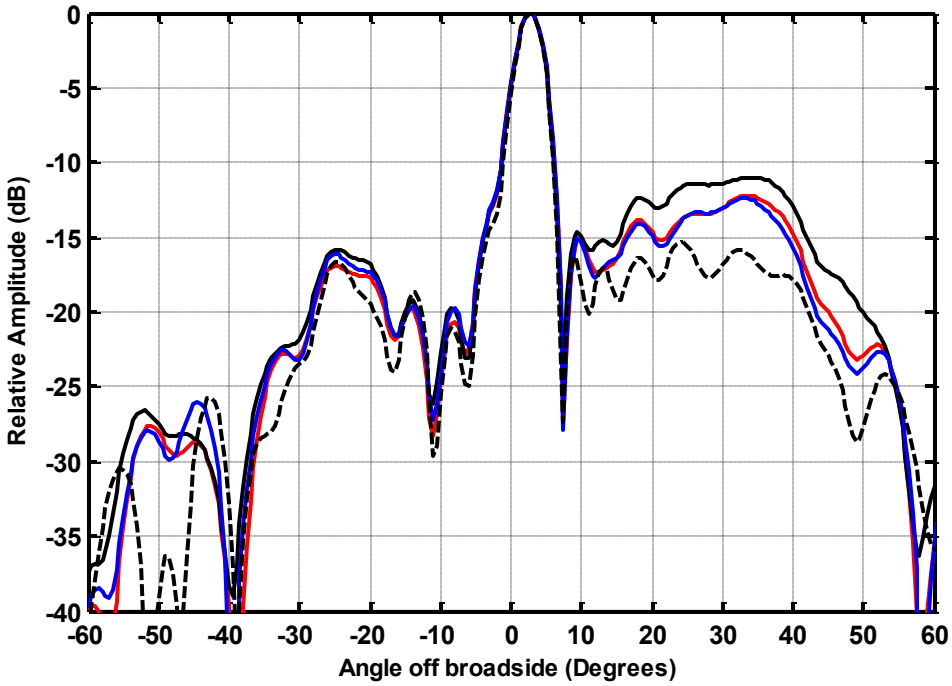

Figure 4.15: Normalized E-plane far-field radiation patterns due to the actual conduction currents on the patches only (——) as in Figure 4.11, the sized-up conduction current on the groundplane (——), the complex summation of the fields due to the above two current contributions (— —), and the complex summation of the fields due to the above two current contributions without sizing-up of the groundplane currents(——) as in Figure 4.11.

C. Behaviour at 27 GHz (Below Centre-Frequency)

Figure 4.16 gives the calculated surface currents on the patches and the groundplane at 27GHz. As in the 33 GHz case, it shows unmistakably that the number of elements that are resonant, and their distribution, has changed compared to those shown in Figure 4.2, since the element reflection phases change with frequency. The resonances have understandably shifted to the larger size patches due to the reduction in frequency, and fewer resonant elements exist. The impact of that can be clearly seen in Figure 4.16(b), where it is clear that now (as at 33 GHz) low current densities reside not only in the vicinity of the Fresnel zone boundary projections on the groundplane but also on the exposed regions of the groundplane. Unlike the 33 GHz case, the amplitudes of the current density on the elements and the unexposed portions of the groundplane are almost of the same order, as evidenced by the curves in Figure 4.16(c). Also, closer examination of the surface plot data in Figure 4.16(b) shows that there is, as for the 33GHz case, a

non-negligible current density on the exposed regions of the groundplane. Recall that is not so at the centre frequency, as shown in Figure 4.2. But, as at 30GHz and 33 GHz, one finds that the phase difference between the element and groundplane currents is still roughly 180° as depicted in Figure 4.17.

Figure 4.18 shows the far-field patterns calculated from the extracted surface conduction currents at 27GHz. Once again, unlike the 30GHz calculated patterns in Figure 4.4, the groundplane and patches in this case separately do not contribute equally to the far-field about the specular direction. Opposite to the 33 GHz case, the far-field contribution due to the currents on the entire groundplane is larger than that of the elements, in spite of the fact that the currents on the unexposed portions of the groundplane are lower than that on the elements, and this imbalance gives a resultant combined far-field pattern with an expected feed image lobe. The larger far-field contribution of the groundplane currents around the specular direction results from the (albeit low) currents that now exist on the exposed portions of the groundplane, due to detuning of the elements at 27 GHz. This is confirmed in Figure 4.19, where the groundplane contribution has been re-calculated with all currents on the exposed regions of the groundplane artificially set to be zero. By suppressing these currents, the amplitude balance between the element and groundplane contributions to the far-field has been restored. Their combined contribution gives a lower feed image lobe, but again not complete elimination such as that at the centre-frequency in Figure 4.4. In a sense the conjecture in [7,8] that the feed image lobe is partly due to regions of the groundplane directly visible to the feed fields is true (at least below the design frequency), but not for the "geometrical exposure" reasons given in [7,8], otherwise one would have feed image lobes present at the centre-frequency as well, which from Figure 4.4 is clearly not the case.

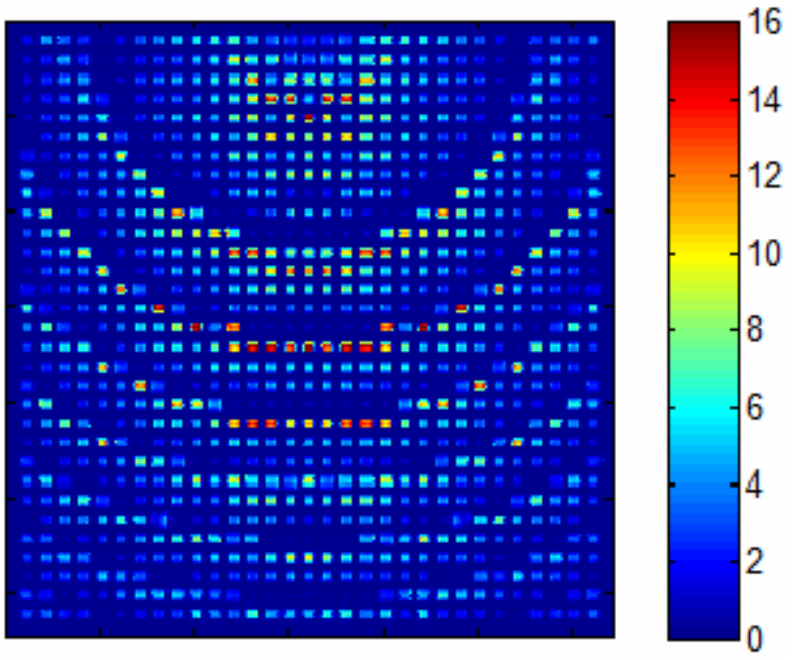

(a)

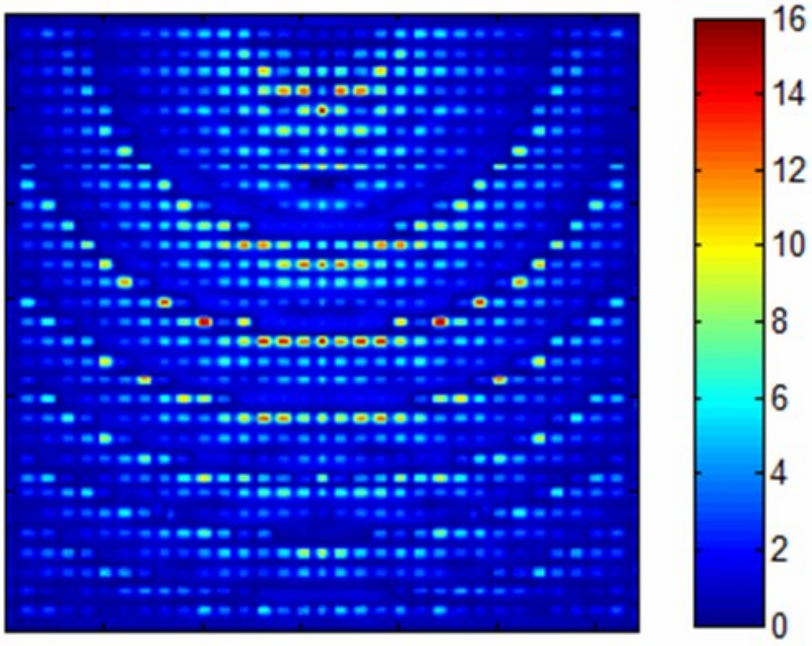

(b)

Figure 4.16: The calculated conduction surface current density at 27GHz on (a) the patch elements and (b) the groundplane.

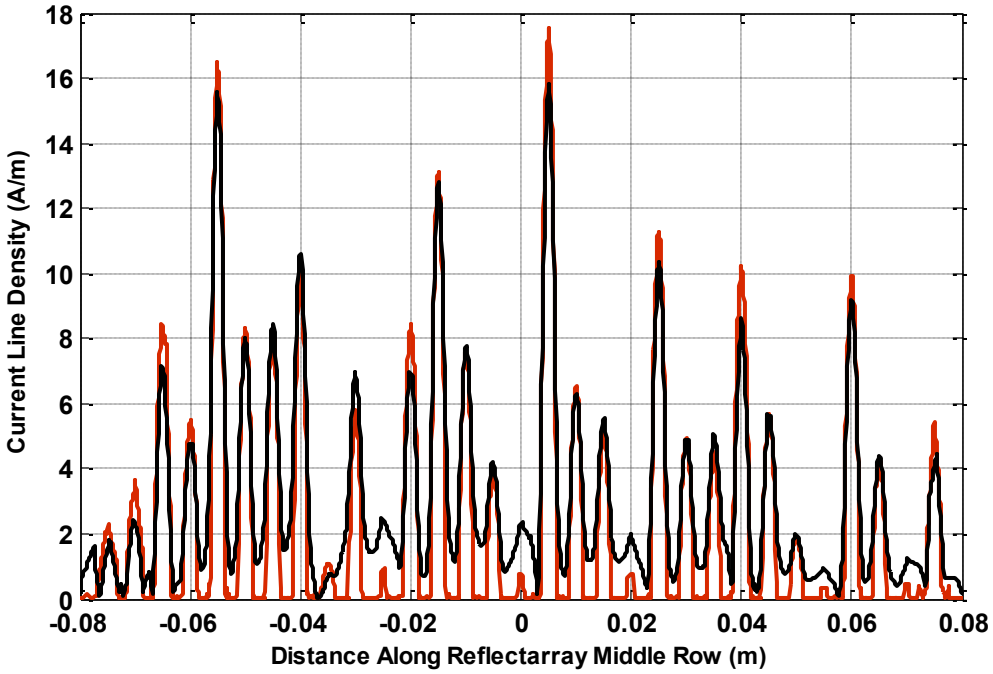

(c)

Figure 4.16 (continued): (c) currents from (a) and (b) as shown at points along the reflectarray middle row on the patches (——) and groundplane (——).

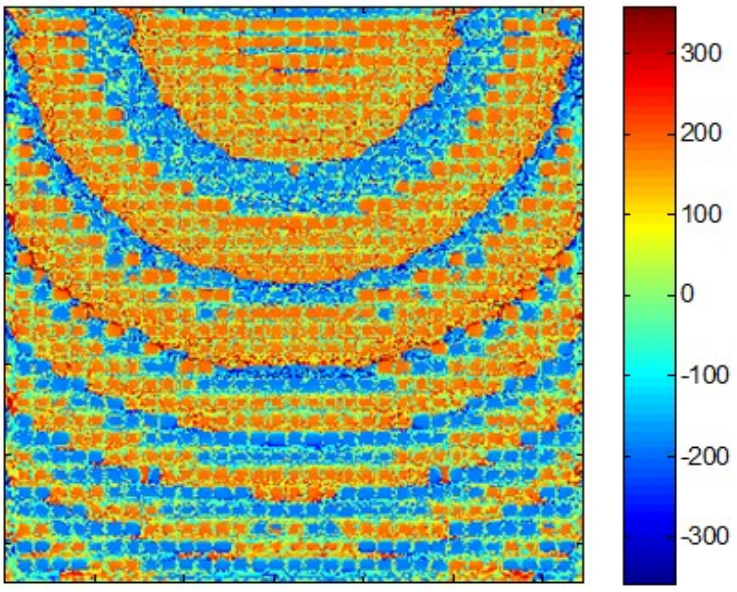

Figure 4.17: Difference between the phases of the conduction currents on the patches and the groundplane at 27GHz.

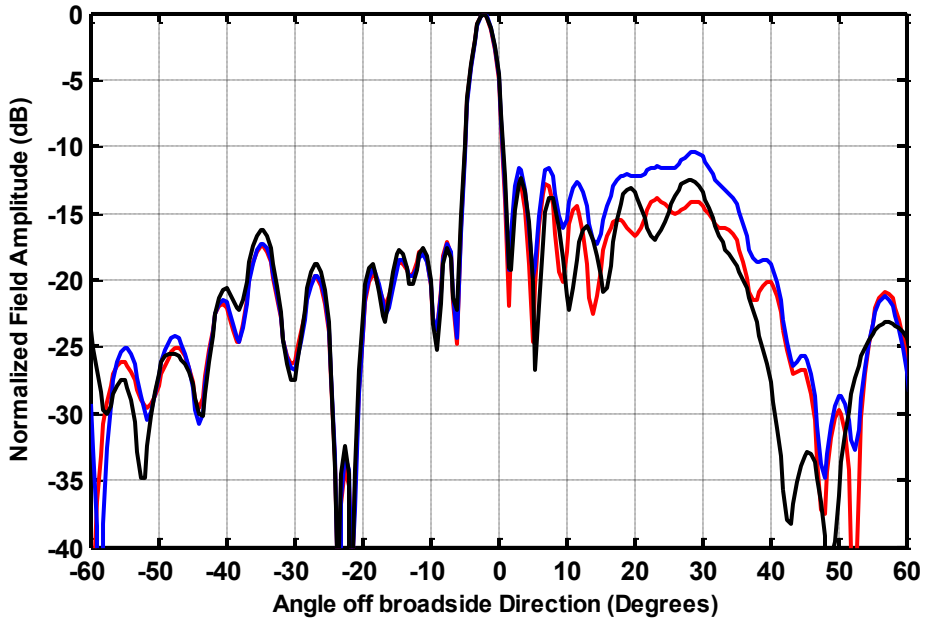

Figure 4.18: Normalized E-plane far-field radiation patterns due to conduction currents on the patches (——), groundplane (——), and both the patches & groundplane (——) calculated at 27GHz.

In order to further emphasize the importance of balanced electric current densities on the elements and groundplane for proper suppression of the feed image lobe we did the following at 27GHz (as done for the 33GHz case): Keeping the current density on exposed regions of the groundplane artificially set to zero (as described in the previous paragraph), we in addition sized-up the magnitude of the current density on unexposed regions of the groundplane to be the same as that on the corresponding elements. We obtain the resultant radiation pattern shown by the dashed blue curve in Figure 4.20. Compared to the result in Figure 4.18, the feed image lobe has been further suppressed by the sizing up of the groundplane currents, but not to the extent shown in Figure 4.4 at the design frequency or in the sub-wavelength reflectarray cases discussed in the next section.

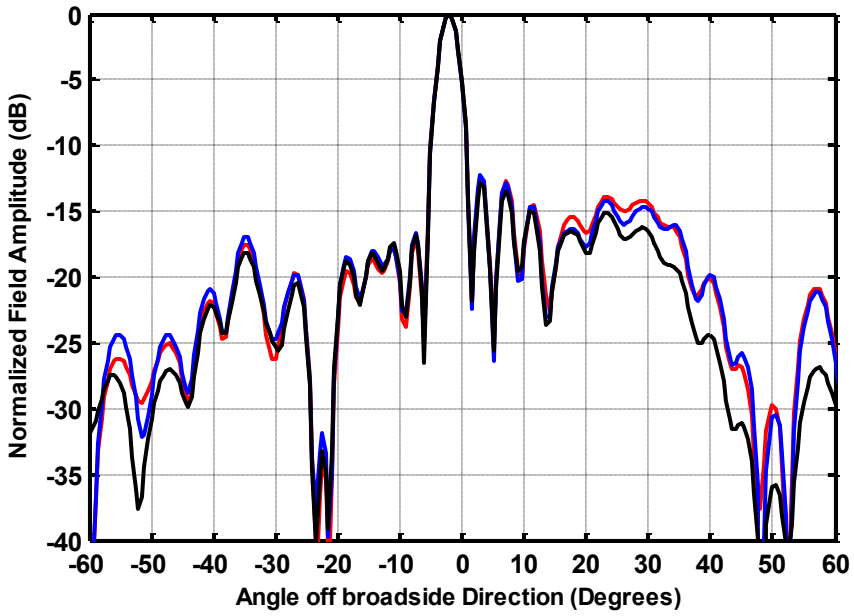

Figure 4.19: Normalized E-plane far-field radiation patterns due to conduction currents on the patches (——), on the groundplane with those on its exposed regions set to zero (——), and on both the patches & groundplane (——), calculated at 27GHz with the true current on the exposed regions of the groundplane.

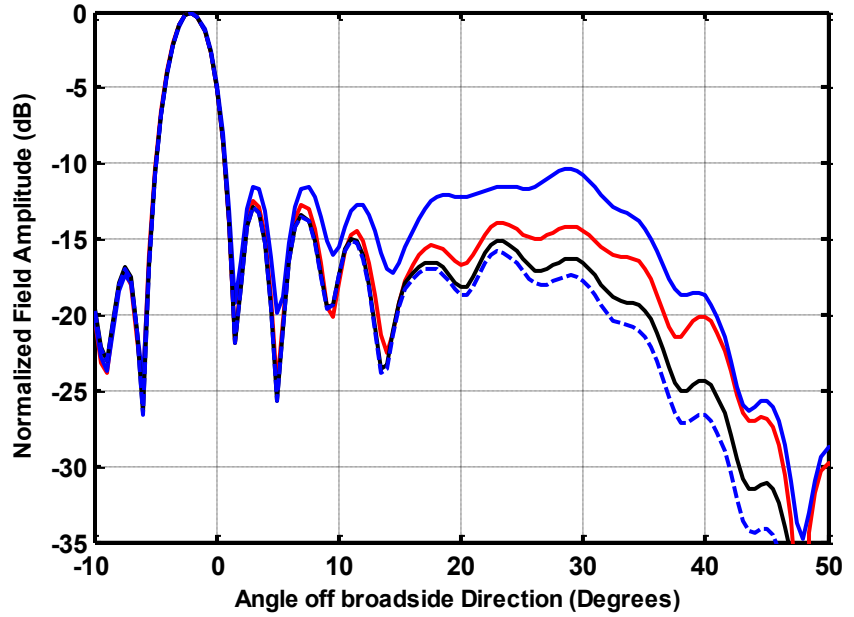

Figure 4.20: Normalized E-plane far-field radiation patterns. Curves (——), (——) and (——) are the same as those (of the same color) in Figure 4.18, repeated here to aid comparison with the additional curve (— — —) which is the combined contribution of the element currents and the sized-up current magnitude on the unexposed portions of the groundplane as discussed for the 33 GHz case. All results shown here are at 27GHz.

4.3 Feed-Image Lobe Reduction Using Sub-wavelength Reflectarray

4.3.1 Introduction

As pointed out in Section 2.2, several authors have advocated the use of sub-wavelength reflectarray designs for improvement in bandwidth [9,10,11] and reduction of losses [12]. We here show that use of sub-wavelength reflectarrays is a means of achieving significant reduction in the feed image lobe as well. In order to demonstrate this we repeated the numerical experimentation of Section 4.2 for a reflectarray of the same dimensions but with sub-wavelength (roughly $\lambda_0 / 3$) inter-element spacing.

4.3.2 Feed-Image Lobe Suppression at Off-Centre Frequencies

It was shown in Section 4.2 that the feed-image lobe appearance is caused by the detuning of the current amplitude on the patches and groundplane at off-centre frequencies, since the elements reflection phases change with frequency. This was observed for a half-wavelength reflectarray case. For an equivalent sub-wavelength reflectarray of same design parameters, the extracted currents at the centre frequency 30GHz and at off-centre frequencies, such as 33GHz, exhibit similar behavior. Quantitative review of the surface current densities shown in Figures 4.21 and 4.22, which are extracted at 30GHz and 33GHz respectively, reveals that at both frequencies there is a strong resonant behavior with close currents amplitudes on the patches and groundplane. The consequence is that this manifests itself through the E-plane far-field patterns computed at 30GHz and 33GHz, which are shown in Figures 4.23 and 4.24, respectively. The patterns are representative of the very significant reduction in the feed image lobe that is achieved using a sub-wavelength reflectarray. In this sub-wavelength reflectarray case the contributions of the elements and groundplane currents combine favourably not only at centre frequency (as for the half-wavelength reflectarray) but also at off-centre frequencies. The currents phases' difference matches that of the half-wavelength reflectarray case; 180° phase difference is prevailing at both 30GHz and 33GHz as shown in Figure 4.25. This further confirms our inference about the detuning role of the current amplitudes in the feed-image lobe creation at off- centre frequencies.

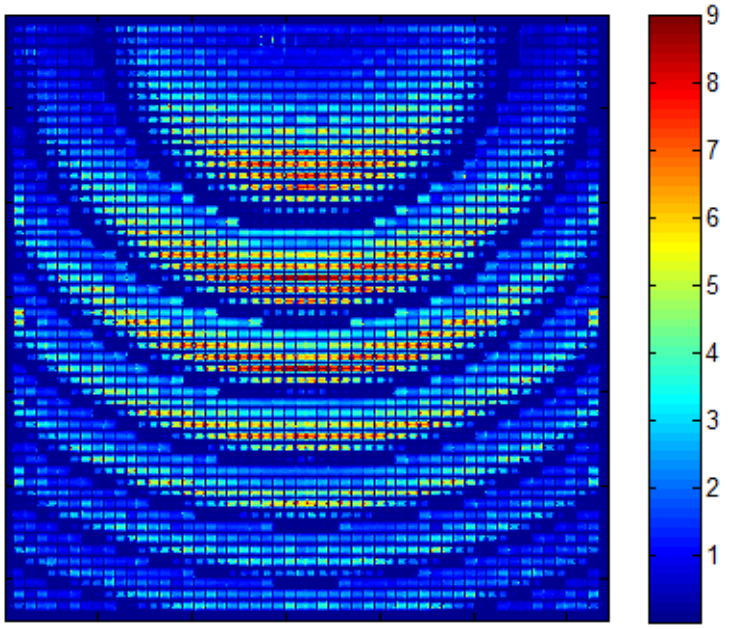

(a)

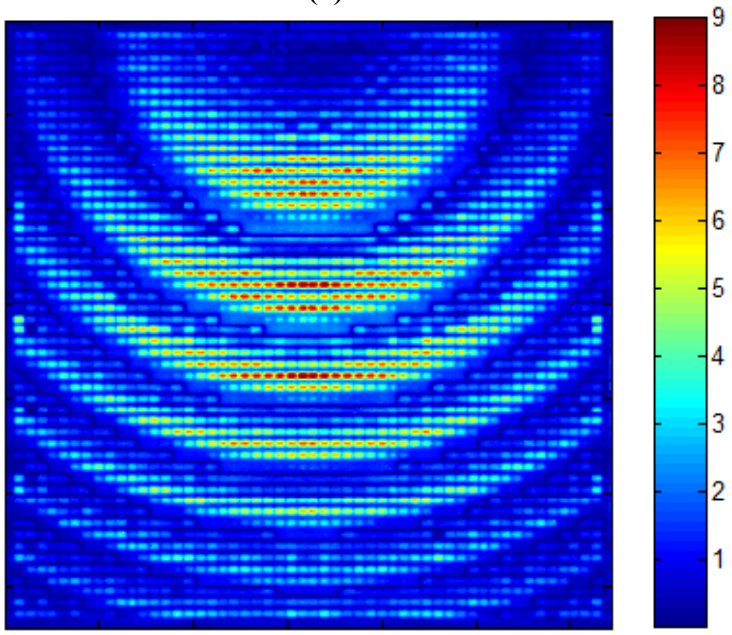

(b)

Figure 4.21: The calculated conduction surface current density on (a) the patch elements, and (b) the groundplane, at 30GHz, for the sub-wavelength reflectarray.

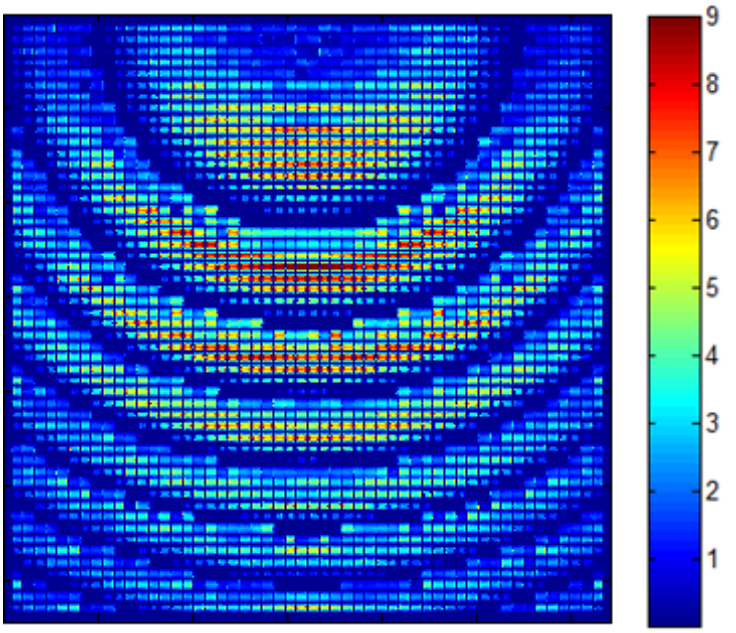

(a)

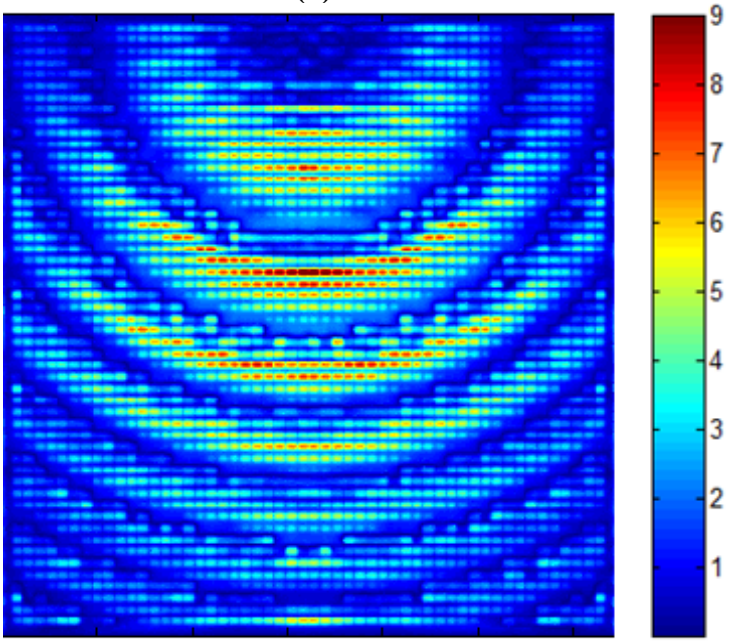

(b)

Figure 4.22: The calculated conduction surface current density on (a) the patch elements, and (b) the groundplane, at 33GHz, for the sub-wavelength reflectarray.

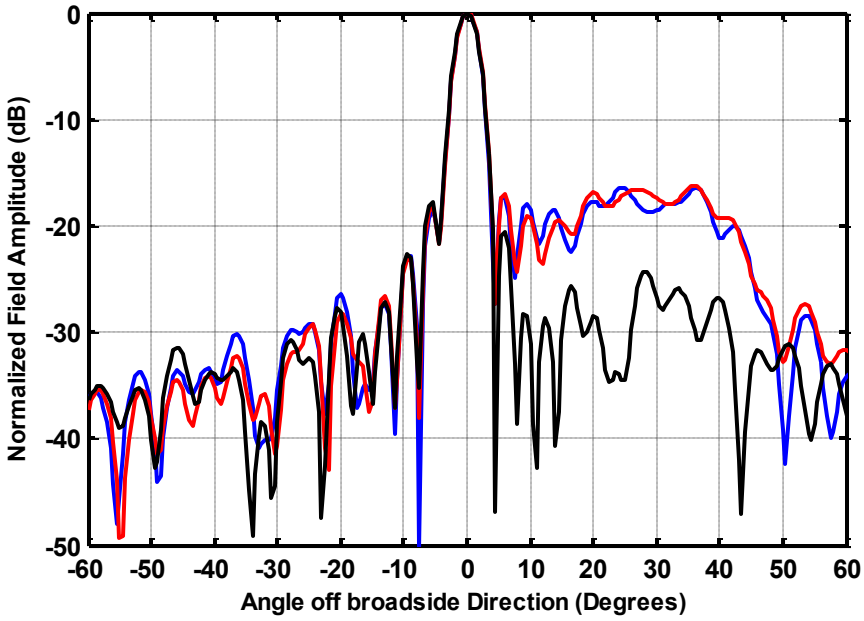

Figure 4.23: Normalized E-plane far-field radiation patterns of sub-wavelength reflectarray due to conduction currents on the patches (——), groundplane (——), and both the patches & groundplane (——) calculated at 30GHz.

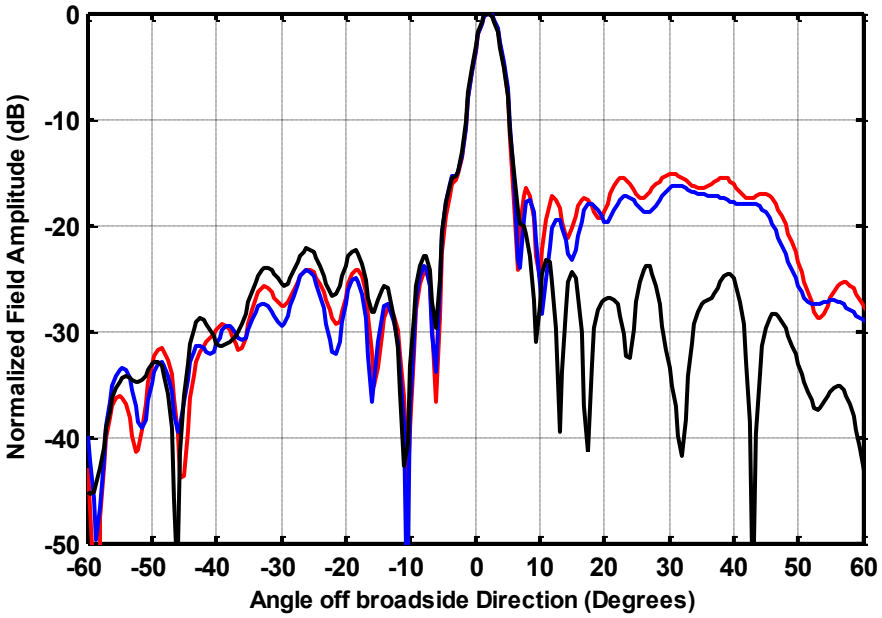

Figure 4.24: Normalized E-plane far-field radiation patterns of sub-wavelength reflectarray due to conduction currents on the patches (——), groundplane (——), and both the patches & groundplane (——) calculated at 33GHz.

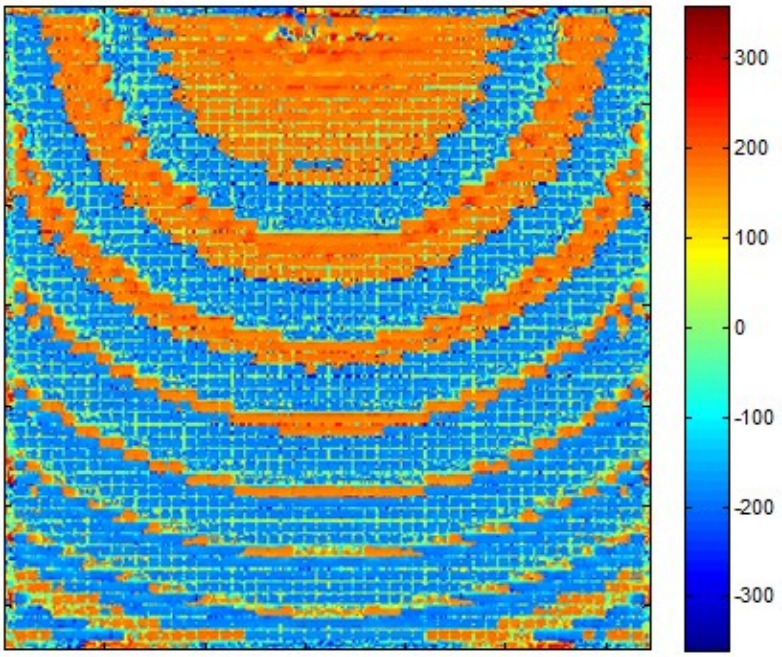

(a)

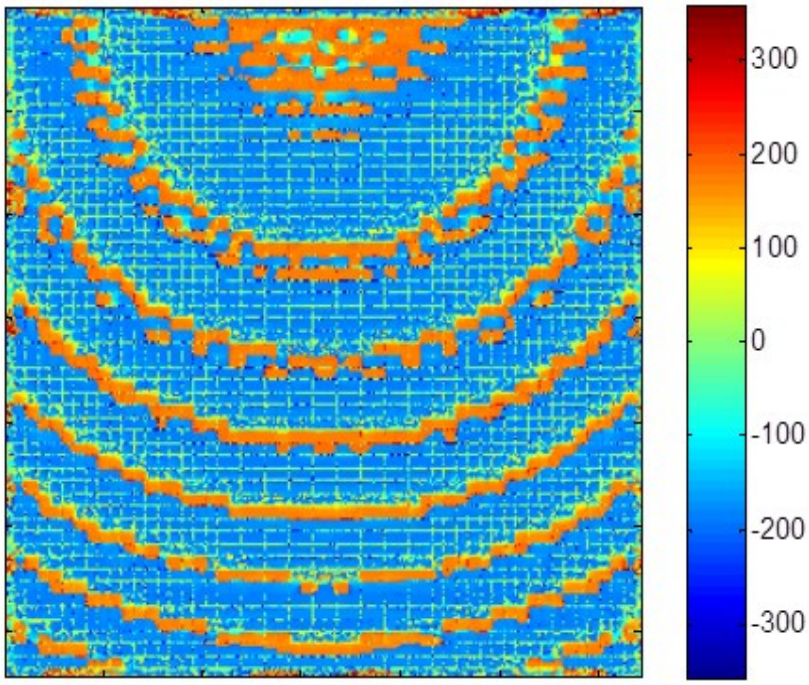

(b)

Figure 4.25: Difference between the phases of the conduction currents on the patches and the groundplane for the sub-wavelength reflectarray (a) 30GHz & (b) 33GHz.

4.4 Far-Field Measurement Results

For further verification of the full-wave modelling technique illustrated in Sections 4.2 and 4.3, and hence the pathology of the feed image lobe, we have performed pattern measurements on fabricated versions of the half-wavelength and sub-wavelength offset-fed reflectarrays, with dimensional and material specifications as given in Section 4.2. The sub-wavelength design has a 3mm (roughly $\lambda_0 / 3$) square unit cell size, whereas this is 5mm for the half-wavelength one. The difference between the two is shown in the close-up photograph of the reflectarrays placed side by side in Figure 4.26.

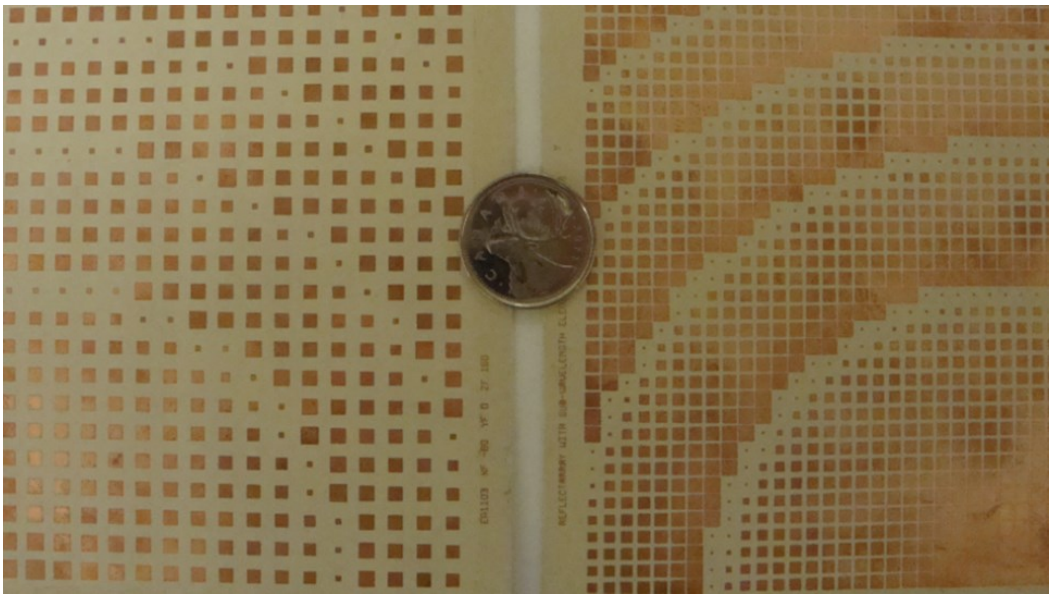

Figure 4.26: Close-up of portions of the half-wavelength and sub-wavelength reflectarrays placed side-by-side. The Canadian 25¢ coin is shown as a size reference.

Measured and computed E-plane radiation patterns of the two fabricated reflectarrays are shown at the same off-centre frequencies as in Section 4.2, namely 27 GHz and 33 GHz in Figures 4.27 and 4.28, respectively. Apart from providing experimental validation of the full-wave model used in the deliberations thus far, the elimination of the feed image lobes through use of a sub-wavelength configuration is obvious from the previous two figures. Indeed, the main differences in the pattern levels of the two reflectarrays occur around the specular direction. Thus the presence of feed image lobes is the principal reason for the gain reduction of the half-

wavelength reflectarray at off-centre frequencies seen in Table 4.1. The suppression of the feed-image lobe contributed to a substantial improvement in the measured 1dB gain bandwidth; the resulting bandwidths were 7.5% for the half-wavelength reflectarray and 12.5% for the sub-wavelength reflectarray. Furthermore, the measured aperture efficiencies at 30GHz are 53% and 49.5% for the sub-wavelength and the half-wavelength reflectarrays respectively. Elimination of the feed-mage lobes at off-centre frequencies is of course also achieved when variable length dipole elements (of 0.5 mm width) are used in the sub-wavelength configuration, as evidenced in Figure 4.29. It is clear that use of a sub-wavelength reflectarray configuration suppresses the feed image lobe.

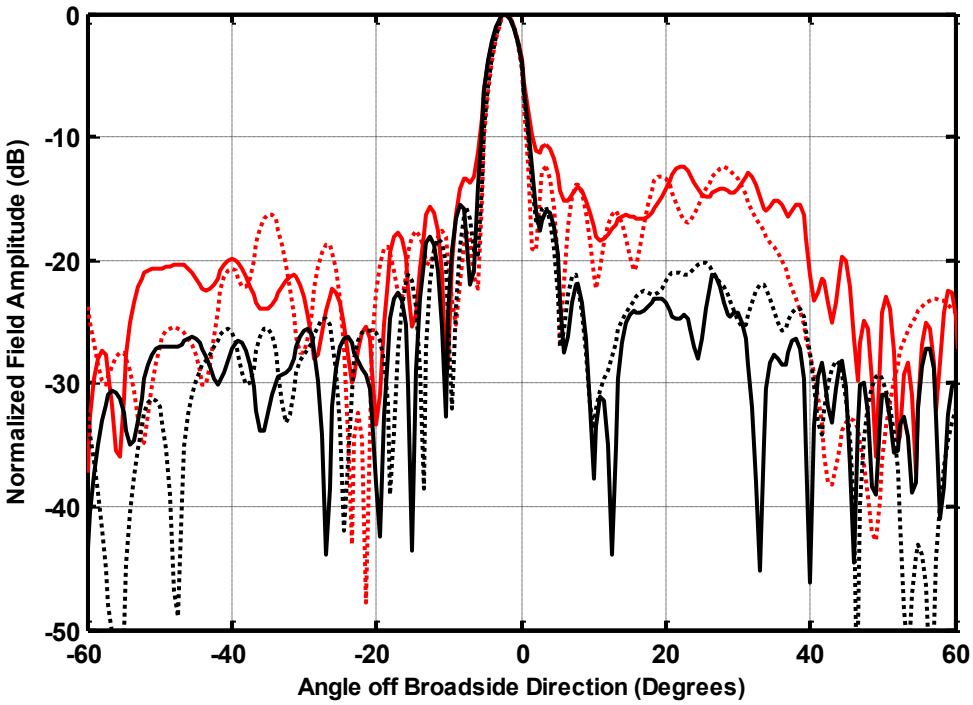

Figure 4.27: E-plane far-field patterns at 27GHz for the resonant reflectarray measured (——) calculated (••••), and the sub-wavelength reflectarray measured (——), calculated (••••).

One might be tempted to explain the reason for the absence of feed image lobes in the sub-wavelength case in terms of reduced groundplane exposure, but we have already discounted this in Section 4.3. The actual reason is the much smaller change (with respect to frequency) in the

element reflection phases when a sub-wavelength lattice is used. This extends the strong resonant behavior, which occurs at the centre frequency, to prevail at off-centre frequencies.

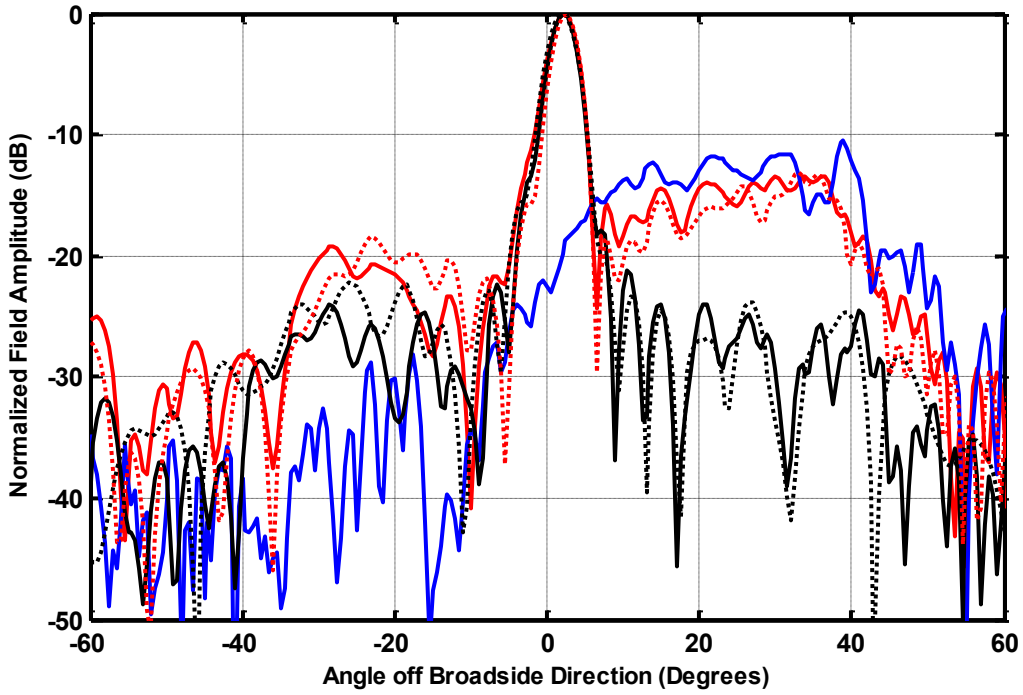

Figure 4.28: E-plane far-field patterns at 33GHz for the resonant reflectarray measured (——) calculated (●●●●), the sub-wavelength reflectarrray measured (——), calculated (●●●●). The measured feed-image obtained by replacing the reflectarray by a perfectly conducting plate is shown as (——).

Table 4.1: Measured maximum gain at different frequencies for the fabricated half-wavelength & sub-wavelength reflectarrays.

Frequency (GHz)	Gain of Half-Wavelength Reflectarray (dBi)	Gain of Sub-Wavelength Reflectarray (dBi)
27	27.8	30.24
28	30.32	30.72
30	31.46	31.74
32	29.11	31.54
33	27.9	31.11

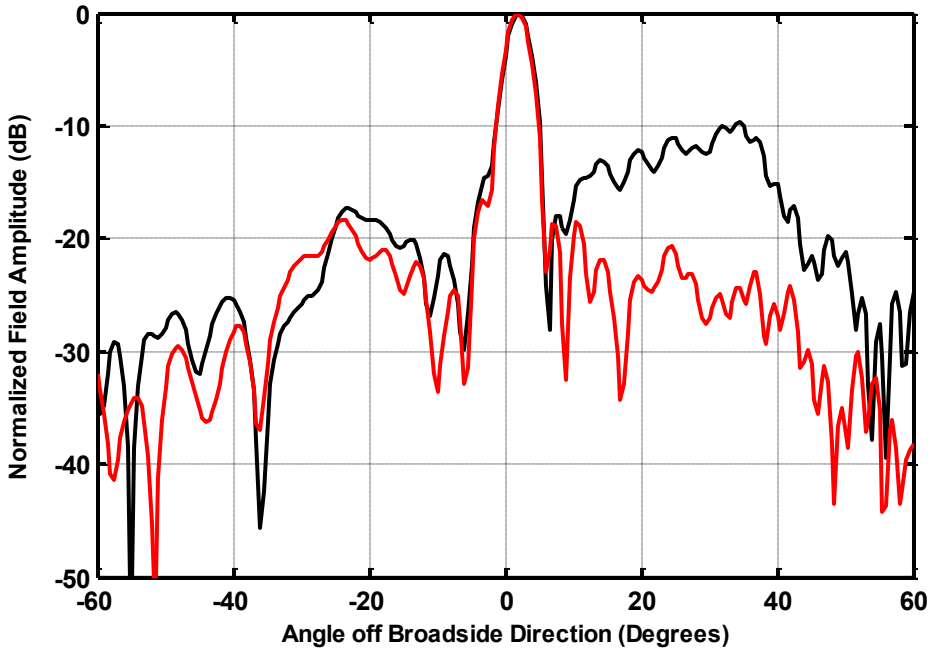

Figure 4.29: Normalized E-plane far-field patterns calculated at 33GHz for the half-wavelength reflectarray with dipole elements (——) mentioned in Part A of Section II, compared to the sub-wavelength reflectarray with dipole elements (——).

The broader bandwidth in the sub-wavelength case is well-known, and is illustrated in Figure 4.30. This figure shows the derivative of the reflection phase with respect to frequency. It gives an indication of how much the element reflection phases will change per unit frequency when we move away from the design frequency. The errors in the reflection phases will plainly be much less for the sub-wavelength reflectarray, which in turn has no feed image lobes. Thus we maintain that the reason for the presence of feed image lobes at off-centre frequencies for the half-wavelength reflectarray is indeed the error in the element reflection phases, as we concluded in Section 4.2. This was also conjectured in [13]. However, it does not appear to be the almost periodic reflection phase error [13] due to the jump in element sizes at Fresnel zone boundaries, but rather the reflection phase errors that result over the entire reflectarray. This can be established by examination of the actual phase of the scattered field over the reflectarray aperture, obtained using the full-wave model. Figure 4.31 reveals the almost-periodic variation of this phase (as suspected by the authors of [13]), shown here at the centre frequency. In spite of this almost periodic phase variation neither of the reflectarrays has feed-image lobes at 30 GHz. Furthermore, as indeed implied in the conclusion to [13], when an actual feed is used to

illuminate the reflectarray (usually with a taper to obtain the best compromise between spillover and illumination efficiency), the influence of those elements near the boundaries of the outer Fresnel zones will be decreased.

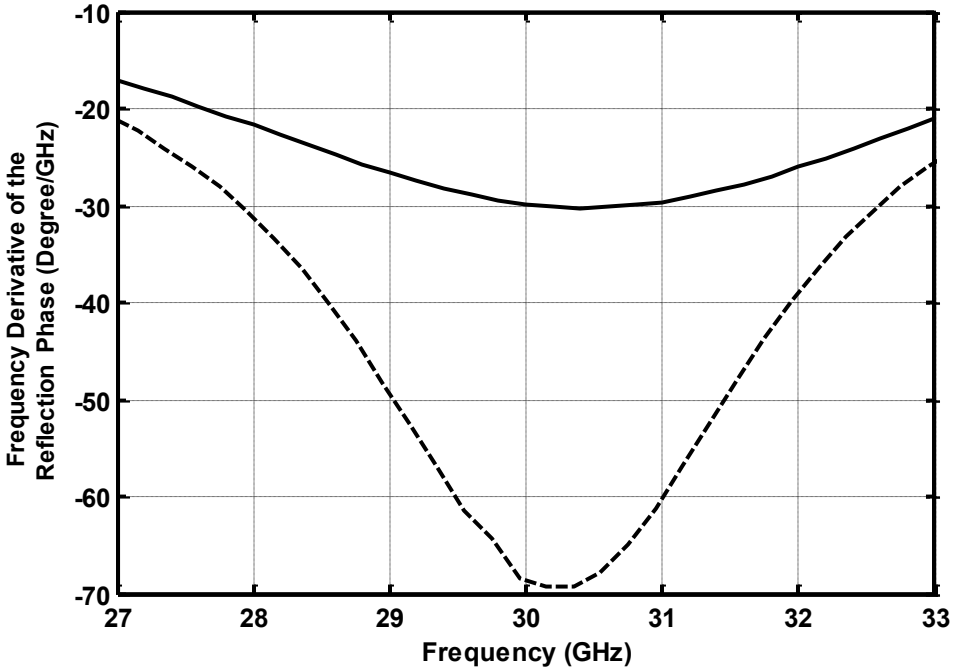

Figure 4.30: Plot of the frequency derivative (in degrees per GHz) of the reflection phase for a patch of length 2.49mm in a half-wavelength lattice (— — —) and a patch of length 2.24mm in a sub-wavelength lattice (——).

A question might arise as to how small the inter-element spacing should be in order to achieve satisfactory suppression of the feed image lobe. We therefore designed and performed full-wave simulations of three additional patch-element reflectarrays with the same design parameters as stated in Section 4.2, but with $0.35\lambda_0$, $0.4\lambda_0$ and $0.45\lambda_0$ spacings. An examination of the results for the (now five) reflectarrays shows the feed image lobe is smaller the smaller the inter-element spacing.

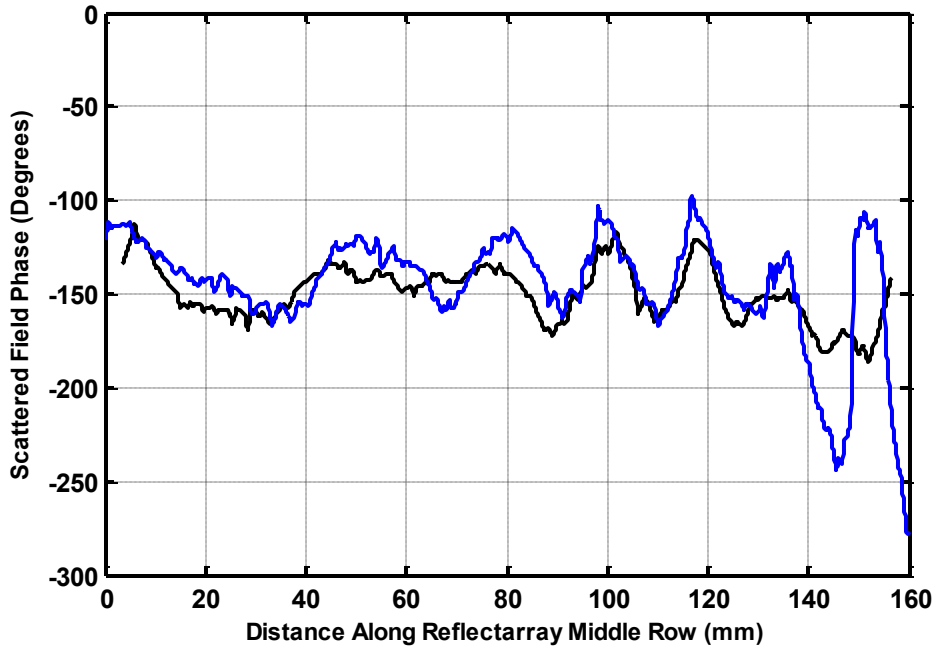

Figure 4.31: Plot of the computed scattered field phase at 30 GHz for the half-wavelength (——) and sub-wavelength (——) reflectarrays. The field was calculated at short distance above the reflectarray surface along the reflectarray Middle row (x-axis in Figure 4.1)

For a given aperture size the number of elements of course increases with decreasing inter-element spacing, as illustrated in Table 4.2. If one wishes to limit the number of elements (eg. because one intends to use electronic reconfigurability) and yet keep the feed image lobes sufficiently suppressed at off-centre frequencies, then an inter-element spacing of $0.35\lambda_0$ might be an acceptable compromise as shown in Figure 4.32.

Table 4.2: Number of elements versus inter-element spacing.

Elements Spacing	Number of Elements in the Reflectarray	Feed Image Lobe Level with Respect to the Main Beam (dB)
$0.5\lambda_0$	961	-14.1
$0.45\lambda_0$	1186	-16.3
$0.4\lambda_0$	1501	-18.4
$0.35\lambda_0$	1961	-22.3
$0.3\lambda_0$	2704	-24.1

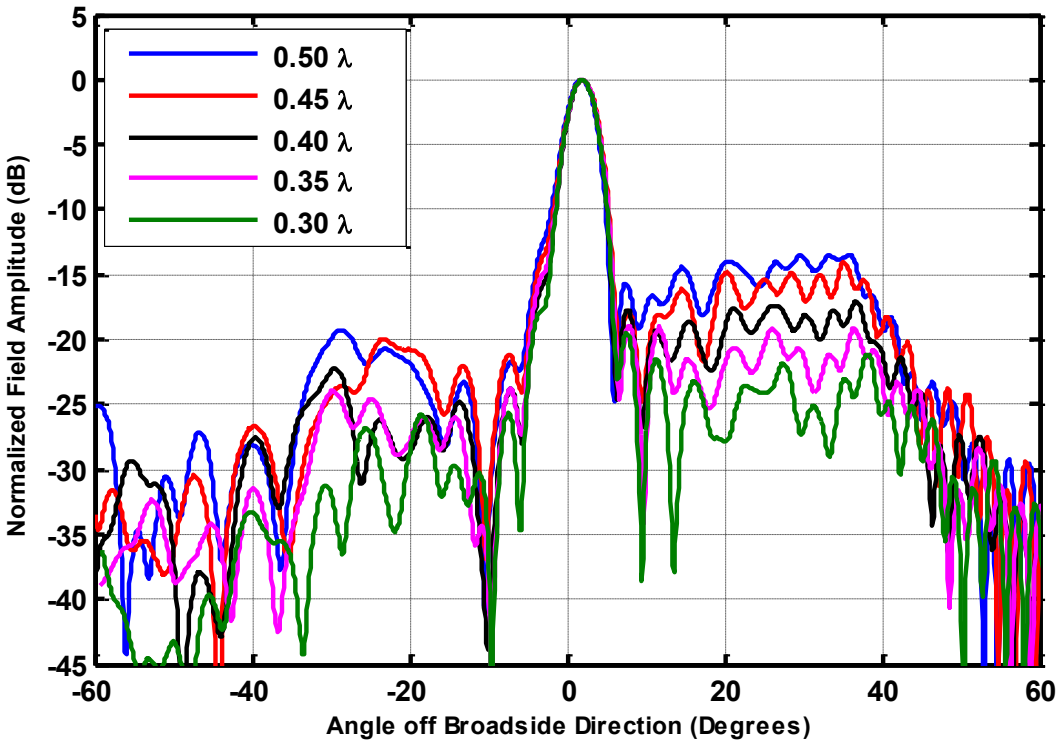

Figure 4.32: Calculated E-plane far-field radiation patterns (at 32 GHz) for reflectarrays of different inter-element spacings.

The Reflectarray's cross polarization level was not given much consideration in this thesis as it is established in the literature that one of the electrical advantages of the reflectarray is the improved cross-polarization performance due to the polarization selectivity that can be obtained with variable patch size elements [14]. This is why they can be used for dual-polarization applications as an alternative to dual-grid reflectors [15]. Nevertheless, Figure 4.33 reveals an interesting observation about reflectarrays of variable size elements cross polarization level; a sub-wavelength reflectarray has a slightly lower maximum cross-pol level compared to its equivalent half-wavelength reflectarray when the cross-pol is calculated at the frequency of the maximum gain of each reflectarray.

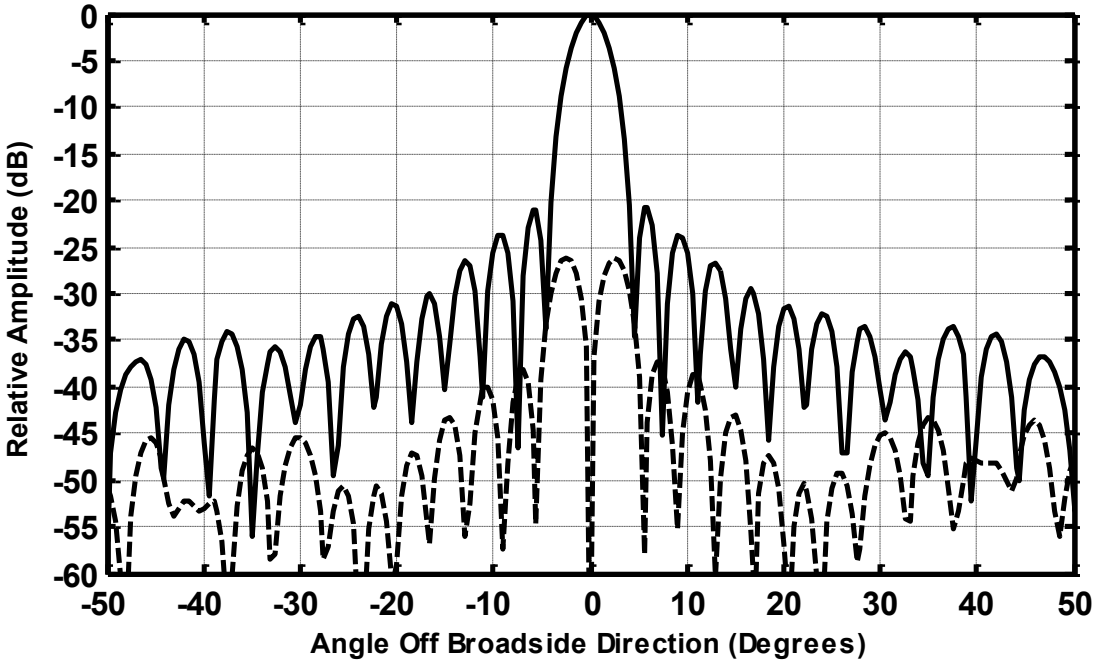

(a). Half-wavelength reflectarray

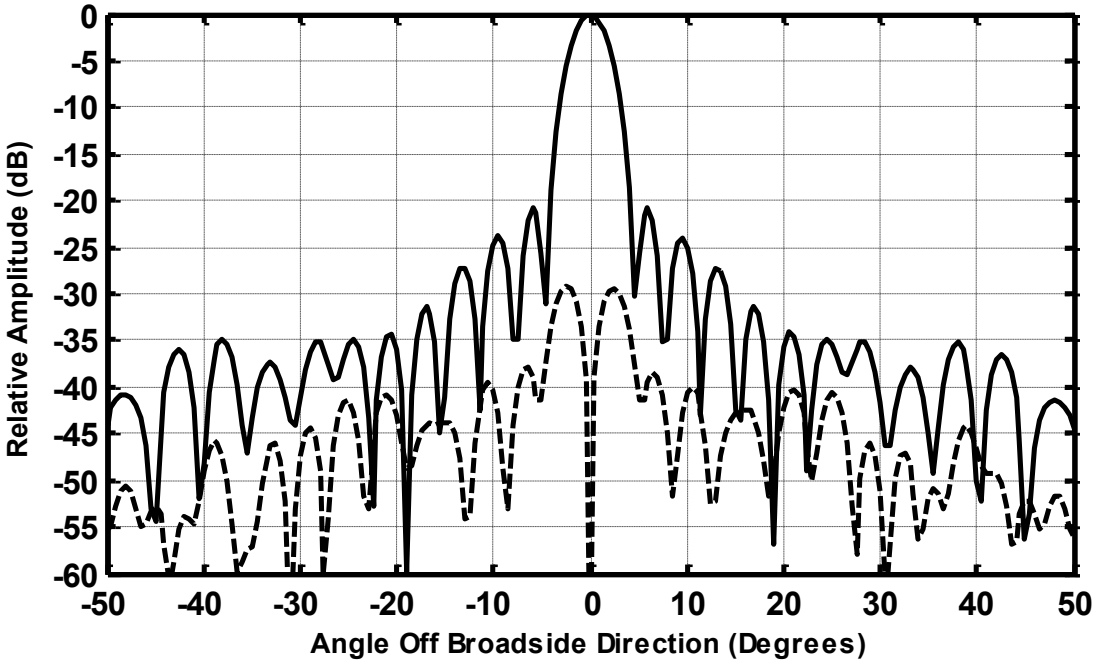

b). Sub-wavelength reflectarray

Figure 4.33: Calculated H-plane far-field radiation patterns at the frequency of maximum gain for each reflectarray. Co-pol (solid), Cross-pol (dashed).

4.5 Concluding Remarks

It has been shown that both the groundplane and the conducting elements contribute to the feed image lobe. This was done by investigating the individual and combined contributions of the conduction currents on the elements and the groundplane to the far-fields of half-wavelength and sub-wavelength reflectarray antennas employing patch-type or dipole-type conducting elements. The individual and combined current density contributions were generated and studied at the centre frequency and some off-centre frequencies. This confirmed that in a properly designed reflectarray (with a complete range of element reflection phases available) a feed image lobe does not appear at the centre frequency because the contributions of the element and groundplane currents interfere destructively around the specular direction. At off-centre frequencies there is an imbalance between the element and groundplane currents, and hence their individual contributions to the far-fields, caused by the changes in the element reflection phases with frequency. This leads to the creation of the feed image lobe in the resultant reflectarray pattern. Use of sub-wavelength reflectarrays has been demonstrated, both theoretically and experimentally, to eliminate feed image lobes in reflectarrays of patch or dipole elements, hence improving reflectarray performance. This work has been reported in [16].

Chapter 4 References

[1] A.Roederer, "Reflectarray antennas", 3rd Antennas and Propagation European Conference, (EuCAP), pp.18-22, April 2009.

[2] HFSS, Ansoft Product Suite, Ansys Inc., USA (www.ansoft.com).

[3] J.Huang and J.A.Encinar, Reflectarray Antennas (Wiley, 2008).

[4] R.Munson and H.Haddad, "Microstrip reflectarray for satellite communication and RCS enhancement and reduction", U.S. Patent 4,684,952, August1987.

[5] S.D.Targonski and D.M.Pozar, "Analysis and design of a microstrip reflectarray using patches of variable size", IEEE International Symposium on Antenna and Propagation Digest, pp.1820-1823, July 1994.

[6] D.R.Jackson, "Microstrip Antennas", Chap.7 in: J.L.Volakis (Edit.), Antenna Engineering Handbook (McGraw Hill, 2007) Fourth Edition, Sect.7.5.

[7] M.Mussetta, P.Pirinoli, R.E.Zich and M.Orefice, "Design of printed microstrip reflectarrays reducing the groundplane reflection", Proceedings of URSI General Assembly, New Delhi, India, June 2005.

[8] J.Budhu and Y.Rahmat-Samii, "Understanding the appearance of specular reflection in offset fed reflectarray antennas", IEEE International Symposium on Antenna and Propagation Digest, pp.97-100, USA, July 2011.

[9] D.M.Pozar, "Wideband reflectarrays using artificial impedance surfaces", Electronics Letters, Vol.43, No.3, pp.148-149, February 2007.

[10] P.Nayeri, F.Yang and A.Elsherbeni, "A broadband microstrip reflectarray using sub-wavelength patch elements", IEEE International Symposium on Antenna and Propagation Digest, USA, June 2009.

[11] P.Nayeri, F.Yang and A.Elsherbeni, "Broadband reflectarray antennas using double-layer subwavelength patch elements", IEEE Antennas and Wireless Propagation Letters, Vol.9, pp.1139-1143, 2010.

[12] J.Ethier, M.R.Chaharmir and J.Shaker, "Loss reduction in reflectarray designs using sub-wavelength coupled-resonant elements", IEEE Transactions in Antennas and Propagation, Vol.60, pp.5456-5459, May 2012.

[13] R.El-Hani and J.Laurin, "Specular reflection analysis for off-specular reflectarray antennas", IEEE Transactions in Antennas and Propagation, Vol.61, pp.3575-3581, July 2013.

[14] D.M.Pozar, S.D.Targonski and H.D.Syrigos, “Design of millimeter wave microstrip reflectarrays”, IEEE Transactions on Antenna and Propagation, Vol.45, No.2, pp.287-295, February 1997.

[15] J.A.Encinar, “Design of two-layer printed reflectarrays using patches of variable size”, IEEE Transactions on Antenna and Propagation, Vol.49, No.10, pp.1403-1410, October 2001.

[16] **E.Almajali**, D.A.McNamara, J.Shaker and M.R.Chaharmir, "Feed Image Lobes in Offset-Fed Reflectarrays: Diagnosis and Solution", IEEE Transaction in Antennas and Propagation, Vol.62, No.1, pp.216-227, January 2014.

CHAPTER 5

Beam Squint in Offset-Fed Reflectarrays: Diagnosis and Solution

5.1 Introduction

Another problem in offset-fed reflectarrays that has not been given enough consideration in the literature is beam squint. As previously stated in Section 2.4.3, beam squint effectively reduces the gain of the reflectarray due to the deviation of the main beam from its design direction at off-centre frequencies. For high-gain antennas with narrow beamwidths, this could also lead to other serious problems as the beam pointing accuracy will be lost. In this chapter most aspects of the beam squint phenomenon are deliberated thoroughly. In Section 5.2 the focal point shift in reflectarrays is studied using a full wave receive-mode analysis applied to different classes of offset-fed reflectarrays. This is reinforced by Fresnel zone boundary considerations and an approximate scalar receive-mode analysis. The impact of important design factors like reflectarray size, focal length and element type on the amount of focal point shift is also established. In Section 5.3 the focal point shift with frequency is shown to be the source of beam squint in offset-fed reflectarrays. This diagnosis is demonstrated using the reconciliation of transmit-mode and receive-mode analyses applied to the same offset-fed reflectarray structure. Most simulation results are then ratified experimentally. This knowledge is used in Section 5.5 to show how a two-feed reflectarray configuration can be used to suppress beam squint in offset-fed reflectarrays. The validity of this solution is established by comparing predicted far-field amplitude patterns with their measured counterparts. Prior to this, in Section 5.4, the gain and bandwidth of two-feed reflectarrays is shown to improve substantially through the use of a sub-wavelength configuration. In Section 5.6 the source of certain high sidelobe levels associated with the two-feed reflectarray configuration is identified, and a solution for these unwanted lobes is proposed and validated. Finally, the chapter is concluded in Section 5.7.

5.2 Investigation into the Focal Region Shift in Reflectarrays

5.2.1 Preliminary Remarks

The focal point of a reflectarray is simply the geometrical optics focal point from which all spatial phase delays [1] are calculated in order to select the element sizes as part of the reflectaray design procedure [2]. Based on this, one would expect that if a feed were placed such that its phase centre is coincident with the focal point, the maximum gain of the reflectarray would be achieved. However, it was shown in [3] that the actual focal point, which is properly predicted using rigorous full wave simulation of the reflectarray, is usually shifted from the geometrical optics focal point due to the finiteness of the reflectarray structure. As a consequence of that, a higher gain value is achievable when the feed is moved away from the geometrical optics focal point toward the actual focal point. This movement of the actual focal point from its geometrical optics location is called focal point shift. Similar focal point concept is used in this chapter to describe the movement of the actual focal point due to frequency sweep in a given frequency band.

In Section 2.5, we discussed a previous study conducted on focal shift phenomenon in reflectarrays [3]. This study includes solely the impact of reflectarray size as well as reflectarray focal length on the focal point shift in centre-fed reflectarrays just at the design centre frequency. Due to the tangible need to investigate the behavior of the focal shift with frequency and its impact on reflectarray performance, which was not done previously, we in what follows of this section investigate this in some detail. The impact of some factors, namely reflectarray size, focal length, element type and lattice size, on the amount of focal shift versus frequency are also examined. Finally the focal point shift is interpreted in terms of Fresnel zone boundary considerations. This indicates the cause of focal point shift by relating the Fresnel zone boundaries to the amount of focal shift at any given frequency

5.2.2 Full wave Receive-Mode Analysis

In order to predict and investigate any reflectarray focal region fields, one should consider performing a full-wave receive-mode analysis on the reflectarray structure. In the receive mode, a linearly polarized plane wave, incident on the reflectarray surface from the direction of the intended main lobe, gives rise to a concentrated field distribution in the reflectarray focal region. Examination of such focal region fields has proved useful in understanding the operation of conventional reflector antennas [4].

Receive-mode analysis entails simulating the complete reflectarray structure, that is, microstrip patches on a grounded dielectric substrate, and then examining the reflected near-field along lines or over certain apertures. When the receive-mode analysis computes the reflected near-field at points along a line, it tells us how the field would vary if we moved a point probe along that line. Figure 5.1 illustrates the receive-mode idea for a centre-fed reflectarray antenna.

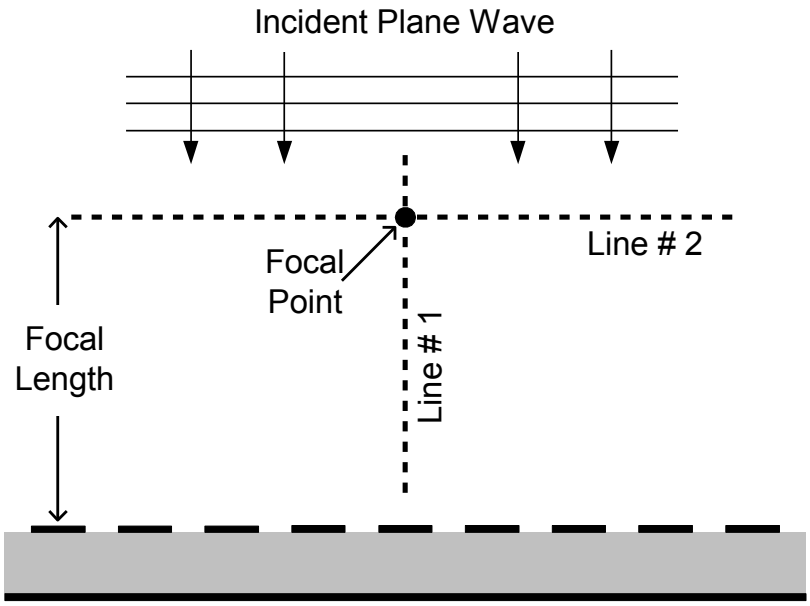

Figure 5.1: Sketch illustrating the configuration used for the receive-mode analysis of a centre-fed reflectarray antenna.

For the purpose of illustration of the receive-mode technique, a centre-fed reflectarray comprised of square patch elements, designed at a centre frequency of 30GHz, with F/D=1 and

D=15.5λ, is simulated in the receive-mode using HFSS [5]. With reference to Figure 5.1, the focal regions fields over Line#1 and Line#2 predicted at 30GHz are shown in Figure 5.2. It is evident that illuminating the reflectarray with a plane wave results in a concentrated field distribution in the reflectarray focal region with a distinct peak near the geometrical focal point.

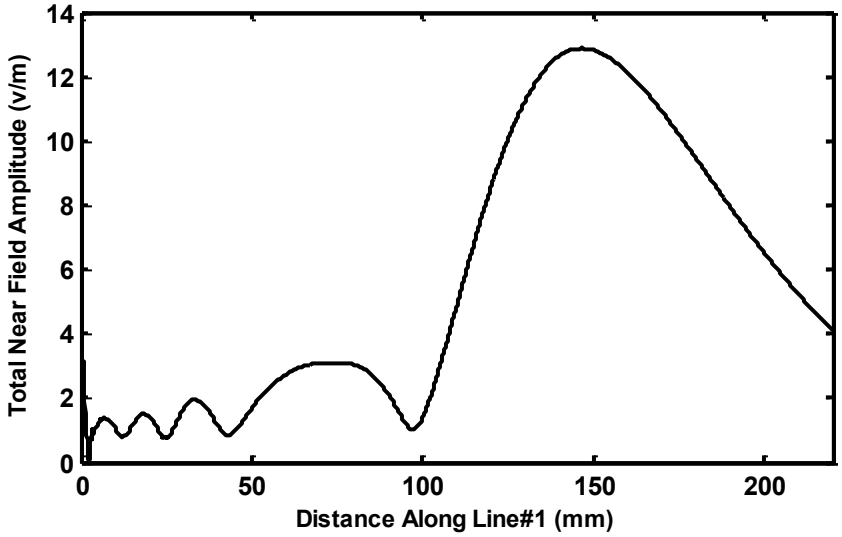

(a)

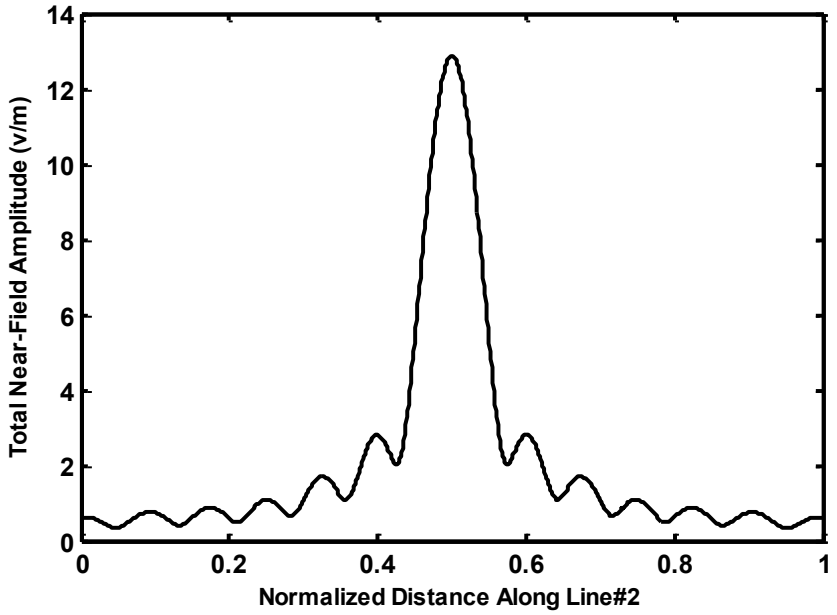

(b)

Figure 5.2: Near electric fields calculated at 30GHz as a function of position a) along Line#1, b) along Line#2 for the centre-fed reflectarray. The reflectarray front surface is at 0 mm.

5.2.3 Focal Point Behavior with Frequency

In order to examine the phenomenon of focal shift with frequency we analyze, using the receive-mode analysis, an offset-fed reflectarray that is designed using the design procedure summarized in Section 2.2.2. We select $F/D=1$ for a square aperture reflectarray with D = 160mm, which is 16 wavelengths (λ) at the center frequency $f_o = 30\text{GHz}$. It is designed for a far-zone main lobe in the broadside direction, using a single-layer 0.508mm thick Rogers 3003 substrate with $\varepsilon_r = 3$. The elements are square patches spaced by $\lambda/3$ (it is a sub-wavelength reflectarray) with 52X52 elements occupying the reflectarray surface. The code HFSS [5] was used to perform the vector full-wave receive-mode analysis in order to investigate the reflectarray focal region fields.

With reference to Figure 5.3, the precise focal point peak position (at 30 GHz) is determined by predicting the focal region field over lines that pass through the design focal point. Line#1, Line#2 and Line#3 are example of these lines.

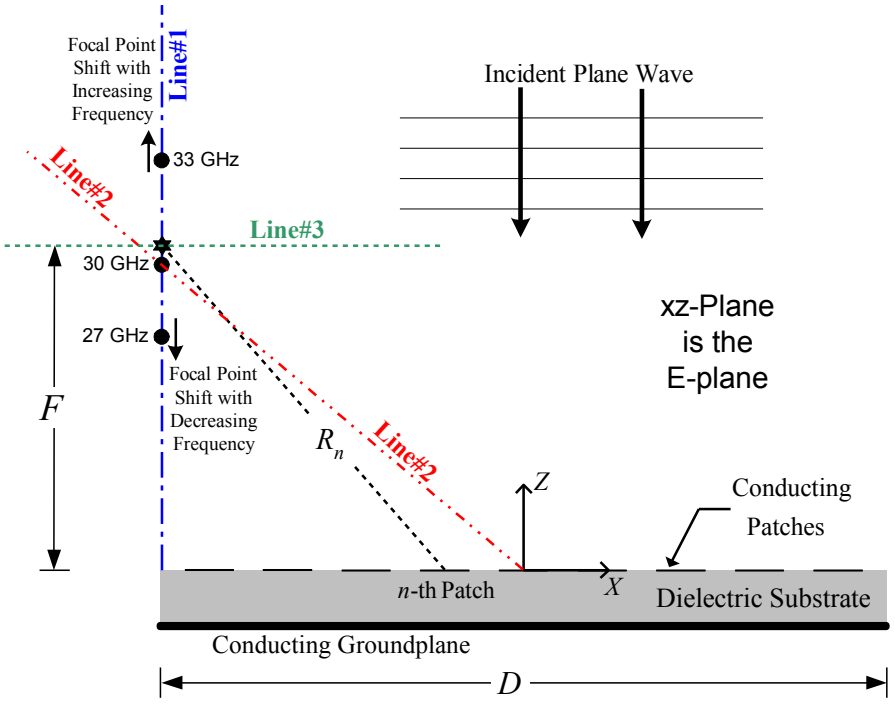

Figure 5.3: Offset-fed reflectarray showing a normally incident plane wave. The coordinate origin is at the center of the reflectarray. The shift of the actual focal point from the geometrical one is shown exagerrated.

The electric field intensity along Line#1, Line#2 and Line#3 that pass through this focal point are shown in Figures 5.4, 5.5 and 5.6 respectively. Examination of these focal region fields reveals that as the frequency is changed the principal shift in the maximum field value (the actual focal point) is vertically along Line#1, with comparatively small shifts off this line. The focal point moves towards (away from) the reflectarray surface as the frequency decreases below (increases above) f_o .

The drop in the value of the received field at the focal point away from the centre frequency is obvious. Close examination of the fields along Line#1 reveals that this drop is due to the fact that the actual focal point shifts along Line#1 away from its location at 30 GHz as the frequency changes.

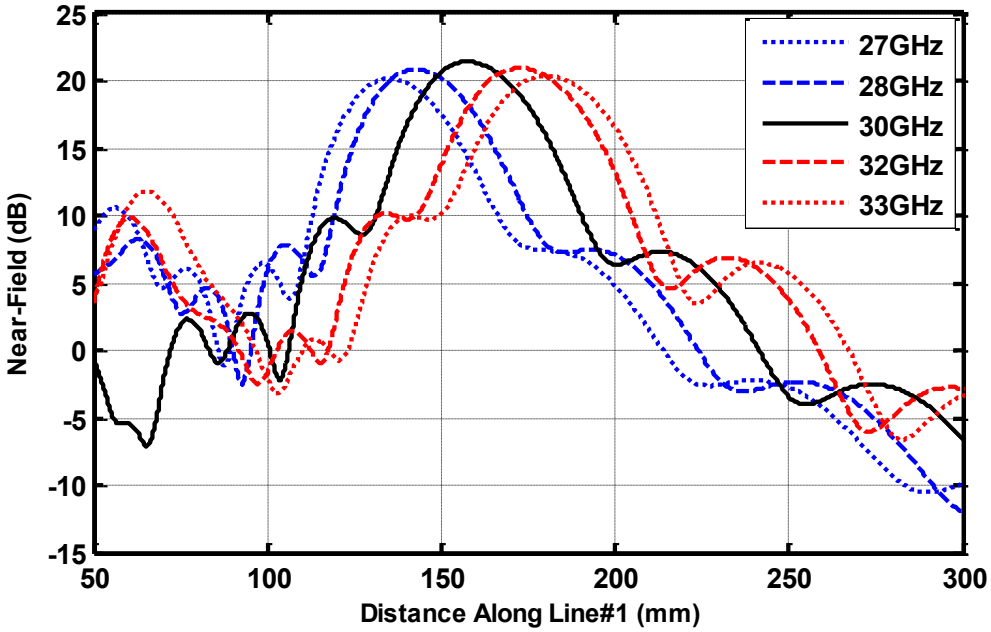

Figure 5.4: Focal field region shift with frequency along Line#1 of the offset-fed reflectarray. The reflectarray front surface is at 0mm.

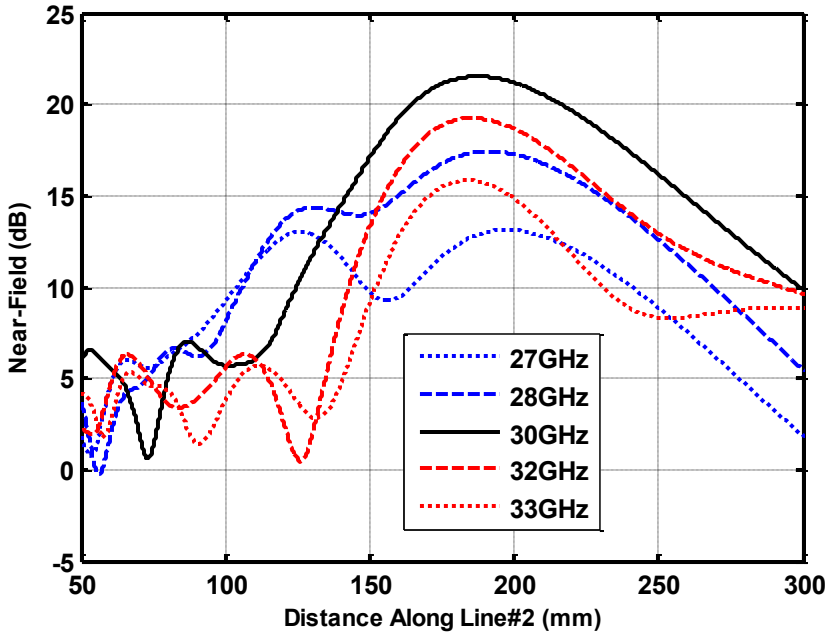

Figure 5.5: Focal field region shift with frequency along Line#2 of the offset-fed reflectarray.

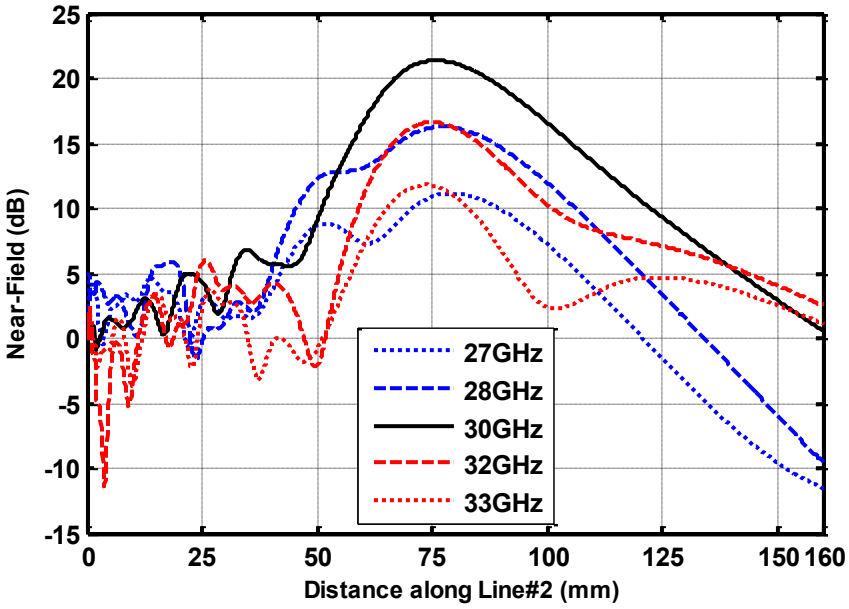

Figure 5.6: Focal field region shift with frequency along Line#3 of the offset-fed reflectarray.

5.2.4 Impact of Geometrical and Non-Geometrical Factors on the Amount of Focal Point Shift in Reflectarrays

A- Reflectarray Size and Focal Length (Geometrical Factors)

In order to investigate the impact of reflectarray size and focal length on the amount of focal shift that occurs at a given frequency, several half-wavelength reflectarrays of different sizes, namely 7.5λ, 15λ and 30λ are analyzed using the full-wave receive-mode technique. Each of the different size reflectarrays is also analysed with different F/D ratios (different focal lengths), namely F/D = 0.6, F/D = 1, F/D = 1.4. This combination of sizes and F/D ratios gives us nine different reflectarrays to simulate. All reflectarrays are designed for a far-zone main lobe in the broadside direction, using a single-layer 0.508mm thick Rogers 3003 substrate with $\varepsilon_r = 3$. The design centre frequency is 30GHz for all cases.

First, we aim to examine the inherent focal shift that is caused by the finiteness of reflectarrays structures at 30GHz. This enables us to determine the location of the actual focal points for all aforementioned reflectarrays in ordered to use these locations as the references in calculating the amount of focal shift at off-centre frequencies. Figure 5.7 shows the amount of focal shift for the different reflectarrays versus F/D ratio. The amount of focal shift for each case is predicted from focal field plots, similar to those given in Figures 5.4 through 5.6.

In Figure 5.7 one can clearly observe the trends in the amount of inherent focal shift based on the size of the reflectarray and the selected F/D ratio. It is evident that for larger reflectarrays (i.e. 30λ) there is very little focal shift particularly when a short focal length is selected (i.e. F/D=0.6). This implies that for practical applications (in which reflectarrays are usually electrically large) this type of focal shift, which we called the inherent focal shift in Section 2.5, will apparently not be an issue.

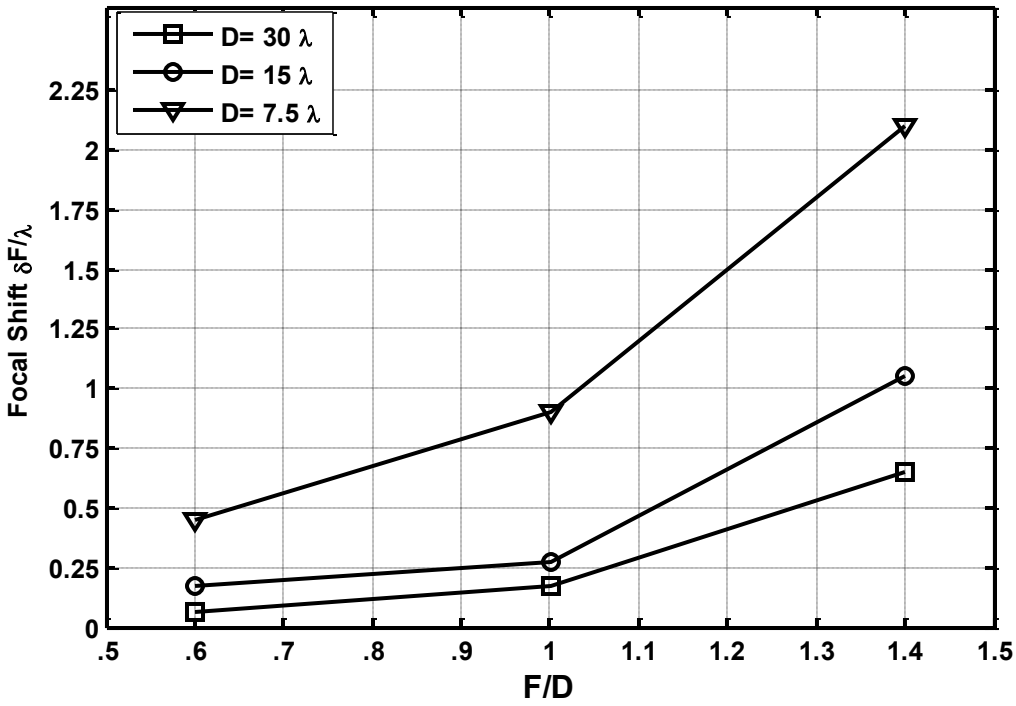

Figure 5.7: Focal shift as functions of F/D calculated at the centre-frequency (30GHz).

In order to fully comprehend the impact of reflectarray size and focal length on the amount of focal shift, the focal shift phenomenon needs to be investigated versus frequency using reflectarrays of different sizes and F/D ratios. To achieve this purpose, the aforementioned differently sized reflectarrays are simulated at off centre frequencies in the band 27GHz-33GHz. Figures 5.8(a),(b)&(c) exhibit the change in focal shift with frequency in terms of wavelengths relative to the actual focal point locations predicted at the centre-frequency 30GHz and shown in Figure 5.7. The negative shifts in Figures 5.8 (a),(b)&(c) represent the movement of the focal point away from the reflectarray surface. This occurs at frequencies above 30GHz.

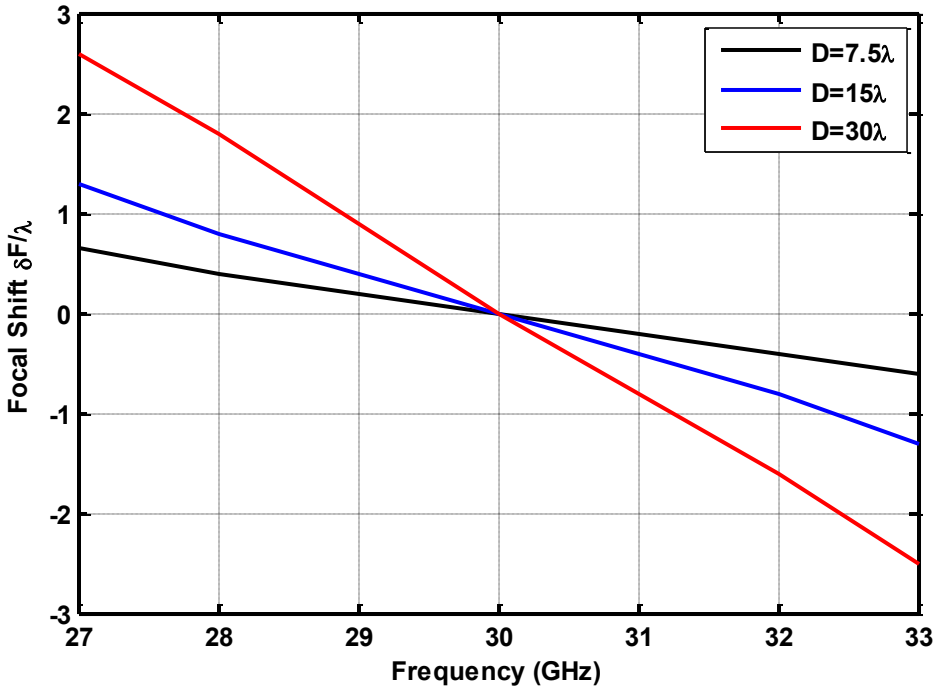

(a)

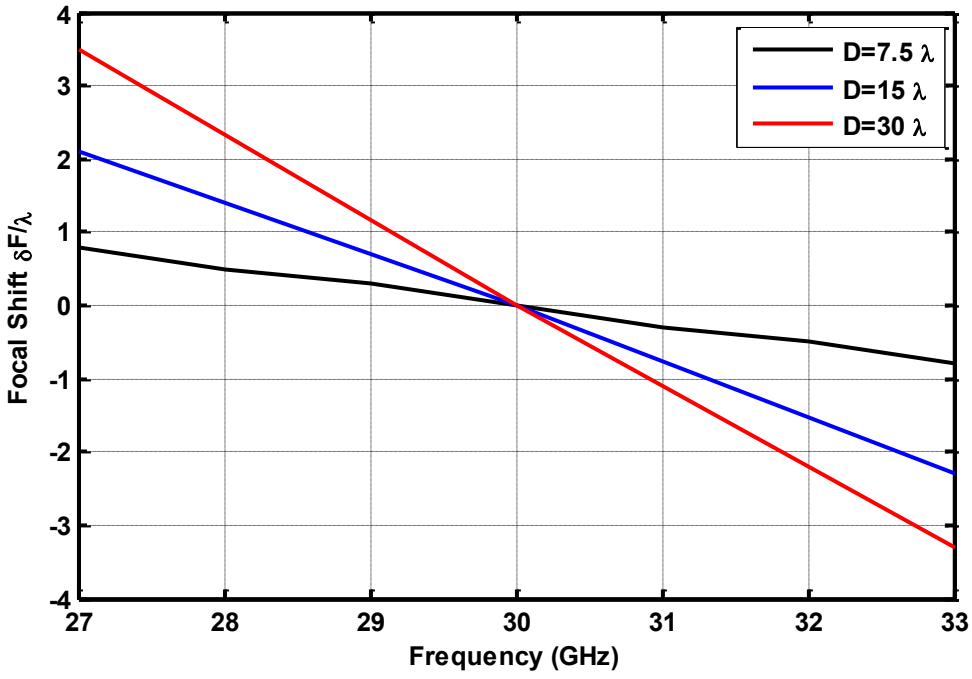

(b)

Figure 5.8: Focal shift as functions of frequency for various reflectarray aperture sizes calculated for a) F/D= 0.6, b) F/D=1.

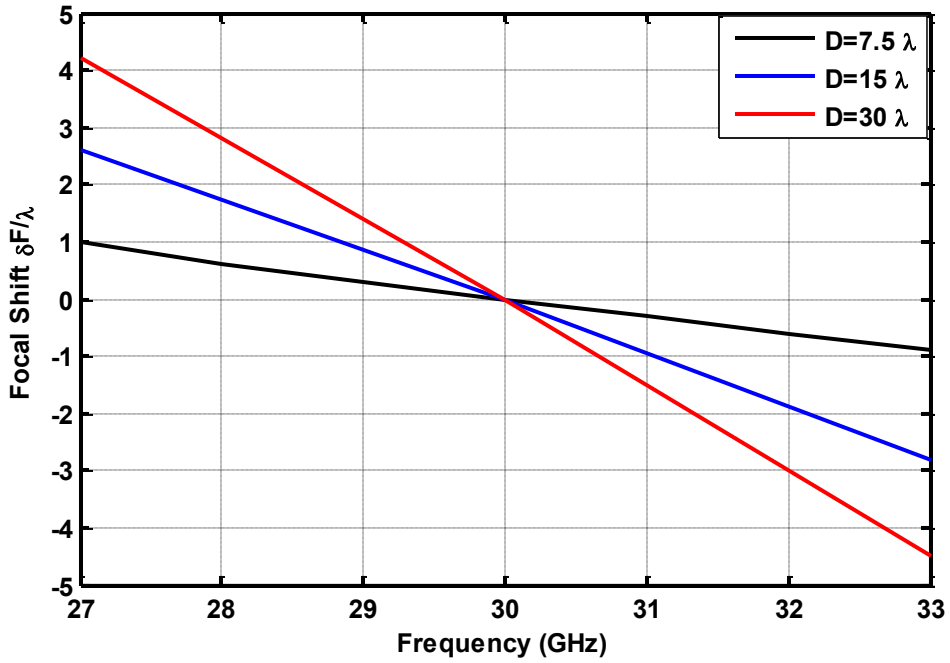

(c)

Figure 5.8 (continued): c) F/D=1.4.

One can see from Figures 5.8 (a),(b) and(c) that the larger the F/D ratio value, the bigger the amount of focal shift for all given reflectarray sizes. For instance, in Figures 5.8 (a) and(c) respectively, the amount of focal shift for D=15λ at 27GHz in both cases increased from 1.24λ for F/D= 0.6 to 2.6λ when F/D=1.4 (close to a 1.4λ change). This big swing in the actual focal point position away from its design location is expected to break the phase synchronism on the reflectarray surface and consequently leads to a considerable degradation in the reflectarray performance. Figure 5.8 also reveals an important fact, namely that for a given F/D ratio the amount of focal shift at off-centre frequencies is proportional to the reflectarray size; the biggest shift for all F/D values in Figures 5.8 (a),(b) & (c) plots occurs when D=30λ. Such results unmistakably point to a new factor that contributes to the limited bandwidth of large size reflectarrays; the substantial focal point shift causes a major misalignment with the feed phase centre (which stays relatively stationary at all frequencies). This worsens the spatial phase delay problem in large reflectarrays [1] because all phases (element sizes) are usually selected based upon a fixed focal point location.

B- Reflectarray Element Type and Lattice Size (Non-Geometrical Factors)

Other factors that could affect the focal point shift in reflectarrays are the element type and their spacing on the reflectarray surface. To investigate the impact of these factors, several reflectarrays of identical size D=160mm and same focal length 160mm (F/D=1), but different element types and spacing, are designed at a centre-frequency of 30GHz. All reflectarrays are designed for a far-zone main lobe in the broadside direction, using a single-layer 0.508mm thick Rogers 3003 substrate with $\varepsilon_r = 3$.The elements type and lattice size of these reflectarrays are summarized in Table 5.1. The patch elements are square; the crossed loop elements are as in [6] but for a single loop as shown in Figure 2.3(d) with d=0.2mm and w=0.8mm. The infinitely broadband element case referred to is not obtained using the full-wave model (where the actual element performance is always properly modeled) but is instead calculated using an approximate scalar analysis: The elements are assumed to be isotropic radiators and infinitely broadband in the sense that the required correction phase at any frequency equals that at the centre frequency ($\psi_n(f) = \psi_n(f_o)$). The contributions of each element to the scalar field at any near-field point are summed. With reference to Figure 5.3, if the distance between the *n*-th element and the observation point is $\overline{r_n}$, then the *n-th* element's contribution there is simply $e^{j\psi_n(f)} e^{-j\omega\sqrt{\mu_0\varepsilon_0}\, r_n} / r_n$, with $r_n = \left|\overline{r_n}\right|$.

Table 5.1: The investigated reflectarray element types & lattice sizes.

Reflectarray Element Type	Lattice Size
Patch	λ/2 & λ/3
Cross Loop	λ/2
Infinitely Broadband	λ/2

The focal point location versus frequency for all the reflectarrays of Table 5.1 is shown in Figure 5.9. It is evident that the element type or lattice size is not a dominant factor in determining the amount of focal point shift. The focal shift amount is close for all reflectarrays, especially at frequencies not very far from the centre-frequency 30GHz.

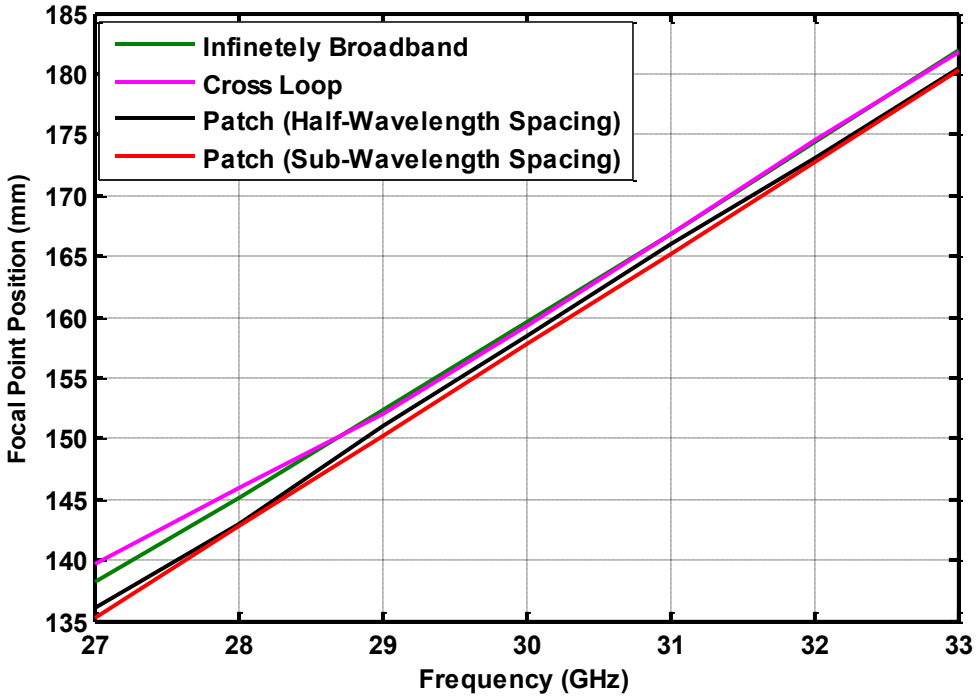

Figure 5.9: Focal point shift versus frequency along Line#1 for reflectarrays of different element type and lattice size.

5.2.5 Fresnel Zone Boundary Considerations

Apart from the non-geometrical factors' impact on the amount of focal shift, it is of note that when the focal length (phase delay paths) of a given reflectarray is changed, the elements' distribution on the new reflectarray surface does change. Regions of big change in element sizes, which highlight the 360 degree phase jumps or so-called "Fresnel zone boundaries", do move on the reflectarray surface when the focal length is changed. An example of such change of Fresnel zone boundary location is depicted in the patch reflectarray layouts shown in Figures 5.10 (a) and (b), designed for two focal lengths 16λ and 24λ, respectively. This change stems from the fact that the phase delay paths change whenever the focal point location is changed. This, in one way or another, relates the focal point shift to Fresnel zone distribution and thus signifies the need to investigate such a relation.

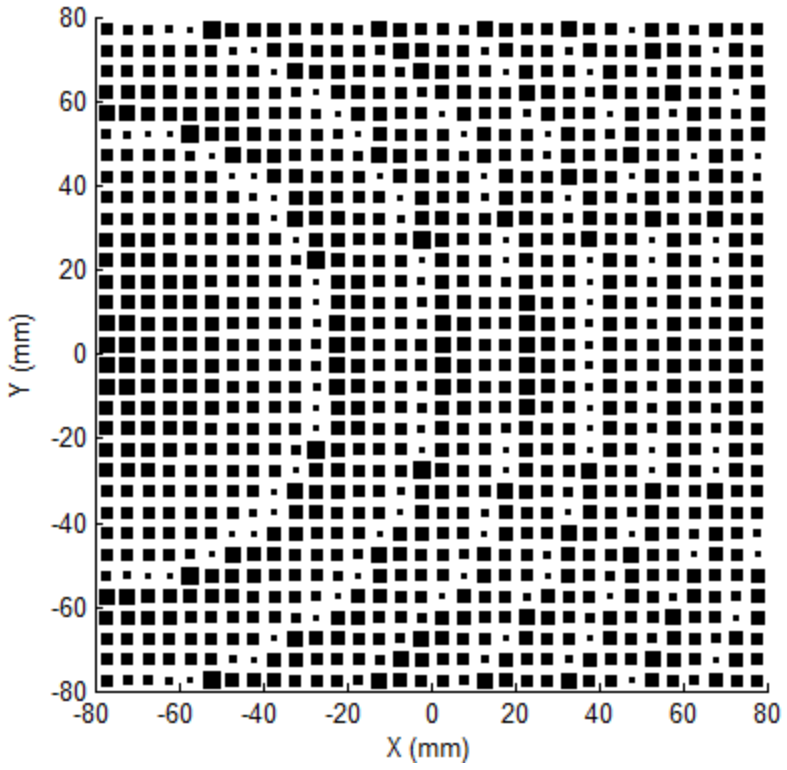

(a)

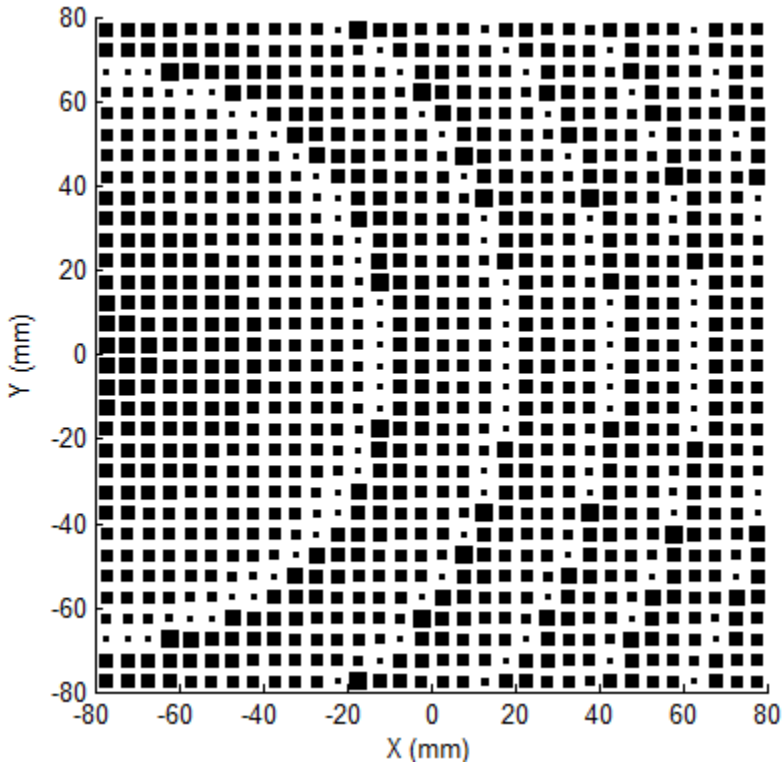

(b)

Figure 5.10: Layouts of a half-wavelength patch reflectarray for a) F=16λ and b) F=24λ, all other design parameters being the same.

The noticeable shift of Fresnel zone distribution with reflectarray focal length change led us to interpret the focal point shift with frequency in terms of the Fresnel zone boundaries. This could further confirm that the focal point shift is caused mainly by geometrical factors. Such an interpretation is included here to show that the focal shift is indeed expected even from basic "optical" type considerations.

With reference to Figure 5.11, the geometrical focal point (P1) is located at $(x = x_{off}, y = y_{off}, z = F)$. In this particular case values $x_{off} = -80\text{mm}$, $y_{off} = 0$ and $F = 160\text{mm}$ have been selected. The distance $R_n = \sqrt{(x_n - x_{off})^2 + (y_n - y_{off})^2 + F^2}$ is that from P1 to the center $(x_n, y_n, 0)$ of the *n-th* reflectarray cell.

An approximate scalar analysis similar to [7] gives the actual phase of the feed field (transmit-mode analysis) at the *n-th* element at any frequency *f* as

$$\phi_n(f) = -A f R_n + \psi_n(f) \tag{5.1}$$

where $A = 2\pi\sqrt{\mu_0 \varepsilon_0}$. In order to obtain a uniform phase over the reflectarray aperture at f_o, and hence a main lobe in the broadside direction, expression (5.1) dictates that the reflection phase of the *n-th* element be $\psi_n(f_o) = A f_o R_n$. This is well-known, but is included here to facilitate the discussion below.

In order to arrive at an approximate expression for the focal shift with frequency we recognize, with reference to Figure 5.12, that the boundary of the first Fresnel zone is defined by [8,Eq.(8)]

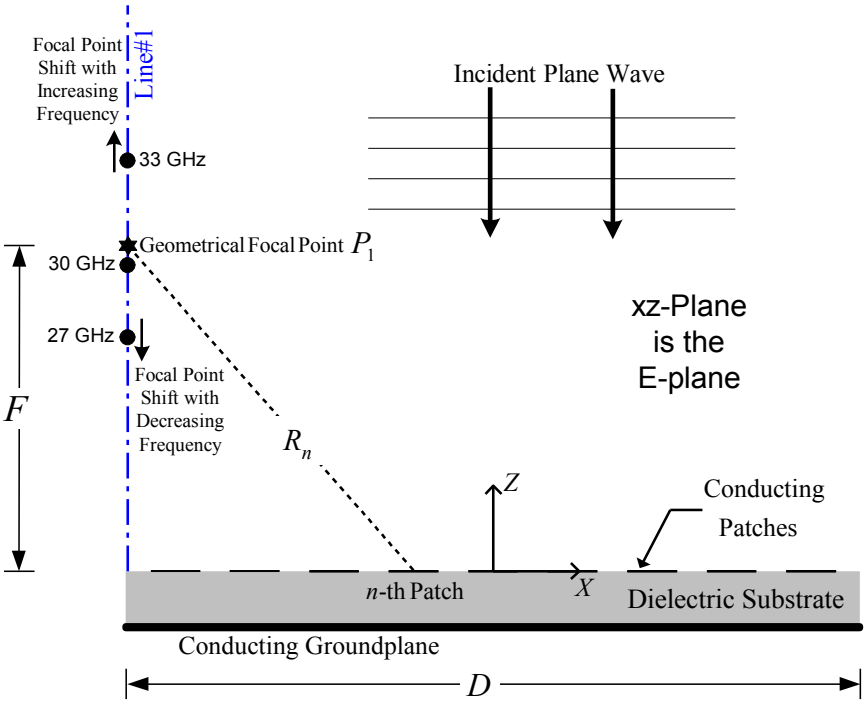

Figure 5.11: Offset-fed reflectarray (with square rim) showing the geometrical focal point P_1 and the focal length F. The coordinate origin is at the center of the reflectarray.

$$\left|P_1P_3\right| - \left|P_1P_2\right| = \sqrt{(x_{fz} - x_{off})^2 + F^2} - F = \frac{c}{f} \tag{5.2}$$

Executing a design at f_o fixes the values of x_{off} and x_{fz} for a given reflectarray. Implicit differentiation of (5.2) with respect to frequency f allows us to write the focal point shift ΔF (along Line#1 in Figure 5.11) from its value at f_o, for a change Δf in the frequency from f_o, as

$$\delta F = \left(\frac{\left|P_1P_3\right|}{\left|P_1P_3\right| - F} \right) \frac{c}{f^2} \Delta f \tag{5.3}$$

Although (5.3) is not a rigorous result, focal point locations predicted using it compare informatively well (in Figure 5.13) to values found from the full-wave modelling discussed before. This further fortifies the results obtained using the full-wave receive-mode analysis in Section 5.2.4.

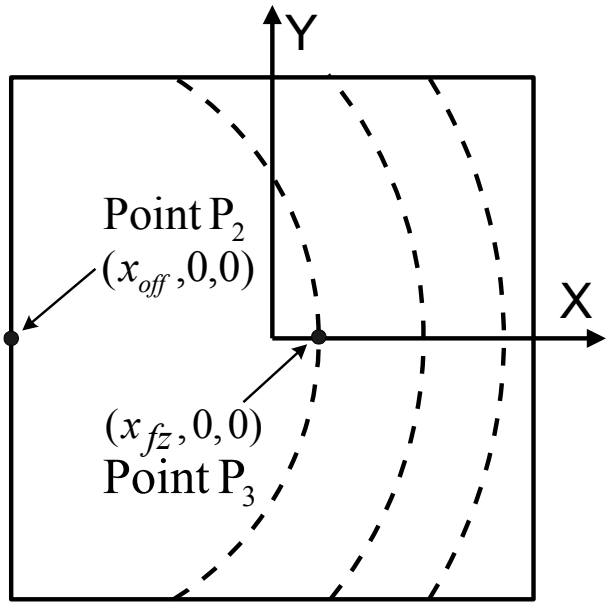

Figure 5.12 Schematic top view of a reflectarray, with dashed lines indicating Fresnel zone boundaries. Point P_1 is shown in Figure 5.11.

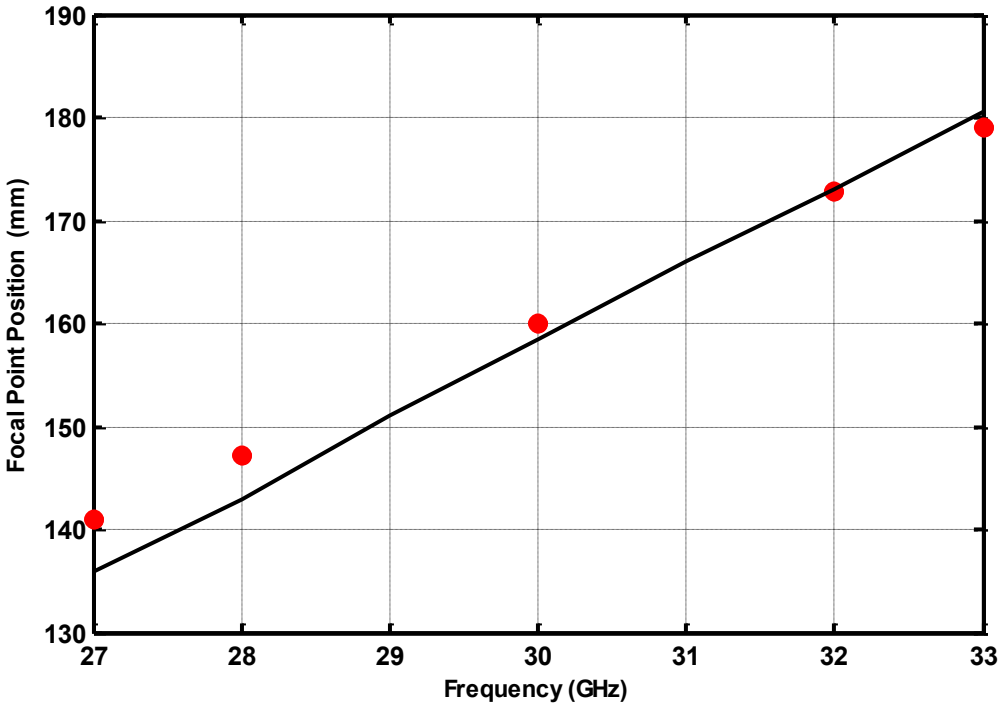

Figure 5.13 Focal point shifts versus frequency obtained using approximate expression (5.3) (•) versus those obtained using full wave modelling for an equivalent half-wavelength patch element reflectarray (—).

5.3 Diagnosis of the Source of Beam Squint in the Radiation Patterns of Offset-fed Reflectarrays

5.3.1 Introduction

Observation of the scattered near-fields will allow us to show that the location of the actual focal point shifts with frequency in a manner that will lead to squinting of the main beam. A full-wave receive-mode and transmit-mode analysis are used to show that it is the shift in the location of the focal point with frequency (caused by non-constant path delays over the surface of the reflectarray) that is principally responsible for the beam squint in offset-fed reflectarray antennas. It is shown that this focal point shift, which implies non-coincidence of the focal point and the feed phase centre at off-centre frequencies, results in a phase distribution over the reflectarray aperture with a slope other than that required to have the main beam in the desired direction. We validate this diagnosis (computationally and experimentally) by showing that if the feed is physically moved to the shifted focal point at some off-centre frequency the main beam pointing direction at this frequency is restored.

5.3.2 Receive-Mode &Transmit-mode Analyses Reconciliation

In Section 5.2.3 it was shown that the focal point of an offset-fed broadside reflectarray shifts from its design position (that is, the center frequency position) at off-centre frequencies. Such shifts were observed to be along a focal line (Line#1 in Figure 5.3) normal to the reflectarray surface. Specific shifts along Line#1, for the same reflectarray illustrated in Section 5.2.3, are given in Table 5.2, which again reveals that even at f_o the focal point is shifted from the nominal focal point (albeit only 0.27λ).

Table 5.2: Specific focal point shifts (along Line#1).

Frequency (GHz)	Focal Point Position z (mm)	Shift from Geometrical Focal Point (mm)
27	**F_2= 136.5**	**-23.5**
30	**F_1= 157.3**	**2.7**
33	**F_3= 180.6**	**20.6**

For further confirmation of the focal point shift trend versus frequency we observed over Line#1, the focal region fields of the offset-fed reflectarray under consideration are calculated at 27GHz, 30GHz and 33GHz over an aperture that cuts through the actual focal point in the y-z plane as shown in Figure 5.14.

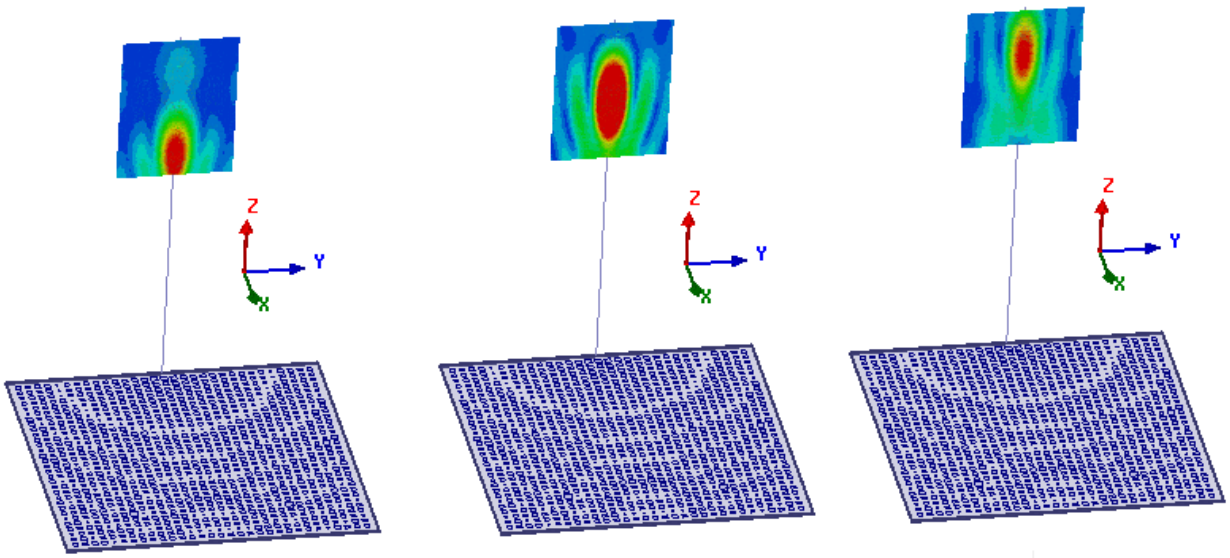

(a) 27GHz **(b) 30GHz** **(c)33GHz**

Figure 5.14: HFSS model output showing the focal region shifts with frequency calculated using the full wave receive-mode analysis . The element layout on the reflectarray surface are shown; the Fresnel zone boundaries are visible.

The reflectarray is next modeled using a transmit-mode analysis, that is, with a pyramidal feed horn (as part of the complete full wave model) illuminating the reflectarray instead of the plane wave used in the receive-mode analysis. The feed phase centre is located at z = F_1= 157.3mm, the actual focal point location determined from the receive-mode analysis, as summarized in Table 5.2. The horn has aperture dimensions 17mm by 22 mm, a flare length of 11.4mm, and an average phase centre located 3.2mm inside the aperture. It is oriented with its beam peak pointed to the centre of the reflectarray as depicted in Figure 5.15.

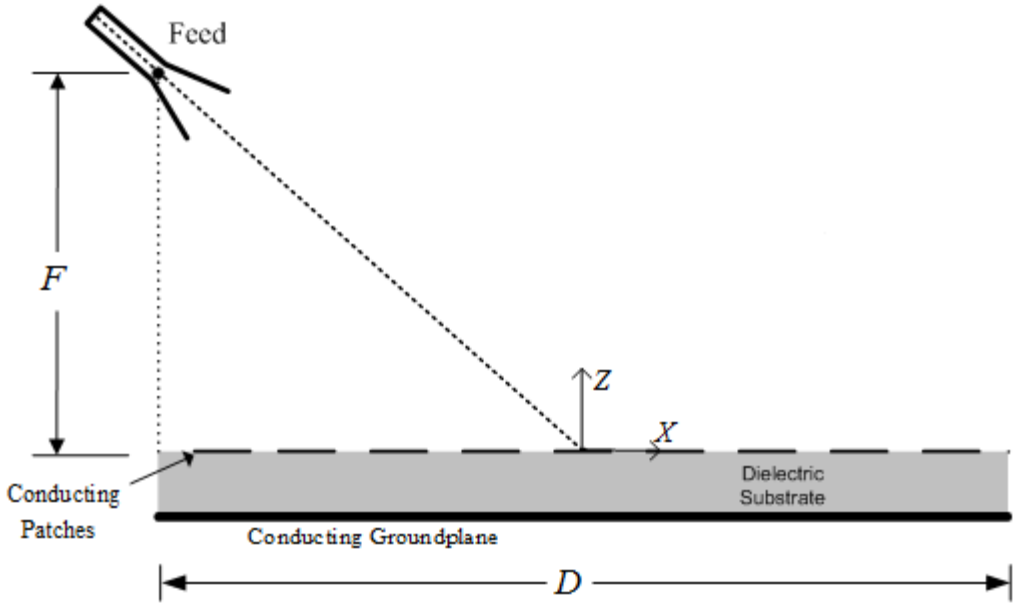

Figure 5.15: Offset-fed reflectarray showing the feed with its beam peak oriented to the centre. The feed is located with its phase centres at the actual focal points z= 157.3mm.

Before proceeding to the full-wave analysis, an approximate scalar analysis using (5.1), and the assumption of infinitely broadband elements defined in part B of Section 5.2.4, gives the phase distribution at points $(x_n, y_n, 0)$ on the reflectarray aperture at any frequency as

$$\phi_n(f) = -A(f - f_o)\sqrt{(x_n - x_{off})^2 + (y_n - y_{off})^2 + F_1^2} \tag{5.4}$$

At any frequency other than f_o the aperture phase distribution (5.4) is not uniform but tilted, causing beam squint. Plots of this phase distribution, along the x-axis, for the example reflectarray under discussion are shown by the solid lines in Figure 5.16. The full-wave model predictions are the rippled dashed lines in Figure 5.16, the ripple being due to the change in the element reflection phases $\psi_n(f)$ with frequency (inherently accounted for by the full-wave model). Full-wave modelling of reflectarrays of other elements reveals that the ripple amplitude is less the more broadband the element. The sloped phase distributions at off-centre frequencies imply scanning (squinting) of the main beam off the designed broadside direction. Even at f_o, if one physically moves the feed away from the geometrical focal point, the phase distribution on the reflectarray becomes sloped (as for solid reflectors).

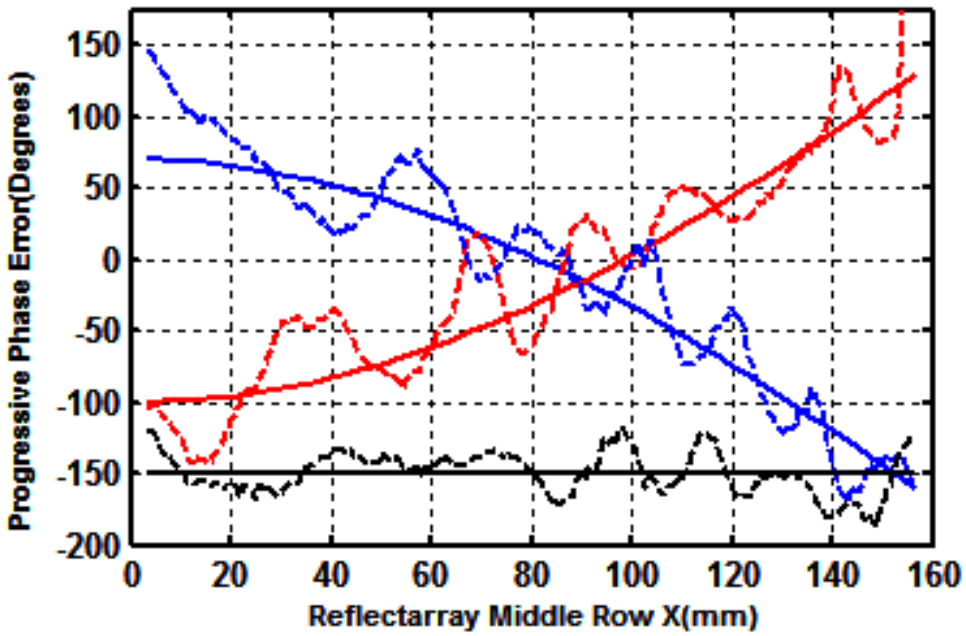

Figure 5.16: The approximately calculated phase distribution of the scattered field along the central row (x-axis in Figure 5.15) on the aperture of the designed reflectarray with infinitely broadband elements at 30GHz(——), 33GHz(——) and 27GHz(——), and the corresponding distributions from the full-wave model at 30GHz (— —), 33GHz (— —) and 27GHz(— —) for patch elements and a $\lambda/3$ lattice. The 30GHz curves are shifted down by 150° for clarity.

If the receive-mode analysis results are reconciled with the actual phase distribution over the reflectarray surface, which is obtained from the same HFSS model but in the transmit-mode, it becomes apparent that the off-centre frequency squinting is due to the focal point shifting away from the feed's physical location; this is made obvious in the next section.

5.3.3 Theoretical and Experimental Confirmation

The far-zone patterns of the offset-fed reflectarray are next examined with the feed at the different locations indicated in Figure 5.17 (and appropriately reoriented). The frequencies indicated in Figure 5.17 denote the fact that locations F_1, F_2 and F_3 are the actual focal point locations at 30GHz, 27GHz and 33GHz, as obtained from Table 5.2. However, with the feed at each of these locations, the radiation patterns will be obtained at all three frequencies. These will be found using the full-wave analysis, and measurements on a fabricated version of the reflectarray under discussion.

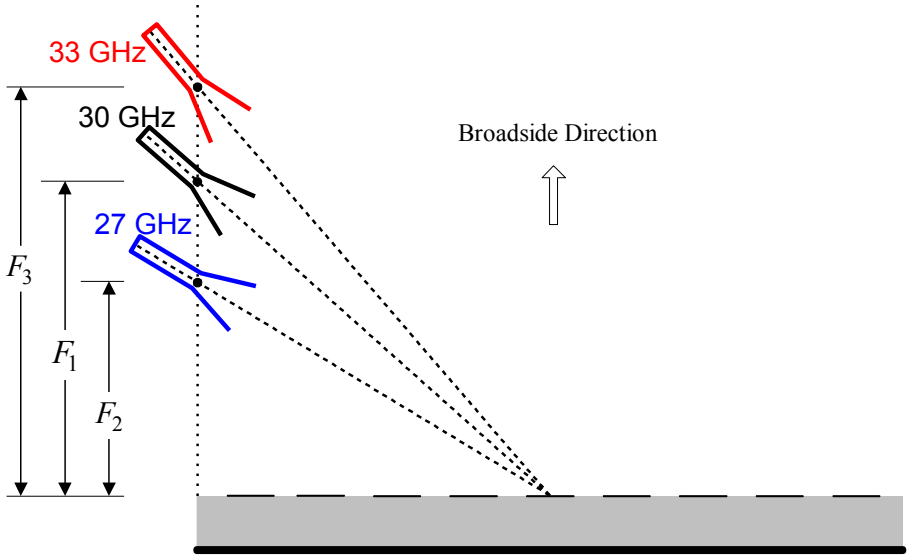

Figure 5.17 The physical movement of the feed horn so that its phase center is coincident with the shifted focal point at the frequencies indicated.

First the feed phase centre was positioned to be coincident with the actual focal point position obtained at the design frequency 30GHz ($z = F_1 = 157.3$mm). The far-zone E-plane patterns are found as shown in Figure 5.18. It is evident that there is no beam squint at 30GHz, as expected from the fact that (as found in Figure 5.16) there is no phase slope at this frequency. Also apparent from Figure 5.18 is the left and right squinting with respect to the broadside direction at 27GHz and 33GHz, respectively. This is compatible with the negative and positive phase slopes at these frequencies shown in Figure 5.16.

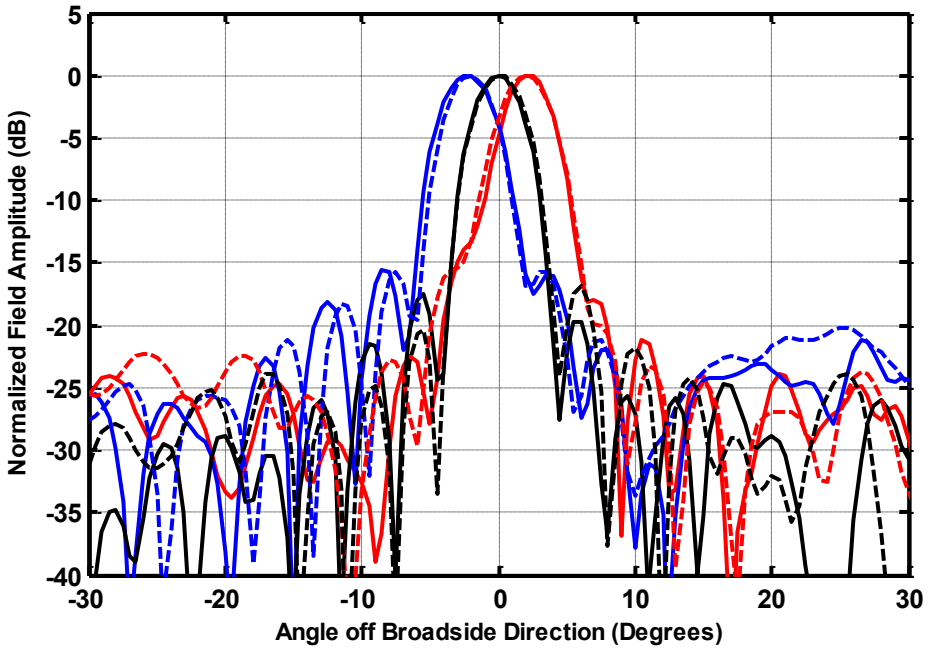

Figure 5.18: E-plane far-zone patterns with the feed phase center at z=F_1=157.3mm. Measured patterns at 30GHz (——), 33GHz(——) and 27GHz(——). Simulated patterns at 30GHz (— —), 33GHz(— —) and 27GHz(— —).

Next the feed is moved to the position of the focal point at 27GHz (z = F_2 = 136.5mm). The pattern (in Figure 5.19) at the three selected frequencies with the feed at this location shows no squint at 27GHz, due to the fact that the feed phase centre is at the true focal point of the reflectarray at this frequency. However, there is now squint at 30GHz and 33GHz, but towards the right in both cases. Once again, the reason is clear from the phase distribution plots in Figure 5.20. The slope has the same sign at 30GHz and 33GHz, but is steeper at 33GHz, and so the extent of the squint is larger there.

The feed was then moved to the predicted focal point at 33GHz (z = F_3 = 180.6mm). There is no surprise that there was then no squint at 33 GHz, whereas the squinting at 27GHz and 30GHz is to the left (opposite to that in Figure 5.19) since their phase distributions have positive slopes (opposite to that in Figure 5.20).

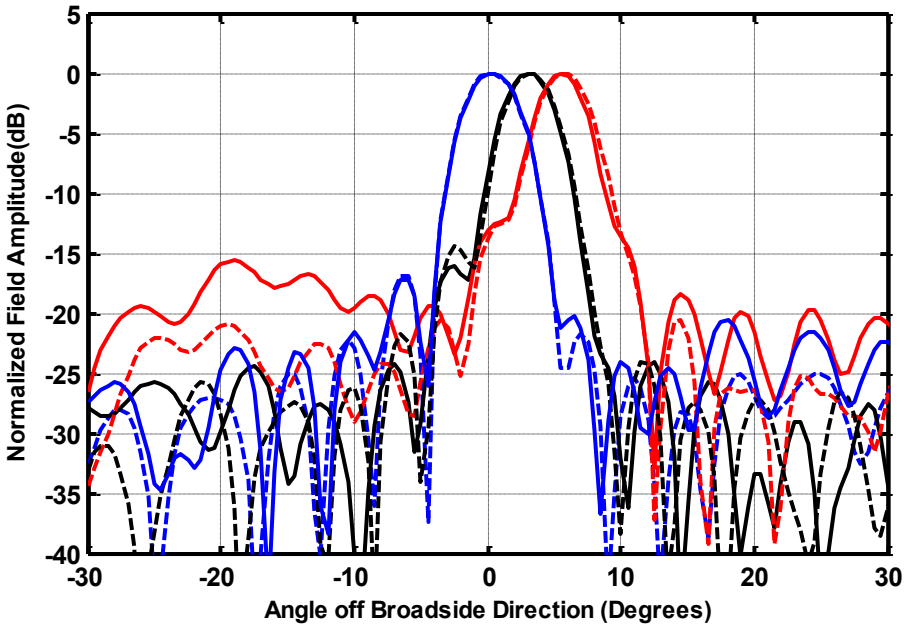

Figure 5.19: E-plane far-zone patterns with the feed phase center located at z=F_2=136.5mm. Measured patterns 30GHz (——), 33GHz(——), 27GHz(——). Simulated patterns at 30GHz (— —), 33GHz(— —), 27GHz(— —).

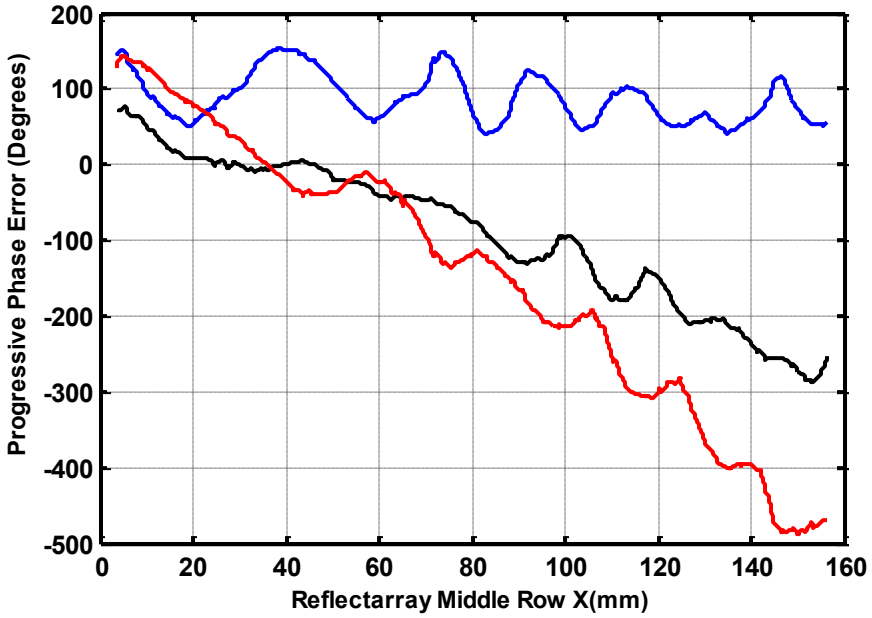

Figure 5.20: The actual phase distribution along the central row (x-axis) of the designed reflectarray at 30GHz (——), 33GHz(——) and 27GHz(——),extracted from the full-wave model. The feed horn phase center is located at z=F_2=136.5mm to coincide with the predicted focal point position at 27GHz.

Finally, Figure 5.21 reveals the beam squint for two completely different element types, whose measured radiation patterns are compared. It is evident that we have almost the same beam squint at off-centre frequencies irrespective of the reflectarray element type used. This result, along with what we observed in Section 5.2.4, emphasizes the smaller influence of the element type compared to the spatial path delay as far as beam squint is concerned.

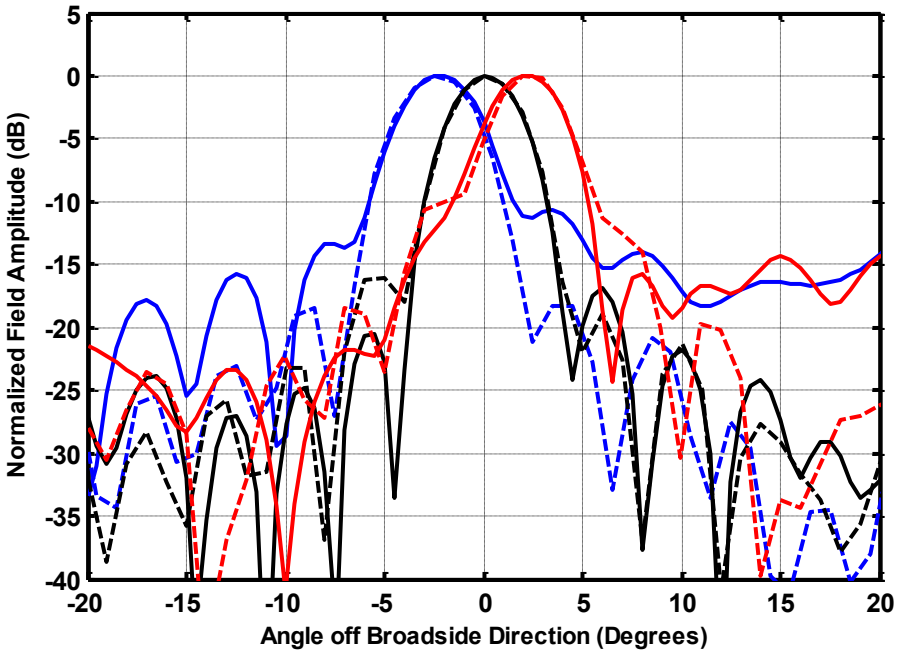

Figure 5.21: Measured E-plane far-zone patterns (revealing the beam squint) with the feed phase centre located at z = F_1 for the reflectarray ($\lambda/3$ lattice) with patch elements (solid lines) and cross ring elements ($\lambda/2$ lattice) (dashed lines) at 30GHz (black), 33GHz (red) and 27GHz (blue).

Figure 5.21 reveals the fact that beam squint is insensitive to the type of element or reflectarray lattice size used. Beam squint is indeed a geometry-dependent differential spatial phase delay issue caused by shifting of the focal point.

5.4 Two-Feed Single-Beam Reflectarray

5.4.1 Introduction

The reconciliation of the full-wave receive-mode and transmit-mode analysis, which was discussed in Section 5.3.2, revealed that the shift in the location of the actual focal point with frequency causes beam squint in offset-fed single-beam single-feed reflectarrays. We used this knowledge to propose and demonstrate a solution to suppress beam squint in offset-fed reflectarrays. It consists of a reflectarray with a single beam but two feeds, located at opposite ends of the reflectarray as shown in Figure 5.22. The proposed solution is focal point-based in the sense that the use of two feeds dictates the presence of two focal points whose shifts with frequency will be shown in Section 5.5 to cancel out any aperture phase tilt on the reflectarray surface, and consequently suppress the unwanted beam squint. Before introducing the two-feed reflectarray as a means to supress beam squint in offset-fed reflectarrays, we aim to improve its design technique and performance as compared to what was reported in [9] for power combining purpose. Thus a simpler way of applying the basic design equation is described, as well as a means to improve two-feed reflectarray performance is discussed in Sections 5.4.2 and 5.4.3, respectively.

5.4.2 Two-feed Single-Beam Reflectarray Elements Phase Realization

In Section 2.2.3 we stated that the idea of a multi-feed single-beam reflectarray was first proposed in [9]. It was developed to simultaneously function as an antenna and spatial power combiner. We here consider the design of two-feed single-beam reflectarrays for the purpose of removing beam squint, which had not been considered in [9]. The design procedure for the above mentioned two-feed single-beam reflectarray was also described in Section 2.2.3. This procedure dictates the use of an optimizing routine [9] in order to obtain ψ_n values that satisfy the required field phase $\angle E_T$ in equation (2.5). The phase realization procedure we used to achieve this goal is simpler and more accurate as no optimization is required; we wish to have a uniform phase distribution over the aperture of the reflectarray, and so at each element we require the phase of the scattered field to be zero. Thus, with reference to Figure 5.22, for each element (i.e. for each

n) we simply need to find the value of the reflection phase ψ_n required to achieve this goal. We can write the total feed field at the *n-th* element as

$$E^{\text{Feed}}(x_n, y_n, 0) = \left|E^{\text{Feed}}(x_n, y_n, 0)\right| e^{-j\phi_{\text{Feed}}(x_n, y_n, 0)} \tag{5.5}$$

where $(x_n, y_n, 0)$ is the centre of the *n-th* element, and then select $\psi_n = \phi_{\text{Feed}}(x_n, y_n, 0)$ for each *n*. Once these required values of ψ_n have been determined for each element, the appropriate database ("S-curve") is used [7] to determine the dimensions of each element in the reflectarray.

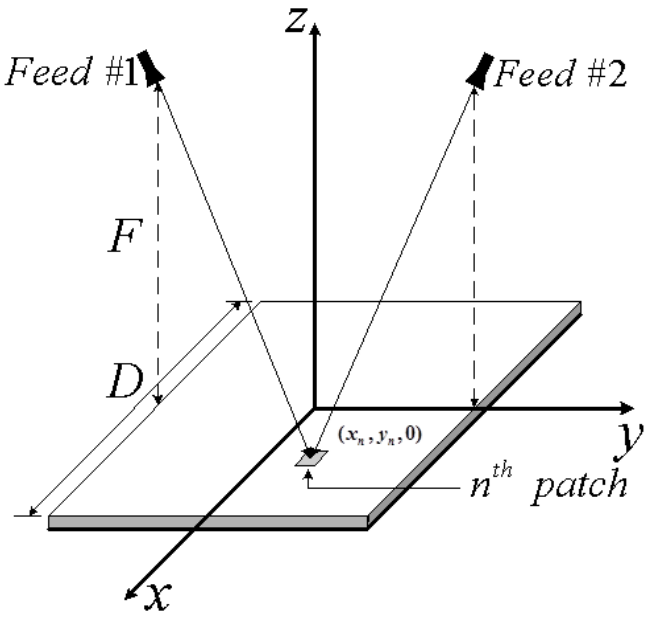

Figure 5.22: The two-feed reflectarray geometry showing the two feeds and the nth patch coordinate.

5.4.3 Improving Two-feed Reflectarray Gain and Bandwidth Using Sub-Wavelength Configuration

A) Preliminary Remarks

No information was given in [9] about the performance of the two-feed configuration at off-centre frequencies, since the work was mainly directed toward establishing and validating the design procedure for the use of multi-feed single-beam reflectarrays as spatial power combiners.

Therefore, we have conducted a full-wave analysis (using FEBI version of HFSS [5]) of the configuration given in [9], and found that its gain, and consequently its power combining efficiency, degrade even at nearby off-centre frequencies. Thus, it was crucial to find a remedy for this problem aspect of two-feed reflectarrays before delving into using it as a means to suppress beam squint. This has been achieved by designing the two-feed reflectarray using a sub-wavelength lattice of $\lambda/3$ spacing rather than the half-wavelength spacing used in [9].

B) Sub-Wavelength versus Half-Wavelength Two–feed Reflectarray

As discussed in Section 2.3, single-feed sub-wavelength reflectarrays have been the subject of intense research recently due to several advantages. Conventional single–feed single-beam reflectarrays which are designed using sub-wavelength elements exhibit improved gain-bandwidth performance compared to their equivalent half-wavelength reflectarrays [10, 11]. This attracted the attention of the author of this dissertation to use sub-wavelength spacing in designing two-feed single-beam reflectarrays to troubleshoot the bandwidth limitation problem mentioned in Part A of the present section.

Although different causes contribute to the improved performance of sub-wavelength elements (like the low quantization error and strong element coupling which were described in Section 2.3), we believe that the low dispersive nature of these elements contributes strongly to their outstanding performance at off-centre frequencies. It was demonstrated in [12] for a loop element that a smaller rate of change of element reflection phase with frequency (that is, smaller $\delta\psi_n/\delta f$) occurs when such an element is incorporated in a sub-wavelength lattice rather than a half-wavelength one. Similar results (not given in [12]) for the rectangular patch elements of interest here are shown in Figure 5.23 for both the sub-wavelength and half-wavelength cases. The details of why quantity $\delta\psi_n/\delta f$ is important were not provided in [12], and so are briefly discussed here. The reflection phases ψ_n are obtained using the infinitely periodic environment simulation in HFSS [5], as is usually done when setting up a design database. The element lengths (L) for both the sub- and half-wavelength cases are selected so that their resonance (where ψ_n = 0°) falls approximately at the design frequency of 30 GHz. This turns out to be $L = 2.23mm$ for the sub-wavelength rectangular patch ($\lambda/3$ = 3mm cell size) and $L = 2.5mm$ for

the resonant rectangular patch ($\lambda/2$ = 5mm cell size). The ψ_n versus frequency data are computed for these specific elements, the $\delta\psi_n/\delta f$ determined numerically, and Figure 5.23 obtained. This figure reveals the much larger values of $\delta\psi_n/\delta f$ obtained for the half-wavelength case than the sub-wavelength one. This fact is important for the following reasons. The reflection phase curves for the elements in question are shown in Figures 5.24(a) and (b) for the two lattice sizes, at three different frequencies. If these curves were all straight lines then the change in ψ_n with frequency would be the same for all elements and the value of $\delta\psi_n/\delta f$ would be immaterial. But it is clear from Figure 5.24 that these curves are not straight but S-shaped (hence their name). Thus elements that have smaller values of $\delta\psi_n/\delta f$ will result in substantially smaller phase errors over the reflectarray aperture at off-centre frequencies. A significant improvement of the reflectarray gain, bandwidth and consequently its power combining performance is thus expected when sub-wavelength elements are used instead of their half-wavelength counterparts, as will next be demonstrated.

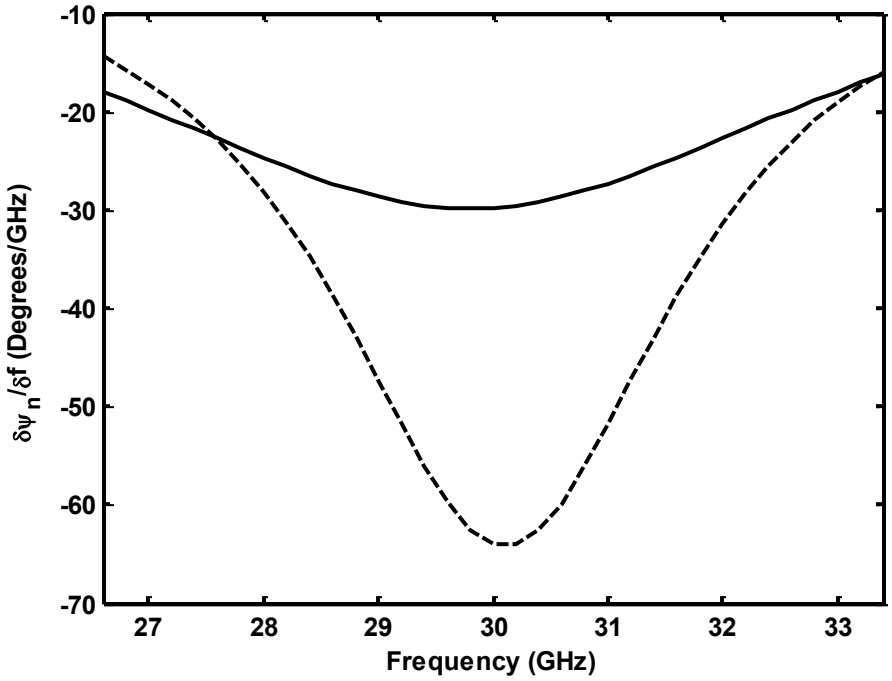

Figure 5.23: Plot of rate of change of element reflection phase with frequency ($\delta\psi_n/\delta f$) for rectangular elements of lattice size $\lambda/2$ (- - - -) and $\lambda/3$ (——).

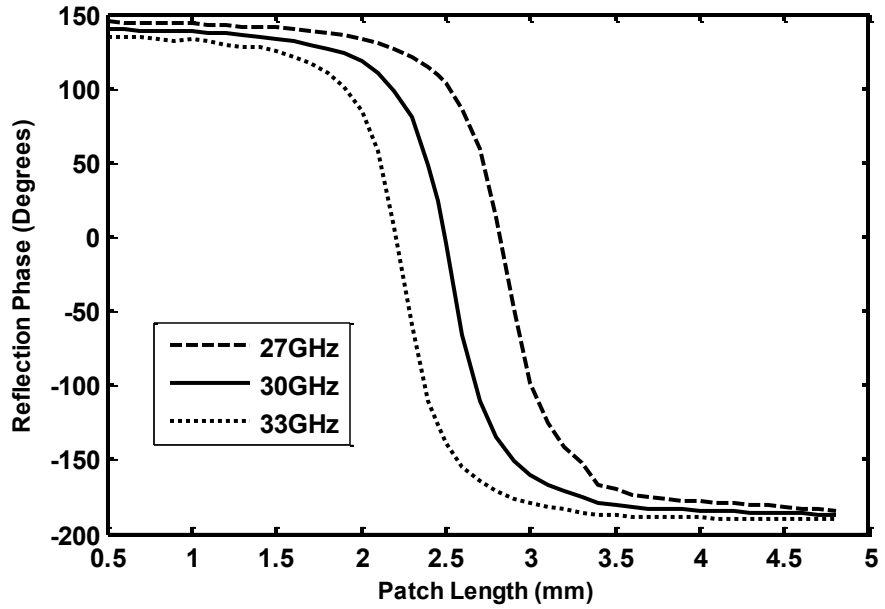

(a)

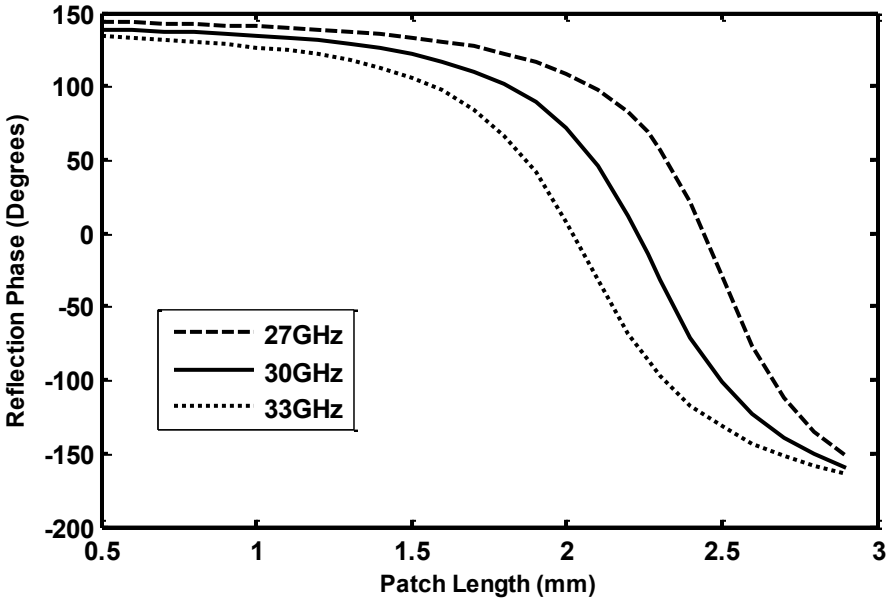

(b)

Figure 5.24: Element reflection phase (ψ_n) versus patch length (L) at different frequencies for the (a) λ/2 and (b) λ/3 lattice. Fixed width is W = 2.5mm.

C) Experimental Verification of the Proposed Designs

Using the design procedure for multi-feed single-beam reflectarrays described in Section 5.4.2, two reflectarrays of the same aperture size, feed location and focal length, but different inter-element spacings, were designed. The elements in both reflectarrays are rectangular patches of fixed width W = 2.5mm printed on a single-layer 0.508mm thick Rogers 3003 substrate with $\varepsilon_r = 3$. Note that this is different from the width (3 mm) used in [9]; this is necessary for the elements of the same width to be able to fit in both a $\lambda/3$ and $\lambda/2$ lattice. The individual patch lengths in the sub-wavelength and half-wavelength designs are of course selected so that each element has the reflection phase (say ψ_n for the *nth* element) required to generate a main beam in the broadside direction when simultaneously illuminated by the two feeds as depicted in Figure 5.22. The resulting sub-wavelength reflectarray has 2704 elements, whereas the half-wavelength one is comprised of 961 elements. In both cases the reflectarray aperture size is 155mm x 155mm, the design frequency 30 GHz, and the feeds positioned such that their phase centres are located at coordinates (0,-77.5,155) mm and (0,77.5,155) mm, so that F=155mm (and hence $F/D = 1$).

Next the sub-wavelength and the half-wavelength reflectarrays were fabricated. Close up views of selected regions of the two fabricated reflectarrays are shown in Figure 5.25. The measured gain versus frequency for both of the two-feed reflectarrays is that in Figure 5.26, and shows a significant gain improvement at all frequencies in the sub-wavelength case. In the case of conventional single-feed single-beam reflectarrays the use of a sub-wavelength lattice provides a wider 1dB-gain-bandwidth but generally not a higher gain [13]. In the two-feed single-beam design constituting the reflectarray power combiner under discussion the sub-wavelength case clearly affords both a higher gain, and a larger 1dB-gain-bandwidth, than the half-wavelength case (11.1% compared to 5.7%). The aperture efficiency, which was calculated for the maximum measured gain values, was consequently improved by using sub-wavelength element (40% was achieved for the sub-wavelength case compared to 29% for the half-wavelength case). In addition to the impact of the $\delta\psi_n/\delta f$ factor discussed earlier, it is deemed that the higher gain of the sub-wavelength combiner also stems from the capability of its elements to better resolve the rather high number of phase jumps extant on the two-feed

reflectarray surfaces compared to that on single-feed reflectarray designs. The larger lattice size of the half-wavelength two-feed reflectarray prevents it from capturing the fine detail of the phase reversal in those specific regions of its surface.

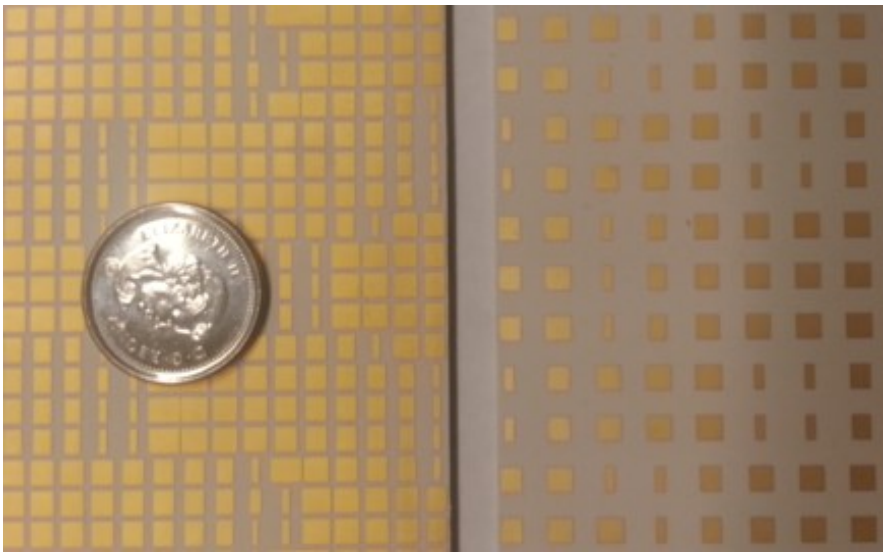

Figure 5.25: Close-up of portions of the sub-wavelength (left) and half-wavelength (right) reflectarrays. A Canadian 10¢ coin is shown as a size reference.

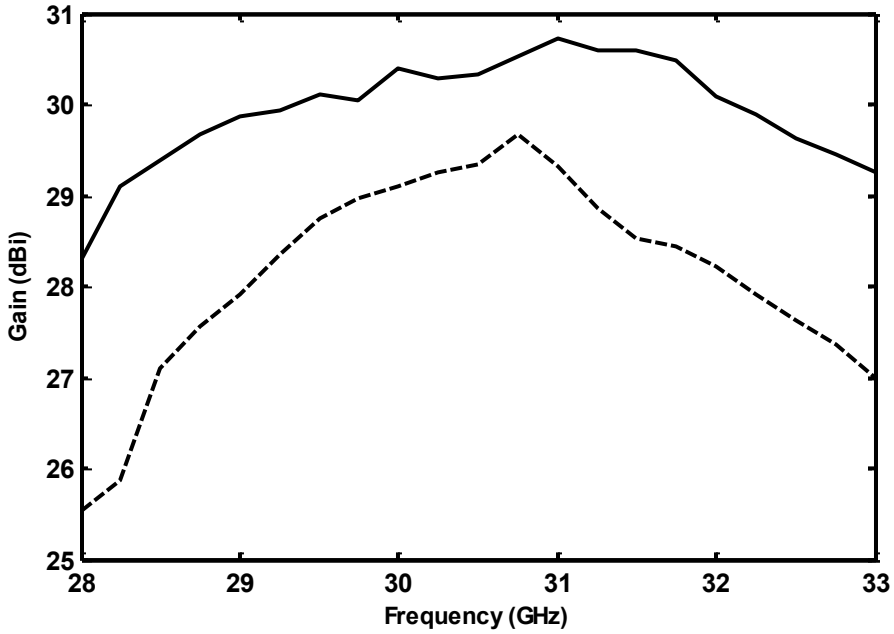

Figure 5.26: Measured gain versus frequency for sub-wavelength (——) and half-wavelength (— — —) reflectarrays.

The power combining efficiency of a given reflectarray combiner is defined as the ratio of the gain when the two-feed design is used to that when a single-feed design is used, for the same aperture physical area. The gains used in the above ratio must each be separately corrected for losses in the feed circuitry needed in the two-feed and single-feed designs. The feed circuitry would be the same for the sub- and half-wavelength two-feed designs just discussed, and so the multiplicative correction factor would in turn be the same. Thus the relative value of the power combining efficiency of the sub-wavelength two-feed reflectarray to that of the half-wavelength case is simply the ratio of their measured gains, since the feed circuitry loss factors will cancel out. This relative measure is shown in Figure 5.27. We note that the measured gain of the present half-wavelength reflectarray and that in [9] differs by less than 0.3dB, and so conclusions on the superiority of the sub-wavelength reflectarray are the same if its performance is compared to the half-wavelength reflectarray combiner in [9].

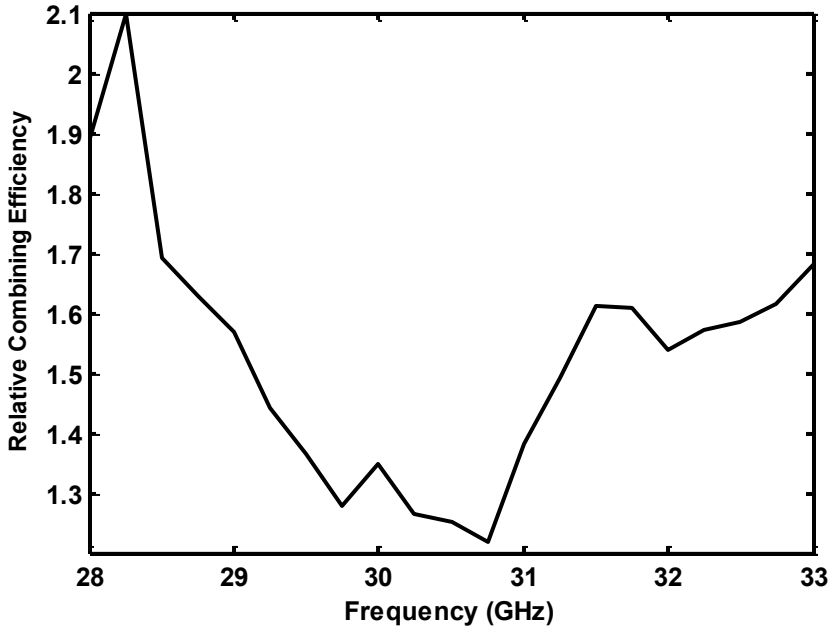

Figure 5.27: Power combining efficiency of the sub-wavelength reflectarray relative to that of the half-wavelength reflectarray.

5.5 Beam Squint Suppression in Offset-Fed Reflectarrays

5.5.1 The Use of Two-feed Reflectarray to Suppress Beam Squint

Although the procedure illustrated in Section 5.4.2 is able to accommodate various sets of feed locations we specifically use the two-feed configuration shown in Figure 5.22, which has the feeds at opposite ends of the reflectarray, in the plane of offset (the yz-plane), for reasons that will shortly be apparent. For the purpose of using the two-feed reflectarray to suppress beam squint, we use the improved sub-wavelength two-feed reflectarray illustrated in Section 5.4.3. With reference to Figure 5.28, P_1 and P_2 are the geometrical focal points of the reflectarray with their coordinates are $(-x_{off}, 0, F)$ and $(x_{off}, 0, F)$, respectively where $x_{off} = 77.5\text{mm}$ and $F = 155\text{mm}$. The resulting element layout for this two-feed single-beam reflectarray design is shown in Figure 5.29; it is clearly different from that of conventional offset-fed single-feed single-beam designs such as theses in Figure 5.10 for example. Noticeable is the fact that the element layout has quadrantal symmetry, in spite of the fact that each of the feeds is offset. Such layout symmetry is reminiscent of an on-axis fed reflectarray, which we know does not exhibit beam squint with changes in frequency. The reason for this symmetry can be seen from Figure 5.28, remembering that identical feeds are placed at P1 and P2. The field incident on the *n-th* patch is the superposition of that from each of the two identical feeds, each of the feed fields having a phase dependent on the distances R_{n1} and R_{n2}, respectively. There will be a corresponding patch (say the *m-th* patch) on the opposite side of the reflectarray for which $R_{m1} = R_{n1}$ and $R_{m2} = R_{n2}$. Because the feeds are identical and are at like locations with respect to the reflectarray, the resultant incident feed field at the *m-th* patch will have the same phase as that at the *n-th* element. Thus the above mentioned *m-th* and *n-th* elements will have the same size. Continuing this argument would reveal that the resultant incident field is quadrantally symmetric, which results in the quadrantally symmetric element layout.

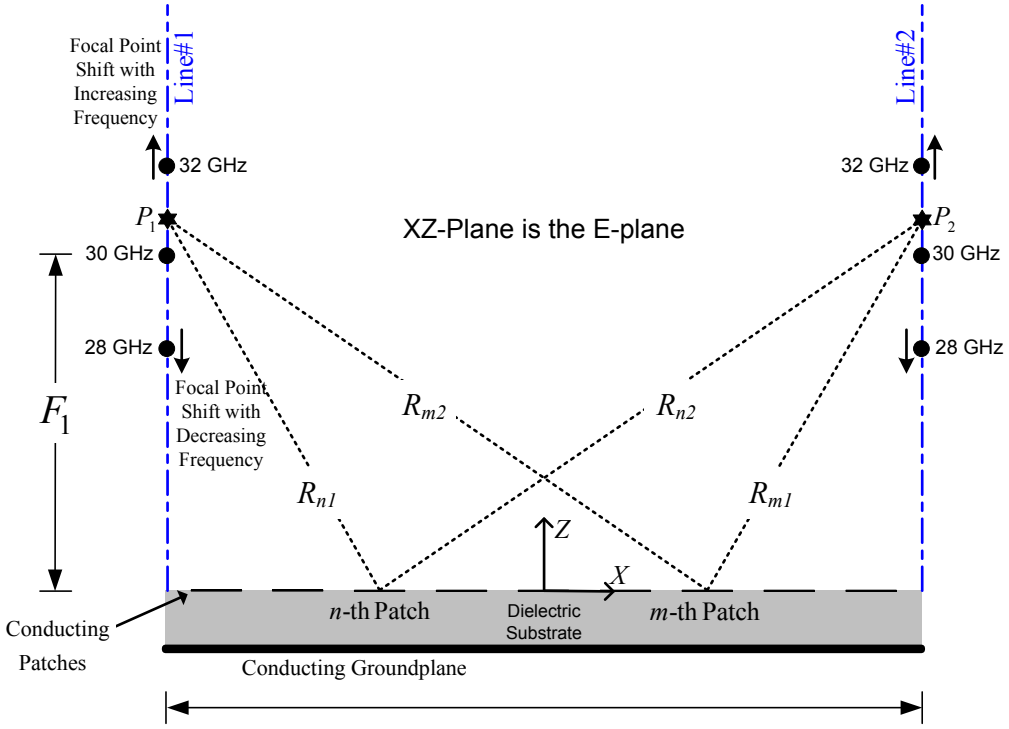

Figure 5.28: Goemtry of the offset-fed reflectarray (with square rim). The coordinate origin is at the centre of the reflectarray. The shift of the focal points with freqency is shown exagerrated.

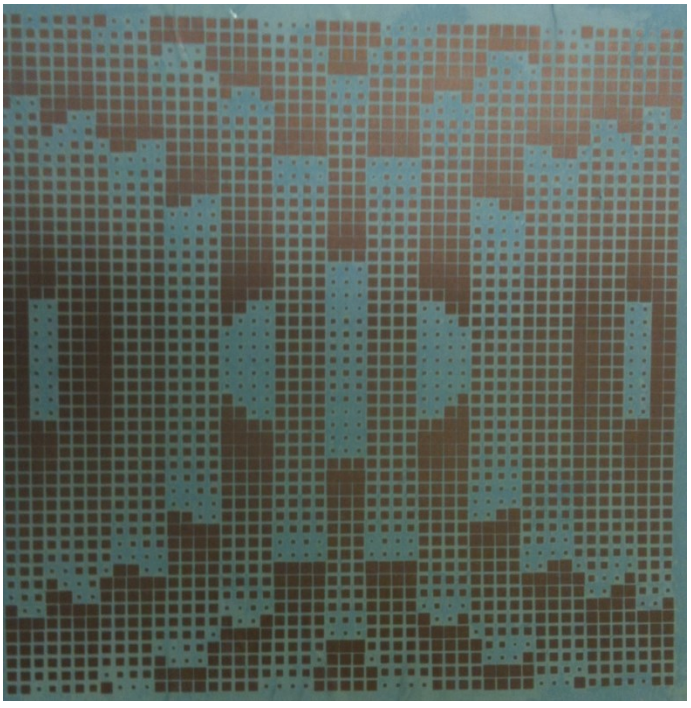

Figure 5.29: Photo of the layout of the fabricated two-feed single-beam reflectarray.

At off-centre frequencies the resultant incident feed field at each element will retain the above symmetry. At such frequencies the element reflection phase will no longer precisely correct for the phase of the resultant incident feed field. However, since the element layout has quadrantal symmetry, although the phase distribution over the reflectarray surface will thus not be uniform (we will see what it actually is in Section 5.5.2) it will be symmetrical and not have any net tilt. Thus we conjecture that there will be no frequency dependent beam squint. Sections 5.5.2 and 5.5.3 demonstrate that this is so using simulation and measurement, respectively.

5.5.2 Full - Wave Analysis of the Two-Feed Reflectarray

We first perform a full-wave receive-mode analysis of the reflectarray in Figure 5.29, with a plane wave incident from the broadside direction (the main beam direction) and the feeds absent, to calculate the scattered electric field in the region of the geometrical focal points. The outcome is shown at three different frequencies in Figure 5.30. These focal region fields reveal that, as expected, the two-feed single-beam reflectarray has identical focal regions on opposite sides of the reflectarray. Furthermore, as the frequency is changed the maximum field locations (the actual focal points) shift vertically within the focal regions. The two focal points move in unison towards (away from) the reflectarray surface as the frequency decreases below (increases above) f_o.

Specific shifts along Line#1 and Line#2 are given in Table 5.3, and shown in Figure 5.31. These reveal that the amount of shift at 28GHz is larger than the shift at 32GHz, and that even at the centre frequency the actual focal point is slightly shifted from the geometrical focal point location by about 0.22λ (as similarly observed in the single-feed case in Section 5.2.3). We use these facts for explanation purposes in discussing the transmit-mode results of the two-feed reflectarray under consideration.

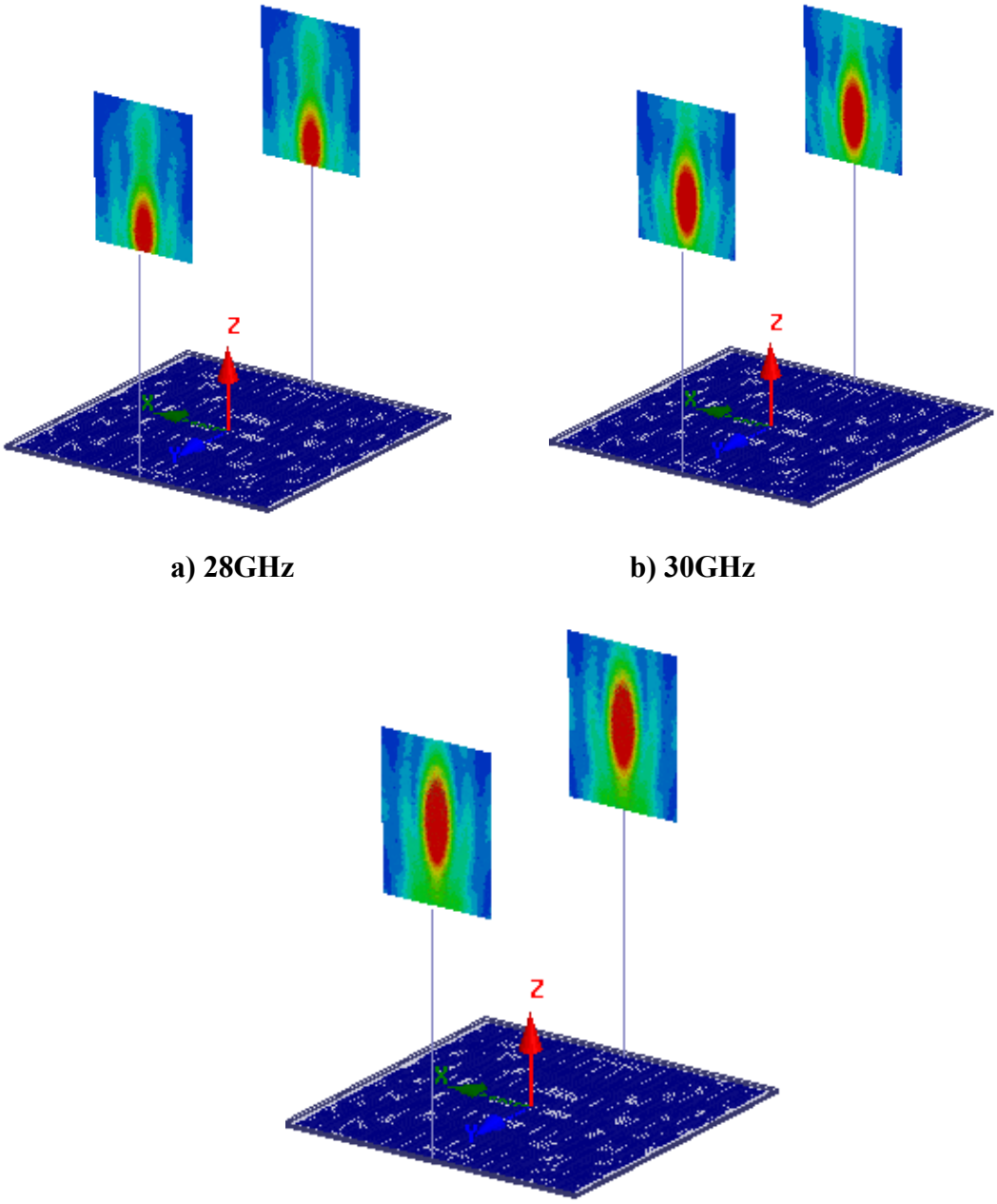

a) 28GHz **b) 30GHz**

c) 32GHz

Figure 5.30: HFSS model output showing the focal region shifts with frequency calculated using the full-wave receive-mode analysis .

Table 5.3: Focal point shift along Line#1&Line#2.

Frequency (GHz)	Focal Point Position z (mm) – Full Wave Model	Shift from Geometrical Focal Point (mm) - Using Full-Wave Model
28	F2 = 134.1	– 18.7
30	F1 = 152.8	2.2
32	F3 = 168.5	15.7

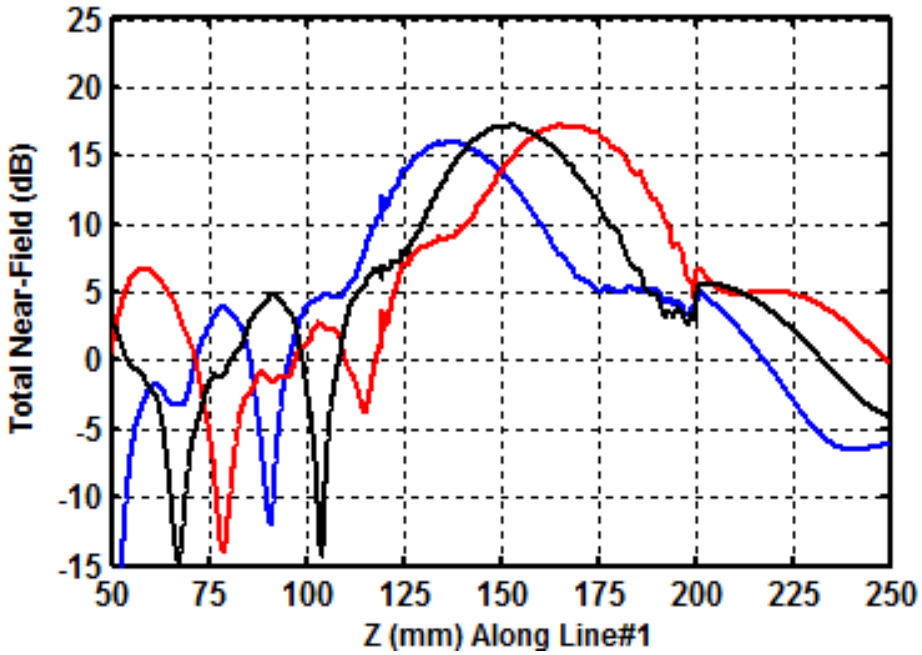

Figure 5.31: Focal field region shift with frequency along Line#1 at 30GHz (——), 32GHz (——) and 28GHz (——).

Next a transmit-mode analysis is carried out with the reflectarray illuminated by two pyramidal horn feeds (which form an integral part of the complete HFSS full wave model), as indicated in Figure 5.32. The feeds are located with their phase centres positioned at $z = F_1 = 0.22\lambda = 152.8$mm (location of the actual focal points obtained from receive-mode analysis at 30GHz, rather than the geometrical focal points at $z = F = 155$mm), with their beam peaks pointed to the centre of the reflectarray.

The horns are identical, with aperture dimensions 17mm by 22 mm, a flare length of 11.4mm, and an average phase centre located 3.2mm inside the aperture. The full-wave simulated far-field patterns under these conditions are shown in Figure 5.33. It is evident that there is no squinting of the patterns at the off-centre frequencies 28GHz and 32GHz. Plots of the phase distribution of the scattered field on the reflectarray surface along its central row (x-axis in Figure 5.32) are shown in Figure 5.34. Although the phase distributions have ripples, they do not exhibit any net tilt over the reflectarray surface. This in effect happens because of the simultaneous migration of the two focal points observed in Figure 5.30.

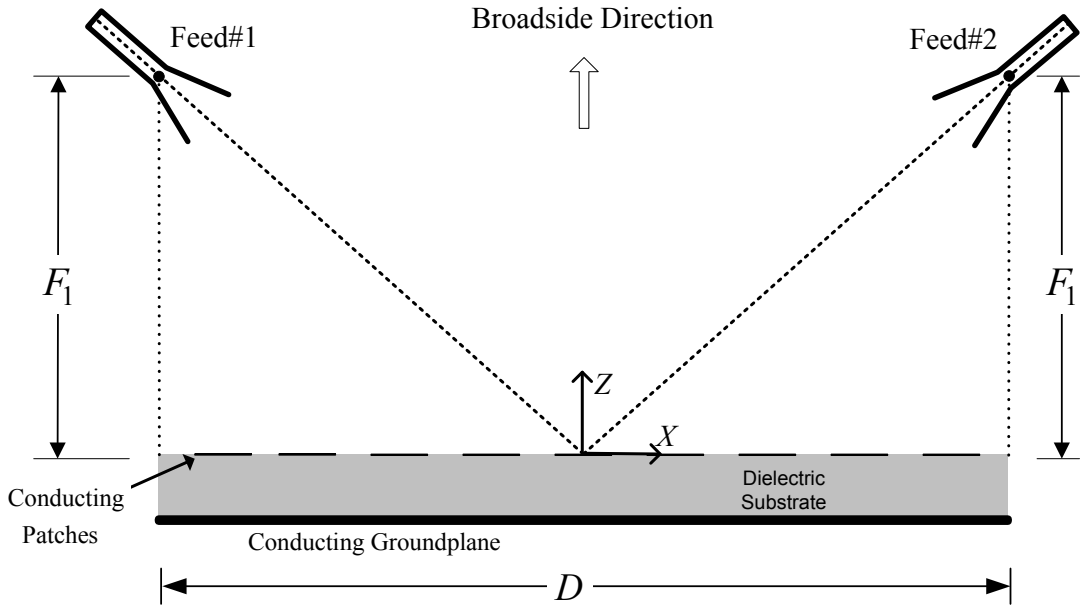

Figure 5.32: Offset-fed reflectarray showing two feeds with their beam peaks oriented to the centre. Both feeds are located with their phase centres at the actual focal points z= 152.8mm.

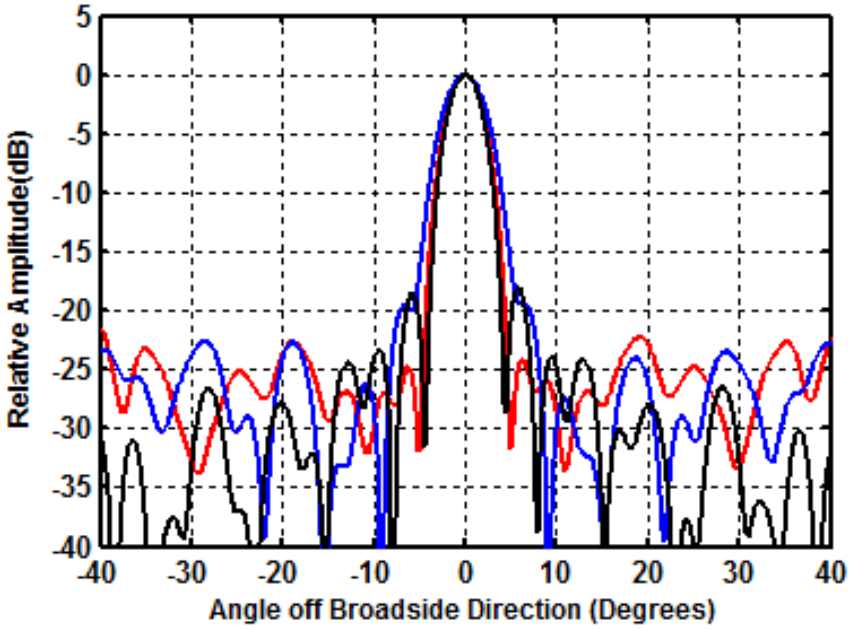

Figure 5.33: E-plane far-zone simulated patterns of the two-feed single-beam reflectarray with the two feed phase centres at z=F_1=152.8m, at 30GHz (——), 32GHz(——) and 28GHz(——). Both feeds are excited.

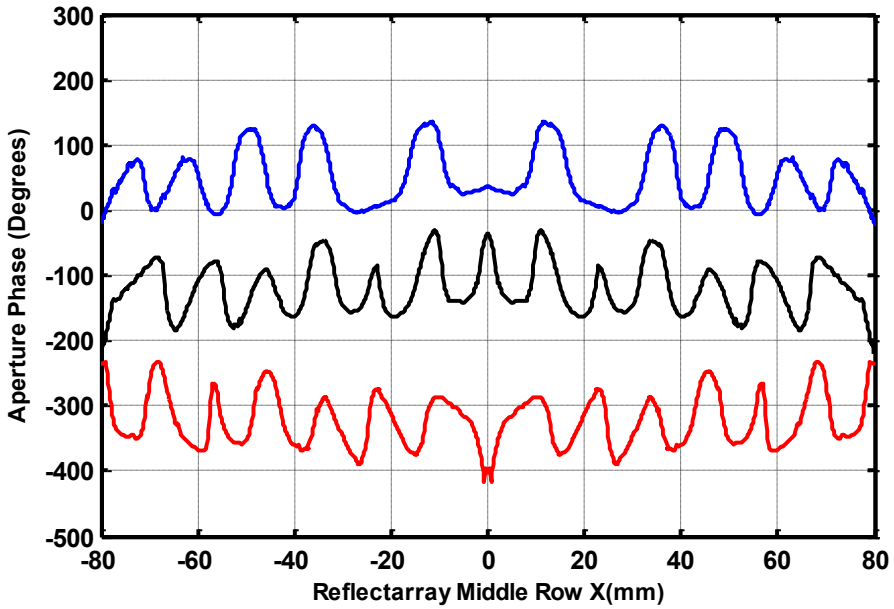

Figure 5.34: The full-wave computed phase distributions of the scattered field along the central row (x-axis in Figure 5.32) of the two-feed single-beam reflectarray at 30GHz (——), 32GHz (——) and 28GHz (——). Both feeds are excited.

When the frequency moves off 30GHz, the focal point shift causes each feed to effectively become displaced from the true focal point by the same amount. This ensures that each feed will cause the same tilt (in the plane of offset) in the scattered field phase over the reflectarray aperture, but with slopes of opposite sign that cause the resultant phase to be symmetrical (albeit not uniform). This is the reason for the suppression of the beam squinting. The peak-to-peak ripple is larger than those reported in Figure 5.16 for a single-feed single-beam reflectarray of almost the same size, element type, feed type, and F/D ratio. This obviously reduces the aperture efficiency, but the reduction in gain of the two-feed single-beam reflectarray at off-centre frequencies (in the broadside mechanical pointing direction) is smaller than when the main beam becomes squinted in the single-feed single-beam case, as will be next argued.

The gain in the mechanical pointing direction of the two-feed reflectarray at centre-frequency is 0.5dB lower than that of the single-feed reflectarray of the same size. However, the gain of the two-feed reflectarray in the mechanical pointing direction is 0.4dB higher than that of the single-feed case at off-centre frequencies 28GHz and 32GHz. In the case of reflectarrays larger than the 15.5λ by 15.5λ ones considered here, the gain advantage of the two-feed reflectarray is expected to be even more significant since squinting away from the mechanical pointing direction will result in much larger drops in gain for larger single-feed antennas with narrower main beams.

5.5.3 Experimental Ratification

Next the far-zone patterns of the fabricated two-feed single-beam offset-fed reflectarray shown in Figure 5.29 were measured and compared to the simulated results. Although the reflectarray was designed to operate with two feeds simultaneously illuminating the reflectarray, we first examined its measured and full-wave simulated far-field patterns with only one feed in use. These far-zone E-plane patterns are shown in Figure 5.35. It is evident that there is no beam squint at centre-frequency 30GHz, whereas squinting to the left and right of the broadside mechanical pointing direction occurs at 28GHz and 32GHz. This is expected when only one feed is used for reasons of phase tilt over the aperture mentioned in Section 5.3.2, and is similar to the situation for the conventional single-feed single-beam offset-fed reflectarray case discussed in Section 5.2.

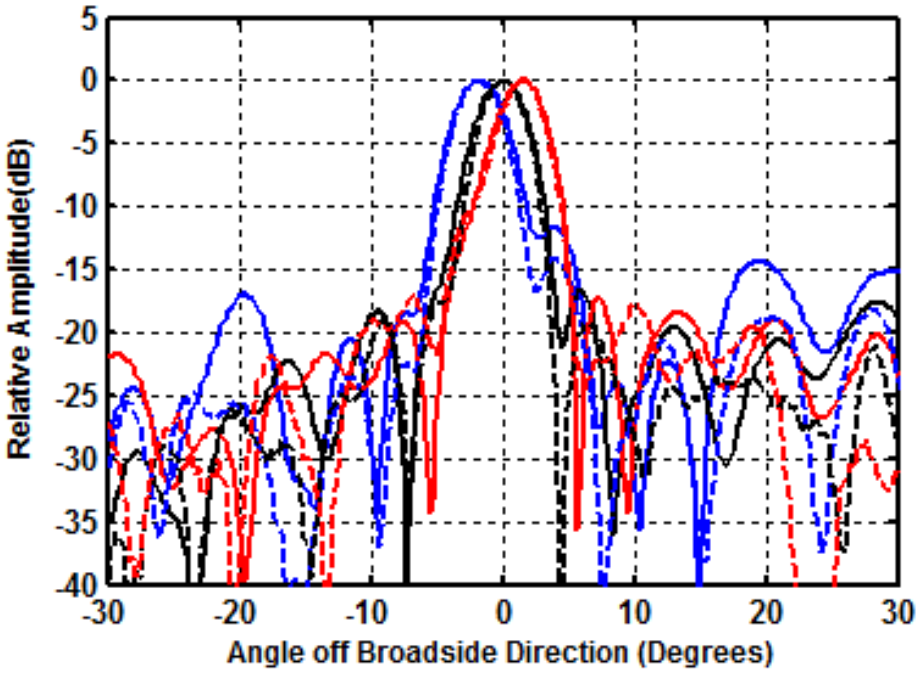

Figure 5.35: E-plane far-zone patterns of the two-feed single-beam reflectarray when only one feed is in use. Measured patterns at 30GHz (——), 33GHz (——) and 27GHz (——). Simulated patterns at 30GHz (— —), 33GHz (— —) and 27GHz (— —).

The symmetry of the two-feed reflectarray under discussion has already been pointed out. In order to obtain the measured patterns when both feeds are used simultaneously we took the complex (amplitude an phase) measured pattern of the reflectarray with only one of the feeds in place (from which Figure 5.30 was obtained). The measured pattern of the reflectarray with only the other feed turned on was emulated by simply rotating the above measured far-zone complex pattern by 180° about the z-axis. These two complex far-zone patterns were then added to gauge what the measured far-zone reflectarray radiation patterns would be if we had actually had two identical feeds. The results are referred to in Figure 5.36 as the measured two-feed single-beam reflectarray far-zone patterns, and are shown along with their simulated counterparts. As expected from the arguments in earlier sections there is no beam squint at any frequency.

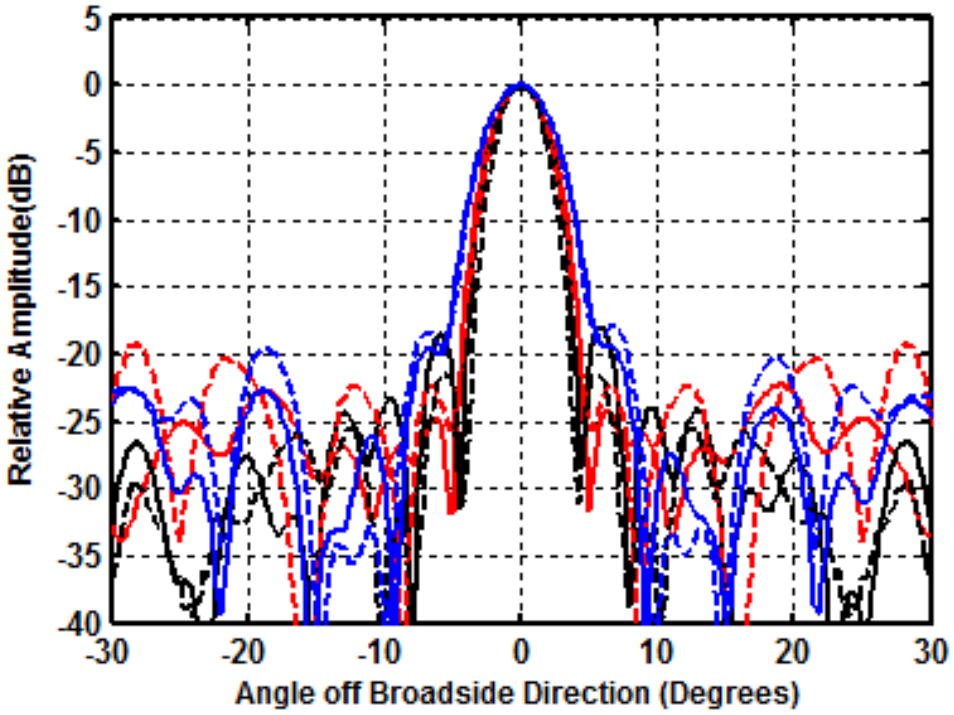

Figure 5.36 E-plane far-zone patterns of the two-feed single-beam reflectarray when both feeds are in use. Measured patterns at 30GHz (——), 33GHz (——) and 27GHz (——). Simulated patterns at 30GHz (— —), 33GHz (— —) and 27GHz (— —).

Although the two-feed reflectarray offers some advantages over the single-feed reflectarray, it suffers from some imperfections that are mainly related to the power splitting process amongst the two feeds. In practice the two feeds are excited using a 3 dB power divider and appropriate lengths of semi-rigid coaxial lines between the power divider output and the inputs to the two feeds. Another issue that degrades the performance of the two-feed reflectarray is the presence of unexpectedly high sidelobes on either side of the main beam in the plane of the feeds, which are visible in the patterns shown in [9], but are not discussed there. The cause of theses sidelobes is identified in the next section (namely Section 5.6), and their mitigation discussed.

5.6 Identification & Mitigation of High Sidelobes in Two-feed Reflectarrays

5.6.1 Introduction

In this section the reason for the presence of unwanted sidelobes in multi-feed single-beam reflectarrays is shown to be a grating lobe phenomenon due to "amplitude clustering" of the scattered field over the reflectarray aperture. A means of controlling the level of these lobes is proposed and validated using full wave analysis and measurements.

5.6.2 Identification of the Grating Lobe Source Using Feed Field, and Scattered Field, Distributions over the Reflectarray Aperture

For the case of the improved sub-wavelength two-feed reflectarray in Section 5.4.3 whose two in-line feeds phase centres are located at coordinates (0,-77.5,155) mm and (0,77.5,155) mm, so that F=155mm and F/D = 1, the full-wave simulation gives the radiation patterns shown in Figure 5.37. The high sidelobes of interest are evident around 60 deg. The goal here is to establish a way of ridding ourselves of these lobes.

In order to ascertain what the underlying cause is for the unwanted sidelobes we first examined the distribution of the ψ_n values for the sub-wavelength reflectarray mentioned above, over the aperture, that were obtained using equation (5.5) for each of its elements. Back-substitution discloses (5.5) is indeed satisfied to within ±0.5°. Thus determination of incorrect values for the required reflection phases is not the source of the problem. We therefore next examine what the actual achieved aperture phase and amplitude distribution looks like.

The feed horns are rigorously modelled using HFSS, so no approximations are made in determining their field amplitude and phase values $E^{\text{Feed}}(x_n, y_n, 0)$ at any observation distance. If the reflectarray structure is removed from the model the feed fields observed over the plane usually occupied by the reflectarray aperture can be observed.

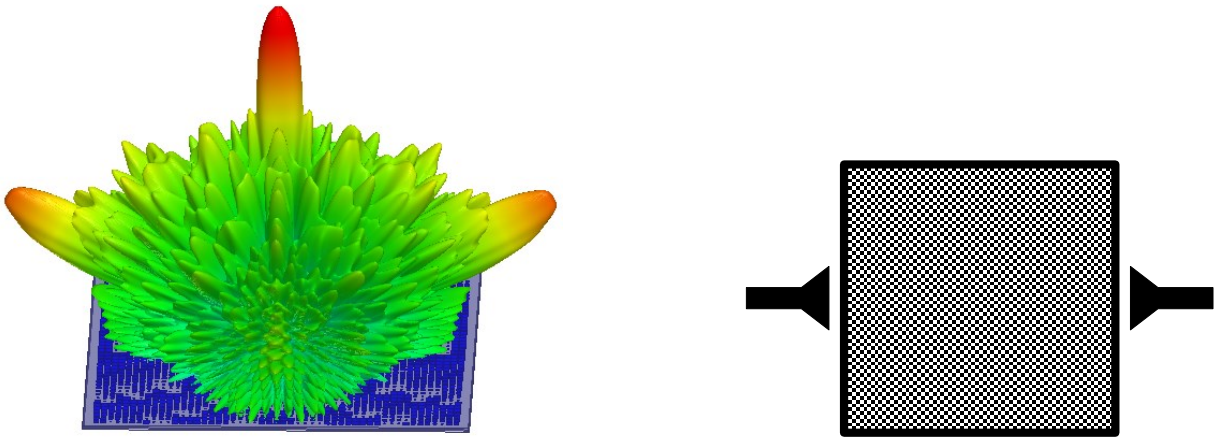

(a) (b)

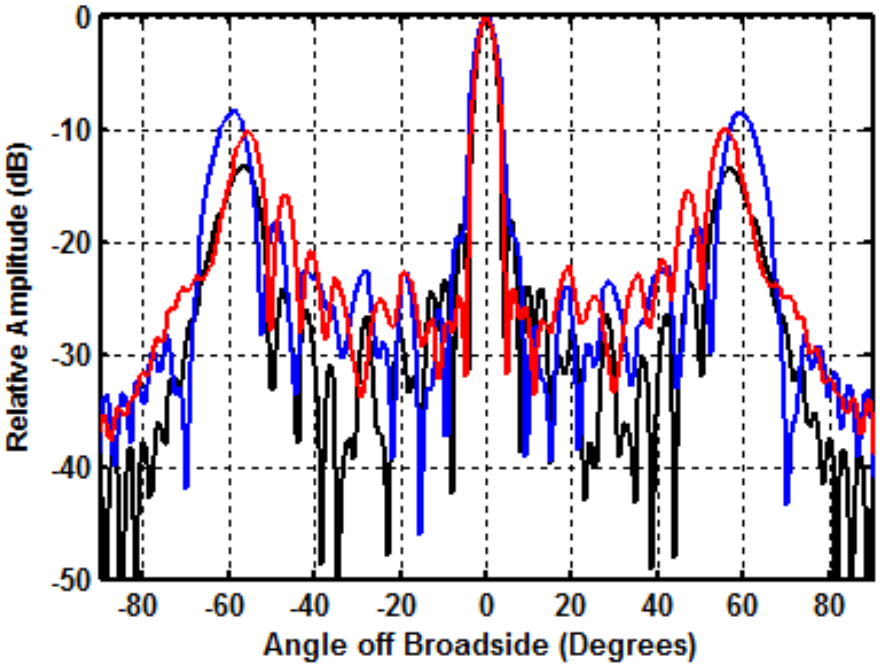

(c)

Figure 5.37: Computed radiation pattern (a), of the sub-wavelength reflectarray configuration in (b), illuminated by two in-line feeds with their phase centres located at coordinates (0,-77.5,155) mm and (0,77.5,155) mm, so that F=155mm and F/D = 1. Pattern cuts in the plane of the feeds are shown in (c) at 30GHz (—), 32GHz (—) and 28GHz (—).

For the reflectarray configuration whose patterns are shown in Figure 5.37, for which two in-line feeds are used with F=155mm, the combined feed field amplitude over the aperture plane with the reflectarray removed is as shown in Figure 5.38(a).If the sub-wavelength reflectarray is now re-introduced into the full-wave model, the computed scattered field from the reflectarray (designed for the given feed locations), just above its surface, is as shown in Figure 5.38(b). The grating-like amplitude pattern of the feed fields results in a reflectarray with a grating-like aperture amplitude distribution ("amplitude clustering"). There are deep nulls between the maxima of this aperture amplitude distribution. The separation between the maxima is roughly 1.1λ. Thus, as far as the pattern in the plane containing the two feeds is concerned, which happens to be the E-plane in this instance, the aperture looks almost like a linear array with inter-element spacing of 1.1λ. This at once identifies the unwanted sidelobes as grating lobes [14]; the far-zone pattern is that in Figure 5.37(a). The phase of the scattered field over the aperture is found to be almost uniform, as intended. There is no grating-like distribution in the H-plane and hence no unwanted grating lobes in that plane, for the in-line feed arrangement being considered here.

In an attempt to decrease the distance (in wavelength terms) between the amplitude clusters we located the two feeds at the same distance above the reflectarray, but in several other positions relative to each other, but the unwanted lobes were not removed. An example of that is when the position of the two feeds is selected to be “orthogonal” (as shown in Figure 5.39) instead of in-line but located at the same height (F=155mm). The orientations of the feeds were of course adjusted so that the field of each feed was properly polarized with respect to the reflectarray elements. Equation (5.5) was used to design the reflectarray, which was then laid out in HFSS. From Figures 5.39 and Figure 5.40 we observe that the unwanted sidelobes no longer appear in the E-plane, but have instead shifted to the diagonal plane. Furthermore, they are higher than they were for the in-line feed case. In other words, the use of orthogonal feeds does not remove the unwanted sidelobes.

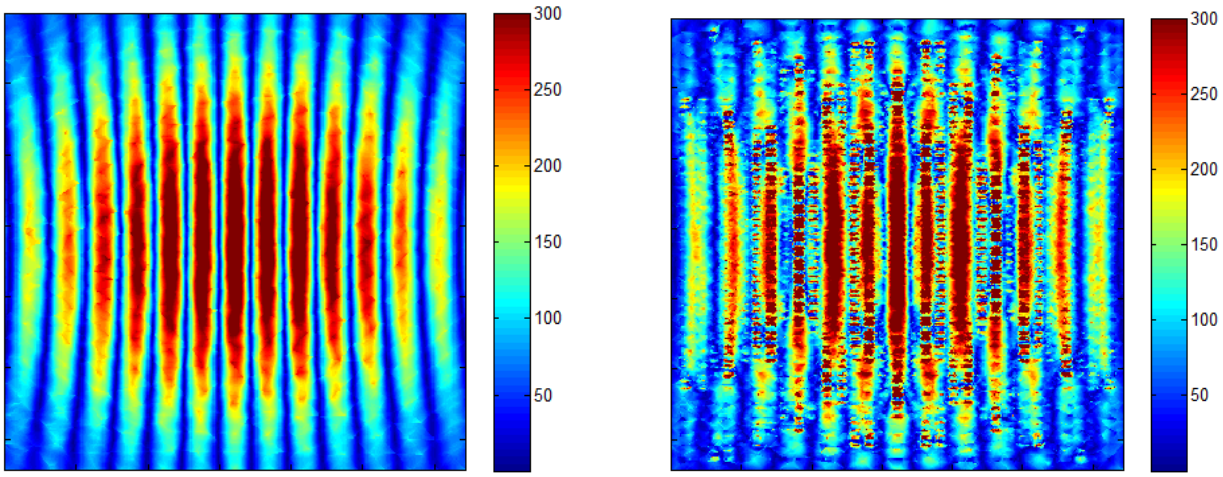

(a) **(b)**

Figure 5.38: (a). Amplitude distribution of fields of the in-line two-feed system over the aperture plane (z = 0) in the absence of the reflectarray, and (b) amplitude distribution of the scattered field, for the case F = 155mm.

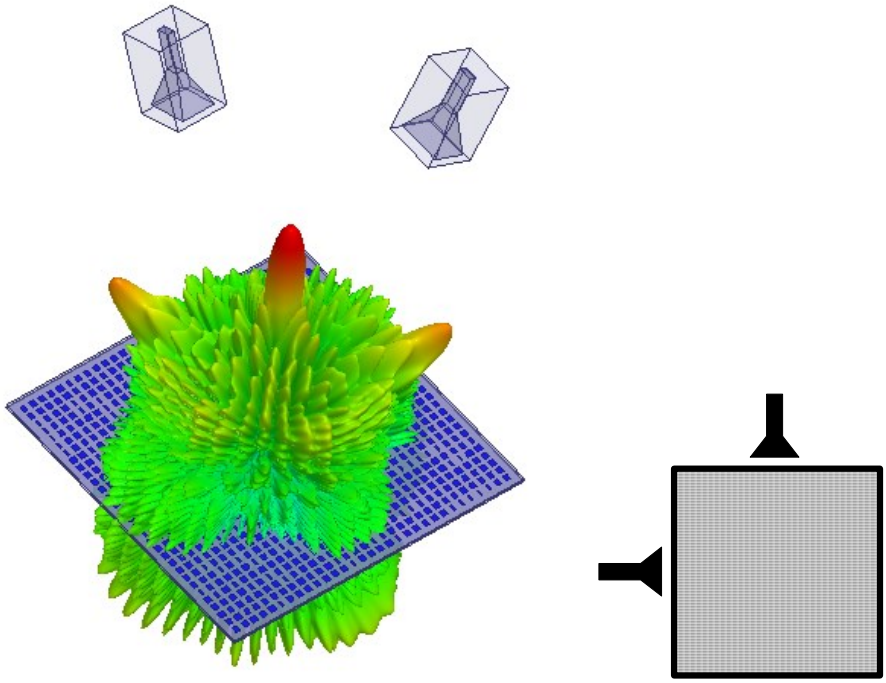

Figure 5.39: Three-dimensional depiction of the radiation pattern (at 30 GHz) for the half-wavelength two-feed reflectarray with orthogonally located feeds, obtained using the HFSS model.

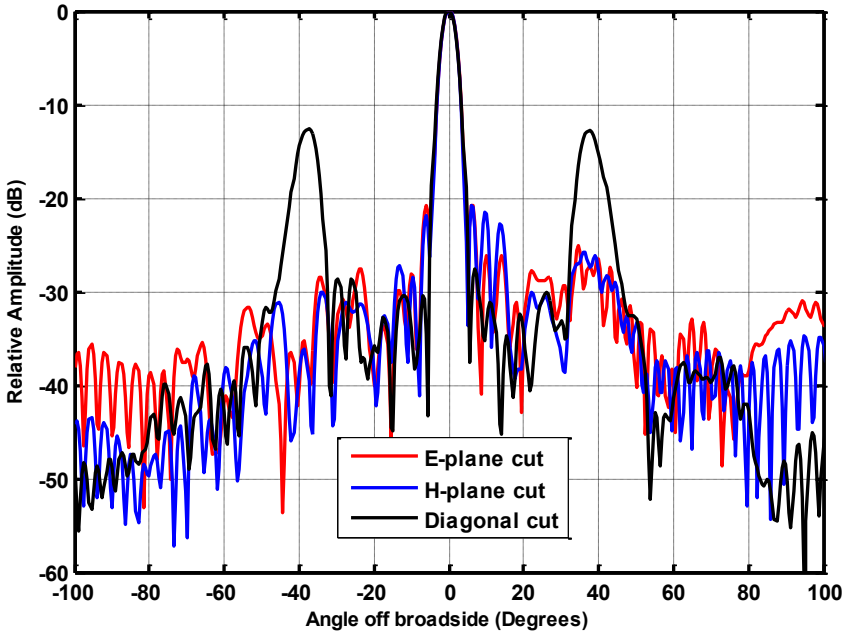

Figure 5.40: Radiation pattern cuts (at 30 GHz) for the half-wavelength two-feed reflectarray with orthogonally located feeds, obtained using the HFSS model. These are cuts through the 3D pattern shown in Figure 5.39.

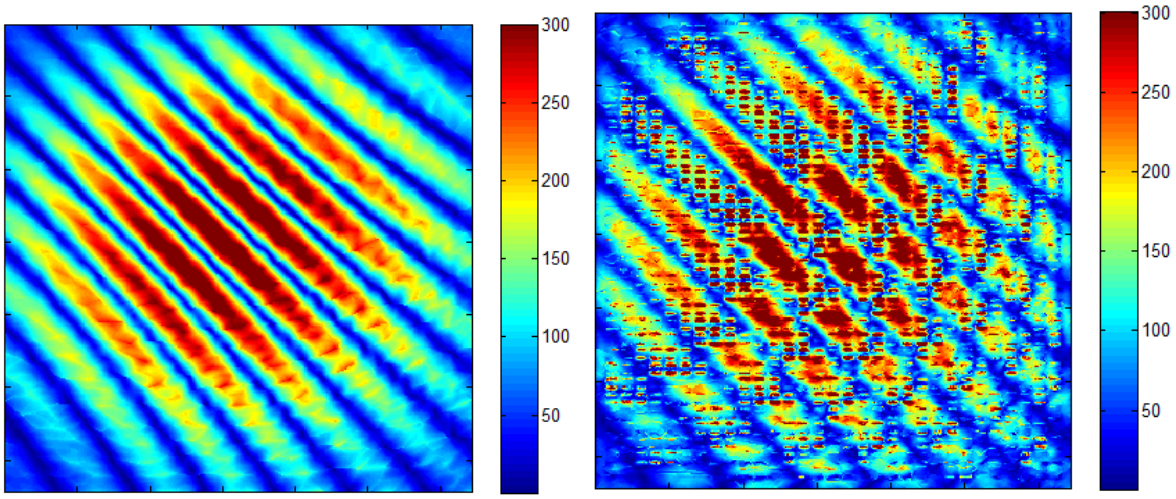

Figure 5.41: (a). Amplitude distribution of the orthogonally-located two-feed system over the aperture plane (z = 0) in the absence of the reflectarray. (b). Amplitude distribution of the scattered field from the reflectarray for the two-feed system. All results shown were obtained using full-wave HFSS modelling of the half-wavelength reflectarray.

The move of the grating lobes to the diagonal radiation pattern cut as shown in Figures 5.39 and 5.40 is due to the corresponding aperture amplitude distribution shown in Figure 5.41. It looks like a linear array of radiating "clusters", with the line of the array at 45° relative to that in Figure 5.38. In this case the spacing between maxima in the aperture distribution is about 1.25λ, which is larger than the 1.1λ for the on-line feeds. This explains why the unwanted sidelobes at 30GHz in Figure 5.40 are higher than those in Figure 5.37 at the same frequency (30GHz). From the preceding discussion, we conclude that the cause of the unwanted sidelobes lies with the imperfect amplitude distribution of the scattered field over the reflectarray aperture, which in turn is due to the imperfect feed field amplitude distribution.

5.6.3 Two-Feed Reflectarrays with Reduced Sidelobes

We next consider the sub-wavelength reflectarray of the two in-line feeds illustrated in Section 5.6.2, but we place the feeds only 100mm above the reflectarray surface, so that their phase centres are located at (0,-77.5,100) mm and (0,77.5,100) mm, with F = 100mm. The amplitude distribution of the combined feed fields over the aperture (with the reflectarray removed) is now that in Figure 5.42(a). It is similar to that in Figure 5.38(a), except that now the separation (along the horizontal axis) between the cluster maxima is only 0.75λ, which means there will not be grating lobes due to it for a broadside main beam. The computed scattered field from the sub-wavelength reflectarray (re-designed for the altered feed locations) is shown in Figure 5.42(b); its amplitude clustering maps to that in Figure 5.42(a), as expected. We next examine the resulting far-field patterns.

The same full-wave simulation model used to obtain the results in Figure 5.42(b) for the sub-wavelength reflectarrays with reduced focal length provides the far-field patterns shown in Figure 5.43(a) and the red curve in Figure 5.43(c). It is clear that the unwanted grating-lobes are gone. We have also shown the computed performance of the a half-wavelength reflectarray designed for the same in-line feed arrangement with F = 100mm. Figure 5.43(b) and the blue curve in Figure 5.43(c) reveal that this half-wavelength design still exhibits relatively high sidelobes, in spite of the fact that the amplitude clustering of the feed field is the same as for the sub-wavelength reflectarray. However, these are of a different nature to the sharper (grating

lobe) unwanted sidelobes of the type observed in Figure 5.37. They are different from what one expects when using a feed system that causes an amplitude clustered illumination of the reflectarray and hence the grating lobe behaviour observed in the previous section even for sub-wavelength reflectarrays. We conjecture that reasons for the difference between the half- and sub-wavelength performance are as follows: With the focal length F = 100mm the incidence angle of the feed field on the elements can be as high as 57°. The reflectarray design is performed here (and elsewhere [15]) using S-curves generated for normal incidence only.

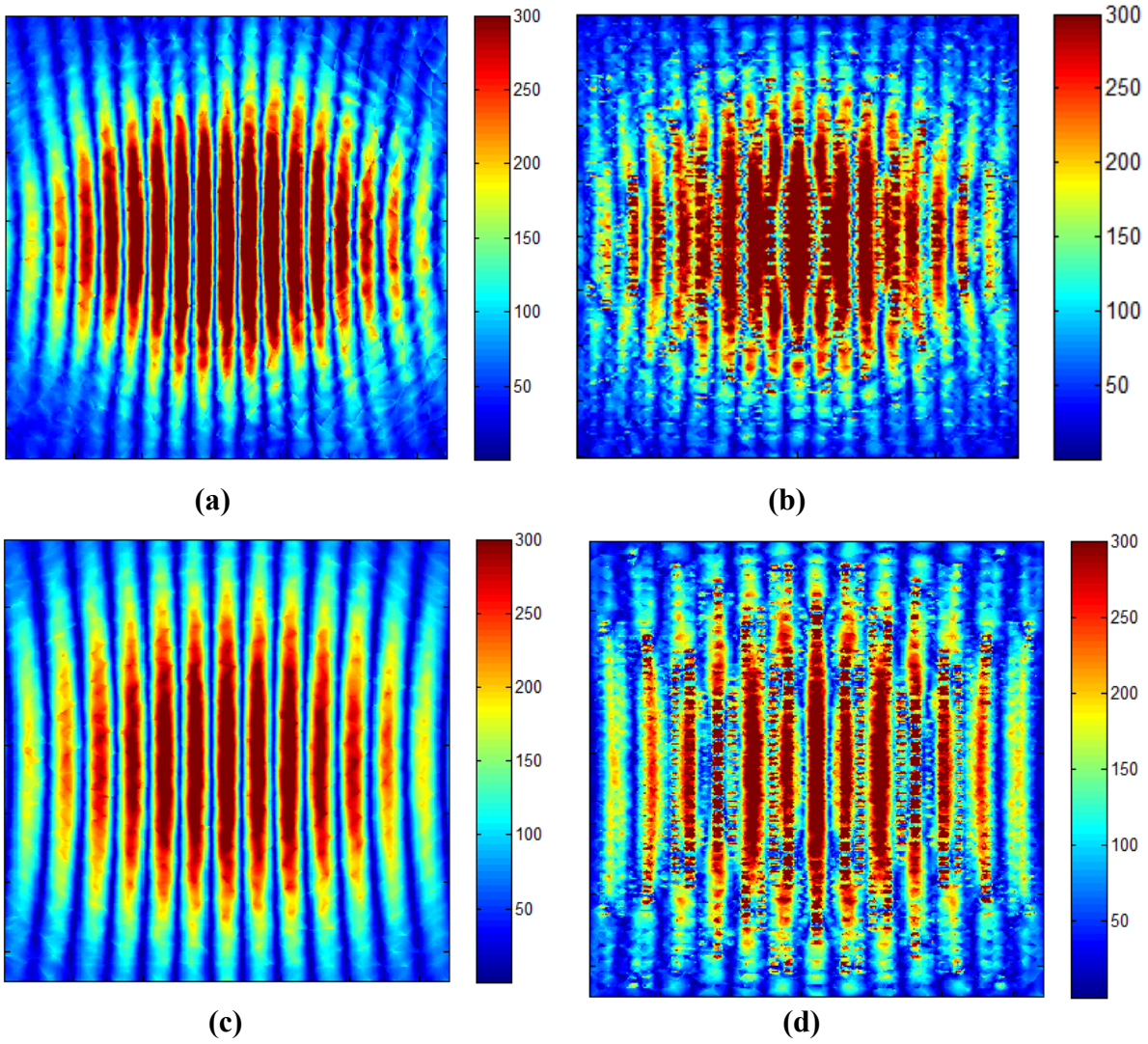

Figure 5.42: (a). Amplitude distribution of fields of the in-line two-feed system over the aperture plane (z = 0) in the absence of the reflectarray, and (b). Amplitude distribution of the scattered field, for the case F = 100mm. (c)&(d) are shown as (a)&(b) in Figure 5.38 for the case F=155mm, but repeated here to hold fair comparison with F=100mm case.

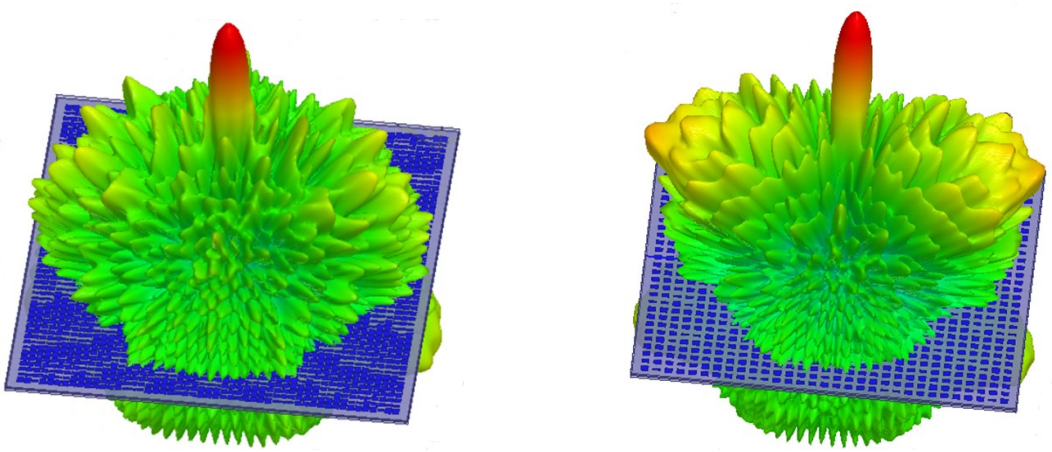

(a) (b)

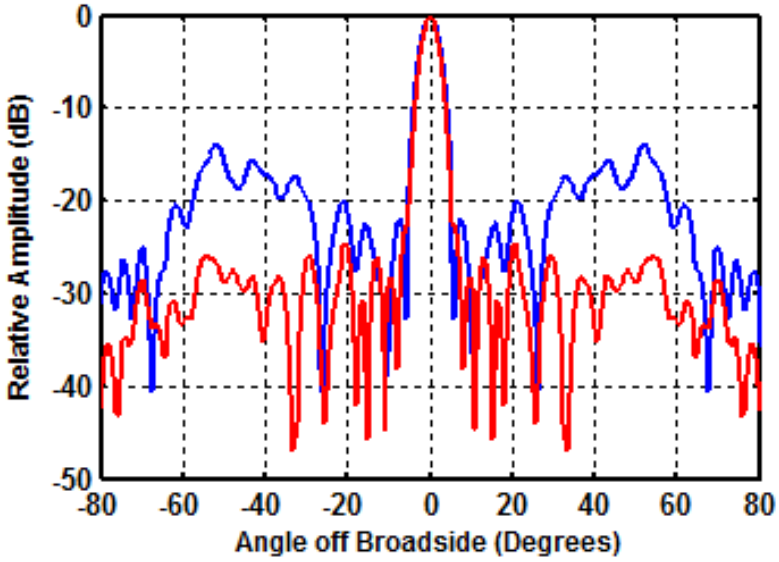

(c)

Figure 5.43: The computed radiation patterns, when the two in-line feeds are used with F = 100mm, are shown in for the (a) sub-wavelength, and (b) half-wavelength, reflectarrays at 30 GHz. The pattern cuts through the plane of the feeds are shown in (c) for the same sub-wavelength (—) and half-wavelength (—) cases.

The half-wavelength reflectarray design using such S-curves is thus less precise than when they are used for the F = 155mm case (in which the incidence angles are always less than 26.5°), and so we obtain insufficiently low sidelobes even though the feed field amplitude distribution

over the reflectarray is shown to suppress the grating lobes in the F= 100mm situation. However, for sub-wavelength inter-element spacing the reflection phase of the elements is less sensitive to angle of incidence, this is proved in Section 6.2.2, and so use of normal incidence S-curves provides a sufficiently precise implementation of the required element sizes even for F= 100mm. Also, feed image lobes are present in offset-fed half-wavelength reflectarrays as what was elucidated in Chapter 4. This phenomenon is likely a second contributor to the high sidelobes for the half-wavelength case in Figure 5.43(c).

5.6.4 Experimental Ratification

Measurements were performed on fabricated versions of the sub-wavelength reflectarrays for operation with two in-line feeds, one reflectarray designed for F= 100mm and the other for $F = 155\text{mm}$. In order to obtain the measured patterns when both feeds are used simultaneously (as intended in practice) we first took the complex measured pattern of the reflectarray with one of the feeds in place. The measured pattern of the reflectarray with only the other feed turned on was then carried out by simply rotating the reflectarray by 180° and re-measuring the complex pattern. These two complex far-zone patterns were then added to find what the measured far-zone reflectarray radiation patterns would be if we actually had two identical in-line feeds. This way to calculate the two-feed reflectarray far-field pattern does not account for the effects of the coupling between the two feeds, and did not include any phase imbalance between the feeds. However, our investigation of these two issues revealed that they have a minor impact on the antenna performance. The simulated far-field pattern was calculated when one feed is turned on; this is rotated as done in the measurement technique described above to obtain the computed patterns with the other feed turned on; these two computed patterns are then added to get the pattern with both feeds turned on. This resultant computed pattern compares closely with those obtained when the patterns are computed (more rigorously) with both feeds turned on in the full-wave model. Regarding the phase imbalance effect, an artificial phase imbalance of 20 degrees, imposed between the two feed ports in the full-wave model, resulted in only 0.13dBi gain reduction without having any impact on beam squint. The measured and full-wave computed pattern cuts in the reduced-F case are provided in Figure 5.44, and confirm the suppression of the grating lobes. The same patterns for the F = 155mm situation are shown in Figure 5.45; the grating lobes are present. It was evident from Figure 5.37 that the grating lobes become

significant at off-centre frequencies, and so their suppression here is expected to slightly improve the antenna gain at such frequencies.

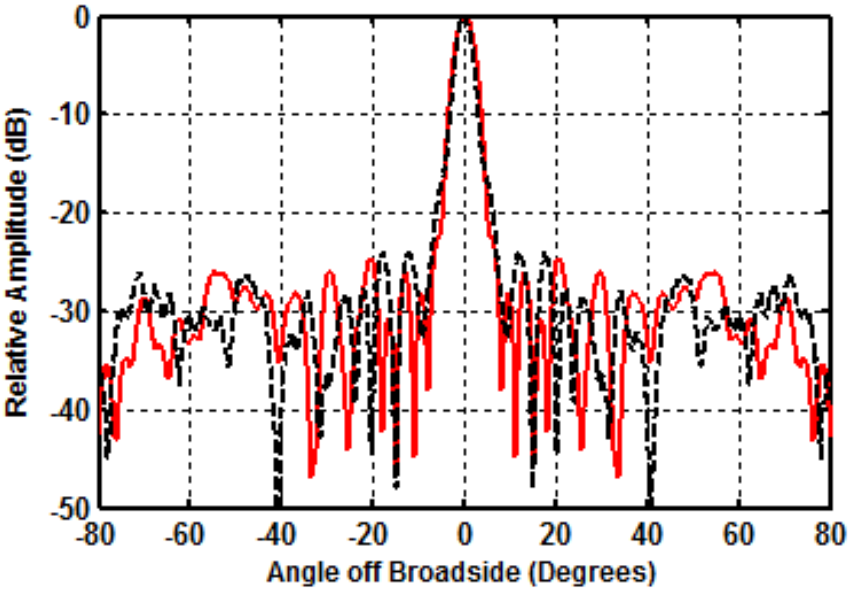

Figure 5.44: The (a) measured (— —), and (b) simulated (——), E-plane radiation patterns of the sub-wavelength reflectarray, when the two in-line feeds are used with reduced F = 100mm. Frequency is 30GHz.

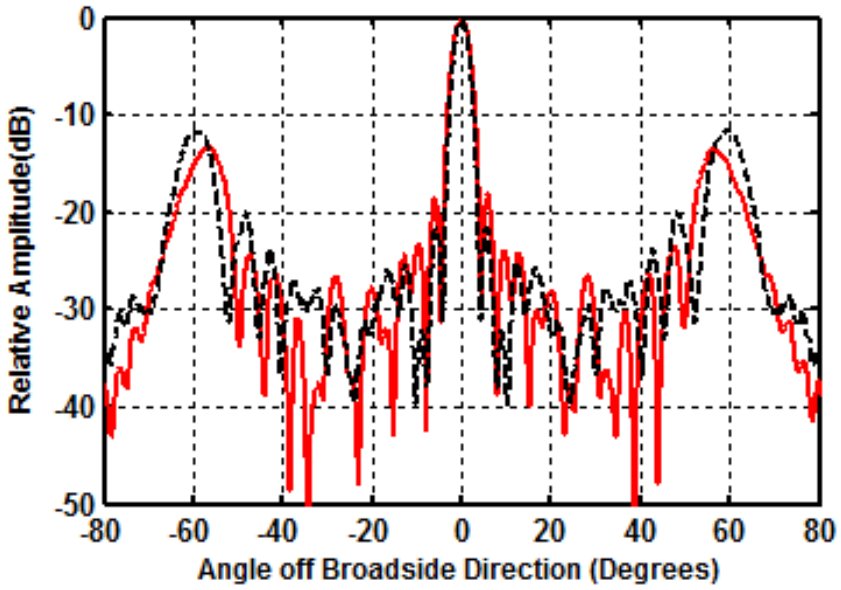

Figure 5.45: The (a) measured (— —), and (b) simulated (——), E-plane radiation patterns of the sub-wavelength reflectarray, when the two in-line feeds are used with F = 155mm. Frequency is 30GHz.

5.7 Concluding Remarks

In this chapter we have discussed beam squint in offset–fed reflectarrays; the source of this unwanted phenomenon was diagnosed and a valid solution was accordingly developed. In Section 5.2, the focal point shift with frequency in offset fed-reflectarrays, which is shown to be the source of beam squint, was thoroughly investigated. The impact of important factors namely, reflectarray size, focal length, element type and lattice size on the amount of focal shift versus frequency was established using a full wave receive-mode analysis. Furthermore, such focal shift was interpreted in terms of Fresnel zone considerations. Ref.[1] showed that for small to moderate reflectarray sizes and F/D ratios commonly used, the effect of differential spatial phase delay on reflectarray gain bandwidth is minimal, with the radiating element properties being the dominant factor. In Section 5.3 we have demonstrated for offset-fed reflectarrays that beam squint with respect to frequency, on the other hand, is due mainly to such differential spatial phase delay rather than the element properties, and causes a shift in the location of the focal point with frequency. In Section 5.4 a simpler implementation of the basic design equation for two-feed single-beam reflectarrays is described. The gain and bandwidth of this configuration is substantially improved by using sub-wavelength element spacing instead of the half-wavelength considered in Ref.[9]. We next in Section 5.5 offered the two-feed reflectarray, whose design was improved in Section 5.4, as a means to suppress the frequency dependent beam squint that occurs in offset-fed reflectarrays. This solution is based on having two focal points but a single beam, with identical feeds placed at each of the symmetrically located focal points. These focal points migrate in unison as the frequency changes (as demonstrated by the full-wave receive-mode analysis), resulting in an aperture phase distribution that does not have a net tilt at any frequency (as demonstrated by the full-wave transmit-mode analysis). Experimental measurements were used to confirm the conclusions of the investigation. Lastly, in Section 5.6, we have identified the cause of grating lobes in two-feed single-beam reflectarrays, and have shown how this might be mitigated. A reduced focal length is needed to ensure a more favorable feed field amplitude distribution over the reflectarray aperture, to provide an in-line two-feed design without unwanted high sidelobes. Portions of the work described in this chapter have already been published in [16],[17], [18], and [19].

Chapter 5 References

[1] D.M.Pozar, "Bandwidth of reflectarrays", Electronic Letters, Vol.39, No.21, pp.1490-1491, October 2003.

[2] J.Huang and J.A.Encinar, Reflectarray Antennas, IEEE Press. New York: John Wiley &Sons, pp.82-85, 2008.

[3] F.Arpin, D.A.McNamara, J.Shaker and A. Ittipiboon, "A Receive-mode analysis of reflectarray antennas", In Proceedings of the ANTEM Symposium, Ottawa, Canada, July 2004.

[4] H.Ling, S.W.Lee, P.T.C.Lam, and W.V.T.Rusch, "Focal shifts in parabolic antennas", IEEE Transactions on Antenna and Propagation,Vol.33, No.3, pp.744-748, July 1985.

[5] HFSS, Ansoft Product Suite, Ansys Inc., USA (www.ansoft.com).

[6] M.R.Chaharmir, J.Shaker, M.Cuhaci and A.Ittipiboon, "Broadband reflectarray antenna with double cross loops", Electronic Letters,Vol.42, No.2, pp.65-66, January 2006.

[7] S.D.Targonski and D.M.Pozar, "Minimization of beam squint in microstrip reflectarrays using an offset feed", IEEE International Symposium on Antenna and Propagation Digest, pp.1326-1329, USA, July 1996.

[8] A.Petosa and A.Ittipiboon, "Design and performance of a perforated dielectric Fresnel lens", IEE Proceedings,Vol.150, pp.309-314, October 2003.

[9] F.Arpin, J.Shaker and D.A.McNamara, "Multi-feed single-beam power-combining reflectarray antenna", Electronics Letters,Vol.40, No.17, pp.1035-1037, August 2004.

[10] J.Lanteri, J.Y.Dauvignac, Ch.Pichot and C.Migliaccio, "Beam-scanning improvement of reflectarrays by reducing the cell size at millimetre waves", Microwave Optical Technology Letters,Vol.48, No.5, pp.966-968, May 2006.

[11] P.Nayeri, F.Yang and A.Elsherbeni, "Broadband reflectarray antennas using double-layer subwavelength patch elements", IEEE Antennas Wireless Propagation Letters,Vol.9, pp.1139-1142, July 2010.

[12] J.Ethier, M.R.Chaharmir and J.Shaker, "Novel approach for low-loss reflectarray designs", IEEE International Antennas Propagation Symposium Digest, USA,pp.373-376, July 2011.

[13] D.M.Pozar,"Wideband reflectarray using artificial impedance surface", Electronic Letters,Vol.43, No.3, pp.148-149, February 2007.

[14] G.Thiele and W.Stutzman, Antenna Theory & Design (Wiley, 1998) Section 3.1.

[15] J.Huang, “Reflectarray Antennas”, Chap.35 in: J.L.Volakis (Edit.), Antenna Engineering Handbook (Wiley, 2007).

[16] **E.Almajali**, D.A.McNamara, J.Shaker and M.R.Chaharmir, “On beam squint in offset-fed reflectarrays", IEEE Antennas Wireless Propagation Letters,Vol.11, pp.937-940, August 2012.

[17] **E.Almajali**, D.A.McNamara, J.Shaker and M.R.Chaharmir, “Beam squint suppression in offset-fed reflectarrays”, IEEE Antennas Wireless Propagation Letters,Vol.12, pp.587-590, April 2013.

[18] **E.Almajali**, D.A.McNamara, J.Shaker and M.R.Chaharmir, “Improved two-feed single-beam power-combining reflectarray antenna ”, Electronics Letters,Vol.49, No.25, pp. 1595-1597, December 2013

[19] **E.Almajali**, D.A.McNamara, J.Shaker and M.R.Chaharmir, “Grating Lobe Control in Two-feed Single-Beam Reflectarrays and Power Combiners ”, IEEE Antennas Wireless Propagation Letters,Vol.12, pp.1268-1271, September 2013.

CHAPTER 6

Angle of Incidence Effects on Reflectarray and Sub-Reflectarray Operation

6.1 Introduction

The effect of the incidence angle of the feed field on the reflection characteristics of the elements in a reflectarray was discussed in Section 2.4.4. In this chapter the matter of incidence angle is taken up in more detail, and so some of that discussion is initially repeated here. We refer to the reflectarray configurations shown in Figure 6.1. It is clear that the incidence angle of the feed fields is different for each element, and that the range of incidence angles clearly changes depending on the F/D ratio. It is well-known to reflectarray designers that, when setting up the database of reflection coefficient phase values (S-curves) using the infinite periodic structure analysis, that these values will be dependent on the angle of incidence of the incoming plane wave. In most cases the S-curves are generated for normal incidence, and then used for design purposes in spite of the above-mentioned incidence angle dependence. Usually such designs turn out to be satisfactory [1, 2] because the F/D is usually larger than unity and hence the largest incidence angle is less than 30°. In the present chapter we wish to examine this issue more carefully in quantitative terms. Section 6.2 sets the stage by carefully reviewing the form of the incident field for oblique incidence when setting up the element reflection phase database. Section 6.3 examines the impact of including incidence angle effects in the design database on half-wavelength and sub-wavelength reflectarray designs for F/D = 1.0 and F/D = 0.5. We show that not only does incidence angle alter the element reflection phase (which is known), but that for oblique incidence the element beamwidth narrows and the element pattern deforms ("bulges" in a direction opposite to the incoming field). For sub-wavelength lattices not only is the reflection phase change with incidence angle less severe than for half-wavelength lattices, but the

element patterns changes are very much smaller too. It is these combined effects that give sub-wavelength reflectarrays their superior gain performance. In Section 6.4 we examine sub-wavelength sub-reflectarrays for the first time. The scattered near-field patterns from sub-wavelength and half-wavelength sub-reflectarrays are studied first on their own. The quality of the scattered spherical phasefront is used as a figure of merit to compare sub-reflectarray performance and hence to establish which of the two types functions better as a sub-reflector in a dual-reflector antenna system. Then we inspect their performance when they are used to illuminate a main-reflector, as would be the case in practice. The gain values obtained for the main-reflector/sub-reflectarray system show the superiority of sub-wavelength sub-reflectarrays particularly when an illumination over a wide angular region is needed. This further confirms the fact that sub-wavelength sub-reflectarrays are much more immune to the angle of incidence effects discussed in Section 6.3. The chapter is concluded in Section 6.5.

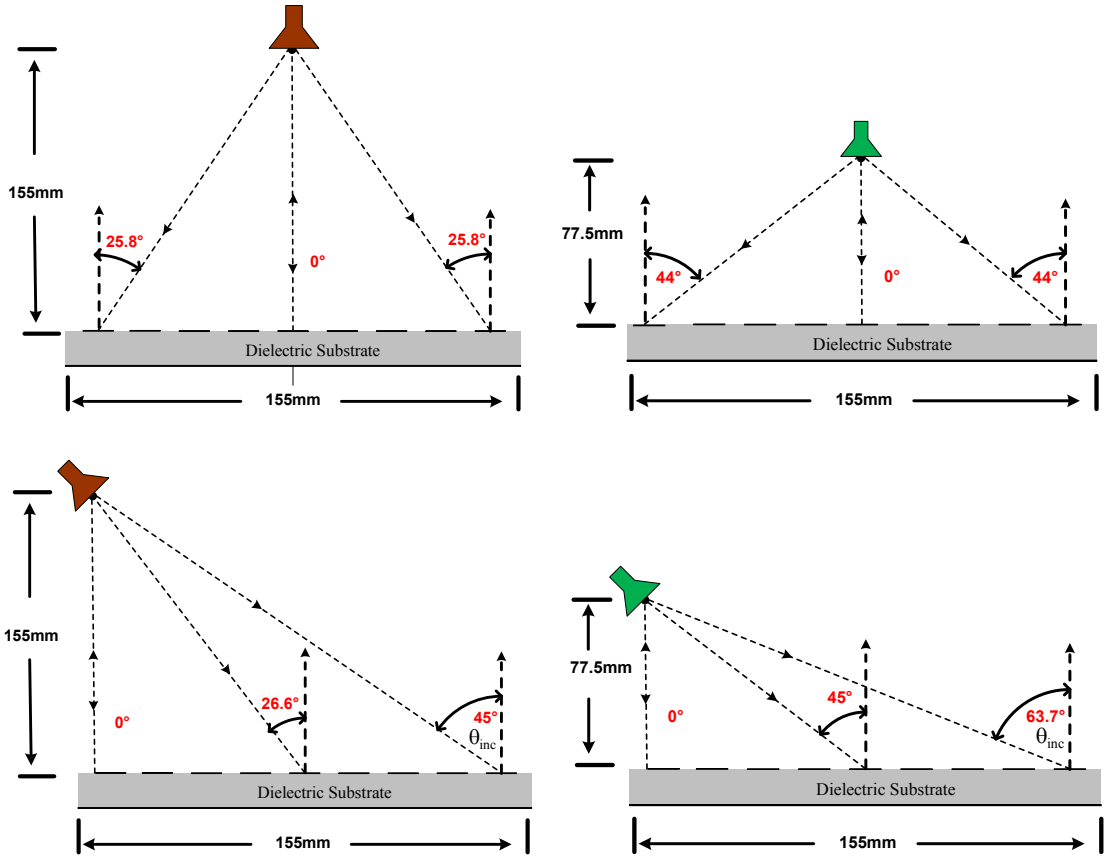

Figure 6.1: Sketches of various reflectarrays with F/D = 1.0 (left) and F/D = 0.5 (right), showing the range of incidence angles.

6.2 Some Background - Oblique Incidence Options

Exactly what is meant by oblique incidence of course needs to be specified precisely. With reference to Figure 6.2, we can set $\phi_{inc} = 0^\circ$ and vary θ_{inc}, or have $\phi_{inc} = 90^\circ$ and vary θ_{inc}, or many other possibilities. The computed reflection phase versus θ_{inc} will not be the same in all cases. Access to some basic expressions for an incoming plane wave will allow us to provide some clarity on this issue, and so are provided next. A plane wave travelling towards the origin from direction $(\theta_{inc}, \phi_{inc})$ has a direction vector $\hat{k}_{inc} = -(\hat{x}\sin\theta_{inc}\cos\phi_{inc} + \hat{y}\sin\theta_{inc}\sin\phi_{inc} + \hat{z}\cos\theta_{inc})$. A plane wave travelling in the $\hat{k}_i$ direction has an electric field $\bar{E}_{inc} = \bar{E}_0 e^{-jk_0\hat{k}_{inc}\cdot\bar{r}}$, where $\bar{E}_0$ is the electric field value at the origin, and vector $\bar{r} = x\hat{x} + y\hat{y} + z\hat{z}$ as usual. Thus the incident plane wave can be written as

$$\bar{E}_{inc} = \bar{E}_0 e^{-jk_0(x\sin\theta_{inc}\cos\phi_{inc} + y\sin\theta_{inc}\sin\phi_{inc} + z\cos\theta_{inc})} \tag{6.1}$$

The electric field vector of the plane wave must be orthogonal to $\hat{k}_i$, and as a consequence

$$\bar{E}_0 = \hat{x}\cos\theta_{inc}\cos\phi_{inc} + \hat{y}\cos\theta_{inc}\sin\phi_{inc} - \hat{z}\sin\theta_{inc} \tag{6.2}$$

θ-polarised incident wave and

$$\bar{E}_0 = -\hat{x}\sin\phi_{inc} + \hat{y}\cos\phi_{inc} \tag{6.3}$$

for a ϕ-polarised incident wave. What these expressions look like for the oblique incidence cases we are interested in here (namely in the x-z and y-z planes) are summarised in Table 6.1.

Table 6.1: Plane wave incident field expressions for TE&TM polarizations.

Wave Type	Alternative Terminology	Plane of Incidence	Incidence Type	Field Expressions
θ-polarised $\phi_{inc} = 0^\circ$	TM	x-z Plane	Oblique	$\bar{E}_{inc}(x,y,z) = (\hat{x}\cos\theta_{inc} - \hat{z}\sin\theta_{inc})e^{jk_0(x\sin\theta_{inc} + z\cos\theta_{inc})}$
			Normal	$\bar{E}_{inc}(x,y,z) = \hat{x}e^{jk_0 z}$
ϕ-polarised $\phi_{inc} = 90^\circ$	TE	y-z Plane	Oblique	$\bar{E}_{inc}(x,y,z) = -\hat{x}e^{jk_0(y\sin\theta_{inc} + z\cos\theta_{inc})}$
			Normal	$\bar{E}_{inc}(x,y,z) = -\hat{x}e^{jk_0 z}$

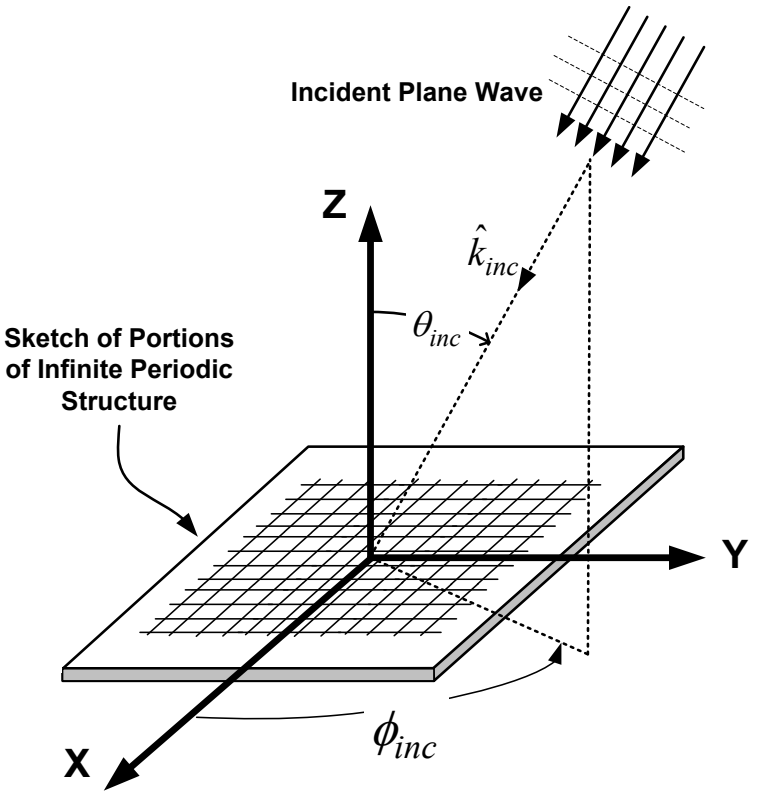

Figure 6.2: An illustration of the oblique incidence of a plane wave on an infinite periodic structure showing θ_{inc}, ϕ_{inc} and $\hat{k}_{inc}$.

6.3 Reflection Phase versus Incidence Angle: Observations and Impact on Reflectarray Gain

Figures 6.3 and 6.4 show[1] the reflection phase (ψ_n) versus frequency for variable size (that is, square) patch elements as a function of size calculated at 30GHz using a substrate with $\varepsilon_r = 3$, and thickness of 0.508 mm. Incidence angle θ_{inc} is a parameter. We observe that the variations of ψ_n versus θ_{inc} for the TM case are larger than for the TE case, and so the TM case is used in the remainder of the chapter. Clearly such variations are smaller for the sub-wavelength reflectarray elements than the half-wavelength ones. So not only is the change of ψ_n versus frequency

[1] Such curves have been shown by others [3], albeit only for half-wavelength reflectarray elements.

smaller for sub-wavelength reflectarray elements, as noted in Section 2.3, but so also is the change with respect to θ_{inc}. The latter is thus also a factor that contributes to the wider gain bandwidth of sub-wavelength reflectarrays mentioned in Section 2.3. One additional aspect related to oblique incidence that has not been studied in detail is the influence of the radiation pattern of individual elements (hereafter referred to as the element pattern, as is usually done in antenna engineering). An examination of this "mechanism" is in line with the goals of this thesis. We therefore extracted the current density on a single element in the infinitely periodic environment using the techniques described in Section 3.3, and so were able to compute the actual element pattern for obliquely incident plane waves. Representative results are shown in Figure 6.5. It is immediately noticed that there is a narrowing of the element beamwidth when θ_{inc} increases from zero. Furthermore, the element pattern becomes deformed. That both the beamwidth narrowing and deformation effects are less severe for the sub-wavelength lattice situation is one more reason for the superior behaviour of sub-wavelength reflectarrays.

If we assume that the element pattern remains the same in the actual reflectarray environment as it would be in the infinite periodic structure environment for the same incident field angle, then the situation in an actual reflectarray is as illustrated in Figure 6.6. The element patterns are important both from the point of view of coupling of the feed field to the elements, and (as in conventional array antennas) the reradiated field from the elements. For instance, when the reflectarray is designed to have a broadside main beam, deformation of an element pattern away from this direction results in its contributing less to radiation in this direction. Thus the further an element is away from a location directly below the feed the less it contributes to radiation in the main beam direction.

In order to examine the significance of these effects, the performance of the following different centre-fed reflectarrays[2] was compared for designs with F/D=1 and F/D=0.5:

■ Half-wavelength reflectarray, with normal incidence assumed for all elements when using the design database.

[2] The six centre-fed reflectarrays were designed specifically for the discussion in this section, and have not been used previously.

■ Sub-wavelength reflectarray, with normal incidence assumed for all elements when using the design database.

■ Half-wavelength reflectarray, with incidence angle accounted for when using the design database. Accounting for the angle of incidence change was achieved by incorporating many phase curves, similar to those in Figure 6.1, in the reflectarray design. By determining the angle of incidence at each element centre coordinate with respect to the feed position, a MATLAB [4] code was used to select the element size from the corresponding generated phase curves data base accordingly.

All reflectarrays were centre-fed and designed using the same substrate properties mentioned early in this section. The half-wavelength reflectarrays had 961 elements (31 x 31), and the sub-wavelength ones 2704 elements (52 x 52). The aperture size and focal length are as shown in Figure 6.1 for the F/D=1 and F/D=0.5 centre-fed cases. In the electromagnetic modeling using HFSS [5] the reflectarrays were fed by the pyramidal horns whose radiation patterns change little over the frequency range. For the F/D=1 case, the feed-horn has an aperture size of 17mm x 22mm whereas for the F/D=0.5 case the feed-horn aperture size was 9.25mm x 13.8mm. This was done to obtain the same 10dB edge taper in all reflectarrays. The fields of the horns were computed separately and then imported into the HFSS electromagnetic model of the finite-sized reflectarrays. Symmetry was used to lighten the computational burden as the gain was calculated at many frequencies for each reflectarray configuration.

The computed gains are shown in Figure 6.7, and the Table 6.2. Several observations can be made:

• In the case of the reflectarray with F/D = 1 (which is used by most authors) there is little difference in the gain performance of the half-wavelength reflectarrays whether incidence angle is included in the design database or not. This confirms what has been said by other authors [1,2].

• However, in the case of the reflectarray with F/D = 0.5 the gain performance of the half-wavelength reflectarray for which incidence angle was included in the design database is significantly superior to that when it is not included. It was seen that the dimensions of as many

as 380 of the 961 elements in the reflectarray changed between 30 and 110 microns when θ_{inc} effects are included in the design. Thus in some cases θ_{inc} effects should indeed be included in the design.

- The sub-wavelength reflectarrays always have a wider gain bandwidth than the half-wavelength ones. This is already known [6,7]. The important new observation here is that they have better performance even when (as done here) incidence angle is not included in the design process. This is a result not only of the fact that element beamwidth changes versus θ_{inc} are small for sub-wavelength lattices, but so too is the element pattern deformation (asymmetry) with θ_{inc}.

For offset-fed reflectarrays, the impact of the angle of incidence is expected to be more significant; from Figure 6.1, it is evident that for a given F/D value the incident angle would be much larger if we shift the feed from its prime-focus location. As a result of this, the use of sub-wavelength elements appears to be necessary in offset-fed configurations particularly when a compact reflectarray (small F/D) is required. To reinforce our observations about the lower sensitivity to the incidence angle of the incoming wave for the sub-wavelength case, the reflection phase versus patch sizes curves were also generated at 28GHz for the half-wavelength and sub-wavelength cases as shown in Figure 6.8. It can be gleaned from Figures 6.8(a) and 6.8(b), which apply to the TM case, that the half-wavelength case is, as expected, still more dependent on the value of the incidence angle than the sub-wavelength case. However, all phase curves in Figures 6.8(a) and 6.8(b) appear to be less sensitive to the angle of incidence compared to the TM cases shown in Figures 6.3(a) and 6.4(a), respectively. This observation stems from the fact that at frequencies below 30GHz (the centre-frequency), like 28GHz under discussion, the element spacing becomes a smaller fraction of a wavelength compared to what it is at 30GHz (the size of unit cell kept the same in both cases). As a result of this, the elements get closer and become more immune to the angle of incidence change as the frequency decreases. This implies that at frequencies above 30GHz the sensitivity to the angle of incidence would become more significant.

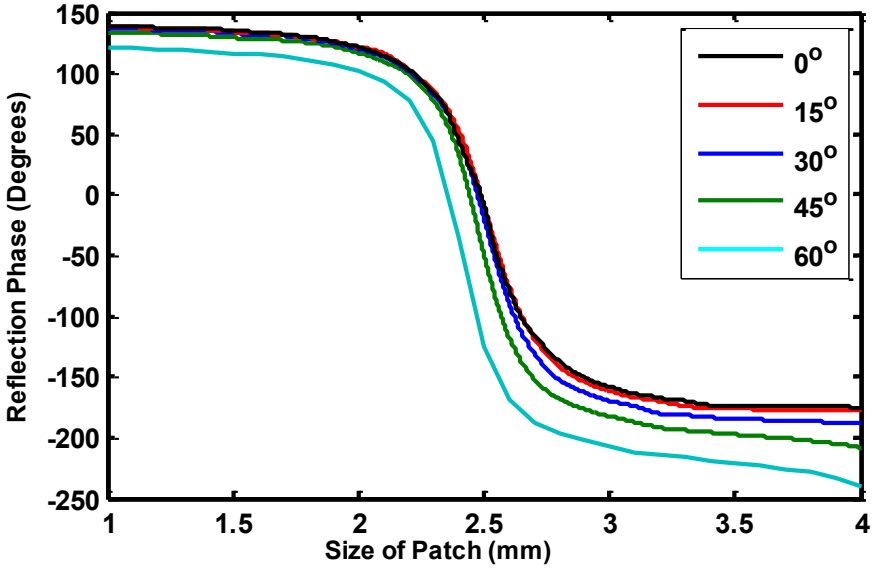

(a). TM Case (θ_{inc} Variation in the x-z Plane)

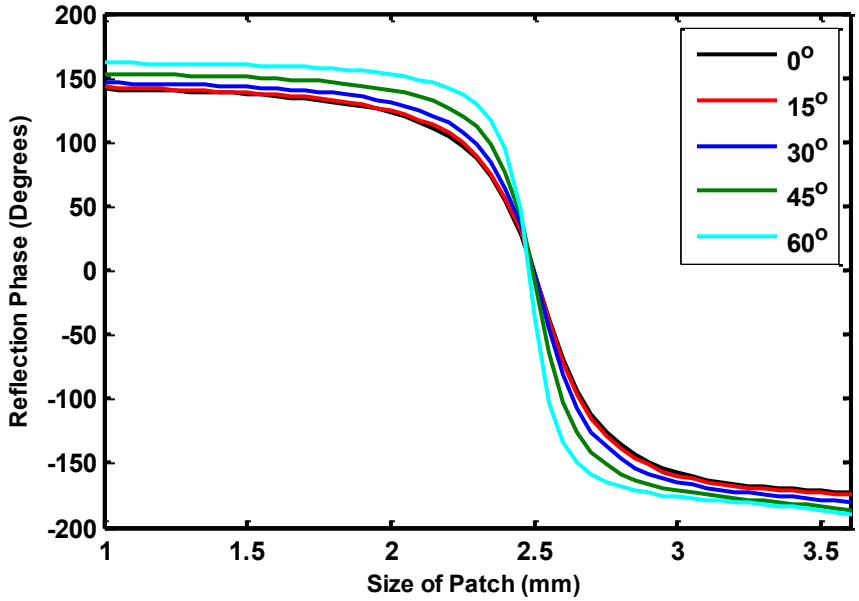

(b). TE Case (θ_{inc} Variation in the y-z Plane)

Figure 6.3: Plots of reflection phase versus element size calculated at 30GHz with θ_{inc} as a parameter, for half-wavelength elements.

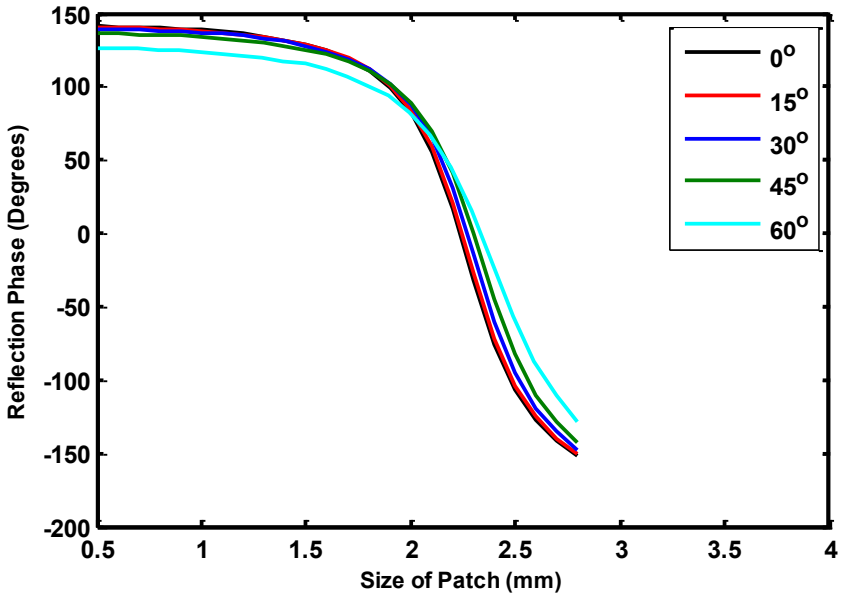

(a). TM Case (θ_{inc} Variation in the x-z Plane)

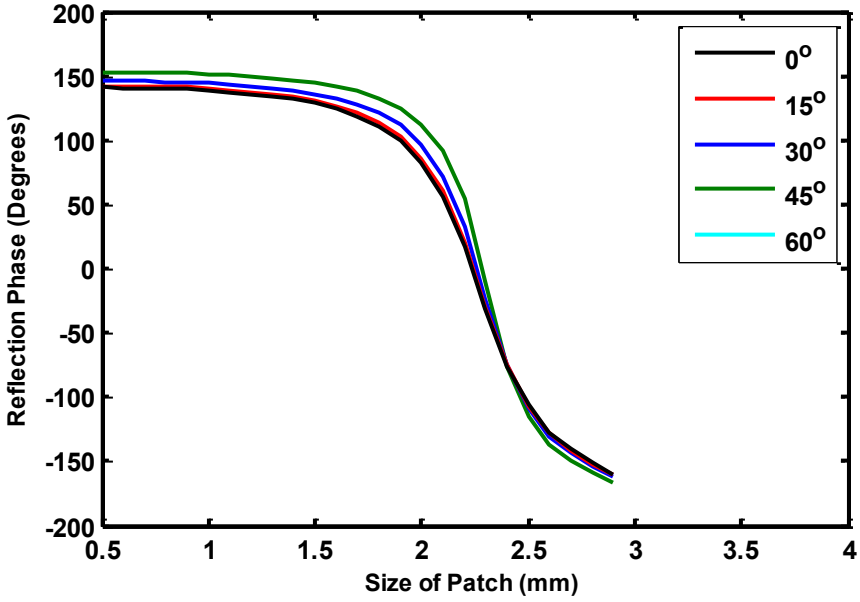

(b). TE Case (θ_{inc} Variation in the y-z Plane)

Figure 6.4: Plots of reflection phase versus element size calculated at 30GHz with θ_{inc} as a parameter, for sub-wavelength elements.

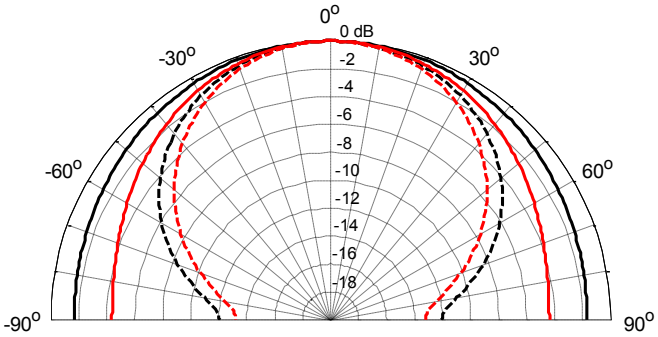

(a). $\theta_{inc} = 0^{\circ}$

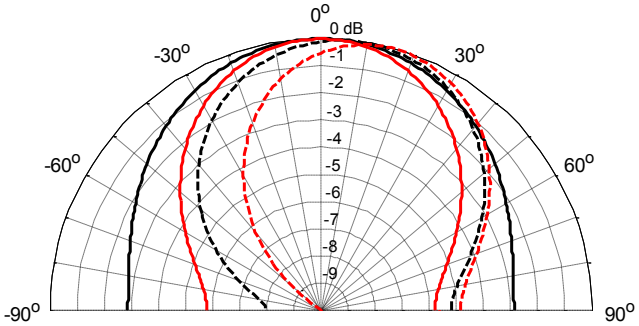

(b). $\theta_{inc} = 30^{\circ}$

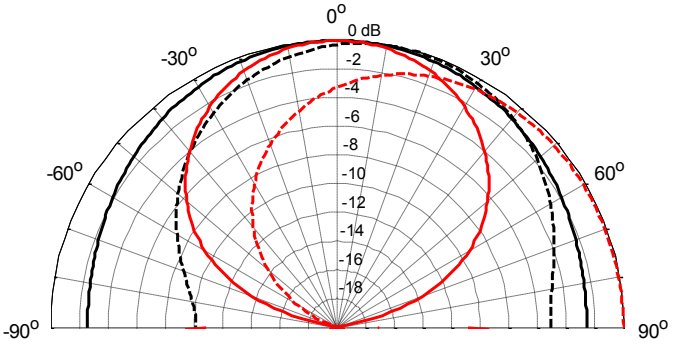

(c). $\theta_{inc} = 60^{\circ}$

Figure 6.5: Element patterns for a square element of size L=2.49 mm at 30GHz. The plots show the E-plane/xz-plane (dashed) and H-plane/yz-plane (solid) results for the half-wavelength (red) and sub-wavelength (black) lattices.

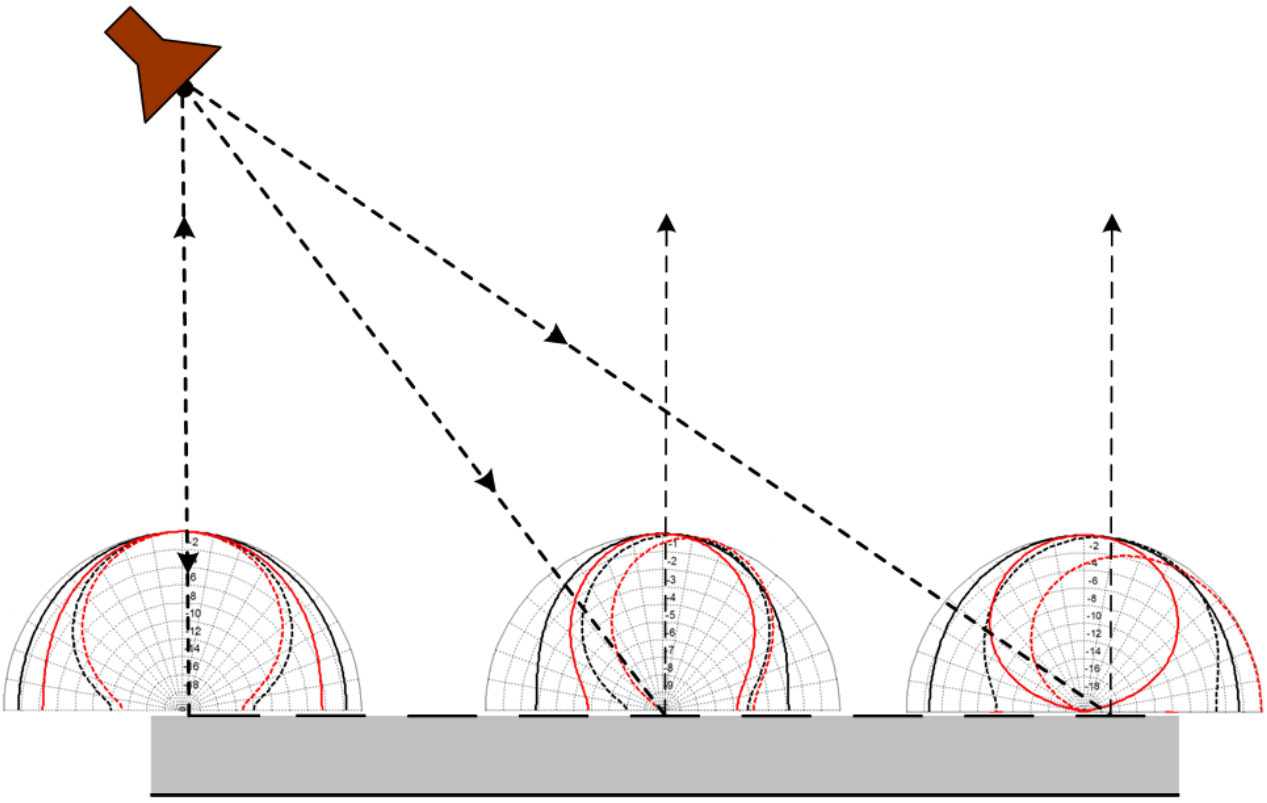

Figure 6.6: The element pattern impact in the actual reflectarray environment.

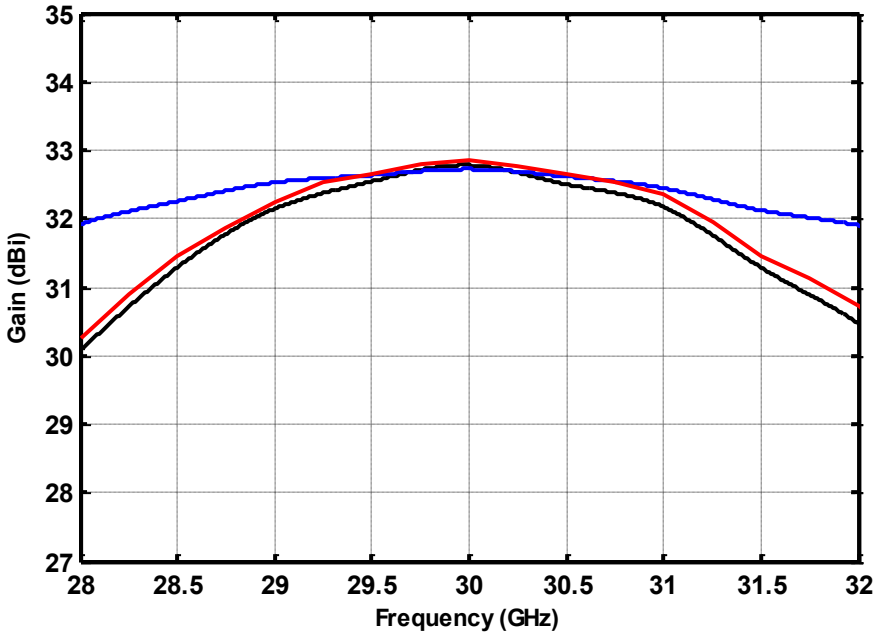

(a). F/D = 1.0

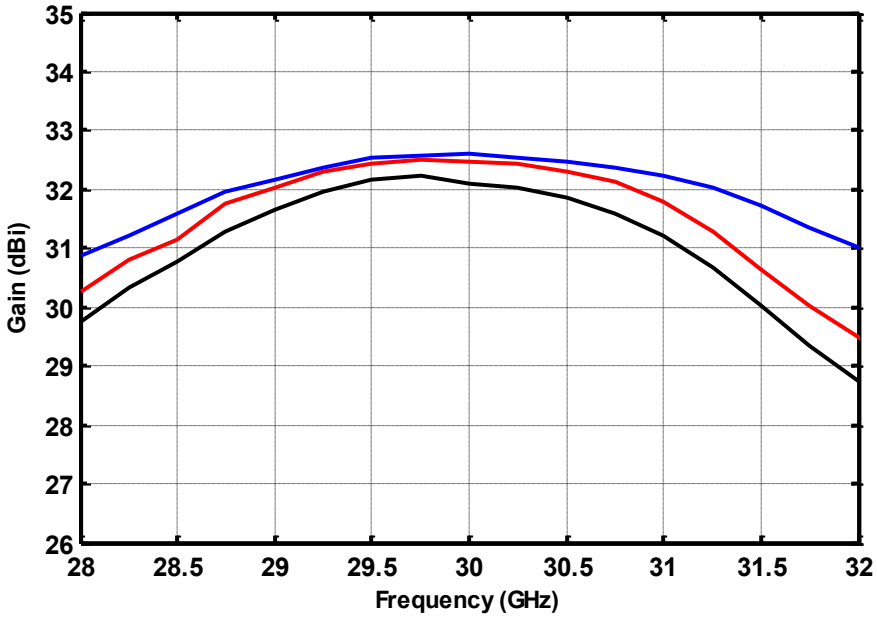

(b). F/D = 0.5

Figure 6.7: Computed gain versus frequency for a reflectarray of square elements designed for a centre-frequency of 30GHz. The plots apply to sub-wavelength (——) and half-wavelength designs (——) with normal incidence assumed in all database values, and a half-wavelength design with incidence angle taken into account in the database (——).

Table 6.2: The computed gain (dBi) at different frequencies for the reflectarrays under consideration.

	Reflectarray Type	28 GHz	30 GHz	32 GHz
F/D = 1	Half-Wavelength (θ_{inc} Assumed Zero for Design)	30.09	32.72	30.49
	Half-Wavelength (Actual θ_{inc} Accounted for in Design)	30.25	32.83	30.71
	Sub-Wavelength (θ_{inc} Assumed Zero for Design)	31.90	32.68	31.88
F/D = 0.5	Half-Wavelength (θ_{inc} Assumed Zero for Design)	29.75	32.08	28.72
	Half-Wavelength (Actual θ_{inc} Accounted for in Design)	30.26	32.47	29.47
	Sub-Wavelength (θ_{inc} Assumed Zero for Design)	30.88	32.59	31.02

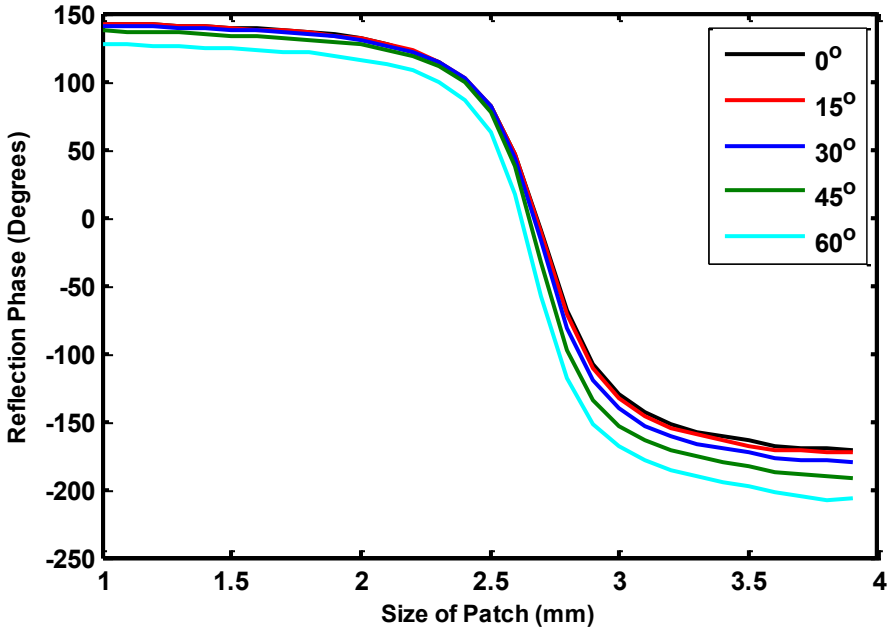

(a). Half-wavelength

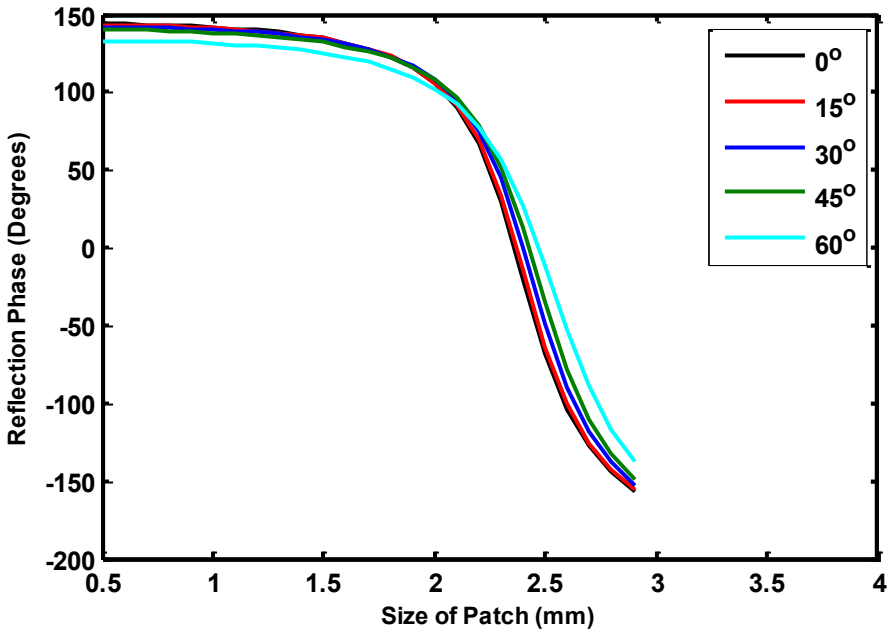

(b). Sub-wavelength

Figure 6.8: Plots of reflection phase versus element size calculated at 28GHz for TM Case (θ_{inc} Variation in the x-z Plane)

6.4 Sub-Wavelength Sub-Reflectarrays

As noted in the previous section, the element pattern is of importance not only from the point of view of interception of the incident feed fields, but also as regards the fields re-radiated by the elements. The latter aspect is especially important as far as the pattern performance of sub-reflectarrays is concerned. This is easily appreciated in a qualitative sense from the patterns shown in Figure 6.9. The sub-reflectarray pattern covers a broad angular sector, whereas that of the main-reflectarray does not. Thus broader element patterns are required for sub-reflectarrays than main-reflectarrays. Because of the element pattern stability with respect to both frequency and incidence angle for sub-wavelength lattices discussed in Section 6.3, we here examine the performance of sub-reflectarrays designed using a sub-wavelength lattice. This does not yet appear to have been done by others. In addition to studying the scattered patterns of such sub-reflectarrays on their own, we also inspect their performance when they are used to illuminate a main-reflector, as would be the case in practice. This might be called the "bottom line" when it comes to evaluating sub-reflectarrays. We use a solid main-reflector so that any performance variation with respect to frequency of the dual-system will principally be due to the sub-reflectarray.

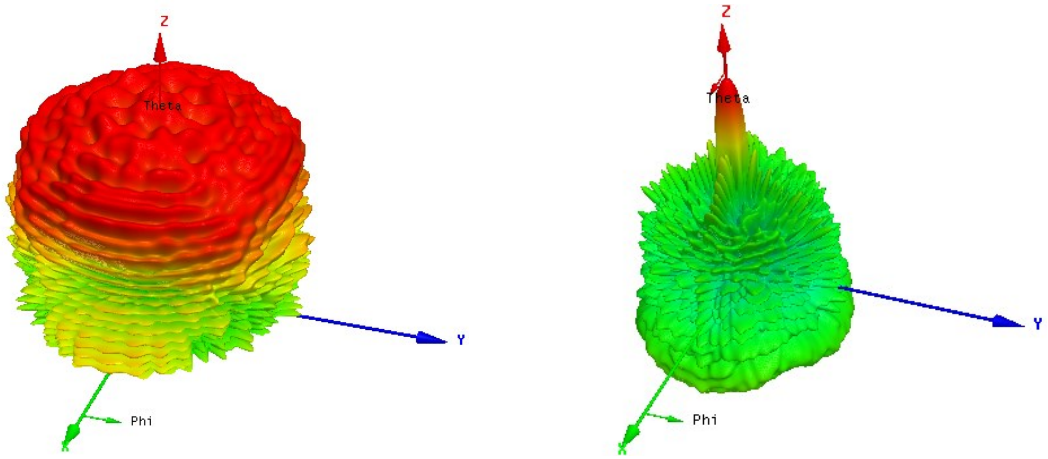

Figure 6.9: Three-dimensional depictions of a sub-reflectarray pattern (left) and main-reflectarray pattern (right).

Figure 6.10 shows two antenna configurations that use a sub-reflectarray but a solid paraboloidal main reflector. These have been designed using the minimum blockage condition as described in [8]. In both cases the largest incidence angle of the feed fields on the sub-reflectarray is 26.6°. However, the angle out to which the sub-reflectarray pattern, and hence the individual element patterns are important is 52.7° and 69.9° for the two different sub-reflectarray eccentricities. For each of the configurations shown in Figure 6.10 sub-wavelength and half-wavelength sub-reflectarrays were designed using equation (2.6). All sub-reflectarrays are comprised of square patch elements printed on a dielectric substrate with $\varepsilon_r = 3$ and a thickness of 0.508mm. Next each sub-reflectarray was simulated entirely using FEBI version of HFSS with the feed-horn included as part of the computational model in order to account for all feed/sub-reflectarray interactions. The HFSS example model is shown in Figure 6.11(b).

As pointed out in Section 2.2.3, a sub-reflectarray converts the incident spherical phasefront from the feed (as in Figure 6.11(a)) to a scattered spherical phasefront that appears to originate from the sub-reflectarray virtual focal point (as shown in Figure 6.11(b)). Therefore the first step in examining a sub-reflectarray performance is to verify the success of such phase conversion by extracting the sub-reflectarray scattered field phases from the sub-reflectarray electromagnetic model. In order to achieve this, the HFSS field calculator was used to obtain the incident and the total reflected fields from the computational models shown in Figures 6.11(a) and (b), respectively. These fields were extracted over an aperture in the x-z plane inside the sampling boxes shown in the same figures. The sub-reflectarray scattered field phases can then simply be obtained by subtracting the incident field from the total reflected field.

Figures 6.12 shows the scattered field phase at different frequencies for the sub-reflectarrays designed to have an eccentricity of 2.22, and radiate effectively over an angular range of -52.7° to 52.7° as per Figure 6.10(a). It is evident that all scattered field phasefronts look spherical and hence satisfy the required phase conversion. Most importantly, the scattered phasefronts are noticeably more uniform at all frequencies for the sub-wavelength sub-reflectarray case (left in Figure 6.12) than for the half-wavelength case (right in Figure 6.12). This is caused by the lower sensitivity of the sub-wavelength sub-reflectarray to the angle of incidence. In Figure 6.13, which applies to the other sub-reflectarrays whose effective eccentricity is 1.45, although all

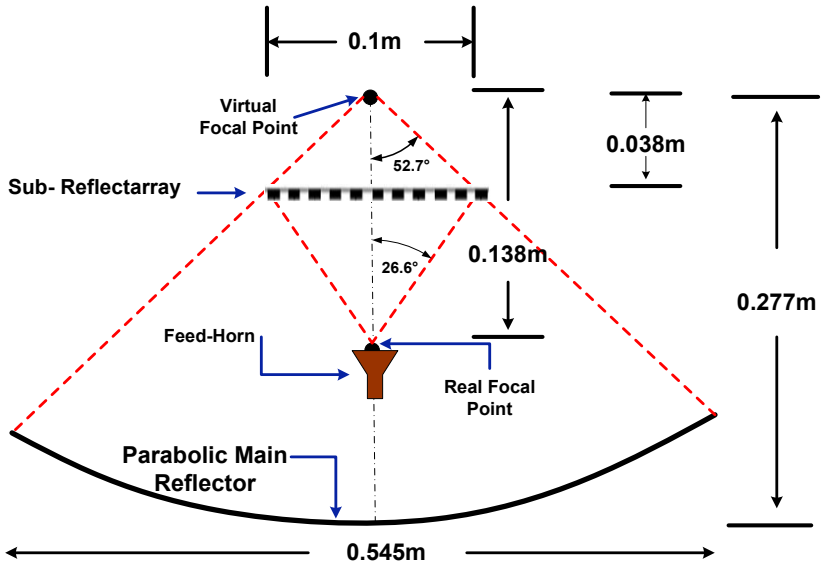

(a). Effective eccentricity of sub-reflectarray is 2.22

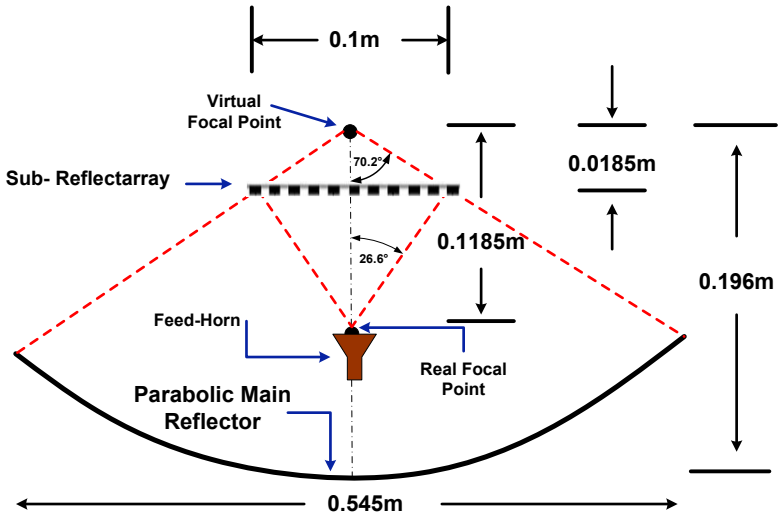

(b). Effective eccentricity of sub-reflectarray is 1.45

Figure 6.10: Main-reflector/sub-reflectarray system geometries considered.

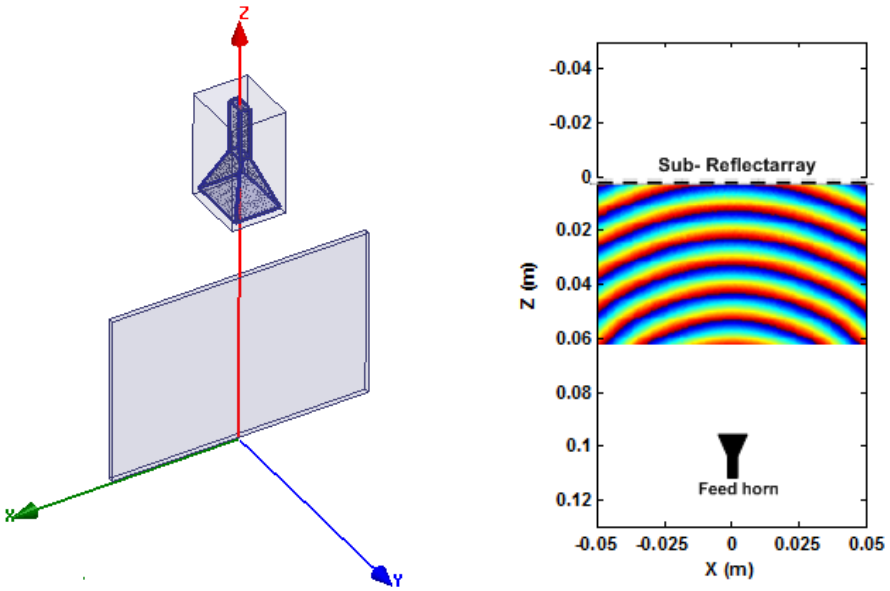

(a).

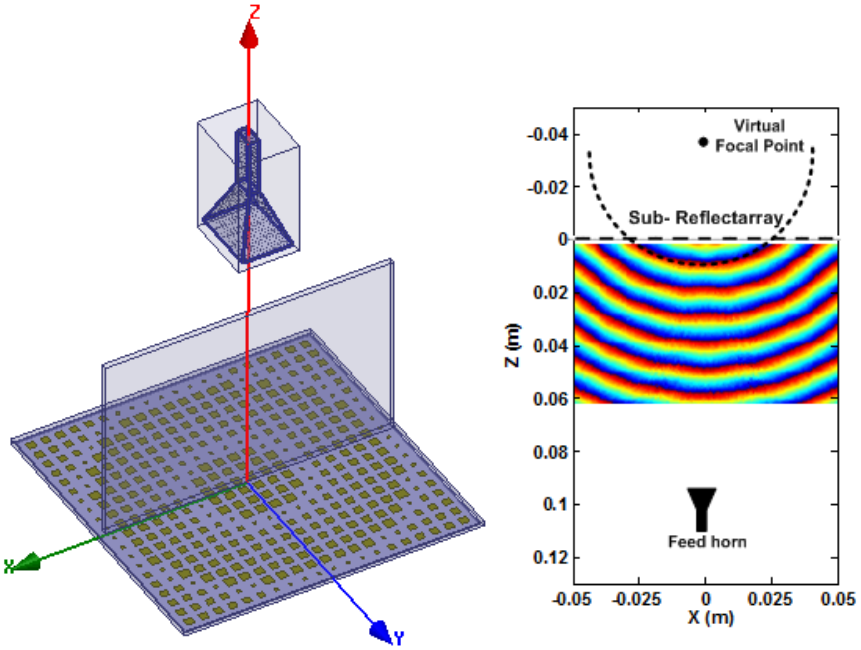

(b).

Figure 6.11: Field sampling "box" defined in HFSS in order to extract (a). the complex fields of the feed, and (b). the complex scattered fields of the sub-reflrectarray.

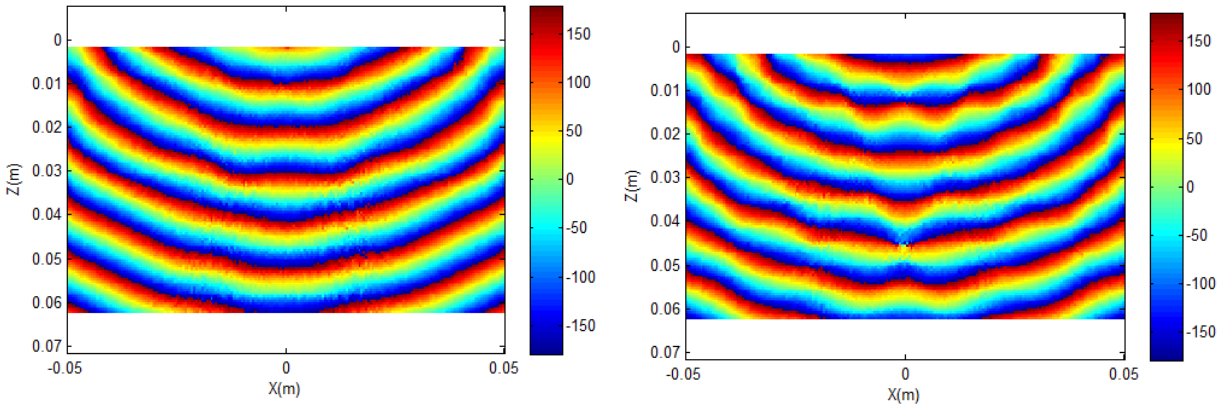

(a). 29 GHz

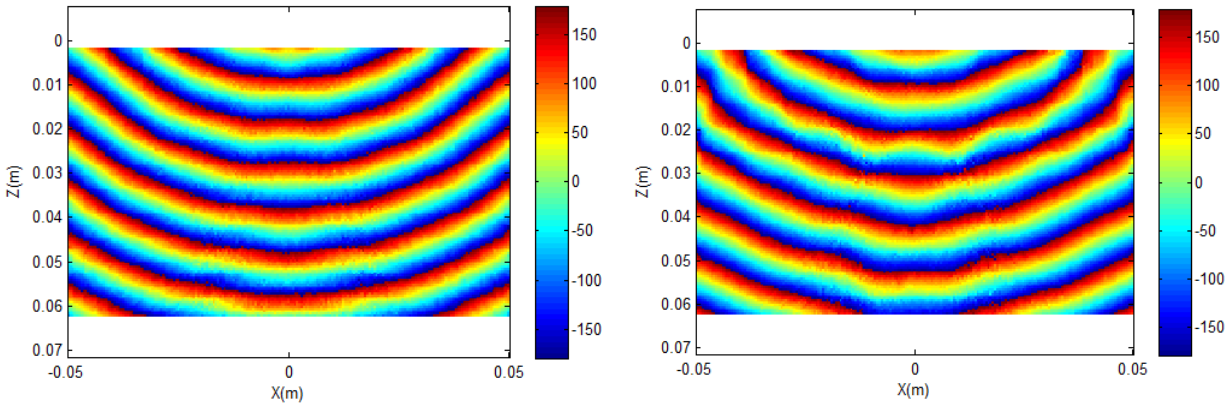

(b). 30 GHz

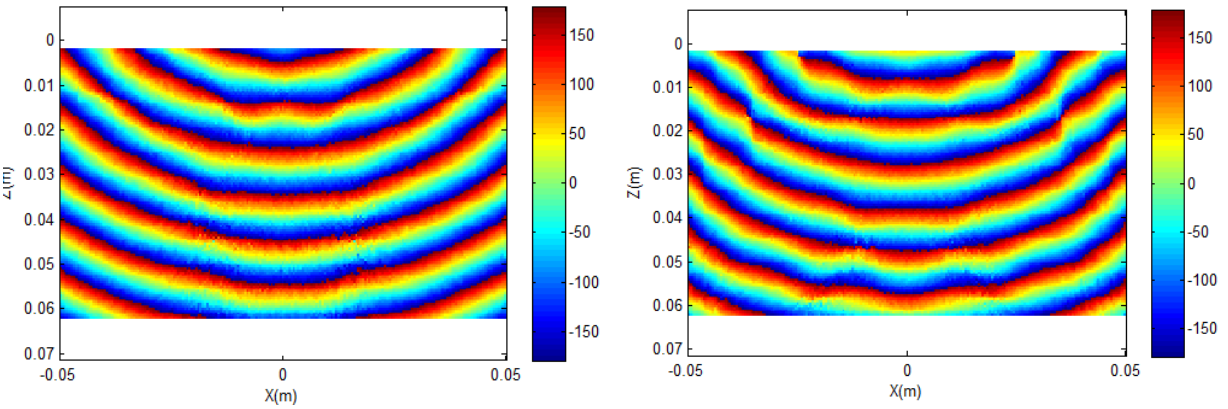

(c). 31 GHz

Figure 6.12: Sub-reflectarray scattered field phasefronts for the sub-wavelength (left) and half-wavelength (right) sub-reflectarrays with effective eccentricity of 2.22. The phase is shown with reference to the virtual focal point in Figure 6.10(a).

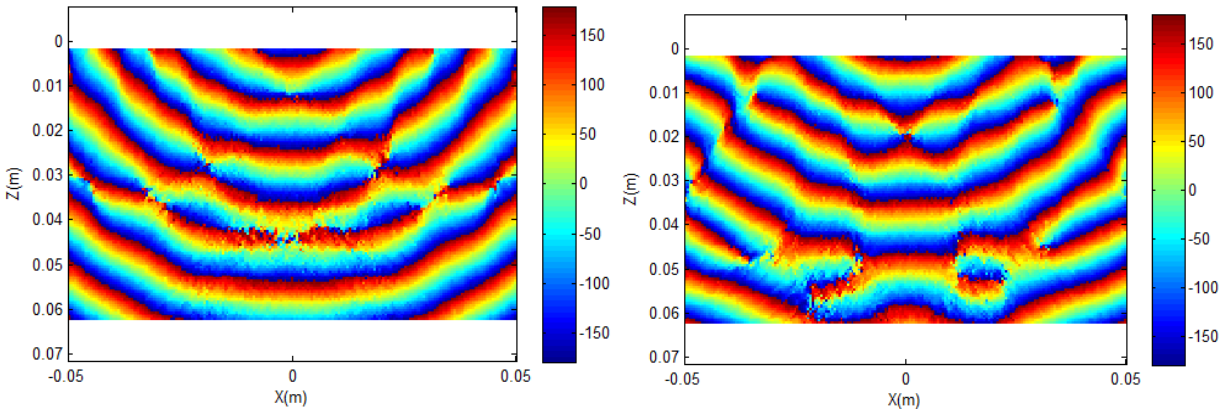

(a). 29 GHz

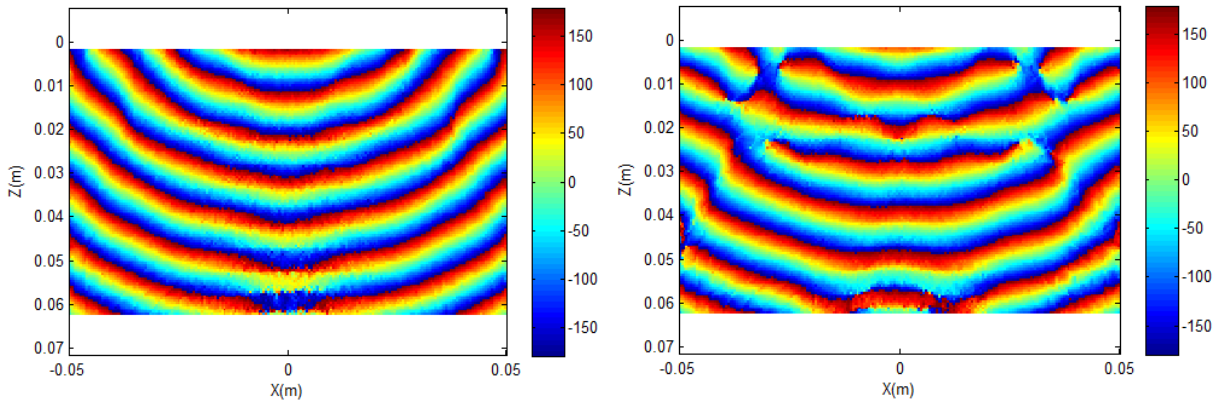

(b). 30 GHz

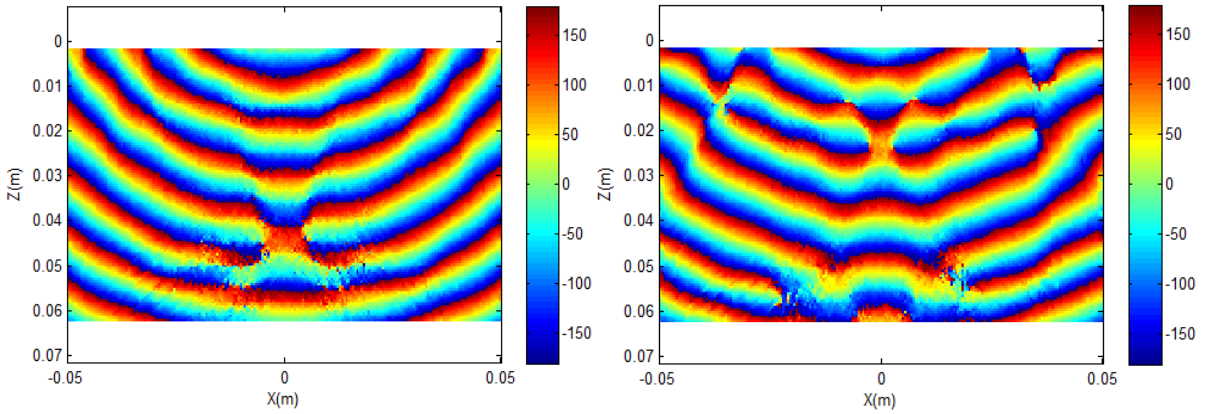

(c). 31 GHz

Figure 6.13: Sub-reflectarray scattered field phasefronts for the sub-wavelength (left) and half-wavelength (right) sub-reflectarrays with effective eccentricity of 1.45. The phase is shown with reference to the virtual focal point in Figure 6.10(b).

scattered phasefronts looks degraded compared to the ones shown in Figure 6.12, the superiority of the sub-wavelength sub-reflectarray performance (left in Figure 6.13) is unmistakable; the half-wavelength sub-reflectarray (right in Figure 6.13) exhibits more phasefront degradation even at 30GHz (the centre frequency). These sub-reflectarrays radiate over a wider angular range of -69.9° to 69.9° and hence they are more prone to the angle of incidence effects. This makes the use of sub-wavelength sub-reflectarray lattices a necessity to minimize the angle of incidence effects discussed in Section 6.3.

Figures 6.14 and 6.15 show the computed scattered near-field of the sub-reflectarrays of 2.22 eccentricity (for a coverage of -52.7° to 52.7°) over a finite-radius sphere, centred at the virtual focal point, that passes through the apex of the solid main-reflector shown in Figure 6.10(a) at 30GHz and 29GHz, respectively. These amplitude and phase patterns are good representatives of the sub-reflectarray fields on the solid reflector surface. The ripples shown in the amplitude and phase patterns are expected in sub-reflectarrays patterns [9]. What matters most in evaluating a sub-reflectarray performance is the phase flatness and the phase ripple depth [9] over the angular range of interest; it is the flatness that confirms there is a spherical phasefront (and certainly not a plane wavefront) from the sub-reflectarray that appears to originate from the sub-reflectarray virtual focal point. The phase patterns shown in Figures 6.14(b), which are calculated at 30GHz, exhibit good flatness over the specified angular region with relatively lower phase errors (ripple depth) for the sub-wavelength sub-reflectarray phase pattern. In Figure 6.15(b), the phase pattern of the half-wavelength sub-reflectarray suffers from high phase error compared to that of the sub-wavelength sub-reflectarray. This further complements the observations discussed on the scattered phasefronts in Figure 6.12.

Next the scattered patterns of the simulated sub-reflectarrays, whose scattered phasefronts are shown in Figures 6.12 and 6.13, were used to illuminate the main-reflectors shown in Figures 6.10(a) and 6.10(b), respectively. This was done by importing the near-fields of the sub-reflectarrays, which were computed at a finite distance from the sub-reflectarray, into the electromagnetic HFSS model of the solid main reflector. The far-zone scattered field from the solid main reflector was then calculated using the integral equation option in HFSS (HFSS-IE). Since the main-reflector/sub-reflectarray geometry was not simulated as one entity, the sub-reflectarray blockage effect was not accounted for in the far-field results. This does not disturb

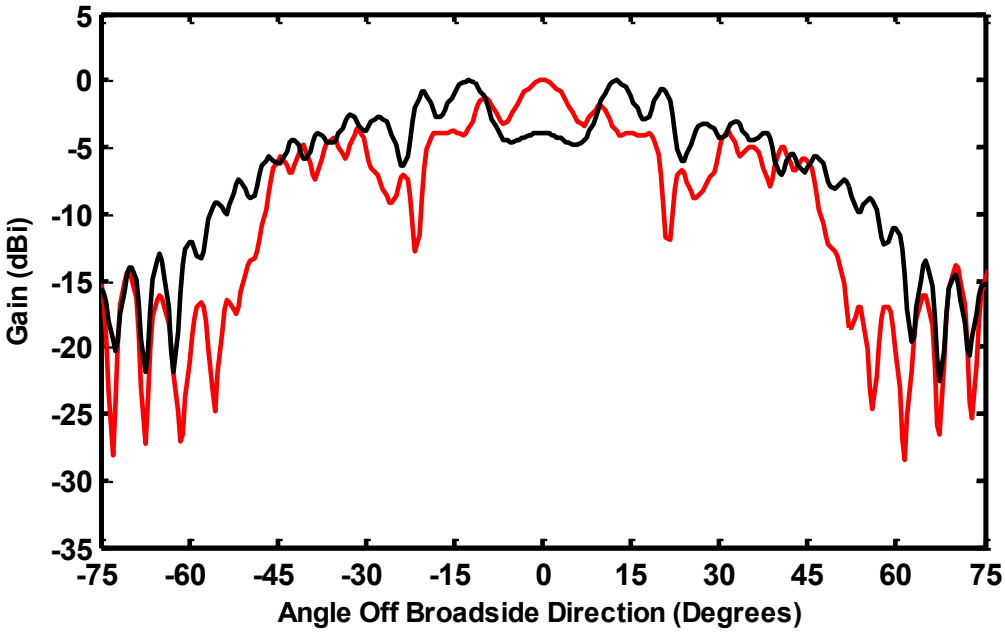

(a). Amplitude patterns

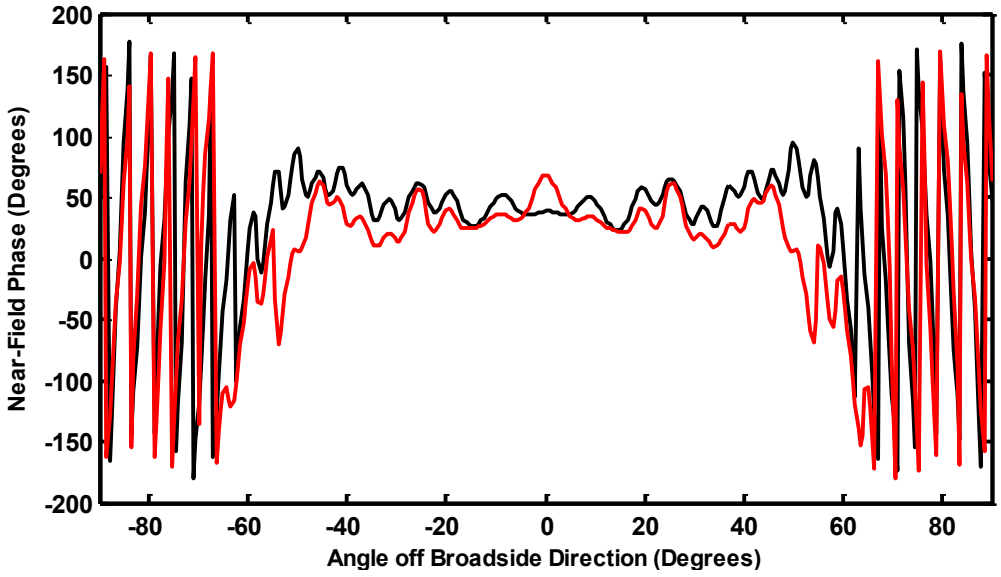

(b). Phase patterns

Figure 6.14: Computed scattered near-field of the sub-reflectarray over a finite-radius sphere, centred at the virtual focal point, that passes through the apex of the solid main-reflector. Results are shown at 30 GHz for the half-wavelength (——) and sub-wavelength (——) cases.

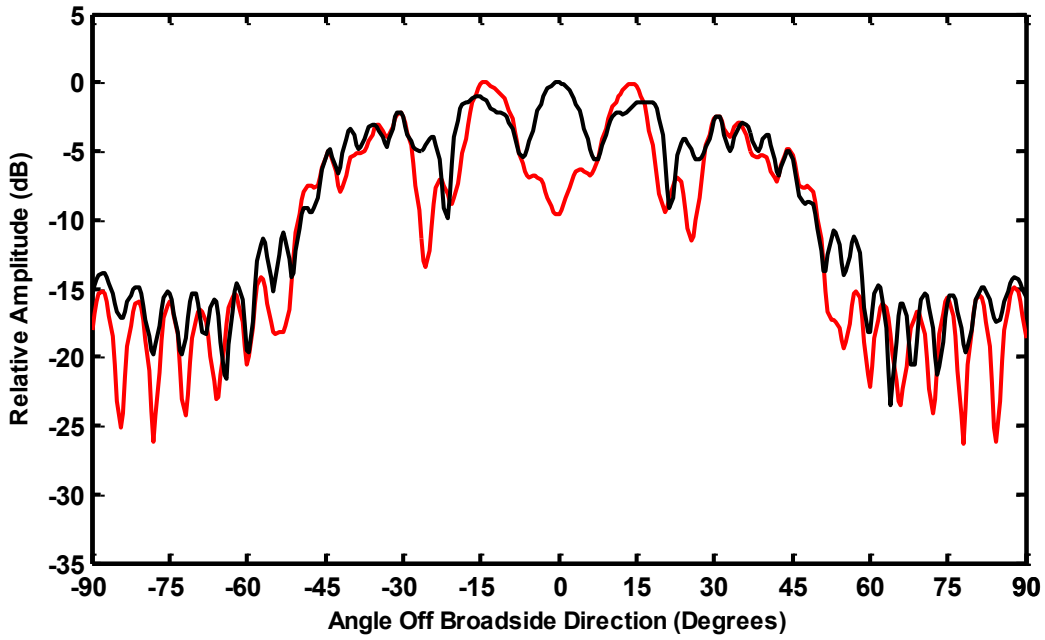

(a). Amplitude patterns

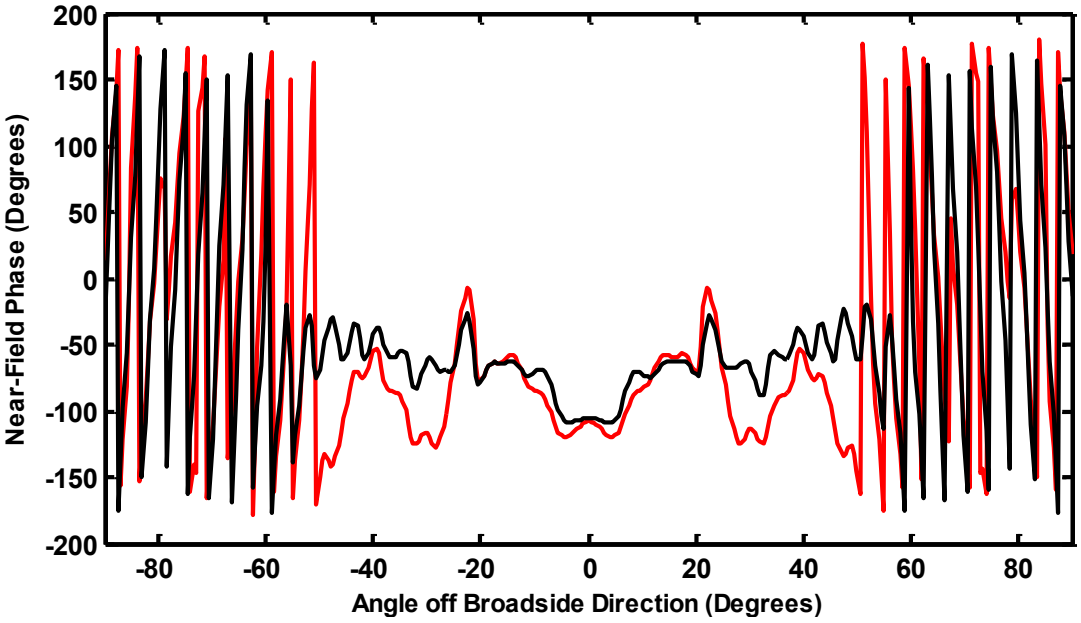

(b). Phase patterns

Figure 6.15: Computed scattered near-field of the sub-reflectarray over a finite-radius sphere, centred at the virtual focal point, that passes through the apex of the solid main-reflector. Results are shown at 29 GHz for the half-wavelength (——) and sub-wavelength (——) cases.

the goal of this study as we wanted to compare the performance of the sub-reflectarrays when they are used to illuminate a main-reflector; the blockage would be the same for all sub-reflectarrays anyway. The computed gain of the solid main reflector/sub-reflectarray antenna systems shown in Figures 6.10(a) and 6.10(b) are listed in Table 6.3. The gain values are consistent with the observation we made in Figures 6.12 through 6.15; whenever a sub-wavelength sub-reflectarray is used to illuminate the solid reflector for a given eccentricity value, the gain values are higher at all frequencies than those obtained when a half-wavelength sub-reflectarray is used. The low gain values when a half-wavelength sub-reflectarray is in use can be confidently blamed to its high sensitivity to angle of incidence particularly when the -69.9° to 69.9° angular coverage area is considered (eccentricity = 1.45).

Table 6.3: Computed gain (dBi) of the solid main reflector / sub-reflectarrray antenna system.

Effective Eccentricity	Sub-Reflectarray Type	29 GHz	30 GHz	31 GHz
2.22	Half-Wavelength	40.78	41.48	41.07
	Sub-Wavelength	41.58	42.07	41.78
1.45	Half-Wavelength	38.87	39.79	39.21
	Sub-Wavelength	40.41	41.26	40.54

Finally Figure 6.16 shows the 3D far-zone patterns of the main solid reflector calculated at 30GHz (the centre frequency) when illuminated by sub-wavelength sub-reflectarrays (left) and half-wavelength sub-reflectarrays (right). These patterns tie in with the gain values calculated at 30GHz listed in Table 6.3; the degradation of the half-wavelength sub-reflectarray performance, which was observed in Figure 6.13(b) (right), generates a high sidelobe level in the radiation pattern of the main reflector/half-wavelength sub-reflectarray system shown in Figure 6.16(b) (right). This led to the reduced gain of 39.79dBi for this system compared to the 41.26dBi gain for its corresponding sub-wavelength sub-reflectarray.

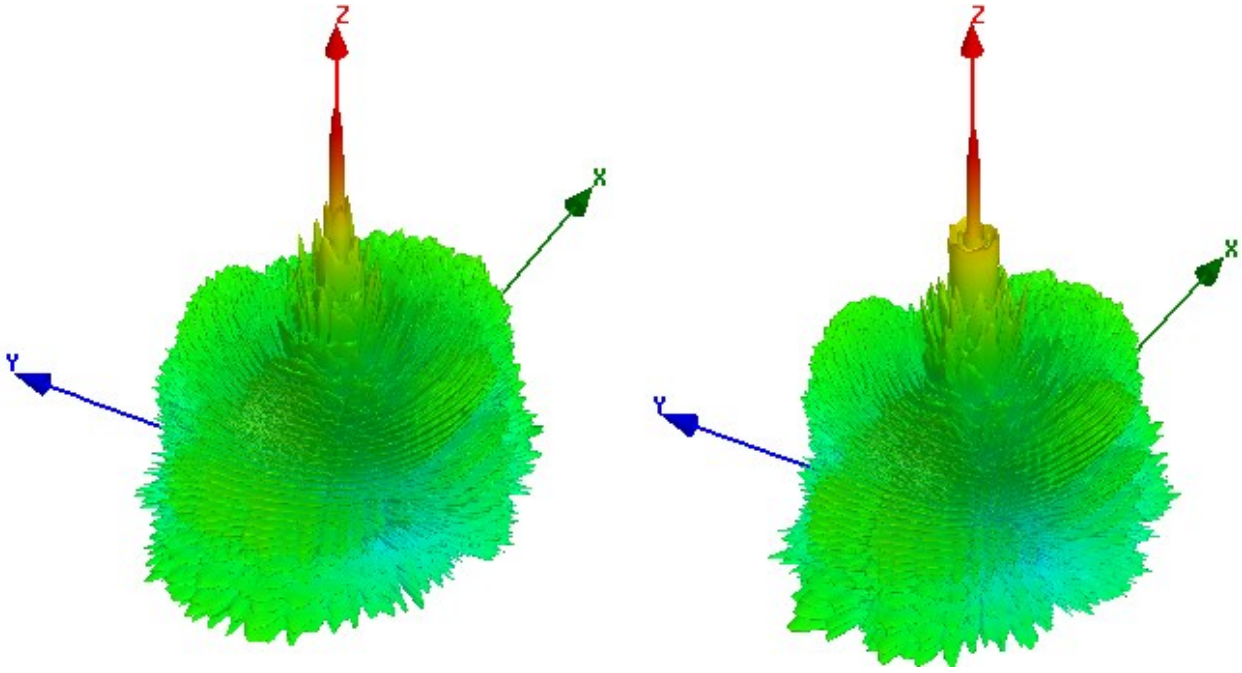

(a). Effective eccentricity of sub-reflectarray is 2.22

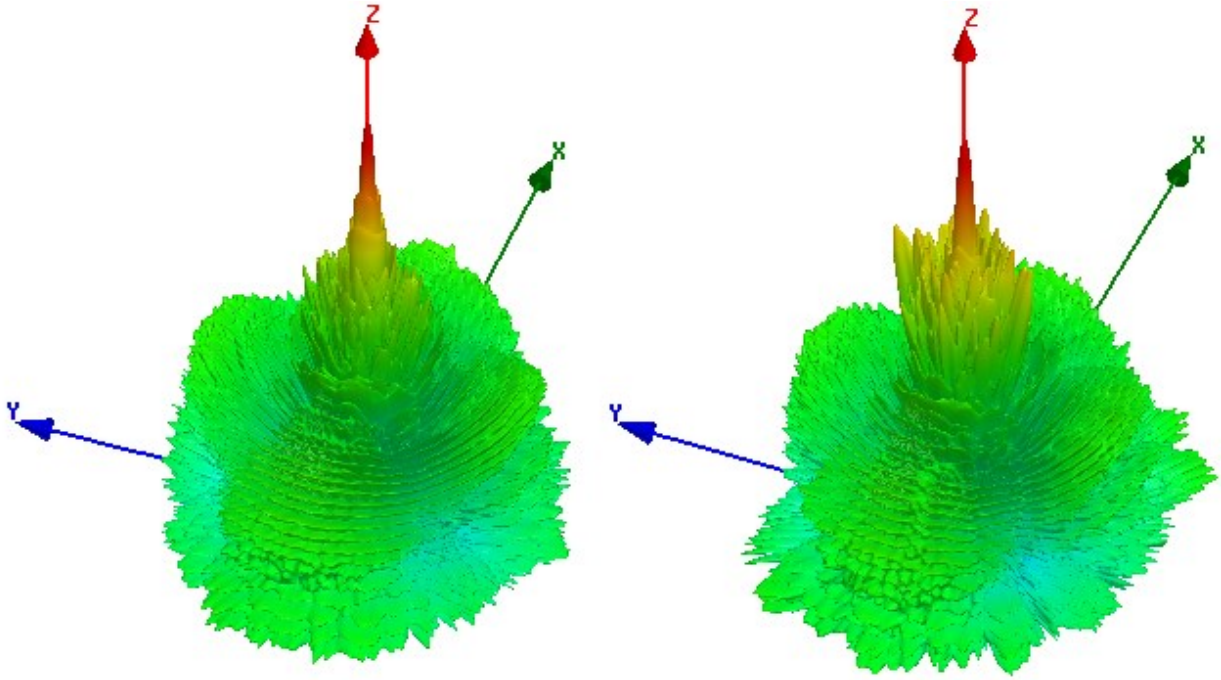

(b). Effective eccentricity of sub-reflectarray is 1.45

Figure 6.16: Radiation patterns of main-reflector/sub-reflectarray system geometries shown in Figure 6.10 calculated at 30GHz. Sub-wavelength sub-reflectarrays results are shown on the left, and the half-wavelength results on the right.

6.5 Concluding Remarks

In this chapter, the angle of incidence effect on the reflectarray and sub-reflectarray operation was investigated. This does not appear to have been done elsewhere in the literature. We began by describing how the feed location with respect to the reflectarray surface affects the angle of incidence value. In Section 6.2, some background on obliquely incident plane waves was illustrated. This is crucially important to understand how we set up the element reflection phase database. In Section 6.3, we first showed that not only does incidence angle alter the element reflection phase, but that for oblique incidence the element beamwidth narrows and the element pattern deforms. We next examined the impact of including incidence angle effects in the design database of half-wavelength reflectarrays, and compared that to sub-wavelength reflectarray designs for F/D = 1.0 and F/D = 0.5. It was shown that the inclusion of the angle of incidence effect in the half-wavelength reflectarray design improves its performance, especially when a small F/D value is considered. However, it was noticed that the sub-wavelength reflectarray decently outperforms the half-wavelength reflectarray performance even when the angle of incidence changes are included in the latter design. This sub-wavelength reflectarray superiority stems from the fact that for sub-wavelength lattices not only is the reflection phase change with incidence angle less severe than for half-wavelength lattices, but the element pattern changes are very much smaller too. Since sub-reflectarrays are more prone to the angle of incidence effects, because they radiate over a much wider angular range compared to main-reflectarrays, it is important to design them using elements that are immune to the angle of incidence change. In Section 6.4, we illustrated that such immunity was achieved when sub-wavelength elements were incorporated in designing sub-reflectarrays. The performance of sub-wavelength and corresponding half-wavelength sub-reflectarrays was first compared by studying their scattered near-fields on their own. The uniformity and flatness of the scattered phasefronts from these sub-reflectarrays were used as a figure of merit to compare their performance. The sub-reflectarrays were then used to illuminate a solid main-reflector to see the impact of their performance on the overall main reflector/sub-reflectarray system gain. The sub-wavelength sub-reflectarrays are shown to outperform their corresponding half-wavelength ones, particularly when the design demands a wide angular coverage. This further confirms the low sensitivity of sub-wavelength sub-reflectarrays to the angle of incidence.

Chapter 6 References

[1] P.Nayeri, A.Elsherbeni and F.Yang, "Radiation analysis approaches for reflectarray antennas", IEEE Antennas and Propagation Magazine, Vol.55, No.1, pp.127-134, February 2013

[2] H.Rajagopalan, X.Shenheng & Y.Rahmat-Samii, "Experimental demonstration of reflectarrays acting as conic section subreflectors in a dual reflector system", IEEE Transactions on Antenna and propagation, Vol.61, No.11, pp. 5475-5484, November 2013.

[3] S.D.Targonski and D.M.Pozar, "Analysis and design of a reflectarray using patches of variable size", IEEE International Symposium on Antenna and Propagation, Vol.3, pp.1820-1823, June 1994.

[4] MATLAB , Mathworks Inc. Available: http://www.mathworks.com.

[5] HFSS, Ansoft Product Suite, Ansys Inc., USA (www.ansoft.com).

[6] P.Nayeri, F.Yang and A.Elsherbeni, "A broadband microstrip reflectarray using sub-wavelength patch elements", IEEE International Antennas Propagation Symposium Digest, Charleston, South Carolina, USA, June 2009.

[7] J.Ethier, M.R.Chaharmir and J.Shaker, "Reflectarray design comprised of sub-wavelength coupled-resonant square loop elements", Electronic Letters, Vol.47, No.22 pp.1215-1217,October 2011.

[8] C.Granet, "Designing classical offset Cassegrain or Gregorian dual-reflector antennas from combinations of prescribed geometric parameters," IEEE Antennas and Propagation Magazine, Vol.44, No.3, pp. 114–123, June 2002.

[9] **E.Almajali**, D.A.McNamara, J.Shaker and M.R.Chaharmir, " Derivation and validation of the basic design equations for symmetric sub-reflectarrays", IEEE Transactions on Antenna and Propagation, Vol.60, No.2, pp.2336-2346, February 2012.

CHAPTER 7

Conclusions and Future Work

7.1 The Contributions of the Thesis

The principal contributions of the thesis are as follows:

- Developing a new understanding of the fundamental operating principles of reflectarray antennas has been an important aspect of this thesis. A technique [1] was found to theoretically determine the separate contributions of the conduction currents (on the conducting elements and groundplane), and polarization currents (in the dielectric substrate), on reflectarray performance for the first time. The extraction of the currents from a rigorous electromagnetic model of a reflectarray, as well as the determination of the fields due to these individual contributions, form the key to the diagnosis of some reflectarray problem aspects, and hence pave the way to mitigate them.

- The real cause of the unwanted feed-image lobe phenomenon, which limits reflectarray antenna bandwidth, was successfully diagnosed using the component-by-component technique mentioned above. Accordingly, and using this novel technique, it was possible to present the use of sub-wavelength elements as a way to mitigate this unwanted phenomenon, which leads to a significant improvement in reflectarray antenna performance [2].

- The real cause of beam squint in offset-fed reflectarrays is diagnosed in this thesis [3]. The observation of reflectarray focal point shift with frequency represents the key approach used to diagnose the cause of this deleterious phenomenon in offset-fed reflectarrays. The solution devised in this thesis to avoid such beam squint [4] allows designers to orient the main beam in the broadside direction without suffering from any unwanted beam squint at off-centre frequencies. The approach devised gives antenna engineers a wide degree of freedom as far as the mounting of such reflectarrays in practice is concerned. The proposed configuration has a bonus advantage in that it can function as a spatial power combiner and antenna at the same time [5], something that will be of increasing utility as wireless communications frequencies increase and more than one solid state source is needed to achieve some required power level.

- Some problem aspects of the configuration used for beam squint suppression, which was the two-feed single-beam reflectarray, were identified and mitigated. First the use of sub-wavelength elements in designing two-feed reflectarrays instead of the half-wavelength ones was proven to substantially improve this antenna gain and bandwidth [5]. Next, the cause of the grating lobes observed in the two-feed reflectarray radiation pattern was identified [6] and a solution was proposed and validated.

- The angle of incidence effect on reflectarray and sub-reflectarray performance is first presented in this thesis. It was shown that not only does incidence angle alter the element reflection phase, which is known, but that for oblique incidence the element beamwidth narrows and the element pattern deforms, leading to performance degradation. This is important not only from the point of view of the coupling of the feed fields to the elements, but also as far as the angular sector within which the reradiated fields are important. It was established accordingly that sub-wavelength elements suffer much less from element pattern deformation compared to their corresponding half-wavelength ones.

- The use of sub-wavelength elements in designing sub-reflectarray antennas is proposed in this thesis for the first time. This was shown to significantly improve sub-reflectarray performance as they are usually used to illuminate large reflectors in compact dual antenna systems and so a wide angular coverage is demanded of them.

- The impact of important factors namely, reflectarray size, focal length, element type and lattice size on the amount of focal shift versus frequency is established. It was consequently shown that the focal shift with frequency is not sensitive to a reflectarray element type or lattice size and hence beam squint in offset-fed reflectarrays was shown to be independent of these element properties. Furthermore, focal shift with frequency was interpreted in terms of Fresnel zone considerations. This was shown to reinforce conclusions obtained using full wave receive-mode analysis [3,7].

7.2 Future Work

The following future work may prove fruitful by developing and utilizing the operating mechanisms examined, as well as the solutions to problem aspects presented, in this thesis:

- The reflectarray operating mechanism explained in Chapter 3 can be utilized in studying the operation and consequently solving problem aspects of similar antennas like the transmitarray; the actual current amplitude and phase distributions on transmitarray conducting elements may reveal much about this type of potentially promising antenna.

- The improved sub-wavelength sub-reflectarrays designed in Chapter 6 can be used as part of a dual-sub-wavelength reflectarray antenna system in which both the sub-reflectarray and the main-reflectarray are designed using a sub-

wavelength lattice to immunize the entire system against the angle of incidence effects.

- The focal shift mechanism illustrated in Chapter 5 can be extended to study the behavior of focal-field regions in sub-reflectarrays versus frequency. This might help in devising a new method to supress beam squint in offset-fed dual-reflectarray antenna systems. This might possibly be achieved at the sub-reflectarray level in such a way that cancels any phase tilt on the main-reflectarray surface at off-centre frequencies.

Chapter 7 References

[1] **E.Almajali**, D.A.McNamara, J.Shaker and M.R.Chaharmir, "An investigation of reflectarray operation using its component current contributions", Proceedings of the 6th European Conference on Antennas and Propagation, EuCAP, Prague, Czech Republic, March 2012.

[2] **E.Almajali**, D.A.McNamara, J.Shaker and M.R.Chaharmir, "Feed image lobes in offset-fed reflectarrays: Diagnosis and solution", IEEE Trans. Antennas Propagation, Vol.62, No.1, pp.216-226, January 2014.

[3] **E.Almajali**, D.A.McNamara, J.Shaker and M.R.Chaharmir, "On beam squint in offset-fed reflectarrays", IEEE Antennas Wireless Propagat. Letters, Vol.11, pp.937-940, 2012.

[4] **E.Almajali**, D.A.McNamara, J.Shaker and M.R.Chaharmir, "Beam squint suppression in offset-fed reflectarrays", IEEE Antennas Wireless Propagat. Letters, Vol.12, pp.587-590, 2013.

[5] **E.Almajali**, D.A.McNamara, J.Shaker and M.R.Chaharmir, "Improved dual-feed single-beam power-combining reflectarray antenna", Electronics Letters, Vol.49, No.25, pp.1595-1597, December 2013.

[6] **E.Almajali**, D.A.McNamara, J.Shaker and M.R.Chaharmir, "Grating lobe control in dual-feed single-beam reflectarrays and power combiners", IEEE Antennas Wireless Propagat. Letters, Vol.12, pp.1268-1271, 2013.

[7] **E.Almajali**, D.A.McNamara, J.Shaker and M.R.Chaharmir, "Observations on the performance of reflectarrays with reduced inter-element spacings", IEEE AP-S Int. Symp. Dig*est*, July 2011, Spokane, Washington, USA.